

DISS. ETH No. 14799

A NUMERICAL ANALYSIS OF CONFINED
TURBULENT BUBBLE PLUMES

A dissertation submitted to the
SWISS FEDERAL INSTITUTE OF TECHNOLOGY ZURICH

for the degree of
Doctor of Technical Sciences

presented by

MASSIMO MILELLI

Dipl. Phys. Univ. Torino
born on September 4, 1970
citizen of Torino, Italy

accepted on the recommendation of

Prof. George Yadigaroglu, Zurich, examiner
Prof. Michel Lance, Lyon, co-examiner
Dr. Brian L. Smith, Villigen, co-examiner

2002

Acknowledgments

This work was funded by the Paul Scherrer Institute (PSI) in Villigen, Switzerland, and by the Swiss Federal Institute of Technology (ETH) in Zurich, Switzerland.

I would like to thank first of all Professor George Yadigaroglu of ETH Zurich who gave me the opportunity to work on this project. He was always ready to bring fruitful suggestions which were really appreciated.

Professor Michel Lance from Université Claude Bernard, Lyon, was kind enough to act as a co-reviewer of this thesis. His unique experience on bubbly flows was extremely useful. He suggested to perform the shear layer calculations described in Chapter 6.

Dr. Brian Smith of PSI, was not simply a supervisor. He initiated the work, he shared his enormous experience on mathematics and CFD (and his office) with me, he reviewed my manuscripts, he helped me in any circumstance and, he was a wonderful English teacher. I can say without any doubt that without his support, I could not have got to the conclusion of the work.

Dr. Michele Andreani of PSI was one of the promoters of the doctoral project. He gave me assistance many times in these four years and his deep knowledge of two-phase flow problems was definitely fundamental.

Dr. Djamel Lakehal of ETH Zurich supported me with the use of the Large Eddy Simulation model of turbulence. His great experience on the subject was of invaluable help to me.

I would like to thank the senior staff of LTH, from Dr. Joerg Dreier, head of the laboratory, to the secretary Verena Knecht for their help in various occasions. I would also like to include Mrs. Margaret Pavletic, secretary at LKT in Zurich for her help in many administrative issues.

I should thank many other people for their support: Padiyath Kumar of PSI, the best system administrator I met, Trevor Dury of PSI for his hints on mesh generation problems, Chidambaram 'Chidu' Narayanan of ETH Zurich for his fortran programs for the Fast Fourier Transform, and all the people who supported me during these years.

Finally I thank my wife Silvia and my son Fabrizio (even though he can not understand), my parents and all my friends, in Italy and in Switzerland who encouraged me during this adventure.

I conclude by remembering the exhaustive words of one of the fathers of the modern physics:

*"Before I die, I hope that someone will explain quantum mechanics to me.
After I die, I hope that God will explain turbulence to me."*

Werner Heisenberg

Contents

Acknowledgments	i
Contents	iii
Abstract	vii
Sintesi	ix
Nomenclature	xi
1 Introduction	1
1.1 Motivation	1
1.2 The physical situation	3
1.3 Literature overview: experiments	3
1.4 Literature overview: modelling	6
1.4.1 Quasi-single-phase model	7
1.4.2 Euler/Lagrange model	7
1.4.3 Euler/Euler model	9
1.4.4 Turbulence modelling	10
1.5 Summary of the thesis	12
2 Comparison of existing models for the case of a bubble plume	15
2.1 Introduction	15
2.2 Experimental set-up	15
2.3 Model set-up	15
2.3.1 Interfacial forces	16
2.3.2 Turbulence models	20
2.4 Calculations	25
2.4.1 Results of different grid set-up	26
2.4.2 Results of different turbulence models	28
2.5 Conclusions	30
3 Random Dispersion Model	49
3.1 Introduction	49
3.2 Model set-up	49

3.3	Test calculations	51
3.4	Bubble plume calculations	54
3.5	Conclusions	56
4	Towards Large Eddy Simulation of Turbulence	63
4.1	Introduction	63
4.2	Governing equations	63
4.3	Code validation	68
4.3.1	Experimental setup	68
4.3.2	Numerical results	69
4.4	Conclusions	75
5	Large Eddy Simulation: grid turbulence	77
5.1	Introduction	77
5.2	3D calculations	77
5.3	2D calculations	81
5.4	Conclusions	86
6	Large Eddy Simulation: shear flow	89
6.1	Introduction	89
6.2	Experimental setup	89
6.3	Numerical setup	89
6.4	Calculations	94
6.4.1	Effects of grid size and lift coefficient	94
6.4.2	Effect of subgrid model	95
6.4.3	Effect of bubble-induced turbulence	95
6.4.4	A new proposal for bubble-induced turbulence	96
6.4.5	Effects of different bubble-induced turbulence terms	96
6.5	Conclusions	96
7	Large Eddy Simulation: bubble plume	117
7.1	Introduction	117
7.2	Numerical setup	117
7.3	Results of the calculations	118
7.4	Conclusions	121

8 Conclusions and future perspectives	135
8.1 Summary and conclusions	135
8.2 Suggestions for future work	137
References	139
Curriculum Vitae	145

Abstract

Complex, 3D mixing of single- and multi-phase flows, in particular by injection of gas and creation of bubble plumes, occurs in a number of situations of interest in energy technology, process and environmental engineering, etc. For all these applications, the basic need is to determine the behaviour of the bubble plume and the currents induced by the ascending gas plume in the surrounding liquid and thereby the consequent mixing in the body of the liquid.

A six-equation, two-fluid model was utilized and transient calculations were performed to study the plume growth, the acceleration of the liquid due to viscous drag, and the approach to steady-state conditions. All calculations were performed using the commercial CFD code CFX4, with appropriate modifications and code extensions to describe the interphase momentum forces and the turbulent exchanges between the phases. Since the $k - \epsilon$ is a single-phase model, an extended version was used, with extra source terms introduced to account for the interaction between the bubbles and the liquid. A new model was advanced to relate turbulent bubble dispersion to statistical fluctuations in the liquid velocity field, affecting the drag and lift forces between the phases. The model is able to account for the dispersion of bubbles due to the random influence of the turbulent eddies in the liquid, such as the empirical *Turbulent Dispersion Force* described in §2.3.1, and has the advantage that no fitting coefficients need to be introduced.

The interphase forces are not the only source of empiricism: the above-mentioned extra source terms introduced into the $k - \epsilon$ model, are patch-ups which introduce *ad hoc* empirical coefficients which can be tuned to get good comparison with the data. Further, the hypothesis of turbulence isotropy has still to be rigorously proved with clean experimental data. The Reynolds Stress Models (RSMs), which are in principle appropriate for this kind of flow (since equations are solved for each component of the Reynolds stress tensor), are unstable and not robust enough, and it is difficult to achieve convergence even for single-phase flows. Therefore, attention was focused on Large Eddy Simulation (LES) turbulence models.

The main advantage of LES for this class of flows is that it captures directly the interactions of the bubbles with the resolved large-scale structures up to the size of the grid (close to the bubble diameter), whereas the interaction with the subgrid scales can be modelled. In other words, the turbulent dispersion of the bubbles is due only to the largest structures, which are calculated directly with LES. Since this is a new area of study, many open questions will need to be addressed: a universally-accepted, two-phase subgrid model does not exist, and the influence of the grid on the simulation is also not clear, since this determines the scales that are going to be resolved. To pursue this approach, the LES model was implemented into CFX-4. First, a single-phase test case has been calculated to validate the model against the data of GEORGE ET. AL., 1977. Second, a simple case (a 3D box with homogeneous distribution of bubbles) has been run to study the modifications induced by the bubbles on the turbulence of the system and the effect of the filter (mesh size). The results have been obtained with the SMAGORINSKY, 1963 subgrid model and were compared with the experimental data of LANCE & BATAILLE, 1991, finding that the turbulence intensities increase with the mesh size, and the optimum configuration requires a mesh comparable to the bubble diameter; otherwise the liquid velocity fluctuations profile is not

captured at all, meaning that the grid is too coarse. The idea recalls the Scale-Similarity Principle of BARDINA ET AL., 1980.

Taking advantage of this experience, two more elaborate situations, closer to reality, were analyzed: the case of a turbulent bubbly shear flow in a plane vertical mixing layer, with calculations compared against the data of ROIG, 1993; and the case of the bubble plume, with calculations compared against the data of ANAGBO & BRIMACOMBE, 1990. A study on the importance of the lift force has been carried out and the results were similar in both cases, with an optimum lift coefficient of 0.25. The results showed good agreement with the experiment, although a more detailed study of bubble-induced turbulence (or pseudo-turbulence) is required. The GERMANO ET AL., 1991 dynamic procedure was successfully tested and a new subgrid scale model for the dispersed phase that requires no empirical constants, was introduced.

Sintesi

La miscela tridimensionale di flussi a fase singola e doppia, in particolare per l'iniezione di gas e la creazione di piume di bolle, avviene in un grande numero di applicazioni ingegneristiche ed ambientali. Per tutte queste applicazioni è determinante definire il comportamento delle piume di bolle e le correnti indotte dal gas che sale nel liquido circostante e il conseguente miscelamento.

È stato utilizzato un modello a due fluidi con sei equazioni, non stazionarie, per studiare la crescita della piuma, l'accelerazione del liquido dovuta alla viscosità e il raggiungimento di uno stato statisticamente stazionario. Tutti i calcoli sono stati effettuati con il codice commerciale di calcolo CFX4, con opportune modifiche per descrivere le forze di accoppiamento del momento e lo scambio di energia turbolenta tra le due fasi. È stato usato un modello di turbolenza $k - \epsilon$, modificato con l'introduzione di nuovi termini, per tenere conto dell'interazione fra le bolle e il liquido. Un nuovo modello è stato introdotto per correlare la dispersione turbolenta delle bolle alle fluttuazioni statistiche del campo di velocità del liquido, le quali modificano le forze di resistenza e portanza. Il modello è in grado di rappresentare la dispersione delle bolle dovuta all'influenza stocastica dei vortici turbolenti nella fase liquida, così come la *Forza di Dispersione Turbolenta* descritta nel paragrafo §2.3.1, con il vantaggio di non avere ulteriori coefficienti da regolare.

Le forze di accoppiamento fra le due fasi non sono l'unica fonte di empiricità: i suddetti nuovi termini nel modello $k - \epsilon$ infatti sono delle correzioni che introducono coefficienti empirici che possono essere regolati a piacere. Inoltre l'ipotesi di isotropia della turbolenza deve ancora essere provata in maniera rigorosa. Il modello RSM che in principio è più appropriato per questo tipo di flusso, dal momento che vengono risolte direttamente le equazioni per le componenti del tensore degli sforzi, non è numericamente stabile e non è facile ottenere la convergenza, anche in condizioni di flussi a fase singola. Di conseguenza, l'attenzione è stata concentrata sul modello di simulazione della turbolenza a grande scala (LES).

Il principale vantaggio del modello LES per questo tipo di flussi è che vengono calcolate direttamente le interazioni delle bolle con le strutture di scala corrispondente al diametro delle bolle stesse e più grandi, mentre le interazioni con le scale minori vengono parametrizzate. In altre parole, la dispersione turbolenta delle bolle, che è dovuta principalmente alle scale di turbolenza maggiori, viene calcolata e non simulata. Dal momento che questa è una nuova area di ricerca, molte questioni devono venire risolte: un modello universale per l'approssimazione delle scale di turbolenza minori (in presenza di bolle) non esiste, e l'influenza della griglia sulla simulazione non è chiara, dal momento che quest'ultima determina le scale che vengono calcolate e quelle che vengono approssimate. Per ottenere queste risposte, il modello LES è stato per prima cosa introdotto nel codice CFX4. In principio il modello è stato convalidato in caso di flusso a fase singola con i risultati di GEORGE ET. AL., 1977. In seguito, è stato introdotto un caso semplice di flusso bifase (una scatola tridimensionale con una distribuzione omogenea di bolle) per studiare l'influenza delle bolle sulla turbolenza del sistema e l'effetto della griglia. I risultati sono stati ottenuti con il modello di SMAGORINSKY, 1963, per le scale di turbolenza inferiori alle dimensioni della griglia, e sono stati comparati ai dati sperimentali di LANCE & BATAILLE, 1991, ottenendo che l'intensità della turbolenza cresce all'aumentare delle

dimensioni della griglia. La configurazione migliore richiede che la griglia sia dell'ordine del diametro delle bolle, altrimenti il profilo delle fluttuazioni del liquido non verrebbe risolto perché la risoluzione della griglia sarebbe troppo scarsa. Questa idea richiama il principio di similarità di scala di BARDINA ET AL., 1980.

Prendendo spunto da questi risultati, sono state studiate due situazioni più complesse e più vicine alla realtà: il caso di un flusso turbolento a due velocità con bolle in un piano verticale, con risultati comparati ai dati di ROIG, 1993; e il caso di una piuma di bolle, con risultati confrontati a quelli di ANAGBO & BRIMACOMBE, 1990. È stato effettuato uno studio sugli effetti della forza di portanza che ha dato in entrambi i casi un risultato simile, con un coefficiente di 0.25. I risultati sono in buon accordo con i dati sperimentali anche se è necessario approfondire lo studio della turbolenza indotta dal passaggio delle bolle. La procedura dinamica di GERMANO ET AL., 1991 è stata testata con successo ed è stato proposto un nuovo modello per la turbolenza delle bolle a scala minore della griglia, il quale non richiede ulteriori costanti empiriche.

Nomenclature

A	$[m^2]$	area
c	$[m^2/s^2K]$	specific heat capacity
C	$[-]$	C_s^2
C_D	$[-]$	drag coefficient
C_{VM}	$[-]$	virtual mass coefficient
C_L	$[-]$	lift coefficient
C_f	$[s^{-1}]$	interphase friction coefficient
C_s	$[-]$	Smagorinsky constant
C_{TD}	$[-]$	turbulent dispersion coefficient
$C_{\mu b}$	$[-]$	constant in Sato model
C_{k_1}, C_{ϵ_1}	$[-]$	constants in $k - \epsilon$ model
C_1, C_2, C_μ	$[-]$	constants in $k - \epsilon$ model
C_{k_2}, C_{ϵ_2}	$[-]$	constants in Simonin and Viollet model
d_b	$[m]$	bubble diameter
d, D	$[m]$	diameter
$D_{l,g}/Dt$	$[s^{-1}]$	substantial derivative
$\partial/\partial x_i$	$[m^{-1}]$	spatial partial derivative
$\partial/\partial t$	$[s^{-1}]$	time partial derivative
dt	$[s]$	time interval
F	$[kg/m^2s^2]$	interfacial forces
\mathbf{g}, g	$[m/s^2]$	gravitational acceleration vector / scalar
N	$[-]$	number of bubbles
p	$[Pa], [bar]$	pressure
Pr	$[-]$	Prandtl number ($\mu c/\lambda$)
\dot{Q}	$[m^3/s]$	volumetric flow rate
\dot{Q}	$[liters/min]$	volumetric flow rate
r	$[m]$	radius
P_l	$[m^2/s^3]$	production term in $k - \epsilon$ model
Re	$[-]$	Reynolds number
Re_b	$[-]$	bubble Reynolds number
T	$[K], [^\circ C]$	temperature
t	$[s]$	time
t_R	$[s]$	residence time
t_E	$[s]$	eddy lifetime
u, v	$[m/s]$	axial / radial velocities in 2D-axisymmetric coordinates
V	$[m^3]$	volume
w	$[m/s]$	axial velocity in 3D cartesian coordinates
x	$[m]$	spatial coordinate
y	$[m]$	spatial coordinate
z	$[m]$	axial coordinate

Greek:

α	$[-]$	volume fraction
α_t	$[kg/ms]$	turbulent diffusivity
Δ	$[m]$	filter width
Δt	$[s]$	time step
$\Delta x, \Delta_x$	$[m]$	grid size

$\Delta y, \Delta_y$	$[m]$	grid size
$\Delta z, \Delta_z$	$[m]$	grid size
δ	$[-]$	Kronecker symbol
ϵ	$[m^2/s^3]$	turbulent dissipation
ϵ_{ijk}	$[-]$	Levi-Civita tensor
k	$[m^2/s^2]$	turbulent kinetic energy
λ	$[W/m\ K]$	thermal conductivity;
μ	$[kg/m\ s]$	dynamic viscosity
μ_t	$[kg/m\ s]$	turbulent dynamic viscosity
ν	$[m^2/s]$	kinematic viscosity (μ/ρ)
ν_t	$[m^2/s]$	turbulent kinematic viscosity (μ_t/ρ)
ω_i	$[s^{-1}]$	vorticity components
Ω	$[m^3]$	integration domain
ρ	$[kg/m^3]$	density
σ	$[N/m]$	surface tension
σ_t	$[-]$	turbulent Prandtl number
σ_{ij}	$[Kg/ms^2]$	deviatoric part of the stress tensor
$\sigma_k, \sigma_\epsilon$	$[-]$	constants in $k - \epsilon$ model
τ_{ij}	$[Kg/ms^2]$	stress tensor

Subscripts:

0	initial, inlet value
a	air
b	bubble
g	gas (air)
i, j	coordinate indices
l	liquid
lam	laminar
tur, t	turbulent
x, y, z	Cartesian components

Superscripts:

sgs	subgrid scale
\tilde{f}, \hat{f}	filtered fields
f'	fluctuation

1 Introduction

*"The Road goes ever on and on
Down from the door where it began.
Now far ahead the Road has gone,
And I must follow, if I can,
Pursuing it with eager feet,
Until it joins some larger way
Where many paths and errands meet.
And whither then ? I cannot say."*
J.R.R. Tolkien (Lord of the Rings)

1.1 Motivation

Nuclear power provides today roughly 15% of the world's electricity generation (IEA - WORLD ENERGY OUTLOOK, 2000). Recent political decisions in certain countries indicate a wish to move to alternative energy sources. In spite of this, it is likely that nuclear power plants will remain operational worldwide. New types of nuclear reactors are being studied (YADIGAROGLU & DREIER, 1998), including Advanced Light Water Reactors (ALWRs), and innovative concepts such as the European Simplified Boiling Water Reactor (ESBWR). A special feature of some of these reactors is passive decay heat removal, which means that, in the case of an accidental depressurization of the primary system, the heat is released to the atmosphere via a passive system which, on the one side, increases safety and, on the other side, reduces capital and operating costs.

The introduction of passive cooling systems means there is a need to study in detail the complex, 3D phenomena (mixing of multi-phase flows) which will occur in the containment volumes surrounding the primary system as, for instance, the pressure suppression pools where condensable gas (steam), non-condensable gases (nitrogen) and water can mix.

In this context, the Paul Scherrer Institute (PSI) initiated in 1991 the ALPHA (Advanced Light Water Reactor Passive Heat Removal and Aerosol Retention) project. In particular, the work carried out in the present study fell within the proposals of the Technology Enhancement of Passive Safety Systems (TEPSS) project (STOOP ET AL., 1997), of the Framework Programme IV of the European Atomic Energy Community, Jan 1996 to Dec 1998. In collaboration with similar laboratories in the Netherlands and in Spain, the work at PSI aimed to make significant additions to the technology base relating to advanced, passive-type Boiling Water Reactors (BWRs).

As part of this activity, research was undertaken to support development of improved countermeasures against pool stratification. These efforts, embodied in the sub-project LINX (Large-Scale Investigation of Natural Circulation and Mixing), were directed towards a better understanding of the most important physical processes taking place in deep-pool, thermal and two-phase plumes, and the testing of concepts for avoiding or minimizing hot, stratified pool regions. The main effort in the programme centers on a medium-scale, highly-instrumented test facility, LINX-2 (see Fig. 1.1), which is used to study multi-phase natural circulation, mixing and condensation phenomena in pressure suppression pools and containment volumes, under prototypic pressure and temperature conditions, and in the presence of non-condensable gases (DE CACHARD ET AL., 1997).

In parallel with the experimental programme, CFD (Computational Fluid Dynamics) models are being assembled, aimed at developing reliable, multi-phase turbulence models for application to mixing and natural circulation problems of the type which fall within the scope of the TEPSS project. First analyses concern bubble-induced mixing in open pools and the present work falls within this context. The aim is in fact the study of the interphase forces and the turbulence induced by the bubbles in the liquid in order to represent them in a more physical way, reducing the number of empirical parameters coming out from the Reynolds Average approach. Therefore we explore the use of more advanced turbulence models, in particular the Large Eddy Simulation (LES) model.

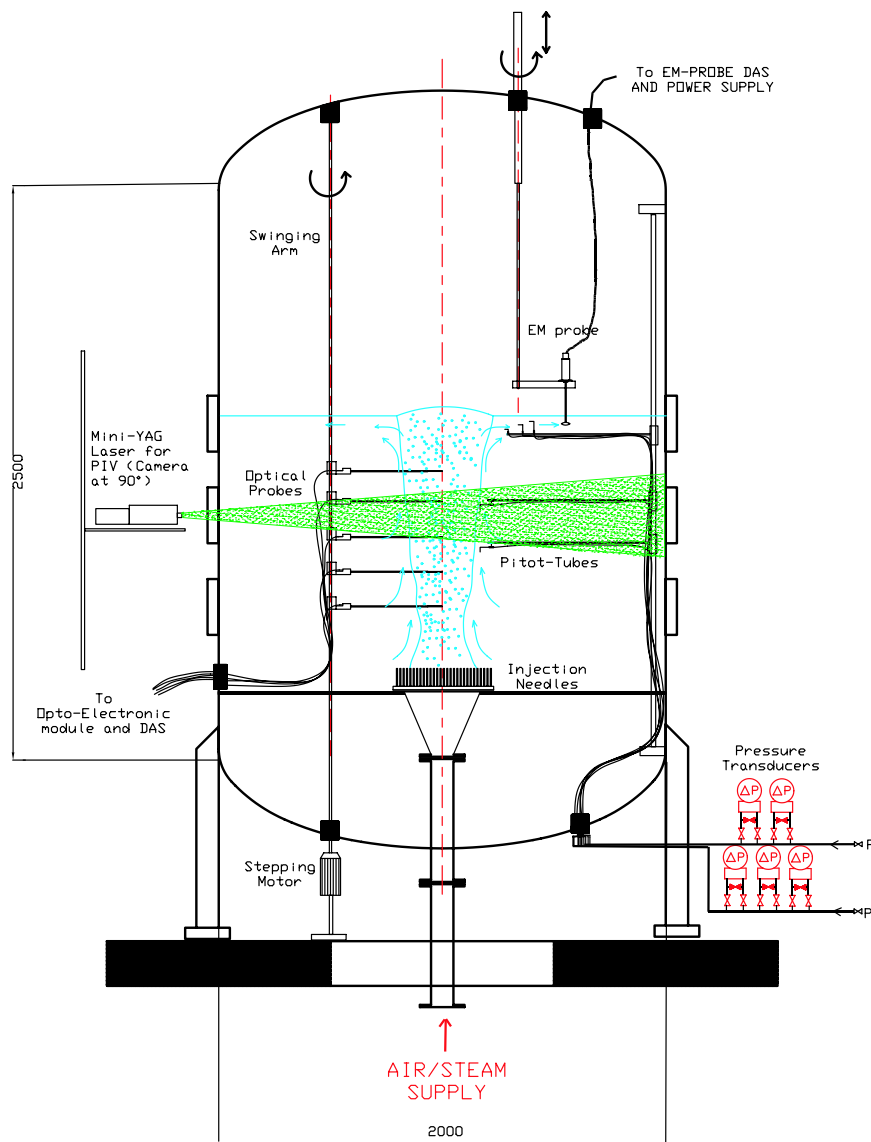


Figure 1.1: LINX-2 experimental facility.

1.2 The physical situation

The dynamics of bottom gas injection in a bath is not completely described by any of the actual models. First, a large range of length scales are involved; second, the phenomena occurring in the bath change depending on the flowrate of gas injection, on the mode of injection, on the bath depth, etc. In order to better describe the phenomena, we can classify them according to their location.

- Near nozzle phenomena: at low gas flow rates, bubbles form at the nozzle and detach individually, while at high gas flow rates the gas exits forming a jet which penetrates a certain distance into the liquid before breaking up into bubbles.
- Gas-liquid plume phenomena: for low gas flow rates the *bubble regime* prevails, consisting of small, non-interacting bubbles. Increasing the flowrate, the bubbles interact more and more and the plume becomes more turbulent with continuous breakup and coalescence of bubbles: this is called the *churn turbulent regime*. As the gas rate increases further we have the *jet penetration regime*, or *spray regime* if the bath is shallow enough.
- Surface phenomena: here the most important effects are the formation of the splash in the region where the gas leaves the bath, and the large-scale wave motion.
- Whole bath phenomena: the most important is the large-scale recirculation set up by the upward motion in the plume. Its importance in industrial processes derives from the fact that it controls mixing throughout the bath.

If it is not specified differently, the specific flow conditions considered here are the following:

- isothermal flow;
- constant liquid density;
- gas density described by the ideal gas law;
- no mass transfer between the phases;
- momentum transfer allowed between the phases;
- bubble coalescence, breakup and interactions neglected (in the modelling);
- no diffusion of gas through the tank walls;
- injection from below.

1.3 Literature overview: experiments

Because of the numerous industrial applications, the problem of injection of gas from below has been widely studied, even though most of the studies have been carried out on the large-scale phenomena which determine the mixing properties. A lot of experimental data are available on this subject; they can be classified into Aqueous experiments (where the liquid is water) and Non-Aqueous experiments (where the liquid is normally a molten metal). A typical experimental set-up is shown in Fig. 1.2.

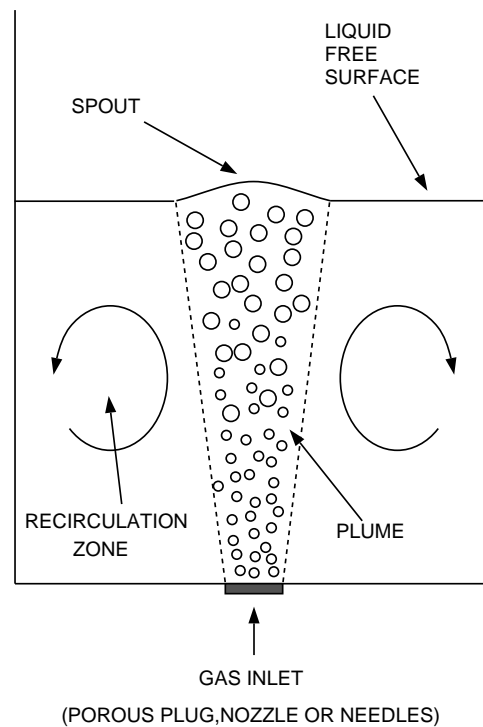


Figure 1.2: Typical experimental set-up.

A detailed overview of the experimental work done on the subject can be found in MILELLI, 1998, but the principal experimental findings will be summarized here. For an air-water system, the spreading of the plume is approximately (but not exactly) linear (TACKE ET AL., 1985), and is also proportional to the gas flow rate (see JOHANSEN ET AL., 1988). The flow is highly three-dimensional, KORJA & SINGH, 1989, CASTELLO-BRANCO & SCHWERTDFEGER, 1994, with precession and swirling occurring also at relatively low gas flow rates (see for instance KUWAGI & OZOE, 1999, and JOHANSEN ET AL., 1988). The zone where the gas discharges from the bath (see Fig. 1.2), has received little attention. Recently, a study has been undertaken by FRIEDL, 1998, where an integral model has been used to predict the interaction of the spout with the atmosphere. The distributions of bubble frequency and gas volume fraction are essentially Gaussian (TACKE ET AL., 1985, IGUCHI ET AL., 1991) while, for the liquid velocity profiles, JOHANSEN ET AL., 1988 did not find the expected Gaussian profile, perhaps because their tank was not large enough to avoid wall effects. ANAGBO & BRIMACOMBE, 1990, defined the profile as sigmoidal, increasing with the axial coordinate and decreasing with the radial one.

Concerning the gas velocity, three zones can be identified (for example CASTILLEJOS & BRIMACOMBE, 1987): in the region close to the injection point there is a steep gradient in bubble velocity radially, and the motion of the bubbles is strongly affected by the gas injection velocity and mode of injection; in the fully-developed flow region, the mean bubble velocity, and the standard deviation of the bubble velocity spectrum, exhibit relatively flat radial profiles, and the bubbles affect the flow only through buoyancy; close to the liquid surface, the axial bubble velocity decreases more rapidly as liquid begins to flow radially outwards from the plume. The same change in bubble behaviour near the inlet was observed by ANAGBO & BRIMACOMBE, 1990, for injection through a porous plug. The slip velocity between the bubbles and the liquid is well represented by the terminal rising velocity of the same size bubble in stagnant liquid, as has been found also by SHENG

& IRONS, 1995. Empirical correlations for the terminal velocity of a single bubble can be found in CLIFT ET AL., 1978 for $d_b > 1.3 \text{ mm}$ as

$$V_T \approx \left(\frac{2.14\sigma}{\rho_l d_b} + 0.505gd_b \right)^{1/2} \text{ m/s} \quad (1.1)$$

and in WALLIS, 1969 for $d_b < 1.3 \text{ mm}$ as

$$V_T \approx 0.33g^{0.76} \left(\frac{\rho_l}{\mu_l} \right)^{0.52} \left(\frac{d_b}{2} \right)^{1.28} \text{ m/s} \quad (1.2)$$

where σ is the surface tension, d_b is the bubble diameter, g is the gravitational acceleration, ρ_l is the liquid density and μ_l is the liquid molecular kinematic viscosity.

Concerning the turbulence properties, some experiments (JOHANSEN ET AL., 1988, GROSS & KUHLMAN, 1992, IGUCHI ET AL., 1995, SHENG & IRONS, 1993, GREVET ET AL., 1992), show a general isotropy of turbulence, while anisotropy (in the direction of gas-motion) is observed in the plume and near the walls by GREVET ET AL., 1992. IGUCHI ET AL., 1995, found the turbulent velocities to be of the same order of magnitude as the mean velocities, and to be Gaussian-distributed. In the experiments of JOHANSEN ET AL., 1988, the axial turbulent component is close to half of the corresponding mean velocity, and is greater than the radial one, except near the surface. Only in the experiment of GROSS & KUHLMAN, 1992, is the radial component larger (almost double) than the axial component, while SHENG & IRONS, 1993, found that the two components are approximately equal.

Many experiments have been performed with non-aqueous systems, especially by Japanese groups, but unfortunately many of these are difficult to categorize since they have been published originally in the Japanese journal *Tetsu-to-Hagane*, and it is not always possible to find the translated version (if there is one). As a consequence, in Table 1 are listed only the more recent works, which also appear in other journals, and of course the non-Japanese works.

Some experiments employ Wood's metal as the continuous phase. Wood's metal is a low-melting-point alloy which consists of 50 % bismuth, 25 % lead, 12.5 % tin and 12.5 % cadmium. It has a melting-point of 70 °C, a density and a viscosity close to those of liquid iron, and a surface tension close to that of mercury.

The dynamics of the plume follows that of the aqueous systems. The spreading was found not to be linear with distance from the source (TACKE ET AL., 1985), giving a cone angle larger than in aqueous systems. However, XIE & OETERS, 1992, using Wood's Metal, found a plume angle between 9-10°, smaller than in air/water systems, while for argon/steel an angle close to 20° was measured by SZEKELY ET AL., 1979, as for aqueous systems. The normalized gas volume fraction and bubble frequency appear to follow a Gaussian distribution (see TACKE ET AL., 1985, CASTILLEJOS & BRIMACOMBE, 1989, XIE ET AL., 1992, IGUCHI ET AL., 1992, IGUCHI ET AL., 1994), also with off-center injection. XIE & OETERS, 1992, in their Wood's metal experiments, found that the *rms* values of the turbulent liquid velocities and the mean liquid velocities follow Gaussian radial distributions and have the same order of magnitude as with air/water systems. CASTILLEJOS & BRIMACOMBE, 1989 found that the mean size of the bubbles decreases with increasing Re , and that their diameters for mercury are greater than for water. This is because, with increasing Re , turbulence and, as a consequence, bubble-breakup, are enhanced, so overall bubble size de-

Dispersed Phase	Continuous Phase	Temperature	Reference Number
Nitrogen	Mercury	Ambient	[1, 2]
Helium	Mercury	Ambient	[2]
Nitrogen	Wood's Metal	100 °C	[3, 4, 5]
Helium	Wood's Metal	100 °C	[3, 4, 5]
Argon	Wood's Metal	100 °C	[3, 4, 5]
Air	Mercury	Ambient	[6, 7]
Argon	Iron	1600 °C	[8]
Argon	Iron	1250 °C	[9]
Argon	Steel	1570 °C - 1600 °C	[10]

Table 1.1: List of experimental works with non-aqueous systems; [1]: TACKE ET AL., 1985; [2]: CASTILLEJOS & BRIMACOMBE, 1989; [3]: XIE & OETERS, 1992; [4]: XIE ET AL., 1992; [5]: XIE & OETERS, 1992; [6]: IGUCHI ET AL., 1992; [7]: XIE & OETERS, 1994; [8]: IGUCHI ET AL., 1995; [9]: IGUCHI ET AL., 1994; [10]: SZEKELY ET AL., 1979.

creases. Then again, the mercury has a larger surface tension, which stabilizes the bubble swarm after breakup.

All these experimental findings indicate that a clean bubble plume experiment has still to be performed. Sometimes the results are ambiguous, and not in agreement with other experiments. As far as the turbulence is concerned, for example, it is still not clear whether the injection of bubbles modifies the isotropy of the liquid, and this is crucial because, from the modelling point of view, the correct understanding of the turbulence leads to a good prediction of the large-scale quantities such as the mixing time, and eventually this is what the industry is interested in. It is likely that the introduction of more advanced measurement tools, such as PIV systems, will increase the basic knowledge of two-phase flow systems such as bubble plumes.

1.4 Literature overview: modelling

There are three categories of models used to describe the entrainment of gases into a stagnant liquid, with or without stratification:

- quasi-single-phase model, in which the rising gas-liquid mixture is assumed to be a homogeneous liquid of reduced density. Here, the geometry of the plume and the gas volume fraction distribution within it are specified as input in the numerical solution scheme;
- Eulerian-Lagrangian two-phase model, in which the Eulerian liquid continuity and momentum equations are solved at the same time as a Lagrangian bubble trajectory equation. Gas void fraction and plume geometry are then determined from the solution of the equations;
- Eulerian-Eulerian two-phase model, in which the continuity and the momentum equations are solved together for both phases considered as interpenetrating media. As in the previous model, all variables are derived from the solution of the equations, and are not set up *a priori*. This is referred to as *two-fluid model*.

1.4.1 Quasi-single-phase model

This model describes the gas/liquid mixture within the two-phase region as a homogeneous fluid having the mixture density, that is

$$\rho_{mix} = \alpha_g \rho_g + (1 - \alpha_g) \rho_l$$

where α_g is the gas volume fraction. In order to model the buoyancy force created by the density difference between the plume and the single-phase regions, the term $\rho_l g \alpha_g$ must be added in the axial component of the momentum equation. The advantage of this model is its simplicity, but the drawback is the fact that the void fraction must be set *a priori* using an experimental correlation; this introduces extra empirical coefficients. Turbulence is taken into account by using appropriate models such as $k - \epsilon$ (GREVET ET AL., 1982, MAZUMDAR, 1992, ZHU ET AL., 1996), or by an *ad hoc* viscosity value (MAZUMDAR & GUTHRIE, 1986, DEB ROY ET AL., 1978). In general, good agreement between the computed and experimental data has been reported, at least away from the plume region. These observations appear to suggest that the bulk flow in a gas-stirred ladle system is dominated by inertial phenomena rather than turbulence (MAZUMDAR & GUTHRIE, 1986). An example is the work of ZHU ET AL., 1996, concerning mixing in a vessel with injection from the base, where the effects of the vessel geometry, nozzle position and position where the tracer is added were studied (see § 1.3).

Though the model can work quite well in a specific situation, it clearly lacks generality and cannot be used to analyze new situations with any confidence. The key to the development of a general model for gas-stirring systems lies in a detailed representation of the motion of the gas bubbles, and their interaction with the liquid phase, both derived from first principles. A good model must also be a predictive tool in new situations, particularly those where experimental data are scarce.

It should be pointed out that the quasi-single-phase model is less fundamental, and therefore less rigorous, because it requires additional empirical input. The other two models are not free from empiricism either: bubble size, drag coefficient and other coefficients for forces accounting for the dispersion of the plume, and for the turbulence, must also be introduced, as described in the following sections.

1.4.2 Euler/Lagrange model

In the Eulerian-Lagrangian model, a quasi-homogeneous, gas-liquid phase is considered within which the paths of the bubbles are tracked. The flow field is calculated in a first step from the balance equations of the gas-liquid mixture, with the mean density varying with the void fraction. In a second step, the gas volume fraction is determined by tracking all individual bubbles of the system in the actual flow field; both steps are repeated until convergence is obtained. An advantage of this formulation comes from the possibility of modelling each individual particle or bubble. Bubble coalescence and breakup can be considered directly and no numerical diffusion will be introduced into the dispersed phase computation since each bubble path can be calculated accurately within a given control volume. But, on the other hand, for dynamic calculations, the tracking of all the bubbles soon becomes overwhelming as the size of the bubble plume increases. Thus, the concept of a *bubble cluster* needs to be introduced, where only a single bubble, representing the center of the cluster, is tracked.

This approach (sometimes called *the trajectory approach*) was first introduced by CROWE ET AL., 1977. Here, the bubble motion is calculated, in a Lagrangian sense, by integrating a force balance equation. This force balance equates the bubble inertia with the forces acting on the bubble, and can be written as (see SHENG & IRONS, 1995, JOHANSEN ET AL., 1987, PARK & YANG, 1996, KUO ET AL., 1997):

$$\frac{\rho_b du_b^i}{dt} = \frac{3\mu_l}{4d_b^2} C_D Re_b (u_l^i - u_b^i) + g^i (\rho_b - \rho_l) + \frac{1}{2} \rho_l \frac{d}{dt} (u_l^i - u_b^i) + \rho_l u_l^i \frac{\partial u_l^i}{\partial x^i} + C_L \rho_b \epsilon_{ijk} (u_b^j - u_l^j) \omega^k \quad (1.3)$$

where u_b^i and u_l^i are the bubble and liquid velocities in the direction x^i , respectively, t is time, ρ_b is the gas density, ρ_l the liquid density, d_b is the diameter of a sphere of equivalent volume, μ_l is the dynamic viscosity of the liquid, $Re_b = \rho_l d_b |u_l^i - u_b^i| / \mu_l$ is the bubble Reynolds number, C_D an empirical drag coefficient, g^i is the gravitational acceleration, ω^k is the liquid vorticity and ϵ_{ijk} is the Levi-Civita tensor. The terms on the right hand side represent the drag, gravitation (buoyancy), added mass, pressure and lift effects respectively. It has to be noted that the liquid velocity is the non-perturbed velocity taken at the point occupied by the centre of mass of the bubble at the time t . The above equation is supplemented by the simple kinematic relationship, defining the trajectories of the bubbles:

$$\frac{dx^i}{dt} = u_b^i \quad (1.4)$$

It is prohibitive to track every bubble released in a pool, so a statistically adequate sample of N bubbles passing through a typical control volume is considered in the estimations of momentum interaction between the two phases. The mean residence time of each bubble in a control volume can then be evaluated by dividing the sum of the residence times t_R of all the bubbles that travel through a particular control volume ΔV by the sample size. The void fraction distribution is then obtained from the mean residence time distribution as

$$\alpha_g = \frac{\dot{Q}}{N \Delta V} \sum_{m=1}^N t_{Rm} \quad (1.5)$$

in which \dot{Q} is the volumetric flowrate of the gas, N is the number of bubbles which visit that control volume, and t_R is their residence time.

The momentum interaction term F_i on the liquid can be deduced in a similar manner, but is in the opposite direction. It can be expressed (in the x direction) as

$$F^i = \frac{\dot{Q}}{N \Delta V} \sum_{m=1}^N \int_0^{t_{Rm}} \frac{\rho_b du_b^i}{dt} dt \quad (1.6)$$

After the trajectory of a bubble is computed, the momentum change induced by the bubble stream that follows the trajectory is calculated. The bubble trajectory and its corresponding momentum

change are thus incorporated in the subsequent calculations for the continuous phase. The dispersed and continuous phase equations are alternately solved until results for both phases change only within certain prescribed limits.

An attempt to include and model the bubble-breakup phenomenon was undertaken in the work of SHENG & IRONS, 1995, where bubbles greater than a critical size were allowed to subdivide into smaller (daughter) bubbles. The critical size was determined from the combined Kelvin-Helmholtz and Rayleigh-Taylor instability theory as (KITSCHA & KOCAMUSTAFAOGULLARI, 1989)

$$d_b = 6.45u_g \left(\frac{\sigma}{\rho_l g^3} \right)^{0.25}$$

where d_b is the critical (volume-equivalent) diameter of the bubble, σ is the surface tension, and u_g is the rise-velocity of the bubble. The local breakup probability was assumed to have a Gaussian distribution, a random number generator being used to determine whether a particular bubble broke up. If this was the case, the number and size of the daughter bubbles were also calculated with a random number generator according to a predefined distribution. Further breakup of daughter bubbles was also permitted.

The Lagrangian scheme is simple and easy to implement in most fluid dynamic codes, but the level of description of the dispersed phase depends on the number of computational "particles" used to represent the field. If each physical particle (or bubble) were to be included, the model would be exact (provided the coefficients involved were known), but the needs for storage and computational speed would then be very high.

1.4.3 Euler/Euler model

The Eulerian-Eulerian model considers the dispersed phase also as a quasi-continuum, with each computational cell of the domain containing respective fractions of the continuous and dispersed phases. The minimum size of a cell must be larger than a single particle (bubble) but, on the other hand, it must be small compared to the scale of the mean flow. The balance equations of the gas and of the liquid phases are solved together on the same grid. With this formulation, the storage requirement depends only on the number of control volumes considered, not on the number of bubbles. Coupling between the two phases is represented with interfacial terms in the momentum equations for the liquid phase, or for both phases, depending on the model.

The governing equations of the two-fluid model can be derived by ensemble averaging of the local instantaneous conservation equations for each phase (DREW, 1983). This results in two sets of mass momentum and energy balances, one for each phase. Since, in the cases studied here, the flow is assumed to be isothermal, the energy equations are not needed. The equations are the following (SMITH, 1999):

$$\frac{D_l}{Dt} (\alpha_l \rho_l) + \alpha_l \rho_l \frac{\partial u_l^i}{\partial x^i} = 0 \quad (1.7)$$

$$\frac{D_g}{Dt} (\alpha_g \rho_g) + \alpha_g \rho_g \frac{\partial u_g^i}{\partial x^i} = 0 \quad (1.8)$$

$$\frac{D_l}{Dt} (\alpha_l \rho_l u_l^i) - \frac{\partial}{\partial x^j} \left[\alpha_l \mu_l \left(\frac{\partial u_l^i}{\partial x^j} + \frac{\partial u_l^j}{\partial x^i} \right) - \alpha_l \rho_l \overline{(u_l^{i'} u_l^{j'})} \right] = -\alpha_l \frac{\partial p}{\partial x^i} + F_l^i \quad (1.9)$$

$$\frac{D_g}{Dt} (\alpha_g \rho_g u_g^i) - \frac{\partial}{\partial x^j} \left[\alpha_g \mu_g \left(\frac{\partial u_g^i}{\partial x^j} + \frac{\partial u_g^j}{\partial x^i} \right) \right] = -\alpha_g \frac{\partial p}{\partial x^i} + F_g^i \quad (1.10)$$

in which

$$\frac{D_l}{Dt} = \frac{\partial}{\partial t} + u_l^j \frac{\partial}{\partial x^j} \quad \text{or} \quad \frac{D_g}{Dt} = \frac{\partial}{\partial t} + u_g^j \frac{\partial}{\partial x^j} \quad (1.11)$$

as appropriate, and where

$$F_l^i = -F_g^i$$

The subscripts l and g refer to the liquid and gas phases, respectively, and x^i are the space coordinates.

The storage and computational time is not excessive in this approach, but closure models are required: the interfacial momentum transfer, F_k^i , which accounts for the buoyancy force, drag force, lift force, virtual mass effect, turbulent dispersion force, and other effects which will be explained in detail in the next Chapter and the Reynolds stress $-\rho_l \overline{(u_l^{i'} u_l^{j'})}$ which is often modelled using a Boussinesq hypothesis and resulting in a $k - \epsilon$ -like model, that is

$$-\rho_l \overline{(u_l^{i'} u_l^{j'})} = \mu_t \left(\frac{\partial u_l^i}{\partial x^j} + \frac{\partial u_l^j}{\partial x^i} \right) - \frac{2}{3} \rho_l k_l \delta^{ij} \quad (1.12)$$

where μ_t is the turbulent viscosity described in the following section.

1.4.4 Turbulence modelling

For each of the previously discussed categories of modelling, a good turbulence model is needed in order to properly describe the behaviour of the liquid phase. In the past, the constant-eddy-viscosity model was used (for instance, DAVIDSON, 1990) because of its simplicity, but normally the trend now is to solve transport equations for turbulent variables. The most popular model of turbulence is the high-Reynolds-number $k - \epsilon$ model (see RODI, 1984) with the empirical coefficients of LAUNDER & SPALDING, 1972. That is,

$$\frac{D_l}{Dt} (\alpha_l k_l) - \frac{\partial}{\partial x^j} \left[\frac{\alpha_l \mu_t}{\sigma_k} \frac{\partial k_l}{\partial x^j} \right] = S_k \quad (1.13)$$

$$\frac{D_l}{dt} (\alpha_l \epsilon_l) - \frac{\partial}{\partial x^j} \left[\frac{\alpha_l \mu_t}{\sigma_\epsilon} \frac{\partial \epsilon_l}{\partial x^j} \right] = S_\epsilon \quad (1.14)$$

where

$$S_k = \alpha_l(P_l - \epsilon_l) \quad (1.15)$$

and

$$S_\epsilon = \alpha_l \left(\frac{C_1 \epsilon_l P_l}{k_l} - \frac{C_2 \epsilon_l^2}{k_l} \right) \quad (1.16)$$

with the shear production term P_l given by

$$P_l = \mu_t \left(\frac{\partial u_i}{\partial x_j} + \frac{\partial u_j}{\partial x_i} \right) \frac{\partial u_i}{\partial x_j}$$

and with

$$C_1 = 1.44, \quad C_2 = 1.92, \quad \sigma_\epsilon = 1.3, \quad \sigma_k = 1.0$$

and

$$\mu_t = C_\mu \rho_l \frac{k_l^2}{\epsilon} \quad , \quad C_\mu = 0.09 \quad (1.17)$$

The basic assumptions of the model are:

- the eddy-viscosity hypothesis;
- isotropic turbulence;
- a linear gradient formulation (in terms of mean flow quantities) for the turbulent fluxes.

Though a single-phase flow model, the $k - \epsilon$ formulation is widely used in literature even in the presence of a second (dispersed) phase. At relatively small gas flow rates, the model gives reasonable predictions for the flow field outside the plume, as was found by SCHWARZ & TURNER, 1988. Nevertheless, within the two-phase region some deficiencies have been found.

- The model overpredicts the mixing time by a factor of two, and underpredicts the spreading of the bubble plume, so that centerline values of void fraction are too high (DANG & SCHWARZ, 1991);
- The turbulence level near the surface of the bath is overestimated by about 50% (SCHWARZ & TURNER, 1988 and SCHWARZ, 1996). This is due to the overprediction of turbulence in strongly curved flows, in this case where the plume impinges on the pool surface;
- In the plume region, the predicted level of turbulence is too low compared with measurements (SCHWARZ ET AL., 1992), in particular, the measured turbulent kinetic energy is twice that predicted by the model (SHENG & IRONS, 1995).

It was demonstrated by ILEGBUSI & SZEKELY, 1992 that the turbulence induced by the presence of the bubbles, at least in the case of buoyancy-driven flows, is not completely isotropic, since it has a preferred direction (the direction of gravity). Moreover the turbulent fluctuations should satisfy the

boundary conditions at the interfaces between the bubbles and the liquid, and those are not taken into account in the $k - \epsilon$ model. On the other hand the bubbles generate a pseudo-turbulence that is not cancelled by the average stress tensor of the gas-phase.

In single-phase applications, anisotropy is generally taken into account by using a viscosity tensor instead of a scalar (RODI, 1984), or by abandoning completely the eddy viscosity concept and deriving transport equations for the Reynolds stresses and Reynolds fluxes directly. In the Algebraic Stress Model, the equations are solved algebraically, whereas in the Differential Stress Model they are integrated. Unfortunately, both models are complicated, not very robust numerically, also contain uncertain empirical constants, and many transport equations need to be solved simultaneously.

In the two-phase context, numerical calculations performed by PARK & YANG, 1997 show that while the $k - \epsilon$ model overpredicts turbulent kinetic energy, it underpredicts the mean velocity with respect to the RSM previously mentioned but, generally speaking, results are comparable. The $k - \epsilon$ model fails only in predicting highly swirling flows, while RSM is in good agreement with experimental results. The same conclusions are given in the work of ILEGBUSI & SZEKELY, 1992.

In order to predict the correct flow field, *ad hoc* adjustments of the five empirical constants in the $k - \epsilon$ model have been tried (see for instance MAZUMDAR & GUTHRIE, 1986), but another approach is to increase the turbulent kinetic energy and the turbulent dissipation using extra production terms in the transport equations for k and for ϵ (1.13, 1.14). The kinetic energy and dissipation are in fact increased by the passage of macroscopic bubbles ($1\text{ mm} \leq d_b \leq 5\text{ mm}$), mainly because of the increased shear and the presence of the wake.

Summarizing the results from a modelling point of view, it can be said that the existing models are not able to describe correctly a bubble plume. It is a complicated situation in which the turbulence is totally driven by the bubbles via the buoyancy force, so that the single-phase models are simply unacceptable, and the patch-ups normally used require too many empirical parameters. This leads to the conclusion that the basic phenomena involved in the motion of a swarm of bubbles is not properly understood. The turbulence modelling is the key point of this kind of two-phase flow; in particular, the turbulence induced by the passage of the bubbles (or pseudo-turbulence), and the turbulence produced in the wakes. A clear understanding of the physical mechanisms of production and dissipation of the bubble-induced turbulence, and of the feedback (via the interfacial forces) that the bubbles have on the liquid, would give the possibility to formulate a more general model. Through this thesis work, we will try to explore possible improvements from the modelling point of view.

1.5 Summary of the thesis

As a first step, in Chapter 2, the existing models for turbulence enhancement (in a standard $k - \epsilon$ model) and for bubble dispersion will be discussed, and their application to free bubble plumes will be compared against published experimental data (ANAGBO & BRIMACOMBE, 1990) in order to look for margins of improvement. It will be seen that uncertainties are large, due to the fact that there are many empirical constants involved in the equations. However, the goal is to better understand the physical phenomena occurring, and to see if it is possible to describe them in a less empirical way. In Chapter 3, a statistical description of bubble dispersion is introduced, namely the Random Dispersion Model (RDM), which is able to replace the empirical formulation of the Turbulent Dispersion Force (TDF). Further, it has been decided to explore the possibility of using more advanced turbulence models.

Since it is difficult to improve the results using the Reynolds Stress Models, as it was discussed

above, the Large Eddy Simulation model (LES) has been employed, for which the large scales of turbulence are solved directly, while the smaller scale effects are modeled. In principle LES looks promising for our applications because only the scales larger than the bubble size contribute to the dispersion of the bubbles (macroscopic effect) and therefore it is important to calculate them instead of modelling them. For this purpose, an LES model has been implemented into the code CFX-4.2, 1997. Details of the implementation of the model are given in Chapter 4, where also the new coding is tested by comparing predictions with experimental data in the case of a single-phase, thermal plume; the experimental data are from GEORGE ET AL., 1977. Since a change in the mesh size corresponds to a change in the filter width, with a consequent change in the definition of the problem, a systematic study of the influence of mesh size in the case of isotropic grid-turbulence (in the presence of bubbles) has been performed, and results compared with the measurements of LANCE & BATAILLE, 1991. These results are shown in Chapter 5. A further validation case is reported in Chapter 6 for a simple two-phase shear flow (ROIG, 1993). The model is then applied to the main application case, the bubble plume experiment of ANAGBO & BRIMACOMBE, 1990, and results presented in Chapter 7. In all cases, results are compared against published experimental data. Finally, in Chapter 8, there are the general conclusions and the perspectives for future work.

2 Comparison of existing models for the case of a bubble plume

2.1 Introduction

The most commonly used way of modeling turbulence in multi-phase flows is to modify the single-phase $k - \epsilon$ model by adding extra source terms into the k and ϵ equations to account for the effects of the dispersed phase on the turbulence generated and dissipated by the carrier phase. These extra terms are added to the right hand sides of eqs. (1.13) and (1.14), as described before. Different models are available in the literature, but the most used are the Simonin model, the Issa model and the RPI group model. They will be described here and compared for the case of a bubble plume, together with models for the turbulent dispersion of the bubbles. The experimental data come from the experiment of ANAGBO & BRIMACOMBE, 1990. The calculations are made using the code CFX-4.2, 1997, and the models are compared within the same numerical conditions. The goal is to check the reliability of the existing models, and to critically investigate their respective merits and drawbacks in order to find ways to improve them.

2.2 Experimental set-up

The experiments were performed using a 1/6th-scale model of a 150-ton ladle, as used in iron foundries. The apparatus consists of a 500-mm-diameter cylindrical tank of Plexiglas* containing de-ionized water to a depth of 400 mm and equipped with a porous plug at the center of the base. The porous element is a fritted glass disc, 60-mm in diameter and 5-mm thick. Distributor plates have been installed in the air-supply pipe to the porous disc to ensure a uniform flow of gas over the cross-sectional area of the plug. A Plexiglas ring baffle with a 496-mm OD and 300-mm ID was positioned 3 mm above the static level of the bath to prevent bath slopping, especially at high gas injection rates. Measurements of gas fraction, bubble frequency, bubble axial diameter, and bubble velocity were obtained by means of a double-contact electroresistivity probe described by CASTILLEJOS & BRIMACOMBE, 1987. The water was made electrically conductive by introducing an appropriate concentration of acid. Measurements were made for a sample size of 800 bubbles at various positions in the plume, once the probe had been located by means of the $z - r$ traversing carriage. Liquid velocity measurements in the bath surrounding the plume were made by means of a Laser-Doppler Velocimeter (LDV). Each mean velocity component (axial and radial) was computed from a sample size of 512 readings. The experiments were performed at room temperature and for three different gas flow rates: 200, 600, and 1200 Ncm^3/s (12, 36, and 72 $liters/min$, respectively), which correspond to specific injection rates of 8.5, 25.3, and 50.5 $cm^3/s\ cm^2$, respectively. The experiment analyzed here corresponds to the lowest gas-flow-rate test performed in the series.

2.3 Model set-up

For the simulations, there are some uncertainties in regards to specifying the gas volume fraction at inlet. In reality, it is likely that the entire plug surface was blanketed by the air, followed by

*Registered trade name

rapid break-up to produce the bubble swarm. The boundary conditions adopted here correspond to perfect packing of uniform spheres, with the gas velocity adjusted to reproduce the total gas flow rate, $\dot{Q} = 200 \text{ N cm}^3/\text{s}^\dagger$:

$$\left. \begin{aligned} \alpha_l &= 0.38 & u_l &= 0.0 \text{ m/s} \\ \alpha_g &= 0.62 & u_g &= 0.1141 \text{ m/s} \end{aligned} \right\} \quad (2.1)$$

in which α_l, α_g are the liquid and gas volume fractions, respectively, at the plug surface, and u_l, u_g are the corresponding axial velocity component. Fortunately, a 2D sensitivity study revealed that results are rather insensitive to the α_g value assumed (SMITH, 1999).

The side wall and base are considered non-slip surfaces and the liquid phase is assumed to be turbulent.

Initially, the water surface lies along a mesh boundary and appropriate values for the gas and liquid volume fractions are assigned to the cells above and below it. That is, $\alpha_l \simeq 0$ and $\alpha_g \simeq 1$ for the cells above the surface, and the converse for those below. Subsequently, level swelling will occur and the volume fractions in the cells close to the surface will change. No artificial surface-sharpening techniques are employed, but the interface remains reasonably sharp as a consequence of local mesh refinement.

In the present application, since there is no mass or heat transfer between the phases, no energy equation is needed (isothermal flow). The momentum exchange terms and the different turbulence enhancement models will be described in the following paragraphs.

2.3.1 Interfacial forces

Inertia (virtual mass) force

$$\mathbf{F}_l^{VM} = -\mathbf{F}_g^{VM} = \alpha_g \rho_l C_{VM} \left(\frac{D_g \mathbf{u}_g}{Dt} - \frac{D_l \mathbf{u}_l}{Dt} \right) \quad (2.2)$$

where the D/Dt operators denote the total time derivatives in the respective phases. It was found by DAVIDSON, 1990, that the inclusion of this force reduces the computational time by having a stabilizing effect on the system. The coefficient for a single spherical bubble $C_{VM} = 0.5$, presented first in the work of LAMB, 1932, is usually adopted also for a bubble swarm (for instance, see SHENG & IRONS, 1995). However VAN WIJNGAARDEN, 1976, found that this value ignores not only the possible non-sphericity of the bubbles, but also the details of the interactions between them. In particular, if one bubble travels in the wake of another, $C_{VM} < 0.5$, but if two bubbles are moving side-by-side, $C_{VM} > 0.5$. So, in general, for a random distribution of bubbles, $C_{VM} > 0.5$ and increases with void fraction, if this is small. However, if the void fraction is equal to one, $C_{VM} = 0$. DAVIDSON, 1990, suggested the following expression:

$$C_{VM} = \frac{1}{2} - \frac{1}{2} \alpha_g \quad (2.3)$$

[†]Flow-rate normalized to STP conditions

and VAN WIJNGAARDEN, 1976,

$$C_{VM} = \frac{1}{2}(1 + K\alpha_g + O(\alpha_g^2)) \quad (2.4)$$

where $K = 2.78$. It should be noted that the simple argument of ZUBER, 1964 produced already a very good approximation of eq. (2.4) with $K = 3$, at least with small values of void fraction.

Buoyancy force

The buoyancy force is imposed, unconventionally, as extra source terms in the momentum equations (1.9), (1.10), and separately for the liquid and gas spaces, i.e. below and above the liquid surface, respectively, as follows:

$$\left. \begin{aligned} \mathbf{F}_g^B &= (\rho_g - \rho_l) \mathbf{g}, & \mathbf{F}_l^B &= 0, & \text{pool} \\ \mathbf{F}_l^B &= (\rho_l - \rho_g) \mathbf{g}, & \mathbf{F}_g^B &= 0, & \text{gas space} \end{aligned} \right\} \quad (2.5)$$

Thus, the gas phase is positively buoyant in the pool region below the surface, and the liquid phase is negatively buoyant in the gas region above the surface; otherwise, there is neutral buoyancy. This formulation avoids the need to specify a reference density, which would be inappropriate for at least one of the phases and would lead to numerical inaccuracies in the treatment of pressure drops for that phase.

Drag force

$$\mathbf{F}_l^D = -\mathbf{F}_g^D = \frac{3}{4}\alpha_g\rho_l\frac{C_D}{d}|\mathbf{u}_g - \mathbf{u}_l|(\mathbf{u}_g - \mathbf{u}_l) \quad (2.6)$$

The interface drag force can be derived from a generalization of that for a single spherical bubble rising in a quiescent liquid, considering small bubbles with constant radius. A different expression for this kind of force is sometimes used (see for instance SCHWARZ ET AL., 1992 or SOKOLICHIN & EIGENBERGER, 1994):

$$\mathbf{F}_l^D = -\mathbf{F}_g^D = C_F\alpha_l\alpha_g(\mathbf{u}_g - \mathbf{u}_l) \quad (2.7)$$

where C_F assumes the value necessary to have the correct slip velocity between the bubbles and the liquid and has been empirically determined by SCHWARZ & TURNER, 1988

$$C_F = 5 \times 10^4 \quad (kg\,m^{-3}\,s^{-1}) \Rightarrow w_g - w_l = 0.20 \quad (m/s)$$

$$C_F = 4 \times 10^4 \quad (kg\,m^{-3}\,s^{-1}) \Rightarrow w_g - w_l = 0.25 \quad (m/s)$$

The advantage of this form of the drag force is the linearity with respect to the slip velocity, possibly allowing a reduction of CPU time, the ability to account for the turbulent velocities directly (see later), and the independence of the bubble diameter. On the other hand, the determination of the coefficient C_F does not have any physical background.

A modified expression for the drag coefficient was used by JOHANSEN ET AL., 1987:

$$C_D = C_{D_0} \left[1 - \left(\frac{d_b}{L_b} \right)^2 \right] \quad (2.8)$$

where C_{D_0} is the drag coefficient for a single bubble and L_b is the distance between the centres of two bubbles. The variation in C_D is due to the fact that a group of rising bubbles tend to follow each other, so it is necessary to modify the standard expression to account for the drag reduction in such circumstances. The measurements of TSUJI, 1982 for two spheres show that in the Reynolds number range from 100 to 200, this is a good approximation. At the moment, a theory for the expression in other Reynolds number ranges is not available. However, it should be noticed that this correlation has been used in the context of a Lagrangian model for the bubbles (JOHANSEN ET AL., 1987).

Concerning the drag coefficient, many empirical or semi-empirical equations have been proposed to approximate the conventional correlation for the drag on a sphere in steady motion, also known as the *standard drag curve* (see CLIFT ET AL., 1978, for a detailed list and discussion), but they are valid for rigid spheres, not for bubbles in general. For this reason, an empirical correlation for bubbles rising in stationary tap water by KUO & WALLIS, 1988 has been used:

$$C_D = \frac{6.3}{Re_b^{0.385}} \quad \text{for } Re_b \geq 100, \quad C_D = \frac{20.68}{Re_b^{0.643}} \quad \text{for } Re_b < 100 \quad (2.9)$$

Anticipating a relative velocity $|\mathbf{u}_g - \mathbf{u}_l|$, of 0.25 m/s , corresponding to the terminal rise velocity of a single 3 mm diameter bubble in a quiescent liquid (1.1), this gives a bubble Reynolds number Re_b of 900 which corresponds to a value of C_D of 0.455. As a consequence, considering the uncertainties in determining the correct slip velocity, a value of $C_D = 0.44$ (which is also deduced from the well known expression of CLIFT ET AL., 1978) has been used.

Lift force

$$\mathbf{F}_l^L = -\mathbf{F}_g^L = C_L \rho_l \alpha_g (\mathbf{u}_g - \mathbf{u}_l) \times (\nabla \times \mathbf{u}_l) \quad (2.10)$$

If a particle (bubble) with a rigid surface moves in a non-uniform flow field, the asymmetry of the wake causes an additional force of interaction, perpendicular to the main flow direction. Investigations of single bubbles in laminar flow (AUTON, 1987) indicate that the force is proportional to the slip velocity and to the liquid vorticity. Since the distribution of the velocities in a plume is Gaussian, the direction of the force is away from the axis of the plume. This effect causes a lateral spreading of the plume. From the experimental observations of SHENG & IRONS, 1995, and the numerical analysis of LOPEZ DE BERTODANO, 1992, $C_L = 0.1$ has been adopted, but different values can be found in the literature: for example, SCHWARZ, 1996, considers $1 < C_L < 1.5$. AUTON, 1987 suggested a value of $C_L = 0.5$ which is valid only for spherical bubbles in a perfect fluid. A more realistic value for deformable bubbles has been proposed by LANCE & LOPEZ DE BERTODANO, 1994 as $C_L = 0.25$. Finally, according to DREW & LAHEY, 1987, the lift force itself is not "objective", while the combination of lift and added mass is. Therefore they recommend $C_L = C_{VM}$.

Turbulent dispersion force

$$\mathbf{F}_l^{TD} = -\mathbf{F}_g^{TD} = C_{TD}\rho_l k_l \nabla \alpha_g \quad (2.11)$$

This force accounts for the dispersion of bubbles due to the random influence of the turbulent eddies in the liquid. It has been derived by LOPEZ DE BERTODANO, 1992, in analogy with the thermal diffusion of air molecules in the atmosphere (Brownian motion). The thermal motion that keeps the molecules away from the ground may be thought of as a thermal diffusion force acting against gravity. The only difference is that the role of the thermal energy of the air molecules is played by the turbulent energy of the liquid. This consideration gives a force proportional to the void gradient, to the turbulent kinetic energy and to the liquid density, with an empirical coefficient which, according to the work of ANGLART ET AL., 1993, is $C_{TD} = 0.1$.

Another derivation of the force was originally proposed by LEE, 1987, and then further developed by DAVIDSON, 1990:

$$\mathbf{F}_l^{TD} = -\mathbf{F}_g^{TD} = \frac{3}{4} \frac{C_D}{d_b} \mu_t \alpha_l |\mathbf{u}_g - \mathbf{u}_l| \nabla \alpha_g \quad (2.12)$$

In this form, the force is proportional to the drag function $\frac{3}{4} \frac{C_D}{d_b} \alpha_l |\mathbf{u}_g - \mathbf{u}_l|$, to the void fraction gradient, and to a dispersion coefficient, which is set equal to the turbulent dynamic viscosity. The reason for this is that the drag on a fluid eddy is greatest, and hence the amplitude of the oscillation is least, when the eddy is moving in the direction of increasing particle (bubble) concentration. The uneven amplitude of such oscillations results in motion of entrained particles or bubbles away from the region of high concentration. The degree of such a dispersion depends on the concentration gradient, the drag force, the frequency and the amplitude of the oscillation. With this kind of formulation one can avoid the use of a further empirical coefficient C_{TD} , taking only the drag coefficient C_D and the turbulent viscosity μ_t . The net effect of the two versions of the force is the same, however, and consists of a diffusion of the dispersed phase away from the axis of the plume, this following from the Gaussian shape of the void fraction distribution. The effect is cumulative with the spreading produced by the lift force, and ensures correct spreading of the plume, as demonstrated in the work of SMITH, 1999.

In contrast, VIOLLET & SIMONIN, 1994, have modelled the dispersion force for bubbles in a rather different way. In this formulation, valid for very small bubbles only, the terms

$$\mathbf{F}_l^{TD} = -\mathbf{F}_g^{TD} = A_d \mathbf{v}_{drift} \quad (2.13)$$

are introduced into the momentum equations (1.9, 1.10), with

$$A_d = \frac{3}{4} \frac{\alpha_g \rho_l}{d_b} C_D |\mathbf{u}_g - \mathbf{u}_l| \quad (2.14)$$

and \mathbf{v}_{drift} a drift velocity between the phases, which depends on the gradient of the void fraction:

$$\mathbf{v}_{drift} = -D_{lg}^t \left(\frac{\nabla \alpha_g}{\alpha_g} - \frac{\nabla \alpha_l}{\alpha_l} \right) \quad (2.15)$$

with D_{lg}^t written in terms of the eddy-bubble interaction time and a fluid-bubble velocity correlation tensor:

$$D_{lg}^t = \tau_{lg}^t \langle \mathbf{u}'_l \mathbf{u}'_g \rangle_g . \quad (2.16)$$

Finally, the group of Gosman (WANG ET AL., 1994) introduced the following expression

$$\mathbf{F}_l^{TD} = -\mathbf{F}_g^{TD} = A_d \frac{\nu_l^t}{\alpha_l \alpha_g \sigma_I} \nabla \alpha_g \quad (2.17)$$

with A_d defined as in (2.14), and where σ_I is a constant which has been given the value of 0.3 for bubbly flow in a cylindrical pipe.

Interfacial pressure

A closure assumption is also needed for the interfacial pressure difference $(p_k - p_{k,i}) \nabla \alpha_k$ (STUHMILLER, 1977):

$$\left. \begin{aligned} p_l - p_{l,i} &= C_p \rho_l |\mathbf{u}_g - \mathbf{u}_l|^2 \\ p_g - p_{g,i} &= 0.0 \end{aligned} \right\} \quad (2.18)$$

This term can be neglected in the gas phase momentum equation because of the low density of the gas. $C_p = 0.25$ for non-interacting spheres in potential flow.

2.3.2 Turbulence models

Simonin and Viollet model

$$S_k = \alpha_l (P_l - \epsilon_l) + C_{k2} C_f \alpha_g \alpha_l k_l \quad (2.19)$$

$$S_\epsilon = \alpha_l \left(\frac{C_1 \epsilon_l P_l}{k_l} - \frac{C_2 \epsilon_l^2}{k_l} \right) + C_{\epsilon 2} C_f \alpha_g \alpha_l \epsilon_l \quad (2.20)$$

where C_f is the interphase friction coefficient given by

$$C_f = \frac{3}{4} \frac{C_D}{d_b} |\mathbf{u}_g - \mathbf{u}_l| \quad (2.21)$$

These terms were introduced by SIMONIN & VIOLLET, 1988 to represent the migration of the gas bubbles through the liquid. This model appeared to be dimensionally incorrect in the work of

ILEGBUSI & SZEKELY, 1990 with a value of 0.5 for both the model coefficients, but it is written correctly in the work of SHENG & IRONS, 1995, and the values of the coefficients are:

$$C_{k2} = 0.75, \quad C_{\epsilon2} = 0.6$$

Simonin model

More recently, a new version of the model has been developed by Simonin (for instance BELF'DHILA & SIMONIN, 1992) in which the bubble fluctuating motion is assumed to influence the fluid turbulence through the following source terms for k and ϵ , respectively:

$$S_k = \alpha_l(P_l - \epsilon_l) + \Pi_k \quad (2.22)$$

$$S_\epsilon = \alpha_l \left(\frac{C_1 \epsilon_l P_l}{k_l} - \frac{C_2 \epsilon_l^2}{k_l} \right) + C_{\epsilon3} \frac{\epsilon}{k} \Pi_k, \quad C_{\epsilon3} = 1.2 \quad (2.23)$$

where

$$\Pi_k = \frac{\rho_g}{\rho_g + \rho_l C_{VM}} \alpha_g C_f [q_{1,2} - 2k + \mathbf{v}_r \cdot \mathbf{v}_{drift}] \quad (2.24)$$

in which

$$\mathbf{v}_r = (\mathbf{u}_g - \mathbf{u}_l) - \mathbf{v}_{drift}, \quad (2.25)$$

and C_f is given in (2.21), \mathbf{v}_{drift} in (2.15). Finally, $q_{1,2}$ is the fluid-bubble velocity covariance given by

$$q_{1,2} = \langle \mathbf{u}'_l \mathbf{u}'_g \rangle_g. \quad (2.26)$$

Issa model

Here (WANG ET AL., 1994), the extra source terms arise from the interphase forces present in the momentum equation and account for the effects of the pressure of the bubbles on the turbulent field. They are derived from averaging, as in the single-phase flow case.

$$S_k = \alpha_l(P_l - \epsilon_l) + 2k \frac{A_d}{\rho_l} (C_t - 1) + \frac{A_d \nu_l^t}{\rho_l \alpha_l \alpha_g \sigma_I} \mathbf{v}_{slip} \cdot \nabla \alpha_g \quad (2.27)$$

$$S_\epsilon = \alpha_l \left(\frac{C_1 \epsilon_l P_l}{k_l} - \frac{C_2 \epsilon_l^2}{k_l} \right) + 2\epsilon \frac{A_d}{\rho_l} (C_t - 1) \quad (2.28)$$

where A_d is defined in (2.14),

$$C_t = \frac{3 + \beta}{1 + \beta + 2\rho_g/\rho_l} \quad , \quad \sigma_I = 0.3 \quad (2.29)$$

and

$$\beta = \frac{12A_d}{\pi d_b \mu_l} \left(\frac{l_e}{d_b} \right)^2 \frac{1}{Re_t} \quad (2.30)$$

with

$$Re_t = \frac{\sqrt{u_l'^2} l_e}{\nu_l} \quad , \quad l_e = C_\mu^{3/4} \frac{k^{3/2}}{\epsilon} \quad , \quad (2.31)$$

$\sqrt{u_l'^2}$ and l_e being, respectively, the *rms* value of the liquid velocity fluctuation and the eddy length scale. The term in the ϵ equation is derived from that in the k equation. In these equations, the coefficient C_t stands for the ratio of the bubble velocity fluctuations to those of the liquid, which are taken to be directly proportional to each other. Measurements obtained by ROIG ET AL., 1993 revealed that for bubbly flow C_t was greater than unity (around 1.5). This means that the turbulence in the liquid is essentially controlled by the fluctuations in the velocities of the bubbles.

In the expression for S_k (Eq. 2.19), the second term is negligible with respect to the first since the scalar product is small. In fact, the maximum slip velocity corresponds to the minimum (axial) void fraction gradient, and the maximum void fraction gradient corresponds to the minimum (radial) slip velocity. As a consequence, this term has not been considered in the calculation. The proposed model for C_t is based on a balance of terms in the instantaneous momentum equation for a single bubble, together with the assumption that the acceleration of a bubble within an eddy is proportional to $\overline{u_l'^2}/l_e$, where l_e is the eddy length scale and u_l' is the *rms* velocity. The constant σ_I has the empirical value of 0.3, which has been found reasonable for bubbly flow in a cylindrical pipe. The model has also been used for studying bubbly air/water flow through a pipe with a sudden enlargement (WANG ET AL., 1994). Additionally, it was used for the prediction of the dispersion of a scalar concentration in a turbulent, shear-free mixing layer (ISSA & OLIVEIRA, 1996). More recently, it has been tested by LATHOUWERS & VAN DEN AKKER, 1999, for a two-dimensional, bubbly mixing layer, in comparison with the model of de Bertodano (see later).

Malin and Spalding model

$$S_k = \alpha_l(P_l - \epsilon_l) + C_{k1}\alpha_g\alpha_l P_l \quad (2.32)$$

$$S_\epsilon = \alpha_l \left(\frac{C_1 \epsilon_l P_l}{k_l} - \frac{C_2 \epsilon_l^2}{k_l} \right) + C_{\epsilon 1} \alpha_g \alpha_l P_l \frac{\epsilon_l}{k_l} \quad (2.33)$$

These terms have been employed by MALIN & SPALDING, 1984 in order to obtain correct spreading rates for single-phase jets and wakes. Originally, the model used an analogy between turbulent and non-turbulent regions of the flow and the two phases in a multiphase context. The intention was to use a two-fluid approach to model single-phase turbulence, but subsequently it has been

used for bubble plume modelling (SHENG & IRONS, 1993, SHENG & IRONS, 1995 and ILEGBUSI & SZEKELY, 1990). The form is the same as the production terms in the standard $k - \epsilon$ model (1.13, 1.14), and therefore represents merely a modification of the coefficients. The constants in (2.31), (2.32) have the following values in the original derivation of MALIN & SPALDING, 1984:

$$C_{k1} = 2.5, \quad C_{\epsilon1} = 2.5,$$

but are not well-established, having been derived using data from just one experiment. Moreover, the experiment involved the injection of hot gas into cold gas, which is still a single-phase situation. More reliable values were found by SHENG & IRONS, 1993 for a real two-phase case, even though they used the model together with that of Simonin and Viollet (SIMONIN & VIOLLET, 1988). The coefficients used in this case were:

$$C_{k1} = 6.0, \quad C_{\epsilon1} = 4.0$$

RPI models

One of the models used by the RPI group has been derived by LOPEZ DE BERTODANO, 1992, and starts from the assumption that, for dilute bubbly flow ($\alpha_g < 0.1$ according to THEOFANOUS & SULLIVAN, 1982, but $\alpha_g < 0.01$ for LANCE & BATAILLE, 1991), the bubble-induced turbulent kinetic energy k_{BI} may be linearly superimposed on that based on shear. He wrote a transport equation for k_{BI} and, adding this to the standard k_{SI} equation, derived from the $k - \epsilon$ turbulence model, he ends up with an equation which is equivalent to (1.13) but with

$$k_l = k_{SI} + k_{BI} \tag{2.34}$$

and

$$S_k = \alpha_l(P_l - \epsilon_l) + \alpha_l \frac{(k_{BIA} - k_{BI})}{\tau} \quad ; \quad S_\epsilon = \alpha_l \left(\frac{C_1 \epsilon_l P_l}{k_l} - \frac{C_2 \epsilon_l^2}{k_l} \right) \tag{2.35}$$

where k_{BIA} is the asymptotic solution of a transport equation for k_{BI} , and may be expressed as

$$k_{BIA} = 0.5 \alpha_g C_{VM} |\mathbf{u}_g - \mathbf{u}_l|^2 \tag{2.36}$$

in which the characteristic time of the bubble is determined from its diameter d_b and slip velocity $\mathbf{u}_g - \mathbf{u}_l$ according to

$$\tau = \frac{d_b}{|\mathbf{u}_g - \mathbf{u}_l|}. \tag{2.37}$$

The equation for k_{BI} is derived in an heuristic manner, and the uncertainties are large. As a consequence, the asymptotic value (2.36) is used instead of solving the transport equation for k_{BI} , and the extra term in the equation for S_k (2.35) then tends to zero.

Another derivation of bubble-induced turbulence is given by LEE ET AL., 1989, also from the RPI group. Based on a dimensional analysis, the extra source terms in (2.35) are written as

$$S_k = \alpha_l(P_l - \epsilon_l) + \frac{k_{BIA}}{\tau} = \alpha_l(P_l - \epsilon_l) + \frac{1}{4}\alpha_g \frac{|\mathbf{u}_g - \mathbf{u}_l|^3}{d_b} \quad (2.38)$$

and

$$S_\epsilon = \alpha_l \left(\frac{C_1 \epsilon_l P_l}{k_l} - \frac{C_2 \epsilon_l^2}{k_l} \right) + 1.92 S_k \frac{\epsilon}{k} \quad (2.39)$$

where $k \equiv k_{SI}$.

Basically, this approach is equivalent to considering the extra term in S_k as the work done by the bubbles moving through the liquid per unit time and volume; that is,

$$S_k \propto \mathbf{F}^D \cdot |\mathbf{u}_g - \mathbf{u}_l| \propto \alpha_g \frac{|\mathbf{u}_g - \mathbf{u}_l|^3}{d_b}. \quad (2.40)$$

Moreover, the turbulent dynamic viscosity is enhanced by the presence of the bubble-induced viscosity, which is modelled according to (2.42); see later.

The models have been used at RPI to predict the bubbly air/water upfbw data of SERIZAWA, 1974, the downfbw data of WANG ET AL., 1987, and the upfbw data of LOPEZ DE BERTODANO, 1992 for fbw in a pipe with triangular cross-section. Overall, the models appear to perform well.

Bubble-Induced Viscosity model

A variant to the previous model consists of calculating the turbulent dynamic viscosity as the sum of a shear-induced and a bubble-induced viscosity, thus

$$\mu_t = \mu_{t,SI} + \mu_{t,BI} \quad (2.41)$$

avoiding the need to solve a transport equation for k_{BI} . In full (SATO ET AL., 1981, or ANGLART ET AL., 1993):

$$\mu_t = C_\mu \rho_l \frac{k_l^2}{\epsilon_l} + \frac{1}{2} C_{\mu b} \rho_l \alpha_g d_b |\mathbf{u}_g - \mathbf{u}_l| \quad \text{with} \quad C_\mu = 0.09, \quad C_{\mu b} = 1.2 \quad (2.42)$$

This simple model is basically a Prandtl mixing-length model, with the bubble radius used for the mixing length, and with $C_{\mu b} \rho_l \alpha_g |\mathbf{u}_g - \mathbf{u}_l|$ as the mean eddy fluctuation.

The effect of introducing this bubble-induced viscosity component in an analysis of the ANAGBO & BRIMACOMBE, 1990 experiments appears to result in an enhanced coupling between the plume and the surrounding fluid, due to increased turbulent shear at the edge of the plume (SMITH, 1997).

A comparison between the models of Simonin and Viollet (first version) and Malin and Spalding against experimental data has been undertaken by SMITH, 1999, and by SHENG & IRONS, 1995. Smith found that the Malin and Spalding model is not able to predict the correct velocity and volume fraction distributions, as measured in the Anagbo and Brimacombe experiment, while the Simonin and Viollet model is more successful. According to Sheng and Irons both models were in good agreement with data from their own experiments, but it must be noted that they used a Lagrangian model for bubble motion, and that bubble breakup was allowed.

Recently, the models of de Bertodano (Lahey group), Issa (Gosman group), and Simonin (latest version) have been evaluated by LATHOUWERS & VAN DEN AKKER, 1999 for turbulent, bubbly flow in a plane vertical mixing layer developing in a square duct, and results compared with the measurements obtained by ROIG ET AL., 1993. The principal findings are summarized here.

- The turbulence level is underpredicted by all three models, although the introduction of bubble-induced turbulence partly improves the results.
- The models of Simonin and de Bertodano slightly underpredict the bubble dispersion, while the model of Issa overpredicts it. The latter result could probably be improved by increasing the empirical turbulent Schmidt number σ_I .

2.4 Calculations

The results of numerical simulations with the previously discussed models are presented now. A sensitivity study of the effect of the grid, and of the turbulence models has been performed. All the calculations have been carried out using the commercial code CFX-4.2, 1997. The scheme used for the spatial discretisation of the advection terms is TVD with Van Leer flux limiter (second order accuracy). It is already known from other studies (see for instance LATHOUWERS & VAN DEN AKKER, 1997) that first-order differencing schemes (UPWIND) suffer from excessive diffusion, while higher order schemes such as QUICK have the disadvantage of being unbounded in areas with large changes in gradients, and therefore are inappropriate for the volume fraction equations, which are physically constrained in the range $[0,1]$. All the other terms in the equations are discretised in space using second-order central differencing. For the time discretisation, a fully implicit backward-difference, time-stepping procedure has been employed.

The interfacial forces used are the following:

- added mass force (2.2), with $C_{VM} = 0.5$;
- buoyancy force (2.5);
- drag force (2.6), with $C_D = 0.44$;
- lift force (2.10), with different coefficients according to the particular authors (see Table 2.2);
- turbulent dispersion force according to the authors' prescriptions (DAVIDSON, 1990 and LOPEZ DE BERTODANO, 1992).

All the authors use an equal pressure assumption, except the RPI group (2.18), but since the inclusion of such a term was not possible in our code, it has been neglected also in that case.

The turbulence models used are the following:

- Simonin and Viollet model (2.19), (2.20);
- BIV (Bubble-Induced Viscosity) model (2.42);
- Lee (RPI group) model (2.38), (2.39), (2.42);
- Issa model (2.27), (2.28).

Tables 2.1 and 2.2 summarize the test cases and the coefficients involved. The turbulent dispersion force introduced by Issa (2.17) uses an empirical coefficient $\sigma_I = 0.3$ in the denominator of the expression, which corresponds to a multiplying coefficient of 3.3.

<i>Case No.</i>	<i>Grid (S/U/F)¹</i>	<i>Turbulent Dispersion Force (D/L/I)²</i>	<i>Turbulence Modelling (SV/BIV/L/I)³</i>
1	S	D	SV
2	U	D	SV
3	F	D	SV
4	S	D	BIV
5	S	L	L
6	S	I	I

1 - S = Standard, U = Uniform, F = Fine

2 - D = Davidson, L = Lahey, I = Issa

3 - SV = Simonin & Viollet, BIV = Bubble Induced Viscosity, L = Lee, I = Issa

Table 2.1: Calculations overview

-	C_{TD}	C_L
S&V	-	0.1
Sato	-	0.1
Lahey	0.1	0.5
Issa	3.3	0.1

Table 2.2: C_L and C_{TD} coefficients

2.4.1 Results of different grid set-up

Three 2D axisymmetric computational grids have been used: the first one consists of 50 meshes in the radial direction, the porous plug covering the first 17 adjacent to the axis of symmetry,

and 80 in the axial direction, of which 55 are below the initial water level. The mesh sizes are in geometric progression with ratio 1.05 in the (outward) radial direction, and are in symmetrical geometric progression in the axial direction with ratio 1.1 in the space occupied by the water, while in the gas space they are in geometric progression (upwards) with ratio 1.11. The second grid is built with 83 meshes uniformly distributed in the radial direction, the porous plug covering the first 10 meshes next to the axis of symmetry. In the axial direction there are 120 meshes uniformly distributed below the initial water level, and 20 in geometric progression with ratio 1.1 in the gas space. Finally, the third grid consists of 70 meshes in symmetrical geometric progression with ratio 1.05 in the radial direction, the porous plug covering the first 15 meshes. In the axial direction there are 99 meshes below the water level, in symmetrical geometric progression with ratio 1.04, and 25 meshes in the gas space in geometric progression with ratio 1.12.

The computational grids are made with 2 blocks, in order to represent the initial water and air volumes, and are shown in Fig. 2.1. The first one (standard) features mesh concentrations towards the axis of the vessel, to resolve the void fraction and velocity profiles in the plume, towards the base, where the air inflow takes place, and at the water surface. In the second grid (uniform), the meshes are uniformly distributed (in the water space) with size $3 \times 3 \text{ mm}$, according to the bubble size. The third (finer) grid includes a better mesh refinement close to the wall in order to better resolve the downward flow region, which could have an important effect on the plume development.

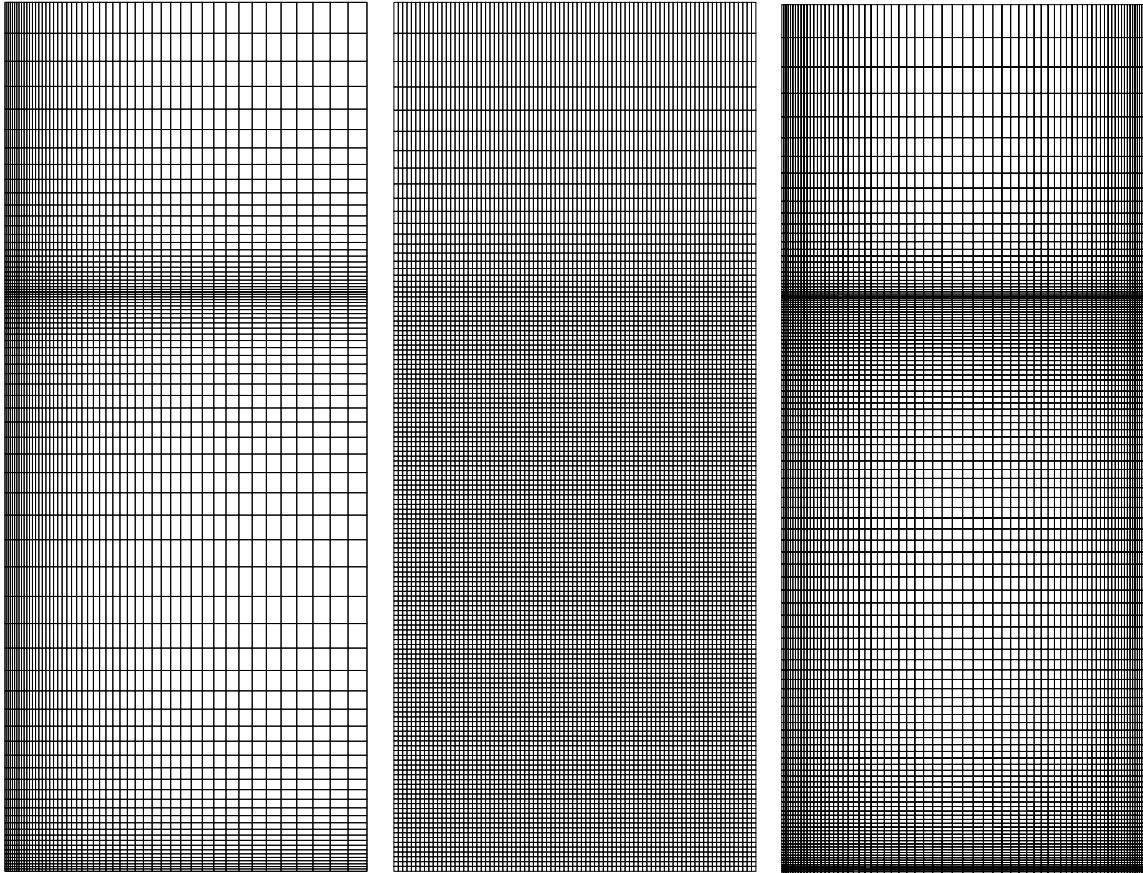


Figure 2.1: Standard grid (left), uniform grid (center) and finer grid (right)

The gas space above the water level has been extended to eliminate the influence of the (pressure-

constant) boundary condition at the top of the model on the flow near the water surface. The adequacy of the axial symmetry assumption has been confirmed in a previous work SMITH & MILELLI, 1998, in which 3D calculations have been carried out and compared against 2D predictions.

The calculations with the different meshes are referred to as Cases 1, 2 or 3, respectively, in Table 2.1. Results are presented in Fig. 2.2 (void fraction profiles) and Fig. 2.3 (velocities profiles). As far as the void fraction is concerned, the major difference is at $x = 300 \text{ mm}$ above the inlet, next to the axis of symmetry, where the discrepancy between the standard (Case 1) and the uniform (Case 2) grid is 8% of the maximum value. Close to the wall, the finer grid (Case 3) is clearly able to better resolve the local velocity profile, which anyway had no influence on the void fraction distribution in the plume. In contrast, the distribution obtained for Case 2 shows a slight underprediction of the velocity (and void fraction) close to the axis of symmetry compared to the other two. In other words, the uniform grid (Case 2) is more diffusive. As a conclusion, the least CPU-expensive grid, which has been referred to as Case 1, is able to resolve the region close to the axis of symmetry, and this seems to be sufficient since the influence of the recirculation region on the plume characteristics (once steady-state conditions have been reached) has been seen to be negligible.

2.4.2 Results of different turbulence models

A comparison between results obtained using each of the four turbulence models described above against the experimental data from the ANAGBO & BRIMACOMBE, 1990 experiment is presented below.

All the plots show the radial distributions of various quantities at 50, 100, 200, 300 and 380 mm elevation above bubble injection. Figures 2.4-2.5 show the void fractions, Figures 2.6-2.7 the gas axial velocities, and Figures 2.8-2.9 the liquid axial velocities. Even though there are no experimental data available for the turbulence quantities, a comparison has been made between the turbulent kinetic energy (k_l), the turbulent dissipation (ϵ_l), and the turbulent viscosity (μ_t), for each of the different models: Figures 2.10-2.11 for k_l , Figures 2.12-2.13 for ϵ_l , and Figures 2.14-2.15 for μ_t , respectively. Finally, Fig. 2.16 shows the centerline axial velocities for each model. There are no data for the liquid, but the comparison is useful to estimate the relative velocity between the gas and liquid phase.

It has to be remarked here that the plots of the experimental data in the original paper of ANAGBO & BRIMACOMBE, 1990 have no error bars. Moreover, none of the two-phase turbulence models have been tested for a bubble plume configuration, except that of Simonin and Viollet (by SHENG & IRONS, 1993).

It can be seen from Figures 2.4 and 2.5 that Case 6 (Table 2.1) is too diffusive (in comparison with the experimental data), indicating that the spreading is greater and the gas-rise velocities are smaller than for the other cases. This effect could be due to the coefficient σ_l in (2.17) which is too small, having been used originally in a different context: viz. a cylindrical pipe, in which wall effects could be important. At $x = 380 \text{ mm}$ the results are less accurate because of the influence of the nearby surface in the pool. On the other hand, Case 4 gives the best void fraction distribution and spreading rate.

A common feature of the calculations is the lack of entrainment at the edge of the plume, which is noticeable since the gas velocities are better defined at the centerline than at the edge itself. Only Cases 1 and 6 appear to have the correct qualitative (but not quantitative) distribution of gas velocities. In other words, the coupling between the pool and the plume is not satisfactory for any of the models employed. Finally, the slip velocity is close to 0.30 m/s , as can be seen in Fig. 2.16,

in good agreement with the predicted value of the rise velocity of a single bubble in a quiescent liquid (WALLIS, 1969).

The liquid velocity has not been measured in the plume, but only outside in the pool, and here the calculations all give similar results; that is, the water recirculation is not correctly described in comparison with the experimental data.

As far as the turbulence quantities are concerned (Figures 2.10-2.15), it is clear for Case 5 that the dissipation is largely overestimated with respect to the other models, resulting in an underprediction of the turbulent viscosity in the plume. As a consequence of this, there is no mechanism for slowing down the bubbles, and their acceleration (Fig. 2.16) is completely wrong. The empirical constant used for the extra dissipation term in (2.39) comes from analogy with the single-phase $k - \epsilon$ model, which in this case could be misleading. Besides, the mechanism of turbulence production, that is the shear work done by the bubbles, does not consider the turbulent energy generated in the wakes of the bubbles, which probably is the main effect, at least in the core of the plume where the void fraction is higher. It has to be pointed out anyway that the shear production of turbulence is the principal effect in a mixing layer process, for which the model works better.

Concerning the model of Issa (Case 6), it should be also stressed that the modelling of C_t , which is the core of this model, has been derived from the single-bubble momentum equation, neglecting the effects of a bubble swarm. In Fig. 2.17 is shown the radial distribution of C_t for each elevation. It can be seen that the range of variation is generally small (between 1.35 and 1.5), with the maximum value on the centerline. This model took inspiration from the experimental results of ROIG ET AL., 1993, who found that in a mixing layer (with 2% void fraction) the ratio of the *rms* of the bubble velocities to the *rms* of the liquid velocities is practically constant with a mean value of 1.5. The extension of those results to the present case anyway has to be made with caution, first because their case has a different geometry, the turbulence is mainly shear-induced and not bubble-induced, and also because of the differences in the void fraction. Other experiments, which look at gas and liquid fluctuations in a plume, would be useful.

Finally, as was already mentioned, Cases 1 and 6 predict a reasonable axial velocity profile in spite of the fact that the velocities are too low with respect to the data; Case 5 predicts a slow acceleration of the bubbles up to $x = 330 \text{ mm}$, and then they decelerate, while Case 4 predicts a constant velocity between $x = 100 \text{ mm}$ and $x = 300 \text{ mm}$. The latter Cases show a physically incorrect behaviour, meaning that the respective turbulence models are not valid (or are incomplete), at least for this kind of application.

A brief note on the steady-state nature of the calculations has to be made. All the calculations have been run for 50 s at least, to ensure a steady-state solution. In fact, looking at Fig. 2.18, which represents the time evolution of the velocities (gas and liquid) and the volume fractions on the centerline of the plume at $x = 100 \text{ mm}$ (Case 1), it is evident that there is some influence of the geometric confinement on the plume due to the establishment of the large recirculation region. This induces a change from one asymptotic state to another after 12-16 s. This time is approximately the time required for the vortex to close the loop. The results shown in SMITH, 1999, referred to the wrong asymptotic state even though the general conclusions are not affected by this result.

In the framework of the code CFX-4.2, 1997, there is the possibility of using other turbulence models, such as the *low Re* $k - \epsilon$, the *low Re* $k - \omega$, the RNG, the RSM and the ASM. As far as the $k - \epsilon$ - like models are concerned, the drawback of the turbulence isotropy is still there. Moreover the *low Re* $k - \epsilon$ model is supposed to improve the calculation close to the walls, where the sublayer is usually calculated with an empirical law of the wall, but this is not the case with a free bubble plume. The RSM or the ASM should be the appropriate models for an anisotropic calculation, since the components of the Reynolds stress tensor are evaluated directly,

but unfortunately the models appear to be too fragile for common use. Indeed, to the author's knowledge, there is no example either of the RSM or the ASM being used for turbulent, transient, two-phase flow (with two-way coupling) calculations.

2.5 Conclusions

Numerical simulations of a bubble plume in a confined pool have been carried out. Different grids and models of turbulence have been tested, together with different dispersion forces.

Three different grids were compared: the first (50×80) featured a fine-mesh resolution close to the axis of symmetry; the second (83×140) mesh was uniform, and the third (70×124) fine close to the axis of symmetry and also next to the wall. The same case (Case 1) has been run with all three grids and the void fraction and velocities distributions in the plume look practically the same for the first and the third grids, while the second one was not able to resolve properly the flow close to the axis of symmetry. Consequently, the first grid (the least CPU-time consuming) has been chosen for the subsequent calculations.

The turbulence models considered here are derived from Simonin and Viollet, Sato, Lee (RPI group) and Issa. Generally the results where the plume is developed, that is at $x = 100, 200$ and 300 mm , are better than at $x = 50$ and 380 mm , where they are less satisfactory, or completely wrong. Additionally, particular care has to be taken to obtain the real steady-state solution, since the walls have a tangible influence on the flow conditions in the plume and on the time-scale of the plume recirculation. Concluding, the model of Simonin and Viollet appears to be the most promising, generally speaking, but no model is completely satisfactory. The reasons for this are many and are listed below.

- All models are based on the $k - \epsilon$ model, which implies turbulence isotropy, which is a concept open to debate since, according to some authors (SHENG & IRONS, 1993 and PANIDIS & PAPAILIOU, 2000), this kind of flow has a bias in the vertical direction induced by the bubbles, while others (LANCE & BATAILLE, 1991) have observed that the isotropy of the turbulent field is not altered by the presence of the bubbles.
- The developing region of the plume, just above the injector, requires better modelling since the void fraction is high and interaction effects are important. In particular, the added mass coefficient probably requires higher order terms. This is clear considering also that the acceleration of the bubbles (and consequently of the liquid) is wrong for each model.
- The impinging region, where the plume reaches the surface and the liquid surface is deformed, is not taken into consideration in any model. In particular, if the production and dissipation of turbulence are not properly defined, there could be an effect on the body of the plume, via the recirculation region.
- The models have been tested with fairly good success for different cases and in different geometries, each time tuning the empirical constants was involved, meaning that the generality of present two-phase models is very limited.
- Regarding this particular experiment, there are probably uncertainties in the inlet conditions and, moreover, error bars are missing from the data. It is hoped that higher quality data will be forthcoming from planned PSI bubble-plume experiments.

It has to be pointed out that the empirical constants used are those suggested by the originators of the models, and no tuning has been done, since it was not the purpose of the work to obtain good results just by modifying the constants. Probably it is possible to get better agreement with the data by tuning some of them, but the basic shortcomings will remain. In fact, all the turbulence models here described are just patch-ups of the single-phase $k - \epsilon$ model. Summarizing, there is clearly room for improvement. If we stay within the framework of the $k - \epsilon$ model, it is worth trying to reduce the empirical constants involved in the problem by examining more closely the closure terms, that is the interfacial forces, such as the added mass force or the turbulent dispersion force, or by expanding the concept of bubble-induced turbulence. The other possibility is to explore the use of more sophisticated (but 'usable') turbulence models. In the continuation of this work, both possibilities will be explored.

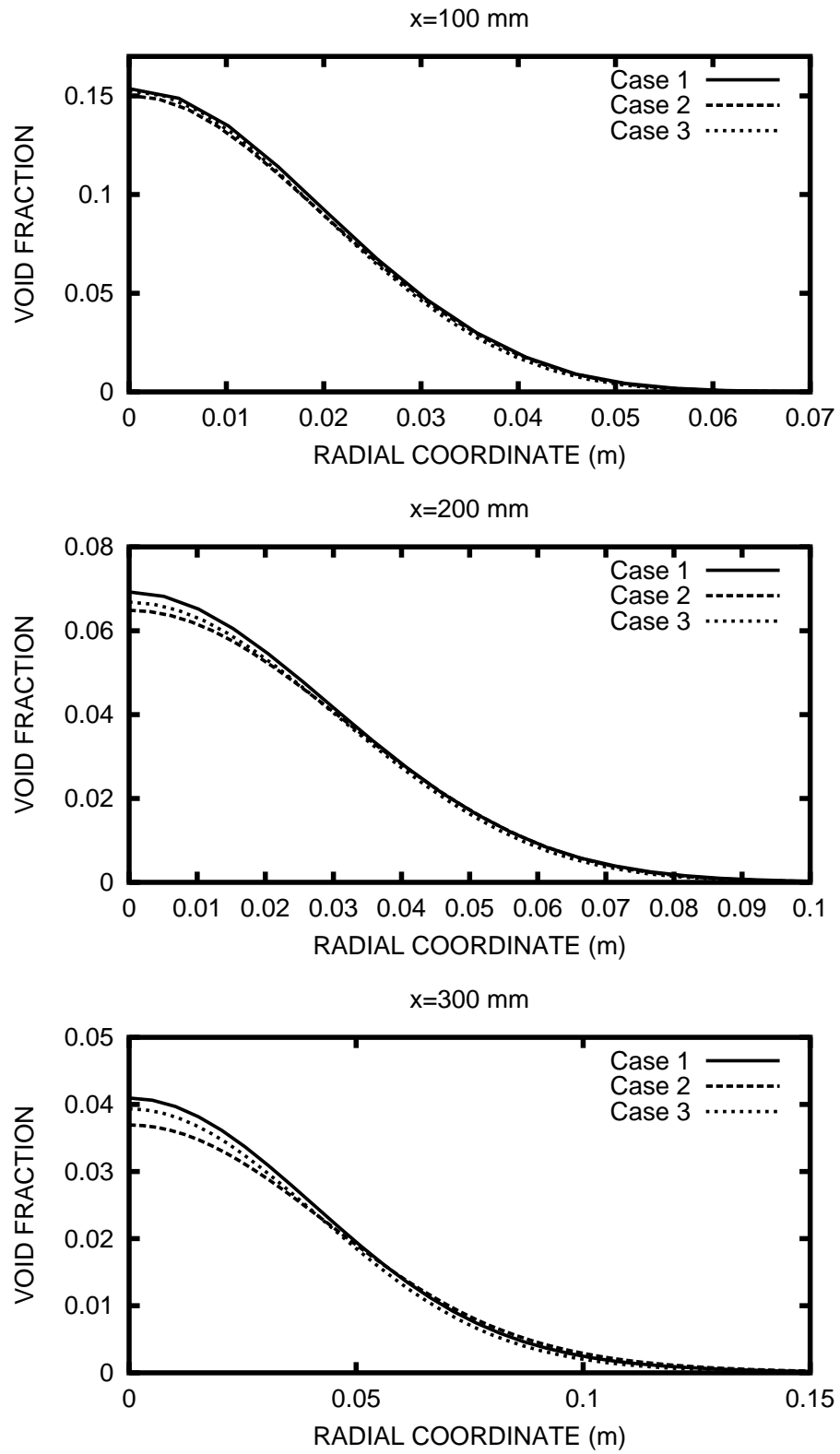


Figure 2.2: Void fraction distributions for different grid set-ups.
Case 1: Standard grid. Case 2: Uniform grid. Case 3: Finer grid.

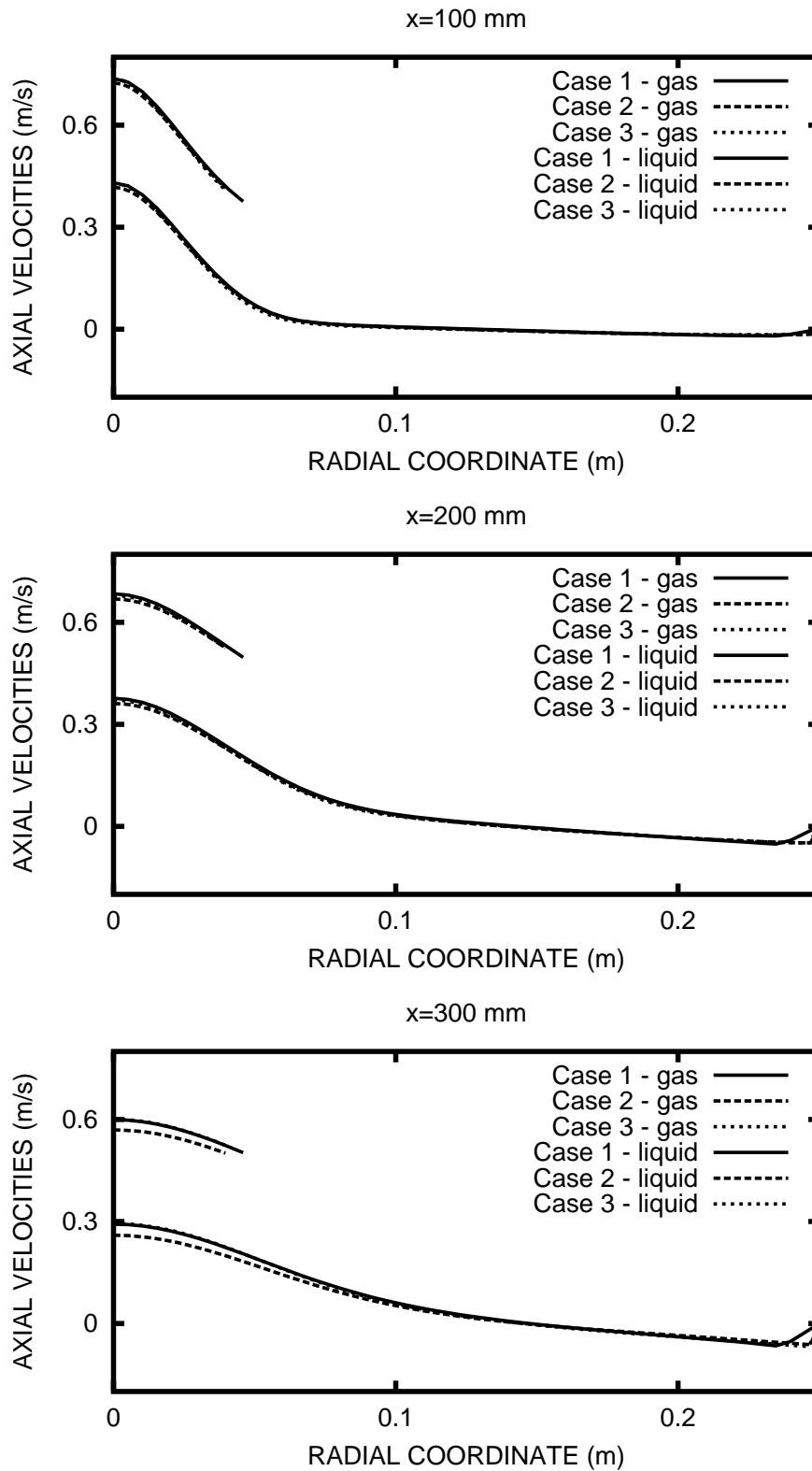


Figure 2.3: Axial velocities distributions for different grid set-ups.
Case 1: Standard grid. Case 2: Uniform grid. Case 3: Finer grid.

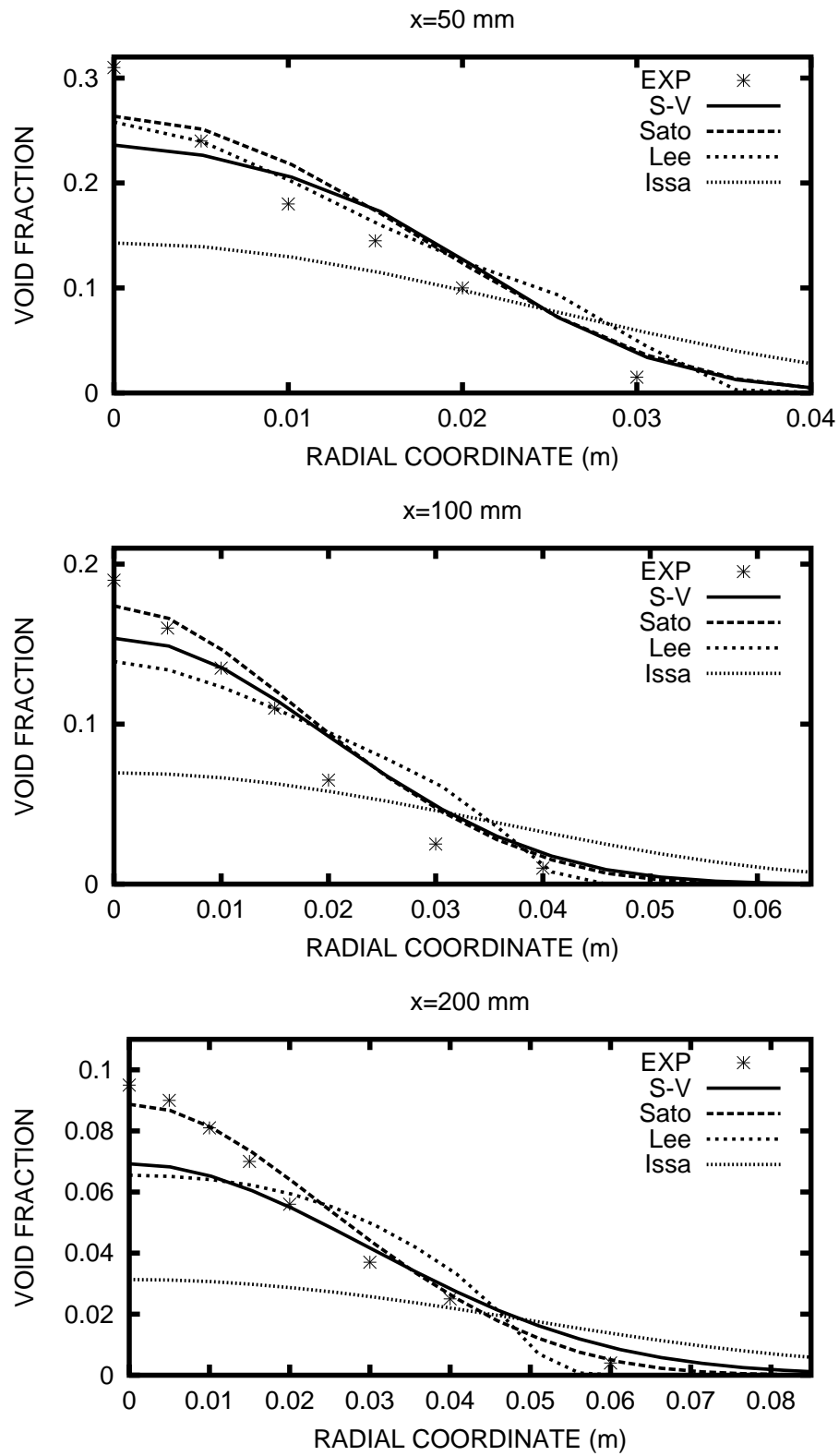


Figure 2.4: Void fraction distributions for different turbulence models (S-V: Simonin and Viollet).

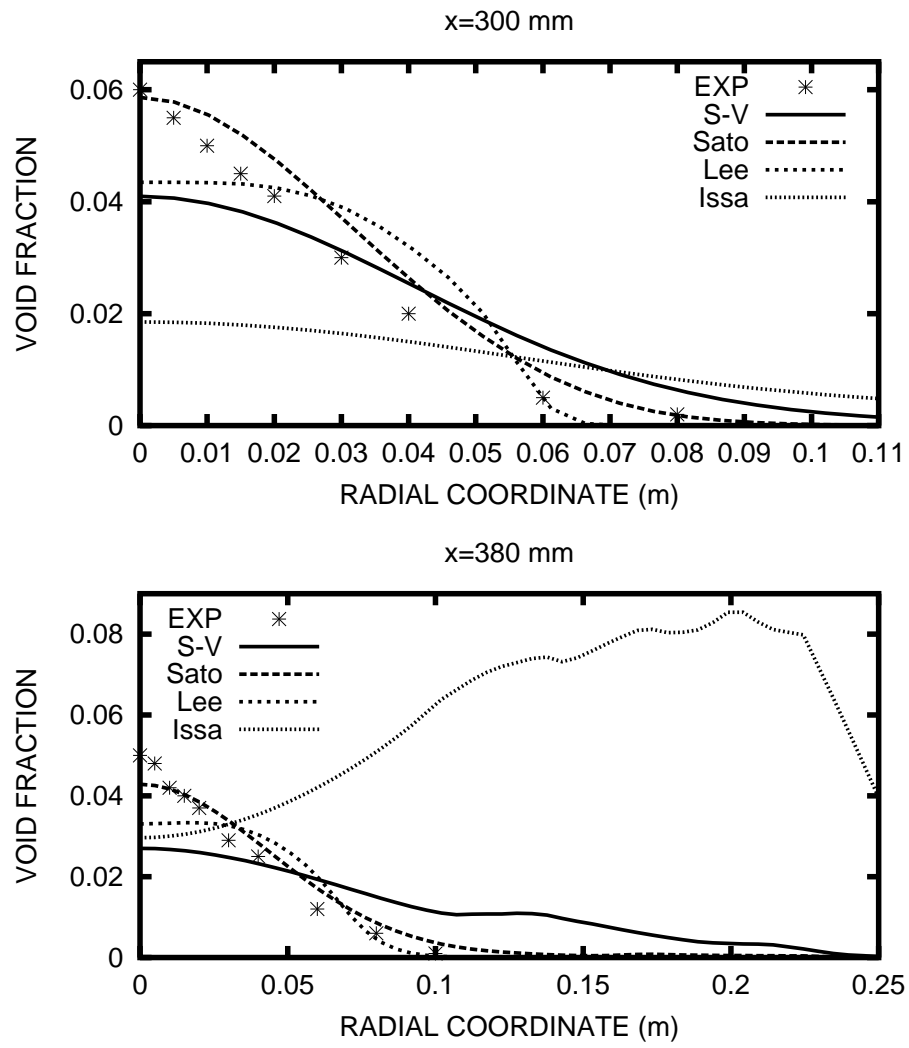


Figure 2.5: Void fraction distributions for different turbulence models (S-V: Simonin and Violet).

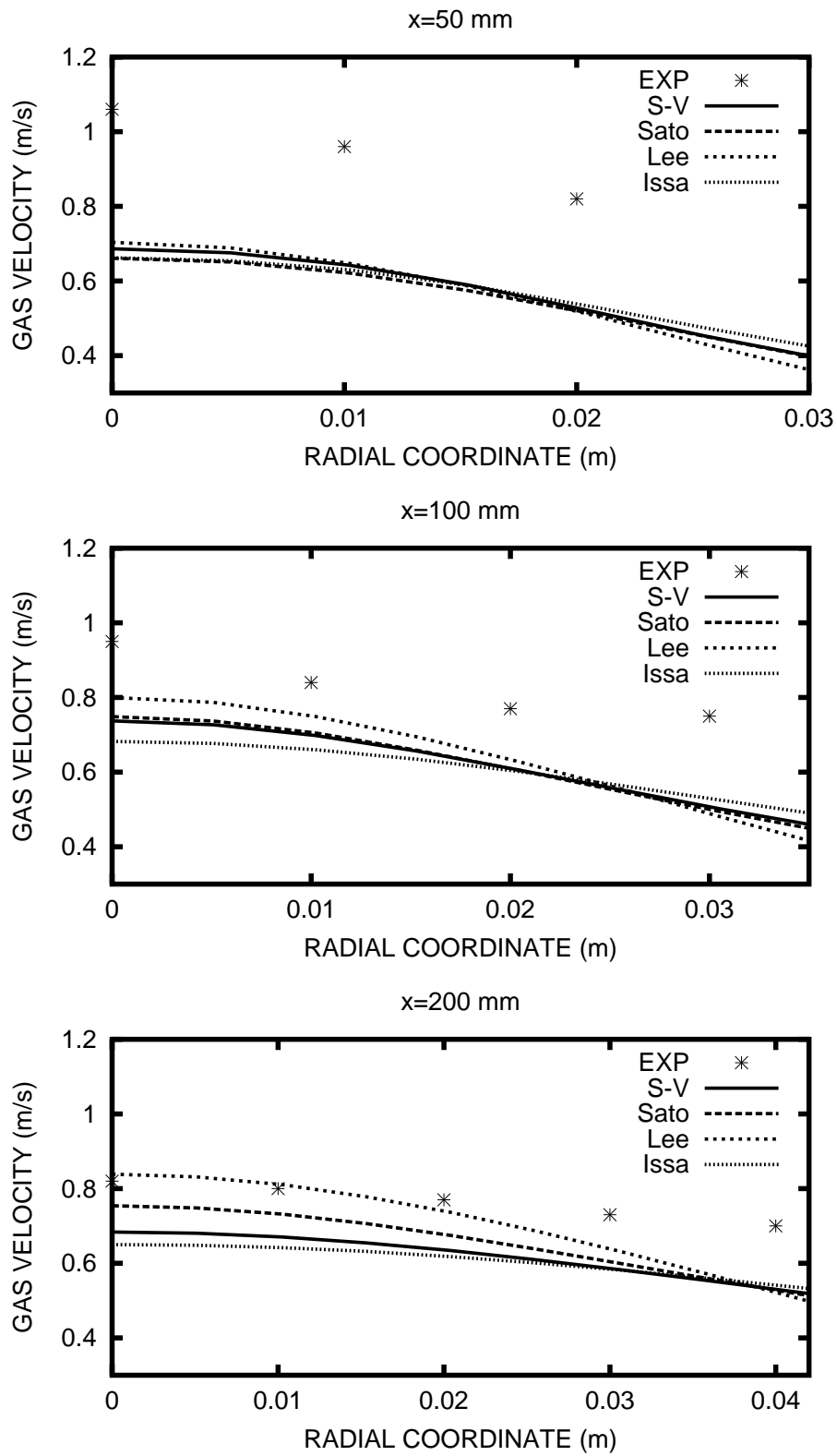


Figure 2.6: Gas velocity (axial component) distributions for different turbulence models (S-V: Simonin and Viollet).

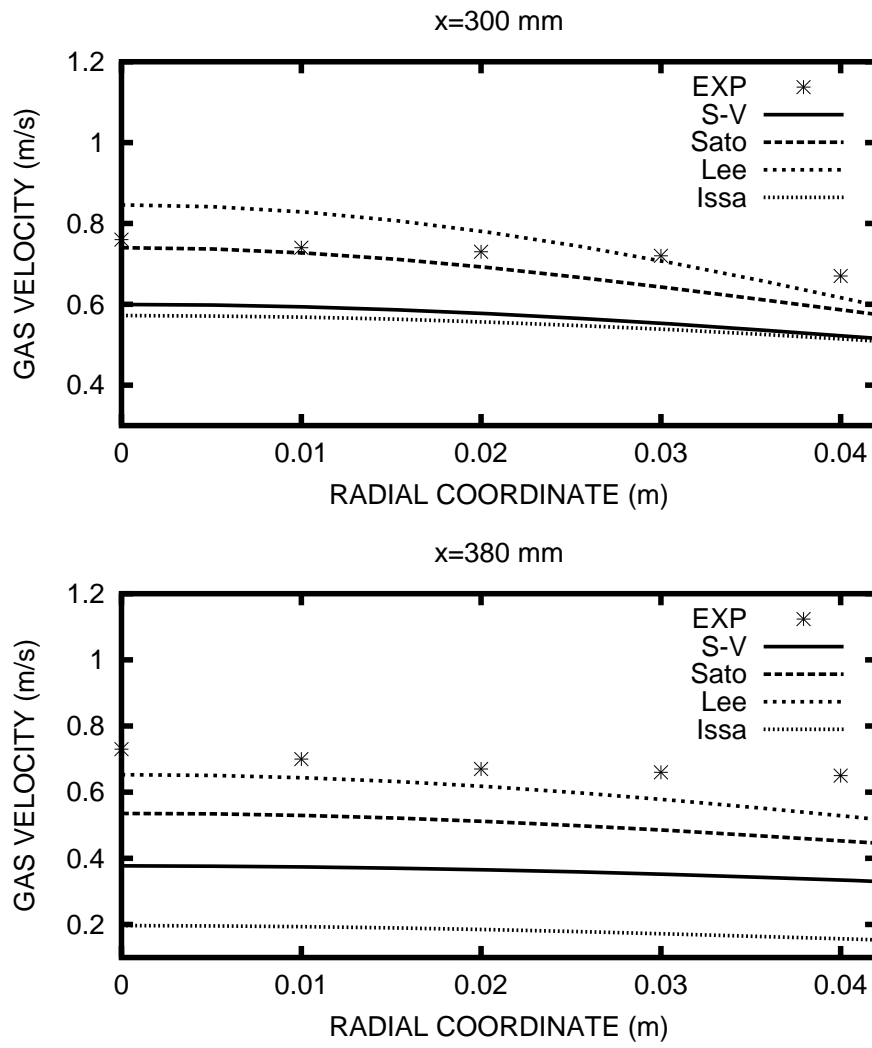


Figure 2.7: Gas velocity (axial component) distributions for different turbulence models (S-V: Simonin and Violet).

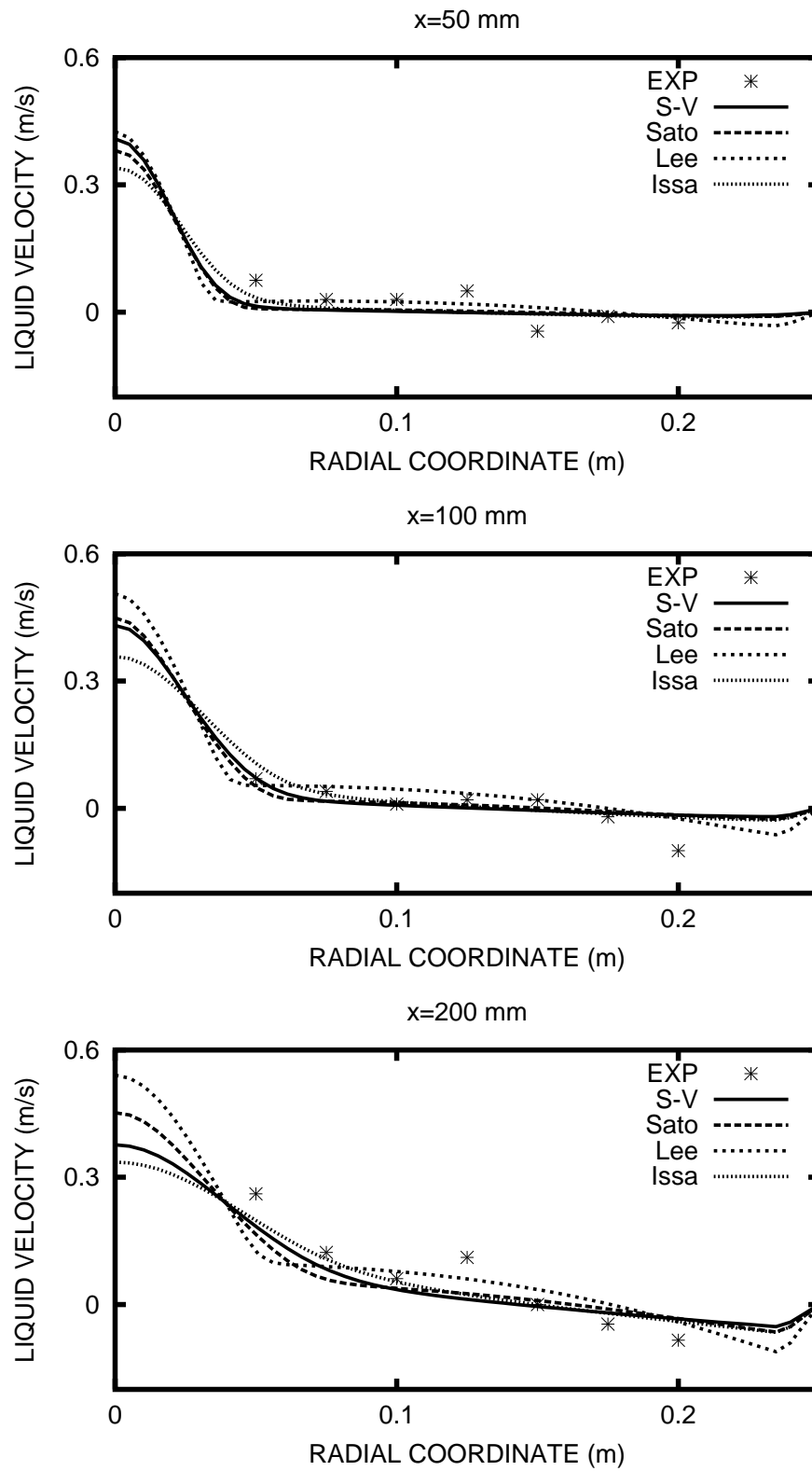


Figure 2.8: Liquid velocity (axial component) distributions for different turbulence models (S-V: Simonin and Viollet).

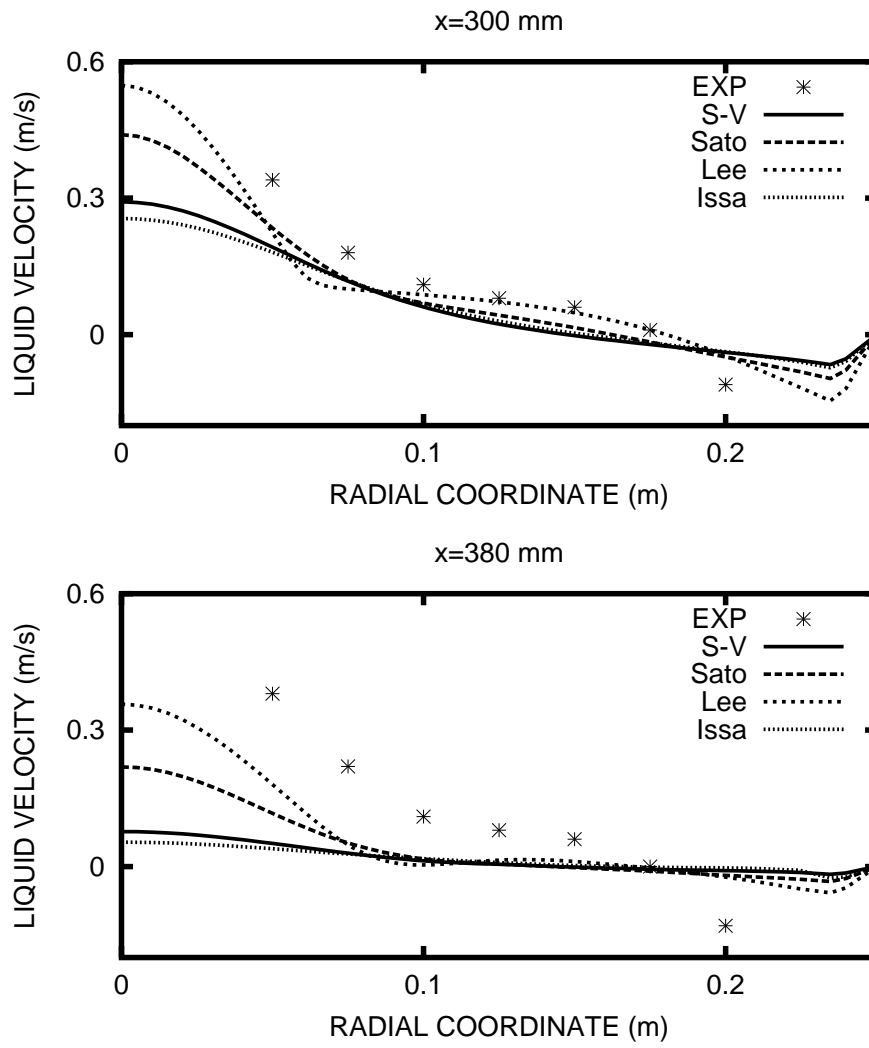


Figure 2.9: Liquid velocity (axial component) distributions for different turbulence models (S-V: Simonin and Viollet).

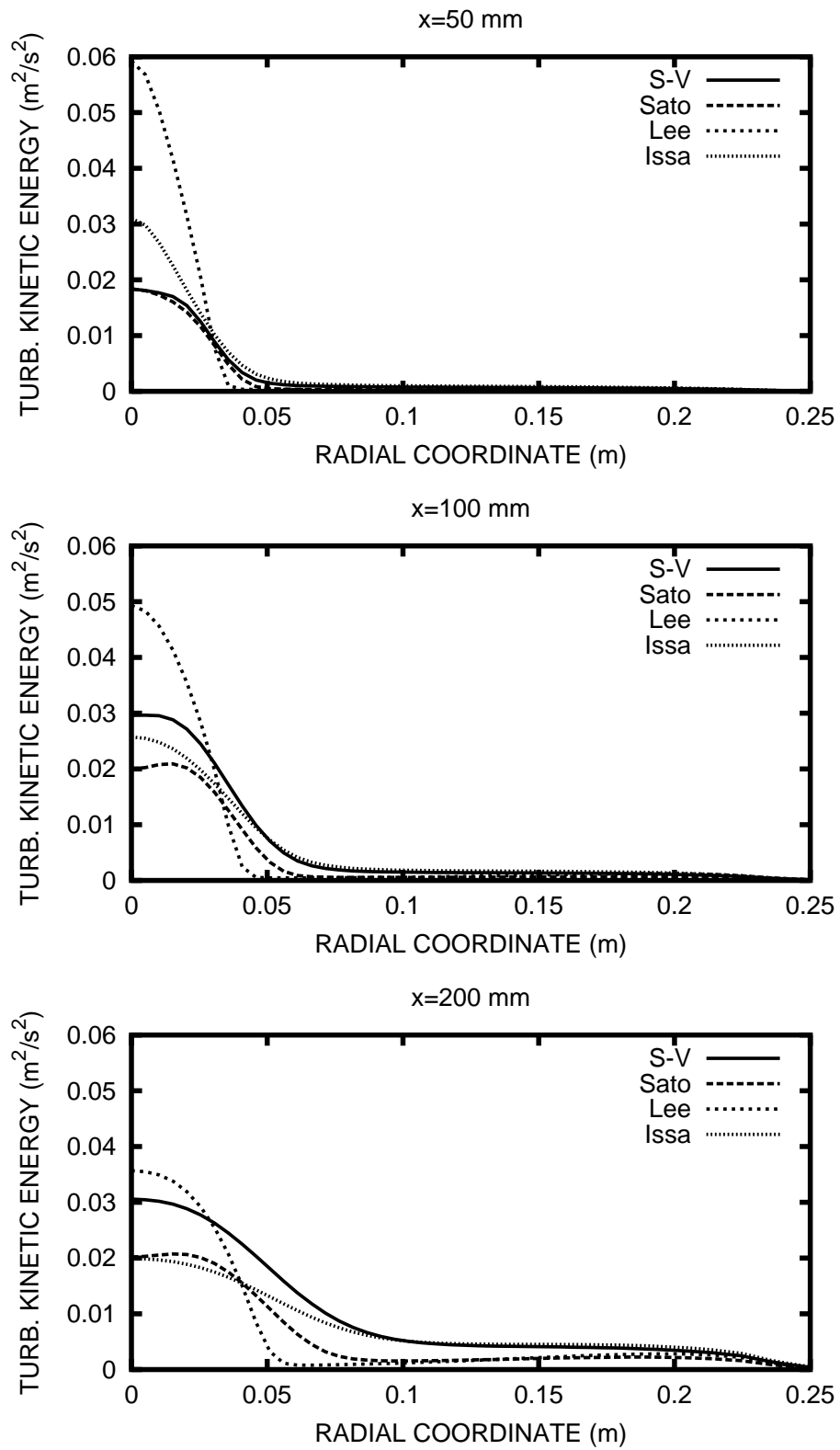


Figure 2.10: Turbulent kinetic energy distributions for different turbulence models (S-V: Simonin and Viollet).

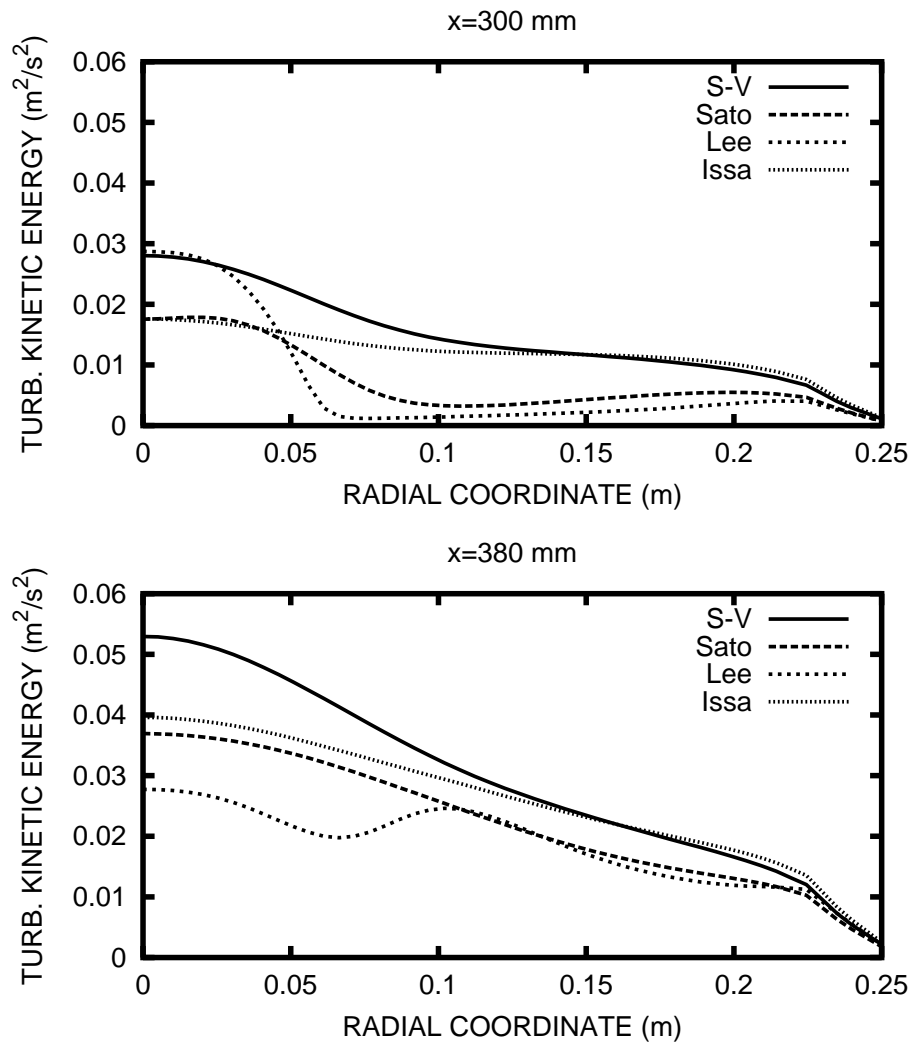


Figure 2.11: Turbulent kinetic energy distributions for different turbulence models (S-V: Simonin and Viollet).

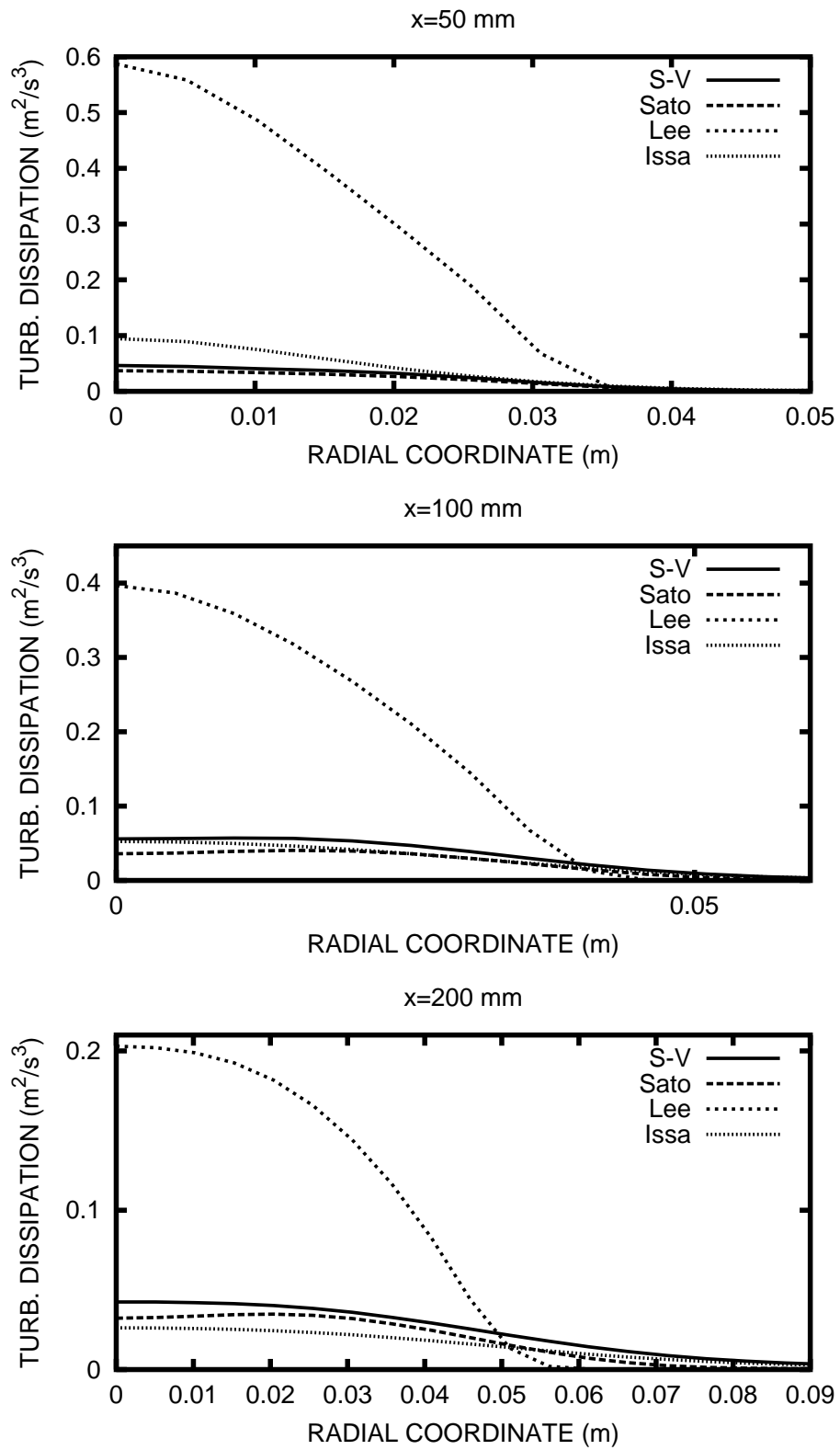


Figure 2.12: Turbulent dissipation distributions for different turbulence models (S-V: Simonin and Viollet).

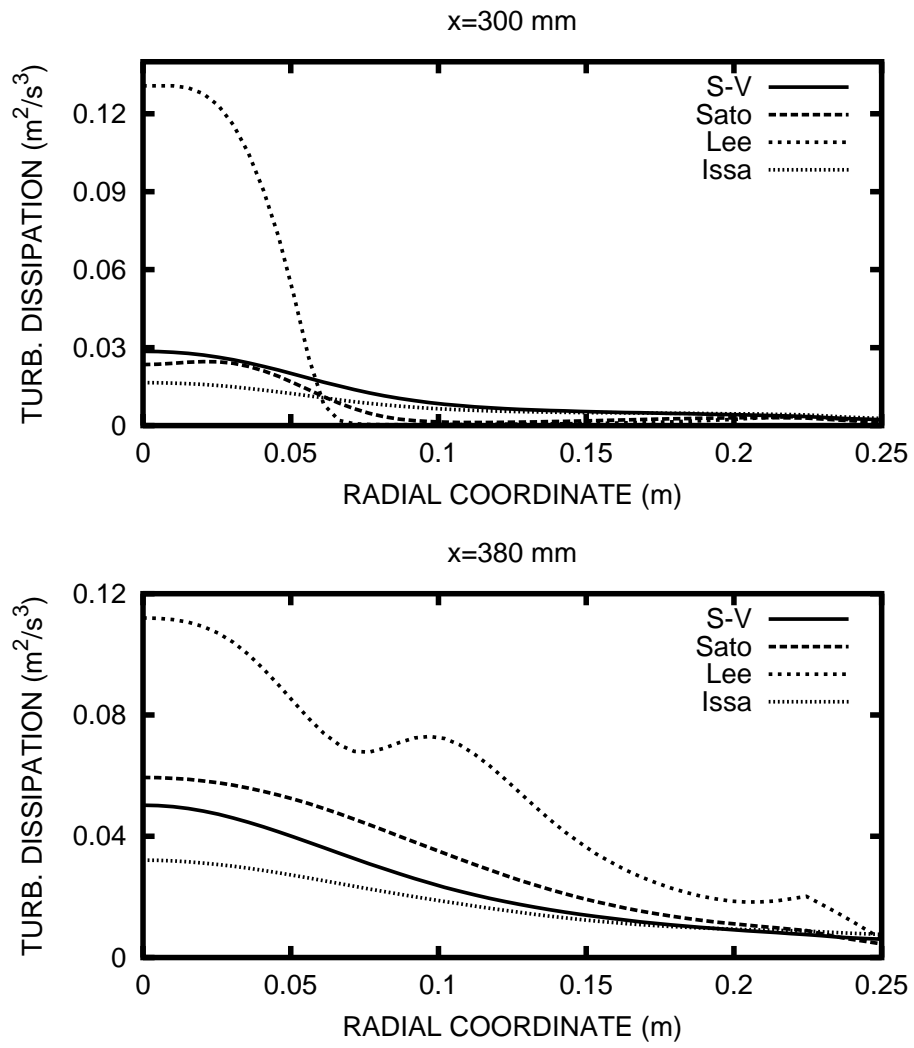


Figure 2.13: Turbulent dissipation distributions for different turbulence models (S-V: Simonin and Viollet).

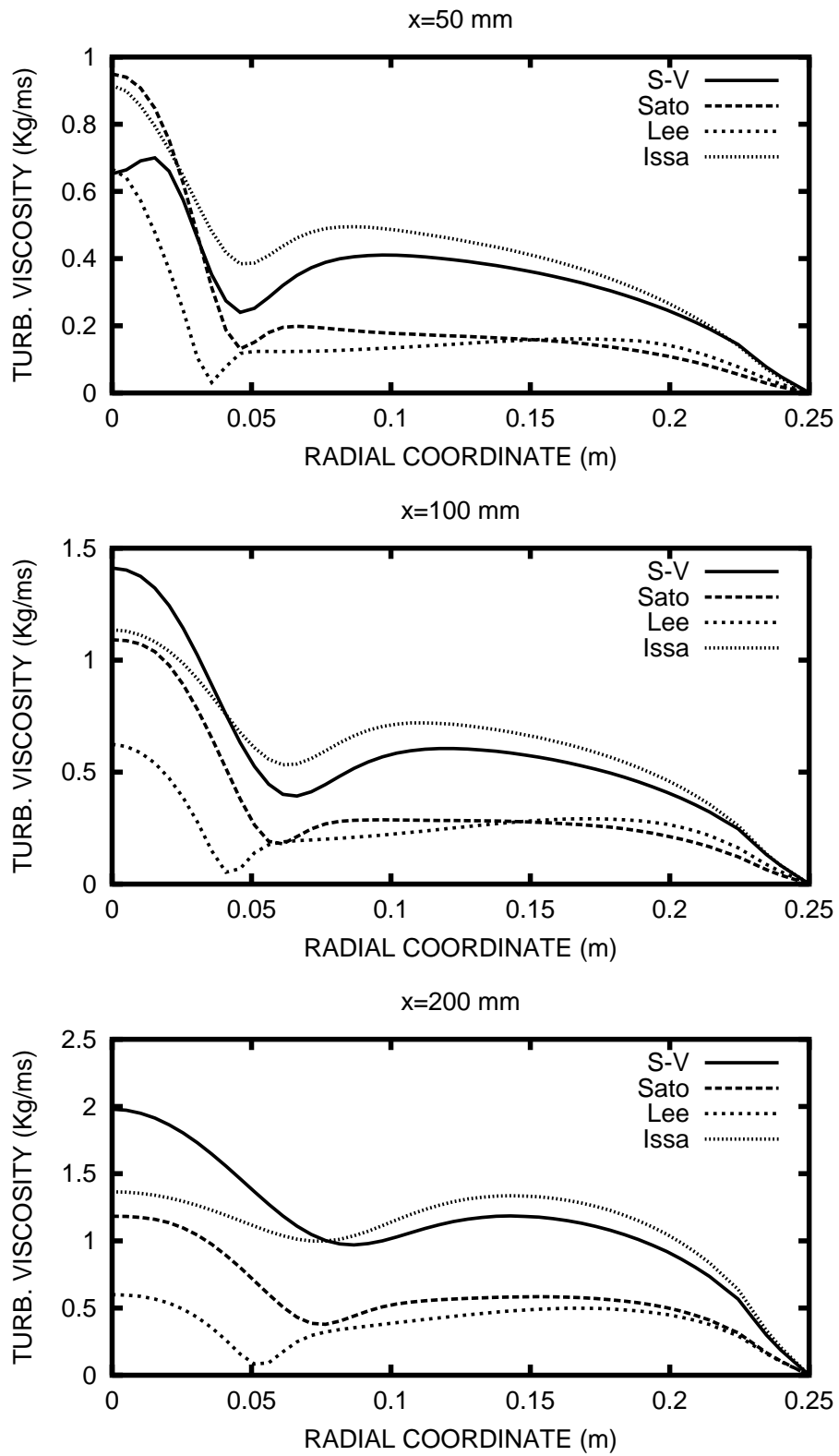


Figure 2.14: Turbulent viscosity (dynamic) distributions for different turbulence models (S-V: Simonin and Viollet).

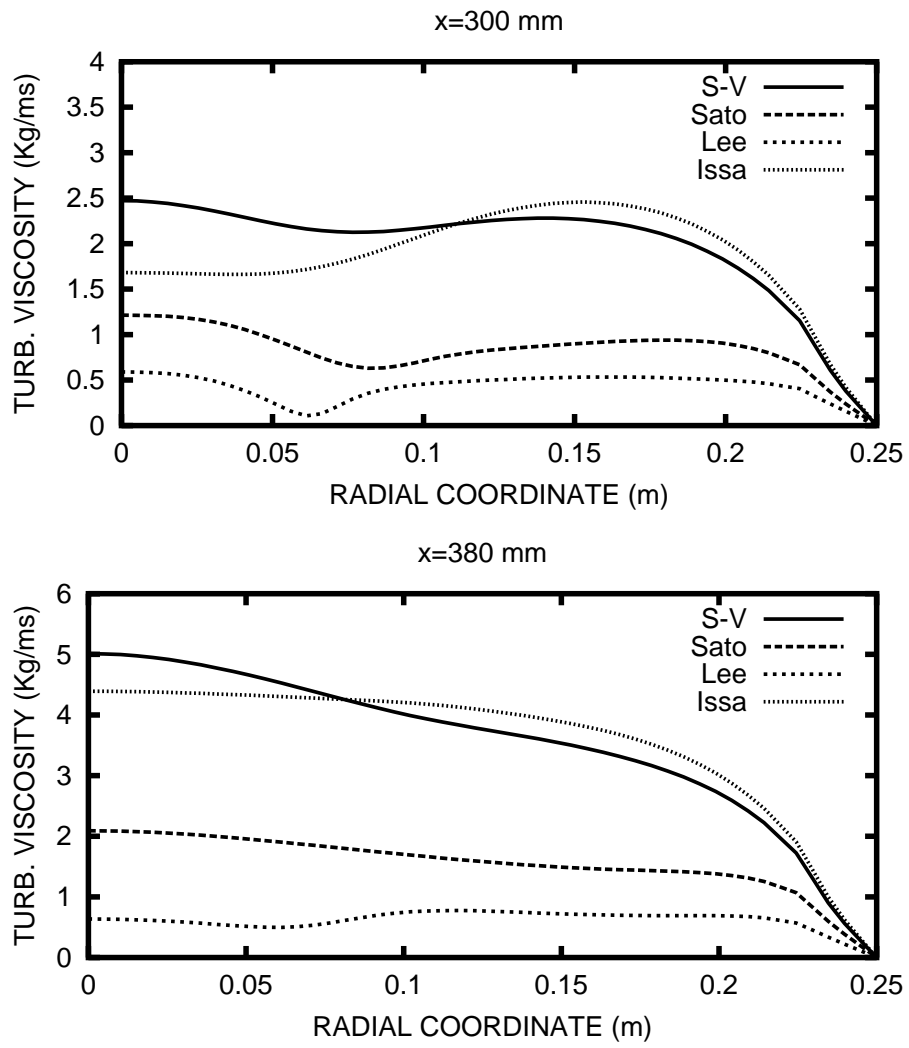


Figure 2.15: Turbulent viscosity (dynamic) distributions for different turbulence models (S-V: Simonin and Viollet).

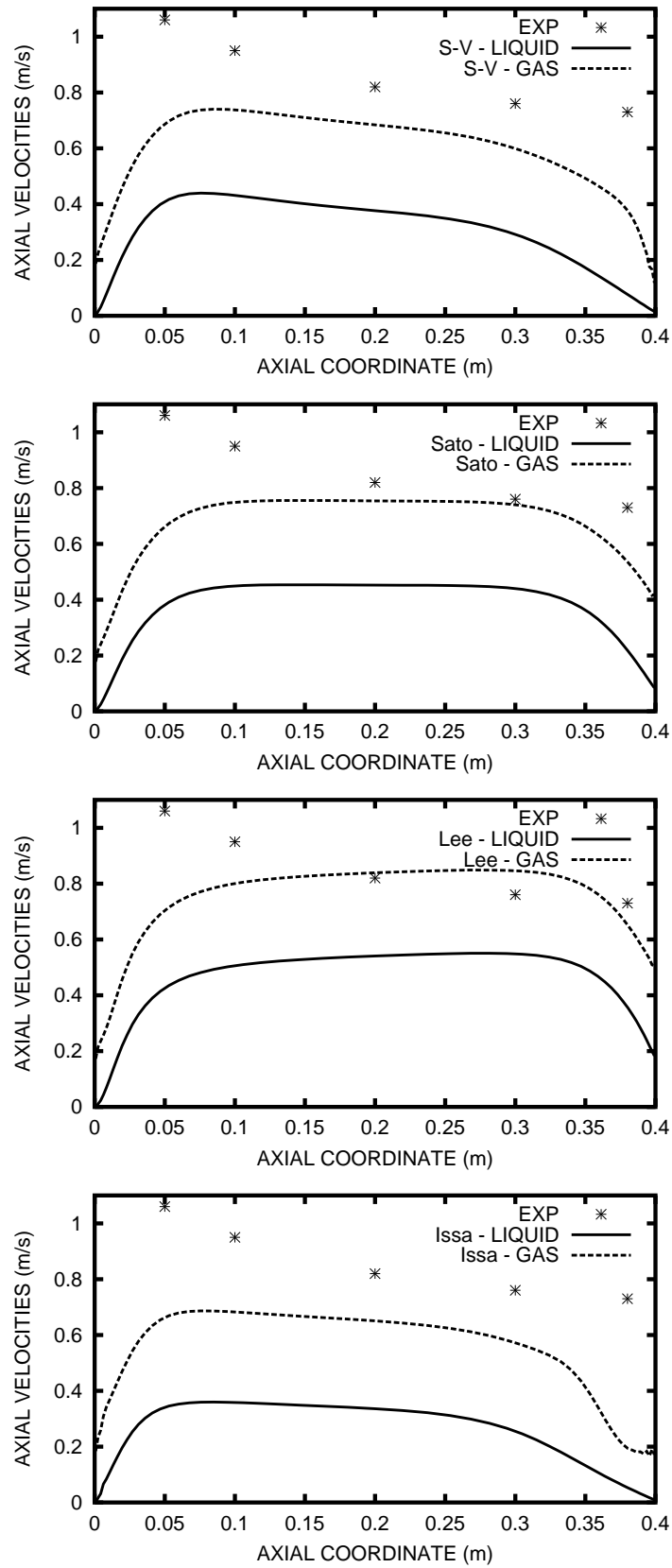


Figure 2.16: Centerline axial velocities distributions for different turbulent models (S-V: Simonin and Viollet)

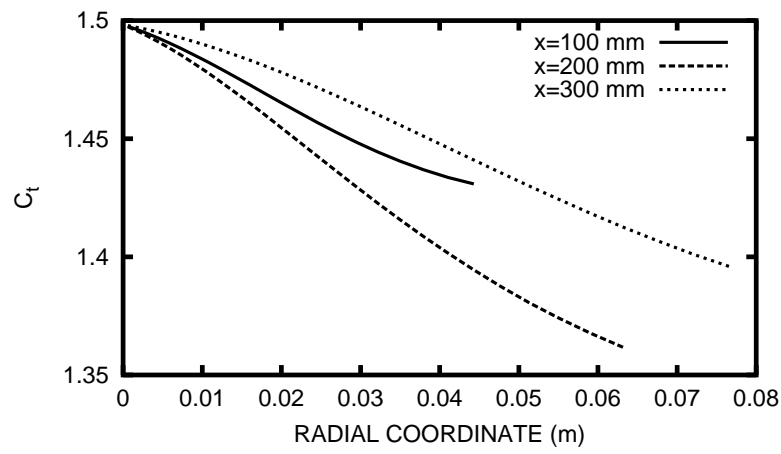


Figure 2.17: Radial distribution of C_t at $x = 100, 200, 300 \text{ mm}$ in case of Issa turbulence model

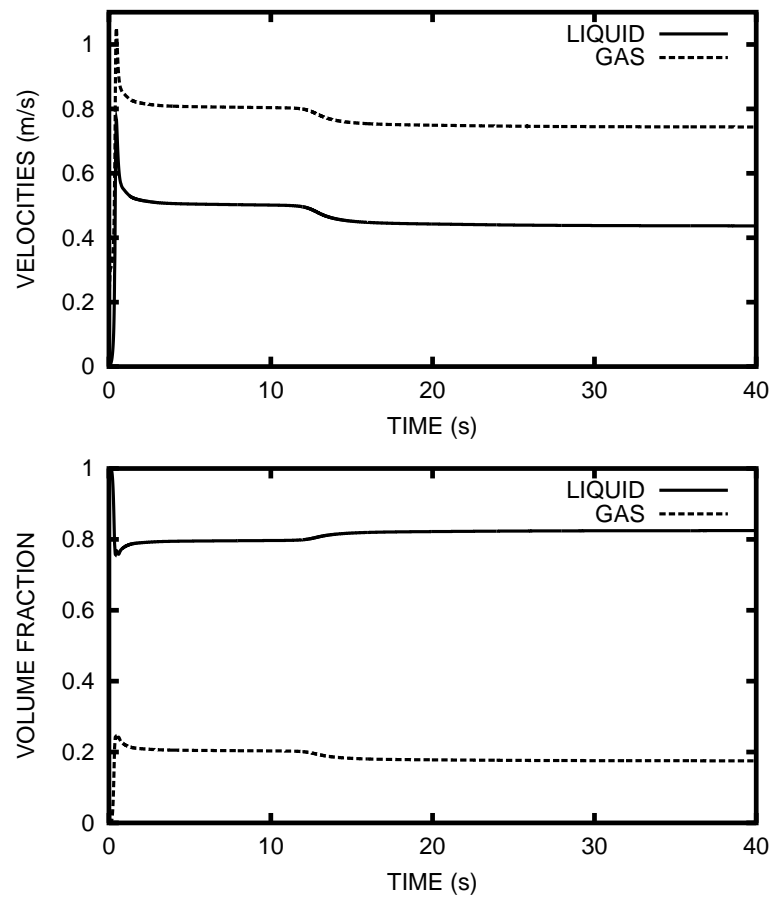


Figure 2.18: Time evolution of velocities (up) and volume fraction (down) at $x = 100 \text{ mm}$ for Case 1

3 Random Dispersion Model

3.1 Introduction

The drag and lift forces depend on the actual relative velocity between the phases, but the Reynolds-averaged equations of motion for the liquid (1.7), (1.9) only provide information regarding the *mean* flow field. To account for the random influence of the turbulent eddies, the concept of a turbulent dispersion force has been advanced. By analogy with molecular Brownian diffusion, the force is set proportional to the local bubble concentration gradient (or void fraction), with a diffusion coefficient derived from the eddy viscosity μ_t (DAVIDSON, 1990):

$$\mathbf{F}_l^{TD} = -\mathbf{F}_g^{TD} = \frac{3}{4}\alpha_l\mu_t\frac{C_D}{d}|\mathbf{u}_g - \mathbf{u}_l|\nabla\alpha_g \quad (3.1)$$

or turbulent kinetic energy k_l (DE BERTODANO, 1992):

$$\mathbf{F}_l^{TD} = -\mathbf{F}_g^{TD} = C_{TD}\rho_l k_l \nabla\alpha_g ; C_{TD} = 0.1 \quad (3.2)$$

A new approach is taken in the present work, where it is shown that it is possible to dispense entirely with artificial turbulent dispersion models by incorporating the statistical, turbulent fluctuations in the liquid directly in the expressions for the drag (2.6) and lift (2.10) forces.

This approach can be seen as an intermediate step between the Eulerian-Eulerian and the Eulerian-Lagrangian formalism and it recalls the so-called Random Walk Models. In fact different computational models are used in literature to simulate particle diffusion employing a stochastic Lagrangian method. They are employed in situations where there is one-way coupling between the phases because the dispersed phase size is smaller than the Kolmogorov micro-scale of turbulence and are known as Random Walk Models (see for instance MACINNES & BRACCO, 1992). A subcategory of these dispersion models uses an approach based on a finite discrete form of the Langevin equation which is supposed to model the turbulent fluctuation velocities in a purely stochastic way. Another class of models is based on the generation of randomly sampled eddies which interact with the particles, whose velocities remain constant during each particle-eddy interaction time and during which the eddy velocity is unchanged. The two categories of models differ because the first provides a continuous fluctuating velocity field (Continuous Random Walk) whereas in the latter the fluctuating velocities change only when the particles encounter a new eddy (Discontinuous Random Walk), see also BOCKSELL & LOTH, 1999.

3.2 Model set-up

The starting point for the *Random Dispersion Model (RDM)* proposed here is to first note that the instantaneous liquid velocity is composed of mean and fluctuating parts according to $\mathbf{u}_l = \overline{\mathbf{u}_l} + \mathbf{u}_l'$, in which the mean velocities are derived from the solution of the mass and momentum equations (1.7), (1.9) and the *rms* values of the fluctuating velocities make up the local mean liquid turbulent kinetic energy k_l according to:

$$2k_l = \overline{u_l'^2} + \overline{v_l'^2} + \overline{w_l'^2} \quad (3.3)$$

in which (u, v, w) are the x, y, z components of velocity. Assuming the turbulence to be isotropic (which is implicit in the formulation of the $k - \epsilon$ model of turbulence):

$$\overline{u_l'^2} = \overline{v_l'^2} = \overline{w_l'^2} = 2k_l/3 \quad (3.4)$$

Accordingly, we assume that the fluctuating velocity components are random deviates of a Gaussian probability distribution with zero mean and variance $\sigma_V^2 = 2k_l/3$. These are obtained by mapping uniform random deviates on the open interval $(0, 1)$ (y coordinate in Fig. 3.1) via the integral of the Gaussian function, as explained in PRESS ET AL., 1989. The uniform random deviate is obtained, in fact, from the random number generator of Park and Miller, with a Bays-Durham shuffle, as programmed in subroutine RAN1 of PRESS ET AL., 1989, and the Gaussian deviate (x coordinate in Fig. 3.1) is returned from an extension of their GASDEV routine, for a distribution of zero mean and variance σ_V^2 . Local fluctuating velocity components are then set according to the following prescription: initially, two calls to the random number generator are made; these are to represent, respectively, the fluctuations u_s and u_e at the start t_s and at the end t_e of the eddy lifetime (JOHANSEN ET AL., 1987), defined as the time during which any particular eddy persist as an entity and is uniquely determined and estimated from the local computed values of k_l and ϵ_l :

$$t_E = t_e - t_s = (3/2)^{1/2} C_\mu^{3/4} \frac{k_l}{\epsilon_l}; \quad (3.5)$$

The coefficient $C_\mu = 0.09$ is the usual one in the Kolmogorov relation for the eddy viscosity:

$$\mu_t = C_\mu \rho_l \frac{k_l^2}{\epsilon_l} \quad (3.6)$$

Consequently, the eddy length scale is defined as

$$l_E = t_E \sigma_V = C_\mu^{3/4} \frac{k_l^{3/2}}{\epsilon_l} \quad (3.7)$$

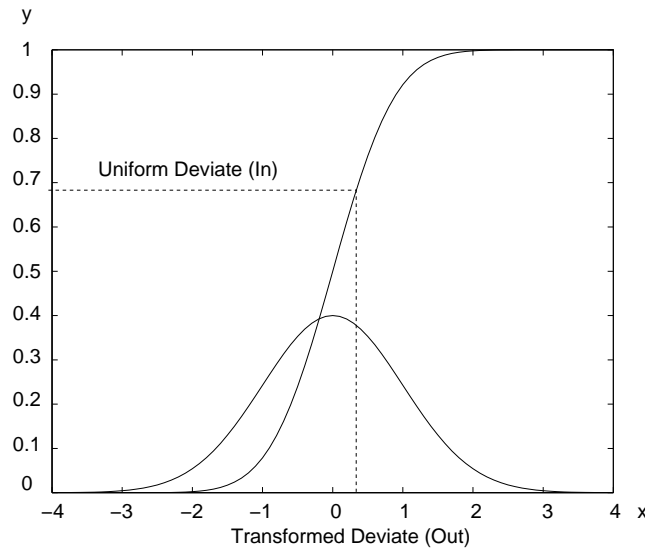


Figure 3.1: Gaussian function and its integral

At intermediate times t , the fluctuating velocity u'_l is obtained using linear interpolation, and once $t > t_e$ a new call to the random number generator is made and the procedure updated. The other fluctuating velocity components v'_l and w'_l are obtained analogously. In Fig. 3.2 are shown our continuous variation method, which has the advantage of taking into account for the inertia of the liquid, in contrast to the discontinuous variation method which has been used by other authors (see for instance PARK & YANG, 1997) in an Eulerian-Lagrangian context. The process described is

carried out for each computational cell independently, and the eddy lifetime period continuously updated according to (3.5). The grid-dependency problem which arises with this approach can be obviated performing a parametric study of the mesh influence as it has already been done in Chapter 2. Note that the variance $\sigma_V^2 = 2k_l/3$ does not take account of any change occurring between t_s and t_e and will therefore only be approximate during the developing stage of the bubble plume. However, once pseudo-steady conditions have been established, there will be little change in k_l and the interpolation performed for intermediate times during the eddy lifetime will ensure continuous transition from one random value to the next. Clearly this approach is based on the assumption that the liquid fluctuations, even in the presence of bubbles which generate pseudo-turbulence, are still Gaussian distributed, as measured by IGUCHI ET AL., 1995 for instance.

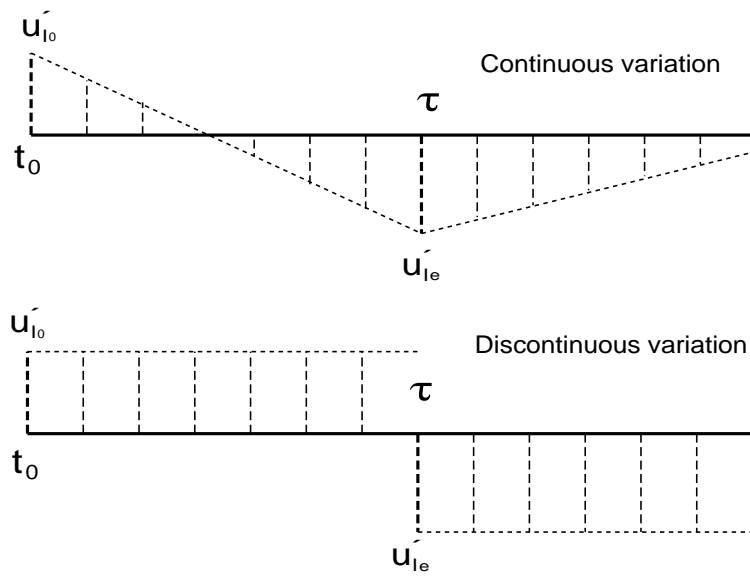


Figure 3.2: Different methods of evaluation for u'_l at each time step

Having obtained estimates of the fluctuating velocity components at each time step, the exact form for the relative velocity between the phases

$$\mathbf{u}_g - \mathbf{u}_l = \mathbf{u}_g - \overline{\mathbf{u}_l} - \mathbf{u}'_l \quad (3.8)$$

may be used in the expressions for the lateral components of the drag and lift forces (2.6), (2.10). Equation (3.8) is used for the drag law component in the lateral directions, where the fluctuations produce dispersion. However, the fluctuations are not used for the axial components of these forces because the empirical coefficients C_D and C_L have been obtained from mean flow measurements of the slip velocity between the phases in the direction of motion.*

3.3 Test calculations

First, a test calculation has been run. The grid is shown in Fig. 3.3. It is a simple 2D case with uniform mesh size ($\Delta = 0.003 \text{ m}$) in which, initially, the void fraction has a Gaussian distribution (Fig. 3.4), according to

*The author is grateful to his colleague M. Andreani for pointing out this fact

$$\alpha_g(x, y) = e^{-10000[(x-0.025)^2 + (y-0.025)^2]} \quad (3.9)$$

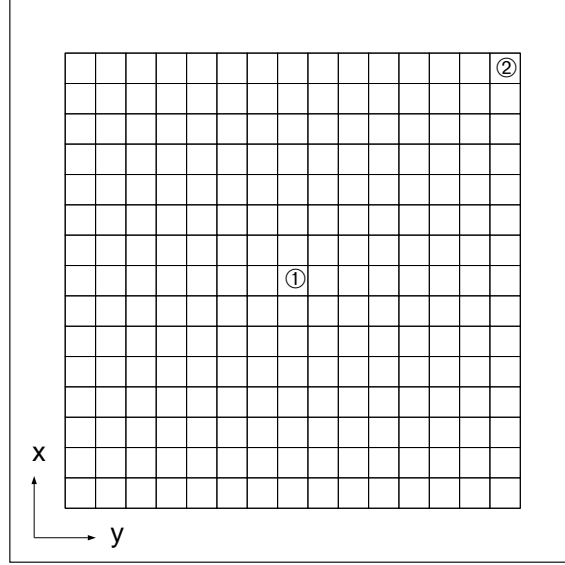


Figure 3.3: Grid setup with the two monitoring points

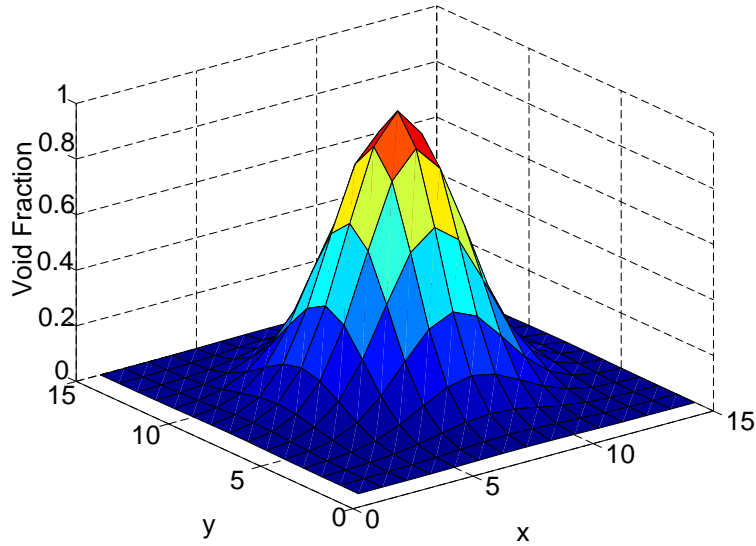


Figure 3.4: Initial void fraction distribution

The goal is to check whether the dispersion mechanism really works, given a certain turbulence intensity. In the calculation there is no interphase force except the drag force (2.6), and there is no turbulence enhancement model. The turbulence quantities are $k = 0.038 \text{ m}^2/\text{s}^2$ and $\epsilon = 0.065 \text{ m}^2/\text{s}^3$, which are approximately the values at the centerline of the bubble plume, 200 mm above the injector, according to the simulation of the Anagbo and Brimacombe experiment described in Chapter 2. In this case, the eddy lifetime is $t_E \approx 0.12 \text{ s}$, according to (3.5), while the eddy length scale is $l_E \approx 0.019 \text{ m}$, according to (3.7). This is important because it shows

that the present grid is appropriate to resolve the flow structures, i.e. the mesh size is smaller than the eddy size. Figure 3.5 shows that the void fraction has indeed spread uniformly, and that the final value is $\alpha_g = 0.126$, which is just the average value of void fraction over the plate.

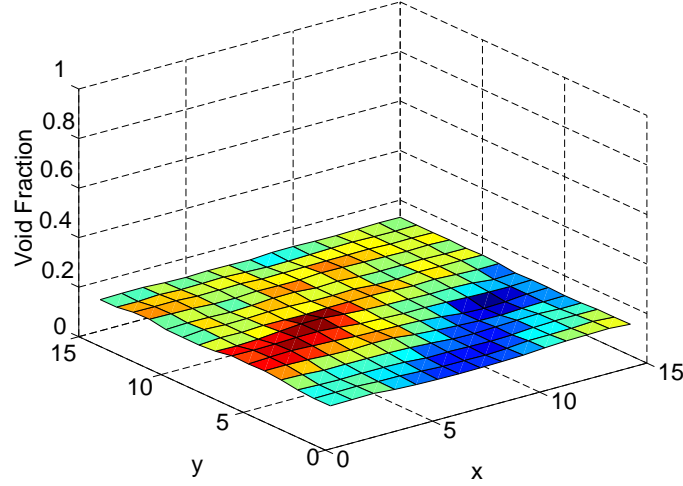


Figure 3.5: Final void fraction distribution

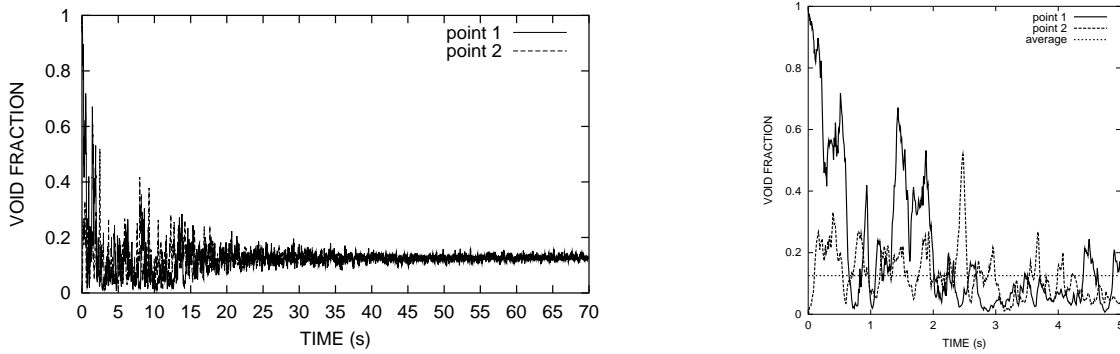


Figure 3.6: Void fraction time-evolution for two different points in the domain with the Random Dispersion Model: full (left), detail (right)

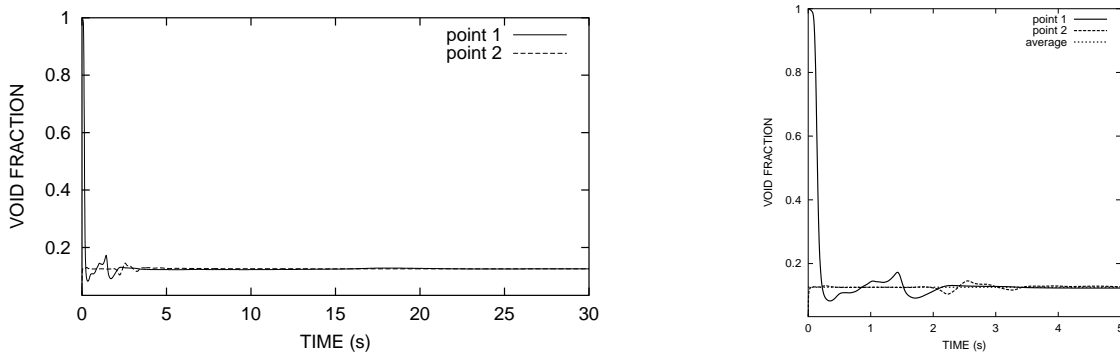


Figure 3.7: Void fraction time-evolution for two different points in the domain with the Turbulent Dispersion Force of DAVIDSON, 1990, (3.1): full (left), detail (right)

A comparison has been made between two calculations: the first with the Random Dispersion Model (RDM), and the other with the Turbulent Dispersion Force (TDF) of Davidson (3.1). Figure 3.6 shows the time distribution of void fraction in two different points in the domain using RDM. Point 1 is in the center of the grid, with an initial value of void fraction $\alpha_g = 1$, while Point 2 is in the upper-right corner, where initially $\alpha_g \approx 0$. The same plot with TDF appears in Fig. 3.7. The difference between the two calculations is evident: with the TDF, the homogeneous distribution is reached after 20 s, while with the RDM, it takes more than 40 s to reduce significantly the fluctuations around the expected value. The reason is clear. The RDM is, by definition, a random process, while the TDF distributes systematically the bubbles in the direction of $\nabla\alpha_g$. Consequently, the time scale is rather different, but the result is the same: that is, both methods are able to spread the void fraction and to produce a homogeneous distribution.

3.4 Bubble plume calculations

With the grid described in § 2.4.1 (Fig. 2.1, left), a number of simulations have been carried out with different model assumptions, in order to identify the major trends. The experimental setup is again the one of ANAGBO & BRIMACOMBE, 1990, which has been described in § 2.2. Transient calculations have been run in all cases, and continued through to steady-state conditions (~ 40 s). Estimates of the plume width at three elevations are compared against experimental data in Table 3.1 for each model. The results have been normalized with respect to the experimental data. Some of the rows in the Table are grouped into pairs to indicate analogous modelling assumptions. The turbulent dispersion force is the one of Davidson (3.1).

Case No.	Model Identifier	Elevation (mm)		
		100	200	300
0.	Expt.	100	100	100
1	No Models	72	48	39
2	TDF + L(0.1)	92	83	79
3	RDM + L(0.1)	74	57	48
4	TDF + L(0.5)	111	100	95
5	RDM + L(0.5)	98	85	76
6	TDF + SV + L(0.1)	115	122	125
6.1*	TDF + SV + L(0.1)	107	108	112
7	RDM + SV + L(0.1)	75	62	60
8	TDF + SV + L(0.5)	127	130	138
9	RDM + SV + L(0.5)	93	80	74
9.1*	RDM + SV + L(0.5)	93	82	75

TDF – Turbulent Dispersion Force, RDM – Random Dispersion Model,
L – Lift force (with coefft.) SV – Simonin and Viollet Model
* Optimized parameters

Table 3.1: A Comparison of Plume Spreading Statistics for Various Model Assumptions

For the base case, Case 1, with no models apart from buoyancy and drag, no spreading of the plume occurs. Cases 2, 3, 4 and 5 show that the (empirical) TDF and (mechanistic) RDM models induce a different plume spreading, depending on the lift coefficient: to obtain the same spreading, the RDM

model requires a larger lift coefficient than that used with TDF. This is because the two phases are shaken uniformly with the RDM approach, and no preferential direction is defined. Cases 2-5 show also the same trend in the vertical direction: the spreading is always more pronounced for $x=100\text{ mm}$ than for the other elevations. Cases 6 and 8 demonstrate that the TDF model is more sensitive to further modelling assumptions, and it is therefore easier to optimize coefficients to obtain a good fit to experimental data; however, such tuning may not be universal. Moreover, it has to be pointed out that the behaviour in the vertical direction is reversed: now the spreading is more apparent at higher elevations; this is due to the turbulent viscosity, which is enhanced by the Simonin and Viollet model of turbulence, and increases with distance from the inlet, as is shown in Figs. 2.14-2.15.

Figure 3.8 shows the void fraction distribution for Cases 2 and 5. The plume spreading is equally predicted, but the TDF model maintains the Gaussian shape because of the Davidson force, while the RDM model has a dip on the axis which originates from the lack of bubble-induced turbulence (which should be greatest on the axis of symmetry). This demonstrates that the RDM model is more closely linked to accurate representation of the turbulence modelling than the TDF model. On the one hand, this is an advantage, since the turbulence intensities in the liquid are coupled directly to the phasic momentum exchange terms, but on the other hand it is a drawback because the turbulence modelling is now totally responsible for the quality of the results. It has to be noted that a lift coefficient of 0.5 is in agreement with the arguments of DREW & LAHEY, 1987 concerning the principle of objectivity, which states that constitutive equations cannot depend on the coordinate systems used to express them, and this is only satisfied if virtual mass force coefficient C_{VM} is equal to the lift coefficient C_L , at least in the case of a single spherical bubble in an inviscid incompressible fluid.

Another set of calculations has been performed using the Random Dispersion Model to test the different turbulence models. The results (void fraction and gas velocity profiles) are shown in Figs. 3.9-3.10. The turbulence models are the ones described in §2.3.2, and the lift coefficient is 0.5 for all the calculations. It has to be pointed out that none of these models have been optimized for use with the Random Dispersion Model, and this explains the discrepancies, which are more evident on the axis of symmetry. In other words, the empirical constants included in the turbulence models were obtained with their respective Turbulent Dispersion Force models. As a consequence, some tuning is needed. Since a tuning of the empirical constants is not the aim of this work, it has been undertaken only for the case with the Simonin and Viollet model, which appears to perform better than the other models, even though the spreading rate is underpredicted (as shown in Table 3.1, Case 9).

The results from two optimized runs are shown in Figs. 3.11-3.12. These are Cases 6 and 9 from Table 3.1, with modified coefficients for the extra source terms for k and ϵ ; see Eqs. (2.19)-(2.20). In particular, $C_{k2} = 0.54$ and $C_{\epsilon2} = 0.43$. These values were found more suitable for these calculations, leading to improved spreading of the plume, especially in the TDF case, as can be seen in Table 3.1. It is interesting to note how the same effect (the reduction of production of turbulent kinetic energy) gives opposite effects for the TDF and RDM models. In the TDF case, the void fraction and the velocities increase, but the spreading decreases because the production of turbulent viscosity is also reduced. On the other hand, the introduction of the RDM procedure tends to increase the turbulent kinetic energy, and the turbulent viscosity production, so that the fluid is too viscous, the velocities are too small, and there is an accumulation of bubbles on the axis of symmetry. Therefore, in this case, the reduction of the extra source terms brings a decrease of bubble accumulation and an increase of the velocities. A further remark has to be made for the RDM cases. In the five cells next to the axis, the lateral fluctuations have been suppressed artificially because of the proximity of the symmetry boundary. This explains the sudden decrease

in the void fraction and the increase of the velocity distributions in this region.

3.5 Conclusions

A *Random Dispersion Model (RDM)* has been proposed to describe turbulent dispersion of bubbles in a two-phase, buoyant plume. Local turbulent intensities in the liquid phase are first derived via an appropriate turbulence model (an extended $k - \epsilon$ model is utilized in the present study), and these are used to provide (statistical) estimates of the fluctuating velocity components throughout the flow field. The unsteady slip velocities thus derived are then incorporated directly into the drag and lift forces on the bubbles.

The RDM model has been validated against published experimental data and is shown to lead to similar plume spreading to that obtained by imposing an empirical *Turbulent Dispersion Force (TDF)*, but it requires a lift coefficient of 0.5, which is actually supported by the theoretical arguments of DREW & LAHEY, 1987, but it is valid only for spherical bubbles in a perfect fluid. Since the new model directly couples the turbulence intensities in the liquid to the phasic momentum exchange terms, it is expected that results would be rather sensitive to the particular turbulence model adopted, more so than for models involving only mean-flow quantities. However, this can also represent a disadvantage, since current turbulence models for two-phase flows are not yet fully developed.

Even though the number of empirical parameters is actually reduced, it was felt that there was still not sufficient confidence in $k - \epsilon$ approaches to two-phase turbulence modelling to pursue this route further. Consequently, we have preferred to move towards more sophisticated and advanced approaches. In the following chapters, the use of the Large Eddy Simulation turbulence model will be explored to check its capability and suitability for our applications.

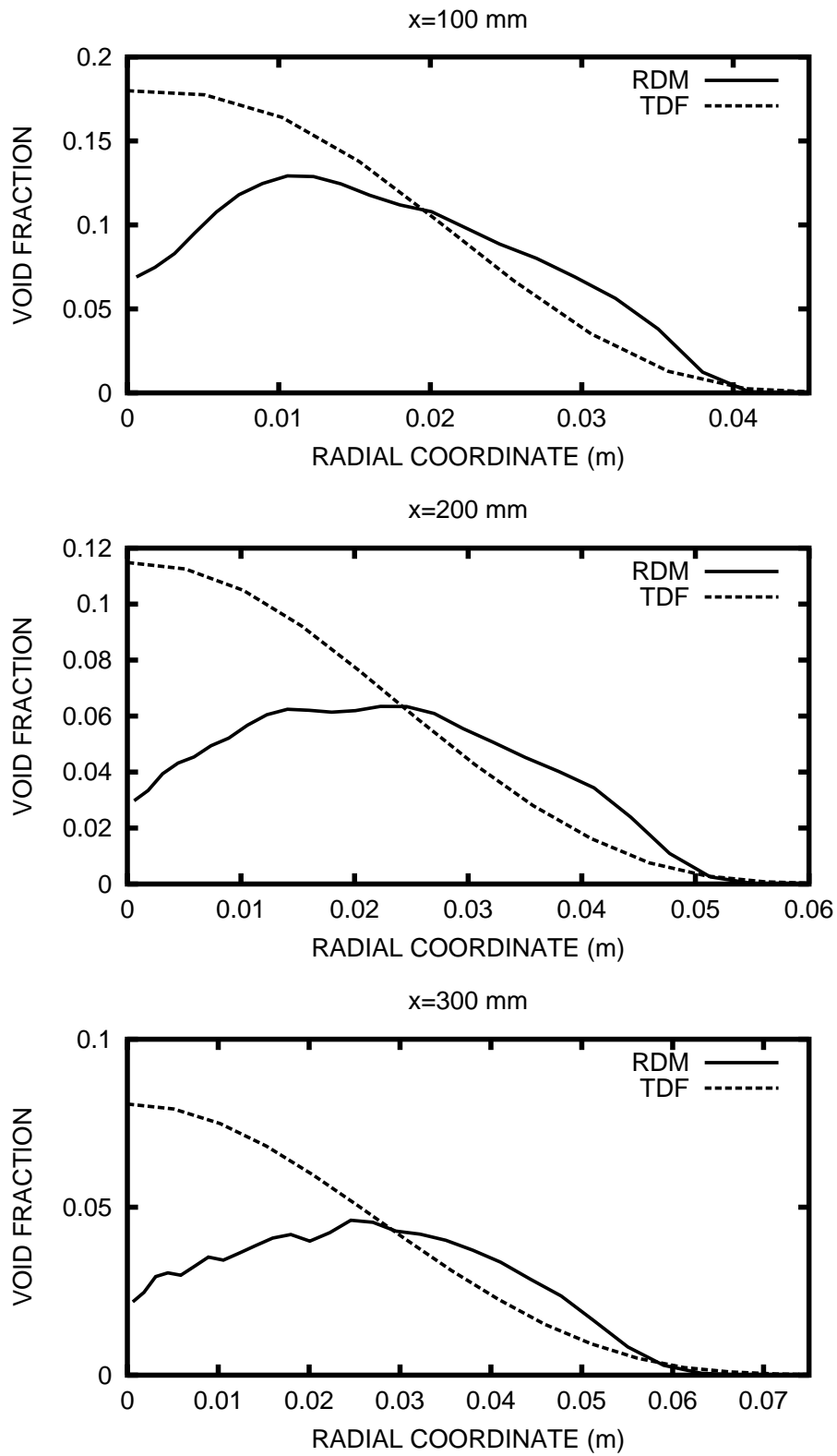


Figure 3.8: A comparison of void fraction distributions using the RDM model (Case 5) and the TDF model of Davidson (Case 2). No turbulence modifications (i.e. standard $k - \epsilon$ model).

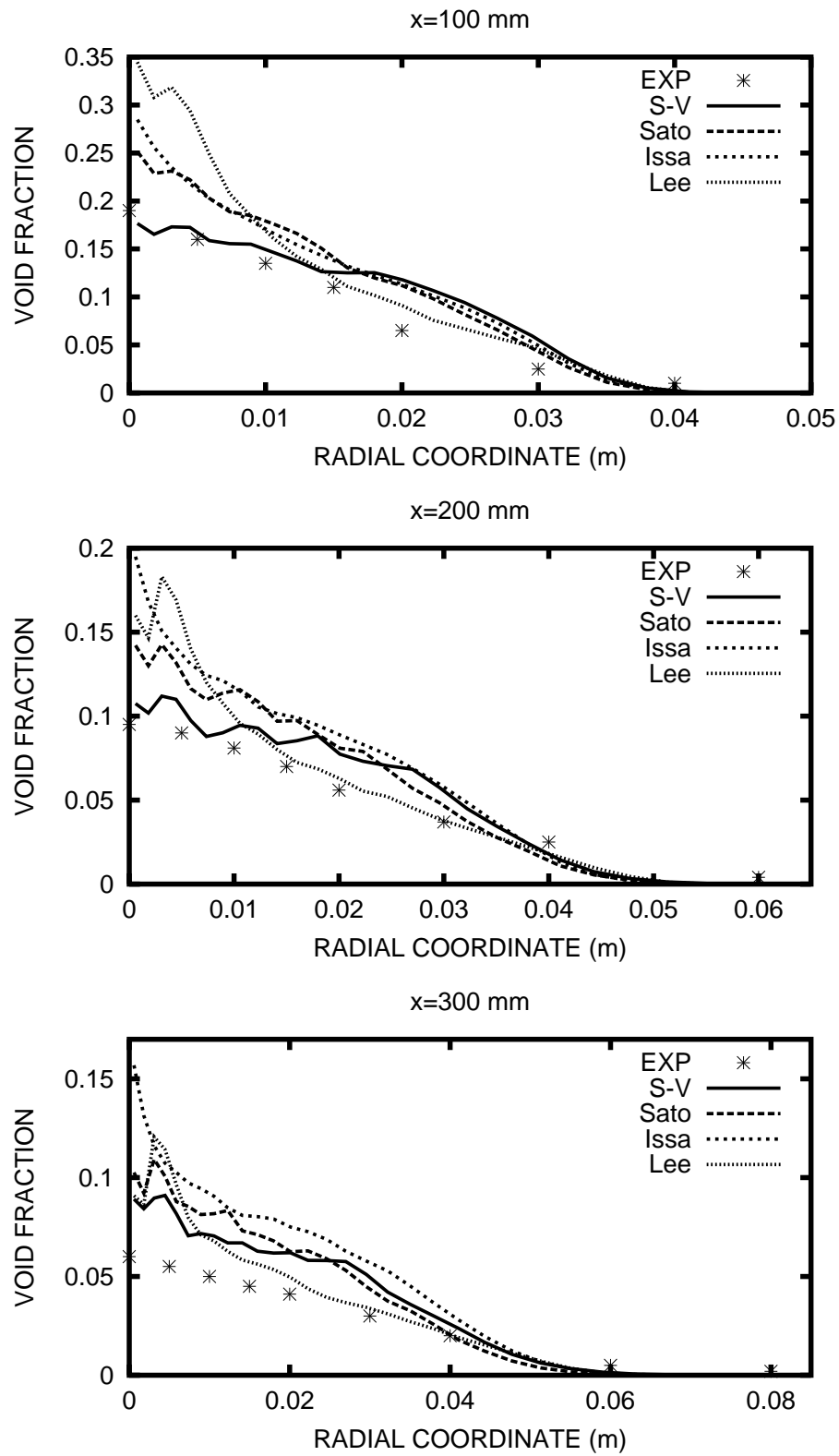


Figure 3.9: Void fraction distributions for different turbulence models (S-V: Simonin and Viollet). All calculations use the RDM model.

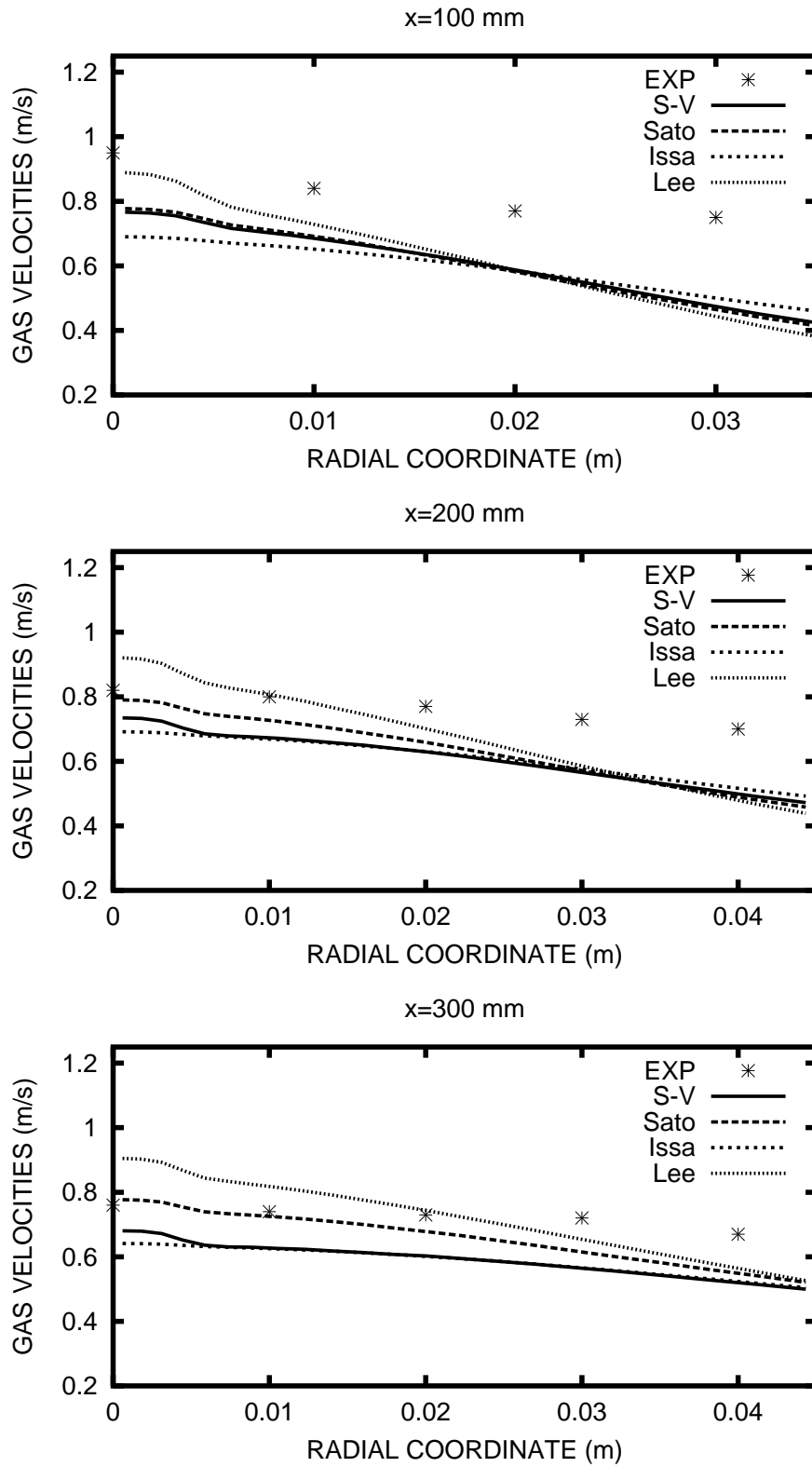


Figure 3.10: Gas velocity distribution for different turbulence models (S-V: Simonin and Viollet). All calculations use the RDM model.

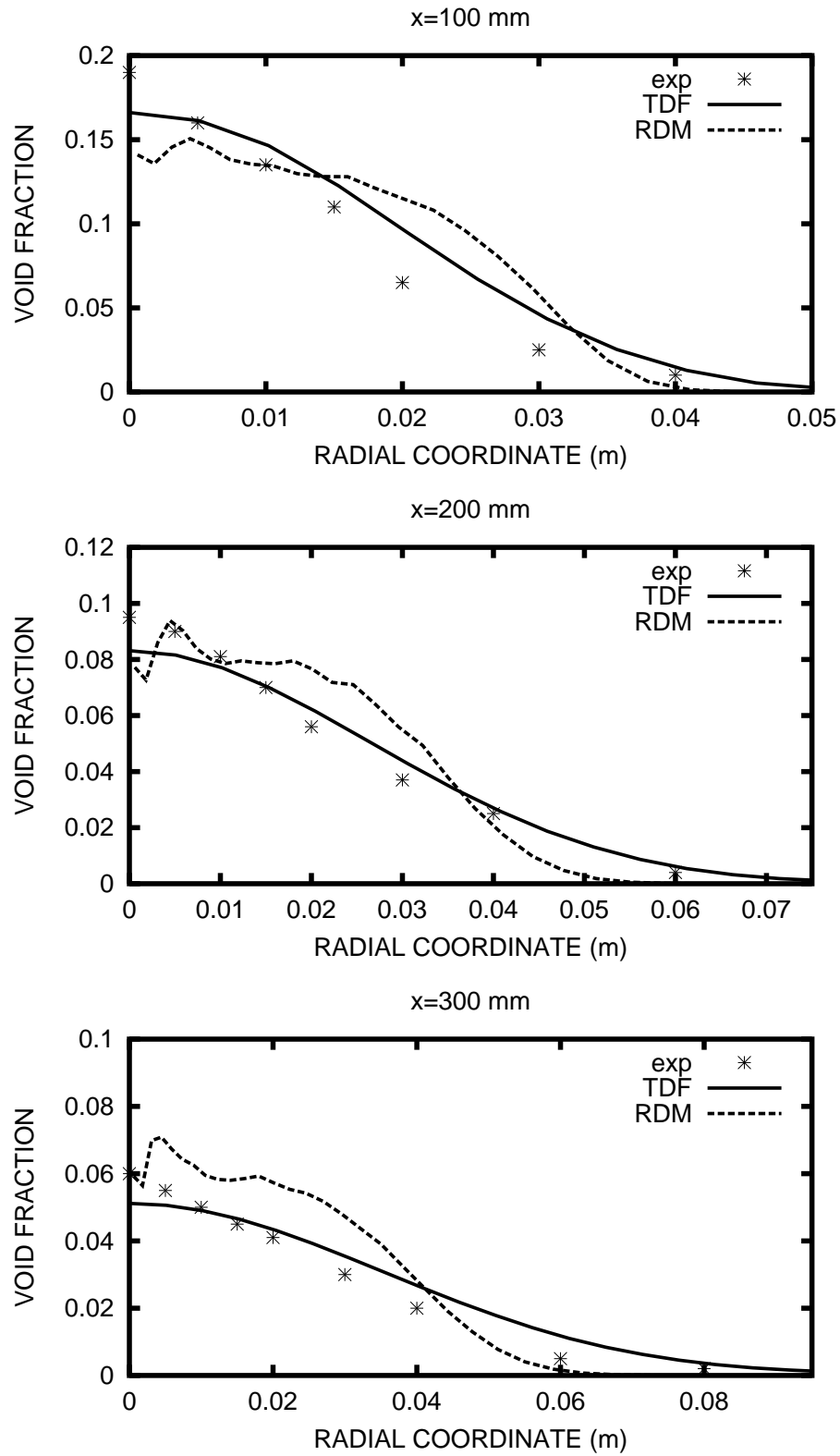


Figure 3.11: Void fraction distribution for two optimized runs with TDF and RDM. All calculations use the Simonin & Viollet turbulence model.

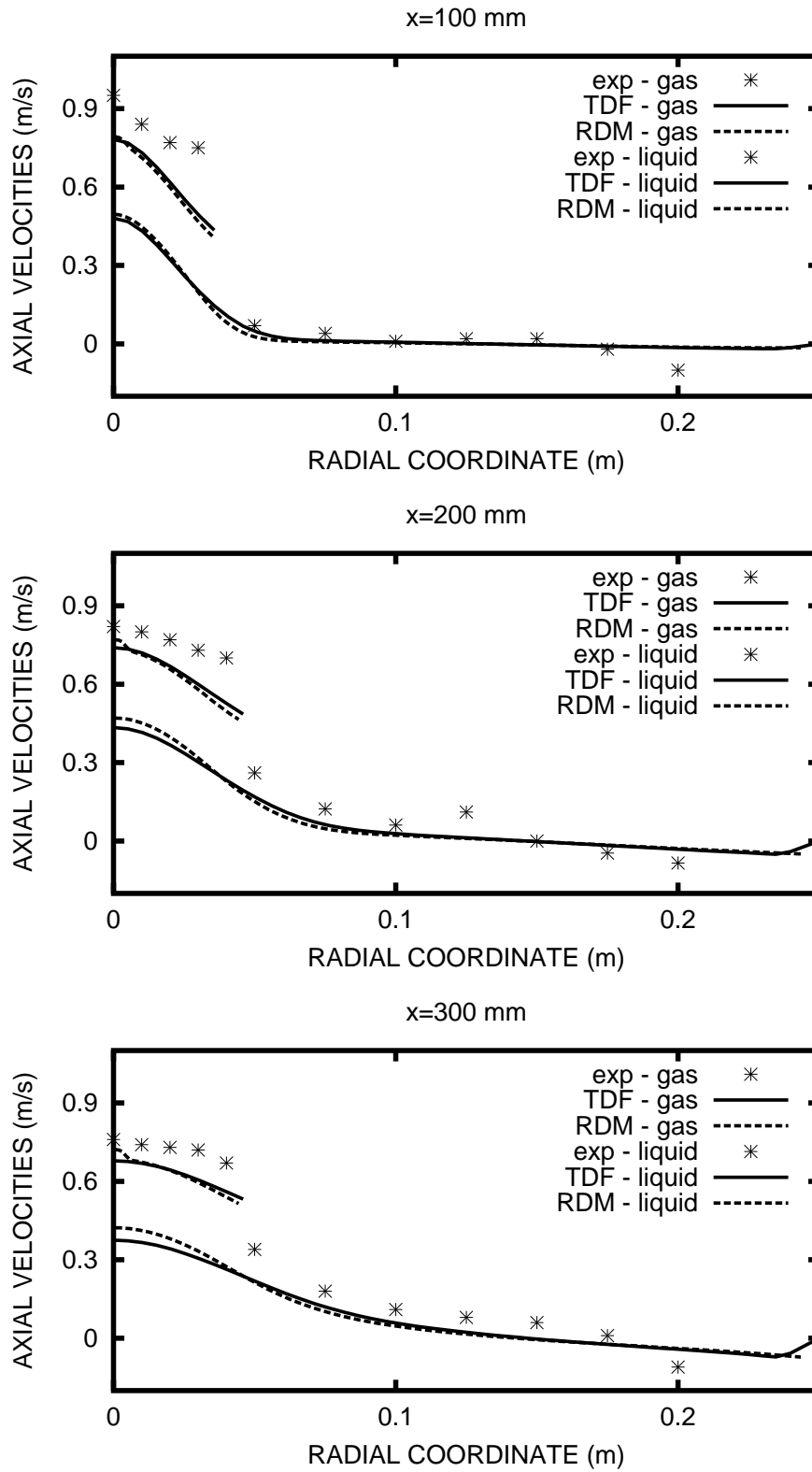


Figure 3.12: Gas and liquid velocity distribution for two optimized runs with TDF and RDM. All calculations use the Simonin & Viollet turbulence model.

4 Towards Large Eddy Simulation of Turbulence

4.1 Introduction

For each class of turbulent flow, it is possible to distinguish two classes of flow structures at the extreme ends of the energy spectrum: the large eddies and the small eddies. The large eddies interact directly with the mean flow field, from which they extract energy. This energy is ultimately dissipated by the smallest scales of motion at the end of a process of continuous energy transfer from the larger flow structures (the energy cascade). The large eddies are responsible for the transport of mass, momentum and energy within the flow, and their size is related to the dimensions of the mean-flow quantities, and the time-scale is of the same order of magnitude as that of the mean flow. The small eddies, on the other hand, are generated by the interaction between larger eddies, and have a dissipative nature. These eddies are characterized by a tendency towards isotropy, and a time-scale smaller than that of the large eddies. Due to the decreasing size of the scales involved, small eddies are generated and destroyed more rapidly than the large ones. The basic idea of LES is to solve directly the anisotropic part of the flow (i.e. the large eddies), which is flow and geometry dependent, and model the isotropic flow structures (the small eddies), whose behaviour is more likely to be localized, and so more universal. The possibility of computing explicitly the non-isotropic part of the flow is one of the main advantages of LES compared to other turbulence approaches for which all the structures are modelled. Nevertheless, one practical limitation exists: the need for a large amount of computing time, since the 3D unsteady Navier-Stokes equations for the large scales must be solved numerically. In LES, the model for the isotropic small scales is related to the grid size, which acts like a filter. The non-resolved (or filtered) part of the flow is modelled with a subgrid model, which should be able to reproduce the removal of energy from larger to smaller eddies. The rationale behind this approach derives from the expectation that in a two-phase flow situation the large scale motions will interact strongly with the bubbles themselves, and will be therefore largely responsible for the macroscopic bubble motion, including dispersion, whereas the subgrid scales will be less important, affecting more the small-scale bubble oscillations.

4.2 Governing equations

Starting from the Navier-Stokes equations for an incompressible flow with constant fluid properties:

$$\frac{\partial u_i}{\partial x_i} = 0 \quad (4.1)$$

$$\rho \left(\frac{\partial u_i}{\partial t} + u_j \frac{\partial u_i}{\partial x_j} \right) = - \frac{\partial p}{\partial x_i} + \mu \frac{\partial}{\partial x_j} \left(\frac{\partial u_i}{\partial x_j} \right) + \rho F_i \quad (4.2)$$

$$\rho\left(\frac{\partial T}{\partial t} + u_j \frac{\partial T}{\partial x_j}\right) = \frac{\lambda}{c} \frac{\partial}{\partial x_j} \left(\frac{\partial T}{\partial x_j}\right) \quad (4.3)$$

the instantaneous flow field can be split into large-scale and subgrid components:

$$f(x_i, t) = \tilde{f}(x_i, t) + f'(x_i, t) \quad (4.4)$$

where the large-scale components $\tilde{f}(x_i, t)$ are derived with a spatial filter function g over the domain Ω :

$$\tilde{f}(x_i, t) = \int_{\Omega} g(x_i - x'_i) f(x'_i, t) dx'_i \quad (4.5)$$

The filter function g has to satisfy the normalization condition

$$\int_{\Omega} g(x_i - x'_i) dx'_i = 1 \quad (4.6)$$

and it has to be symmetric and with a constant filter width Δ in order to commute with differentiation (LEONARD, 1974).

The most important filters are the top-hat filter

$$g(x_i - x'_i) = \begin{cases} 1/\Delta & \text{if } |x_i - x'_i| < \Delta/2 \\ 0 & \text{otherwise} \end{cases} \quad (4.7)$$

and the Gaussian filter

$$g(x_i - x'_i) = \sqrt{\frac{6}{\pi\Delta^2}} e^{-6(x_i - x'_i)^2/\Delta^2} \quad (4.8)$$

The application of (4.5) to (4.1)-(4.3) yields

$$\frac{\partial \tilde{u}_i}{\partial x_i} = 0 \quad (4.9)$$

$$\rho\left(\frac{\partial \tilde{u}_i}{\partial t} + \tilde{u}_j \frac{\partial \tilde{u}_i}{\partial x_j}\right) = -\frac{\partial \tilde{p}}{\partial x_i} + \frac{\partial}{\partial x_j} \left[\mu \frac{\partial \tilde{u}_i}{\partial x_j} + \rho(-\widetilde{u'_i u'_j})\right] + \rho \tilde{F}_i \quad (4.10)$$

$$\rho\left(\frac{\partial \tilde{T}}{\partial t} + \tilde{u}_j \frac{\partial \tilde{T}}{\partial x_j}\right) = \frac{\partial}{\partial x_j} \left[\frac{\lambda}{c} \frac{\partial \tilde{T}}{\partial x_j} + \rho(-\widetilde{u'_j T'}) \right] \quad (4.11)$$

This set of equations is closed with the introduction of the subgrid-scale (*sgs*) stresses

$$\tau_{ij} = \tilde{u}_i \tilde{u}_j - \widetilde{u_i u_j} = -\rho(\widetilde{u'_i u'_j}) = L_{ij} + C_{ij} + R_{ij}$$

where the three terms on the *rhs* are respectively

- the Leonard stresses $\tilde{u}_i \tilde{u}_j - \widetilde{u_i u_j}$ which represent interactions between resolved scales that result in subgrid-scale contributions;
- the cross terms $-(\widetilde{u_i u'_j} + \widetilde{u'_j u_i})$ which represent interactions between resolved and unresolved scales;
- the Reynolds stresses $-\widetilde{u'_i u'_j}$ representing interactions between small, unresolved scales.

and the *sgs* fluxes

$$h_j = \tilde{u}_j \tilde{T} - \widetilde{u_j T} = -\rho(\widetilde{u'_j T'})$$

The terms τ_{ij} and h_j must be modeled and the most common way is the following:

$$\tau_{ij} - \frac{\delta_{ij}}{3} \tau_{kk} = \mu_{sgs} \left(\frac{\partial \tilde{u}_i}{\partial x_j} + \frac{\partial \tilde{u}_j}{\partial x_i} \right) = 2\mu_{sgs} \widetilde{S_{ij}} \quad (4.12)$$

and

$$h_j = \frac{\mu_{sgs}}{\sigma_{sgs}} \frac{\partial \tilde{T}}{\partial x_j} \quad (4.13)$$

where

$$\mu_{sgs} = \rho(C_s \ell)^2 \sqrt{2\widetilde{S_{ij} S_{ij}}}, \text{ with } \ell = (\Delta x \Delta y \Delta z)^{1/3} \quad (4.14)$$

The model was introduced by SMAGORINSKY, 1963. Equation (4.12) is the analogue of the eddy-viscosity model, while (4.13) has been derived following the Reynolds analogy in which σ_{sgs} is the subgrid Prandtl number. The coefficient C_s (Smagorinsky constant) links the model to the physics of the inertial subrange, and is not uniquely defined in a numerical simulation. The following range of values have been used by various authors for the two fitting constants:

$$C_s = 0.1 - 0.33, \quad \sigma_{sgs} = 0.3 - 0.9 \quad (4.15)$$

Recently, GERMANO ET AL., 1991 proposed a new eddy-viscosity model in which the coefficient is calculated dynamically; that is, the coefficient C_s varies spatially and temporally. In this way, no *a priori* knowledge of the constant is needed, and the *sgs* stresses (and fluxes) obtained vanish for laminar flow and at solid boundaries in a physically correct way. In addition, if there is an inverse energy cascade, the constant should be able to take negative values.

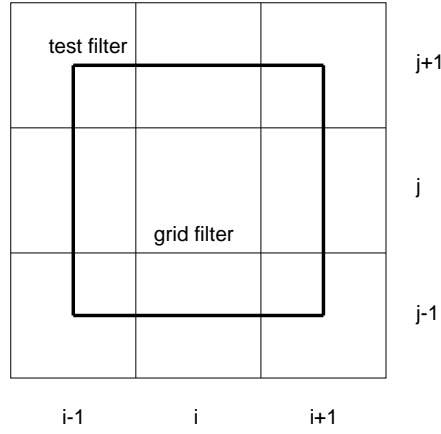


Figure 4.1: 2D view of grid and test filter

The application of a spatial test filter of width $\hat{\Delta} \sim O(2\Delta)$ to the equations, see Fig. 4.1, gives subtest-scale stresses:

$$T_{ij} = \hat{u}_i \hat{u}_j - \widehat{u_i u_j} \quad (4.16)$$

The Smagorinsky model is assumed to hold for both the isotropic part of the subgrid and for the subtest-scale stresses. This gives, in analogy with Eq. (4.12),

$$\tau_{ij} - \frac{\delta_{ij}}{3} \tau_{kk} = 2\mu_{sgs} \widetilde{S}_{ij}, \quad \mu_{sgs} = C\Delta^2 |\widetilde{S}| \quad (4.17)$$

and, from Eq. (4.16),

$$T_{ij} - \frac{\delta_{ij}}{3} T_{kk} = 2\mu_{sgs} \widehat{S}_{ij}, \quad \mu_{sgs} = C\hat{\Delta}^2 |\widehat{S}|. \quad (4.18)$$

The idea of Germano is that the two stresses (4.17) and (4.18) may be related to the test-filtered Leonard term via the algebraic identity $\Lambda_{ij} \equiv T_{ij} - \tau_{ij}$ and, consequently,

$$\Lambda_{ij} - \frac{\delta_{ij}}{3} \Lambda_{kk} = 2C\alpha_{ij} - 2\widehat{C\beta}_{ij} \quad (4.19)$$

with

$$\alpha_{ij} = \hat{\Delta}^2 |\hat{S}| \hat{\tilde{S}}_{ij} \text{ and } \beta_{ij} = \Delta^2 |\tilde{S}| \tilde{S}_{ij}. \quad (4.20)$$

The Leonard (LEONARD, 1974) term Λ_{ij} is the resolved small-scale stress, that is, the stress in the test window between the test scale and the grid scale. In the original formulation, it was assumed that C was a slowly varying function of space. This was the justification for taking it out of the filtering operation, but in general, the assumption is not consistent. The problem can be avoided by averaging C in one or more spatial homogeneous directions. Equation (4.19) involves symmetric second-rank tensors giving (together with continuity equation (4.1)) five independent equations for C . LILLY, 1992, suggested to apply a least-squares approach to minimize at each point the errors of the independent equations. Defining Q_{ij} as the residual of (4.19) according to

$$Q_{ij} = \Lambda_{ij} - 2CM_{ij}, \quad M_{ij} = \alpha_{ij} - \hat{\beta}_{ij} \quad (4.21)$$

and by minimizing the square of the residual with respect to C

$$\frac{\partial Q_{ij} Q_{ij}}{\partial C} = 0, \quad (4.22)$$

the dynamic constant is obtained as

$$C = \frac{\Lambda_{ij} M_{ij}}{2M_{kl} M_{kl}}. \quad (4.23)$$

The application of the same procedure to the energy equation (4.3) gives for the turbulent Prandtl number

$$\frac{1}{\sigma_{sgs}} = \frac{P_i R_i}{C R_j R_j} \quad (4.24)$$

with

$$P_i = \widehat{\tilde{u}_i \tilde{T}} - \hat{u}_i \hat{\tilde{T}}, \quad R_i = \hat{\Delta}^2 |\hat{S}| \frac{\partial \hat{\tilde{T}}}{\partial x_i} - \Delta^2 |\tilde{S}| \frac{\partial \tilde{T}}{\partial x_i}. \quad (4.25)$$

The constants are evaluated during the calculation, and are functions of time and space. The only adjustable parameter is the ratio between the test and grid-scale filter widths.

The value of C may become negative, allowing subgrid scale turbulence to back scatter kinetic energy to the larger grid scales; this phenomenon has also been found in DNS calculations. The

drawback is that if the total viscosity becomes negative the calculations are no longer stable in a numerical sense. An option is to limit the value of the total viscosity or diffusivity with a lower bound, taken to be zero. This allows limited negative values for C .

4.3 Code validation

4.3.1 Experimental setup

The most rigorous derivation of the LES equation set is obtained in phase space, by Fourier transformations of the variables, assuming that the large eddies include all the wavenumbers k up to a cut-off k_c . With this formulation, the filter width is $\Delta = 2\pi/k_c$. If it is not possible to operate in phase space, the formulation is in terms of physical space variables, and the filter width is given by the mesh size $\Delta = (\Delta x \Delta y \Delta z)^{1/3}$ or $\Delta = (\Delta x^2 + \Delta y^2 + \Delta z^2)^{1/2}$, according to different authors. Since an LES model was not implemented in the commercial code CFX-4.3, 1999, it had to be programmed into the code. In detail, the *sgs* diffusivity $\alpha_{sgs} = \mu_{sgs}/\sigma_{sgs}$ was added in the subroutine USRDIF, and the *sgs* viscosity μ_{sgs} in the subroutine USRVIS.

There are already a few examples of the use of LES approaches with the code CFDS-FLOW3D, Release 2 (BURNS ET AL., 1989), the predecessor of CFX-4.3, 1999, with single-phase flow in simple geometries (CIOFALO, 1996, for instance). The aim here was to test the code implementation with a highly buoyant flow like a thermal plume, and then to extend the study to the two-phase case of interest (i.e. a bubble plume). In order to do this, a calculation has been made to simulate the experiment of GEORGE ET. AL., 1977: an investigation of the velocity and temperature fields in an axisymmetric, single-phase, turbulent buoyant plume; the working fluid was air. A view of the experimental setup is shown in Fig. 4.2.

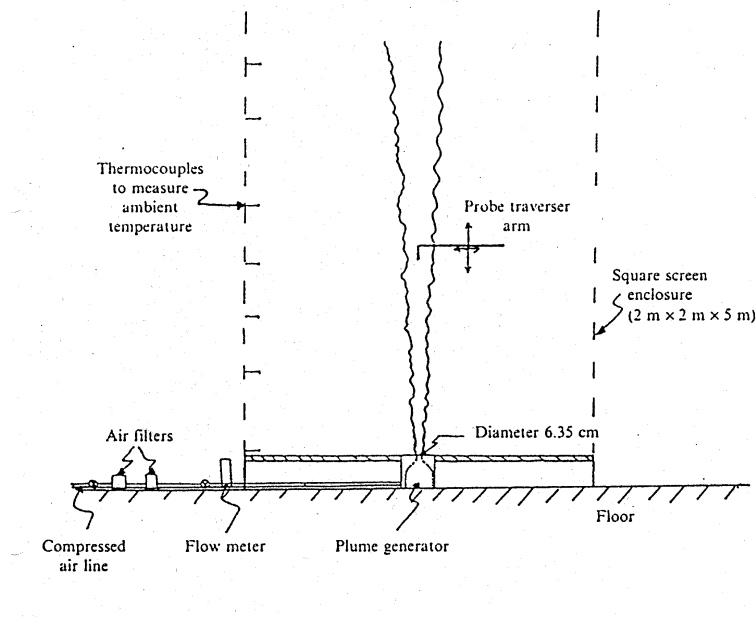


Figure 4.2: Experimental setup of the buoyant plume investigation of GEORGE ET. AL., 1977.

The entire apparatus was placed in a square shelter $2.44 \times 2.44 \times 2.44 \text{ m}^3$. The source temperature

at the inlet was $300\text{ }^{\circ}\text{C}$, and the exit velocity was 0.67 m/s (calculated from the measured heat flux). The ambient air temperature remained at $29 \pm 1\text{ }^{\circ}\text{C}$. Flow visualization was achieved by injecting smoke into the chamber. There was no evidence of laminar behaviour above a distance of two exit diameters, and there was no evidence of plume wandering either visually or in the data reported; the inlet diameter was $D = 0.0635\text{ m}$. The source exit conditions correspond to a Reynolds number of 870, and a densimetric Froude number of 1.4. Measurements of mean and fluctuating quantities were taken at distances 0.508, 0.762 and 1.016 m above the source, which correspond to $z/D = 8, 12, 16$, respectively. Mean buoyancy and velocity radial profiles have been normalized using F_0 , which represents the buoyancy produced per unit time, and is defined as

$$F_0 = 2\pi \int_0^\infty -wg \frac{\rho - \rho_\infty}{\rho} r dr = 0.01\text{ m}^4/\text{s}^3. \quad (4.26)$$

A least squares fit to the buoyancy and velocity profiles yields, respectively,

$$-g \frac{\rho - \rho_\infty}{\rho} = 9.1 F_0^{2/3} z^{-5/3} e^{-65r^2/z^2}, \quad (4.27)$$

$$\bar{w} = 3.4 F_0^{1/3} z^{-1/3} e^{-55r^2/z^2}. \quad (4.28)$$

Both profiles are found to be self-preserving. *Rms* values of w and T , obtained from dual-wire measurements, non-dimensionalized by the centerline values \bar{w} and $\overline{\Delta T} = \overline{T} - T_\infty$, respectively, are also presented in the paper. As far as the experimental errors are concerned, the authors indicate a centerline overestimate of turbulence intensity due to direction ambiguity of 20%, but their estimate at $r/z = 0.1$ indicates that the measured value of $\sqrt{w'^2}$ may be too high by as much as 40%. In a plume dominated by buoyancy, substantial velocity fluctuations are expected to be induced by temperature fluctuations, thus resulting in a high correlation coefficient. The measurements of the radial distribution of this coefficient, defined as

$$\frac{\overline{w'T'}}{\sqrt{\overline{w'^2}}\sqrt{\overline{T'^2}}}, \quad (4.29)$$

gave an average constant value of 0.67, which is greater than the values usually obtained for heated forced jets, showing the important role of buoyancy in the plume in this case.

4.3.2 Numerical results

In order to optimize the *cpu*-time usage, the numerical domain was reduced to a cylinder with radius 0.175 m , which included the maximum extension of the plume, and of height 0.8 m . In this way, only the measurements at $z = 0.508\text{ m}$ were considered. Symmetry and constant pressure boundary conditions were applied, respectively, to the sides and to the top of the domain. There

were $\approx 700,000$ grid points, uniformly distributed in the vertical direction, giving $\Delta z = 4\text{ mm}$, radially varying in the other directions, with a minimum dimension $\Delta x = \Delta y \approx 1\text{ mm}$ close to the centerline. The grid is shown in Fig. 4.3.

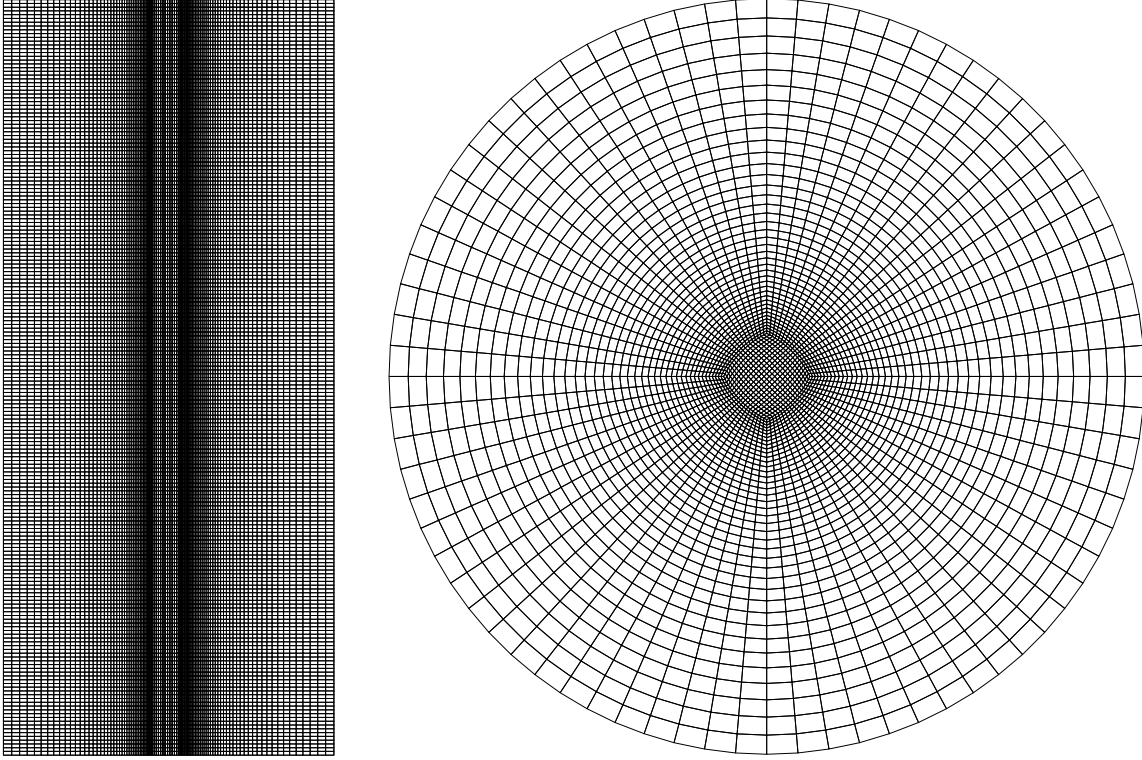


Figure 4.3: Side view (left) and top view (right) of the grid

The time interval was fixed to 0.001 s in order to fulfill the Courant number criterion, and the calculation using our extended version of CFX-4 was continued for $\approx 12,000$ time steps. Average values were calculated from the last 10,000 time steps, once pseudo-steady-state conditions had been established, as can be seen in Figs 4.4 and 4.5 which show, respectively, the centerline axial velocity and temperature as functions of time at $z = 0$ (inlet) and $z = 0.508\text{ m}$. A second-order, central-differencing scheme was used for the spatial discretization, while a first-order, fully-implicit, backward-differencing scheme has been employed for the time discretization, because the second-order accuracy introduced stability problems. The SIMPLE-C algorithm has been employed for the pressure-velocity coupling. The turbulent Prandtl number and the Smagorinsky constant (4.15) were defined as 0.6 and 0.32, respectively. The inlet turbulent intensity was set to 16%, a value which seems to be reasonable according to the authors of the paper.

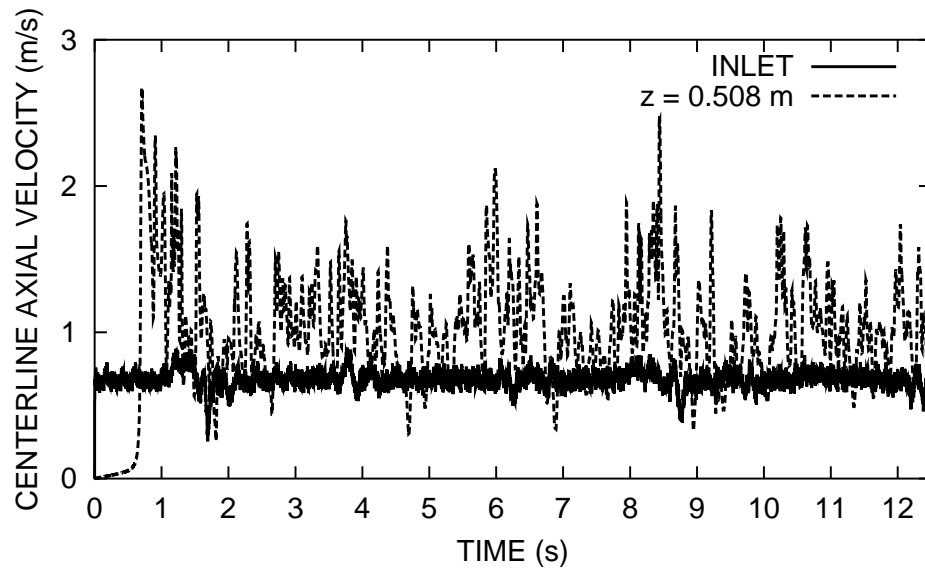


Figure 4.4: Time evolution of the centerline axial velocity at $z = 0$ (inlet) and $z = 0.508$ (first measurement point).

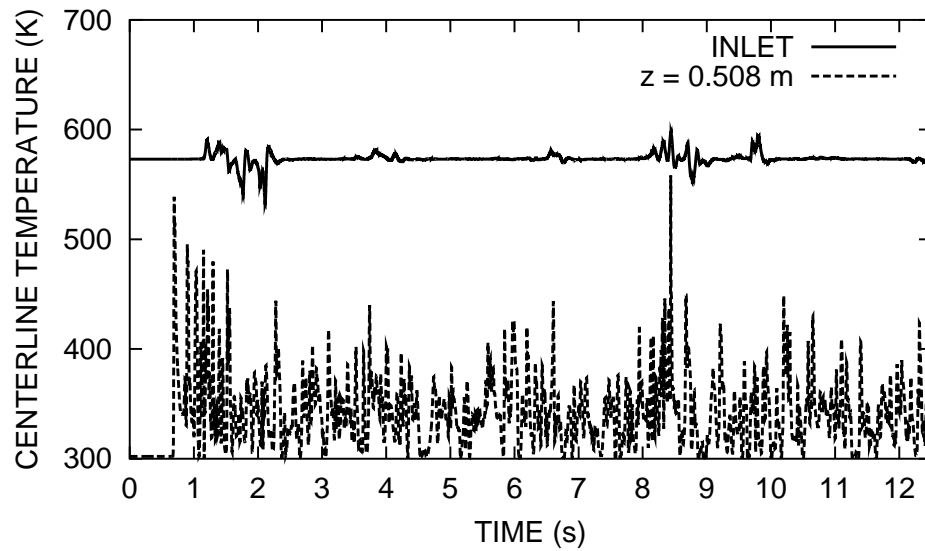


Figure 4.5: Time evolution of the centerline temperature at $z = 0$ (inlet) and $z = 0.508$ (first measurement point).

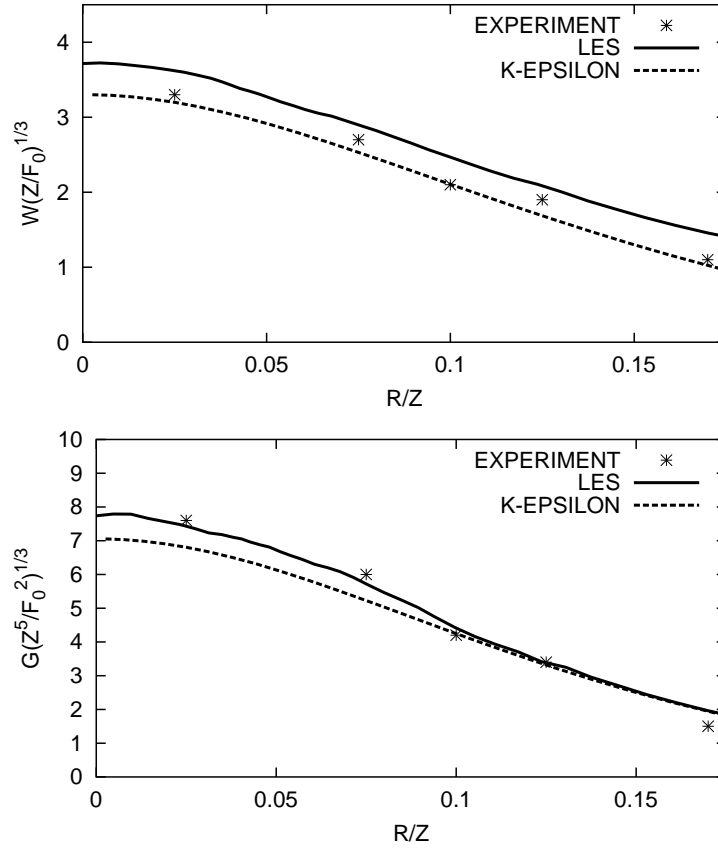


Figure 4.6: Radial distributions of the mean axial velocity (top) and the mean buoyancy (bottom) at $z = 0.508 \text{ m}$, normalized by the distance z from the inlet, and by the buoyancy parameter F_0 (Eq. 4.26), respectively.

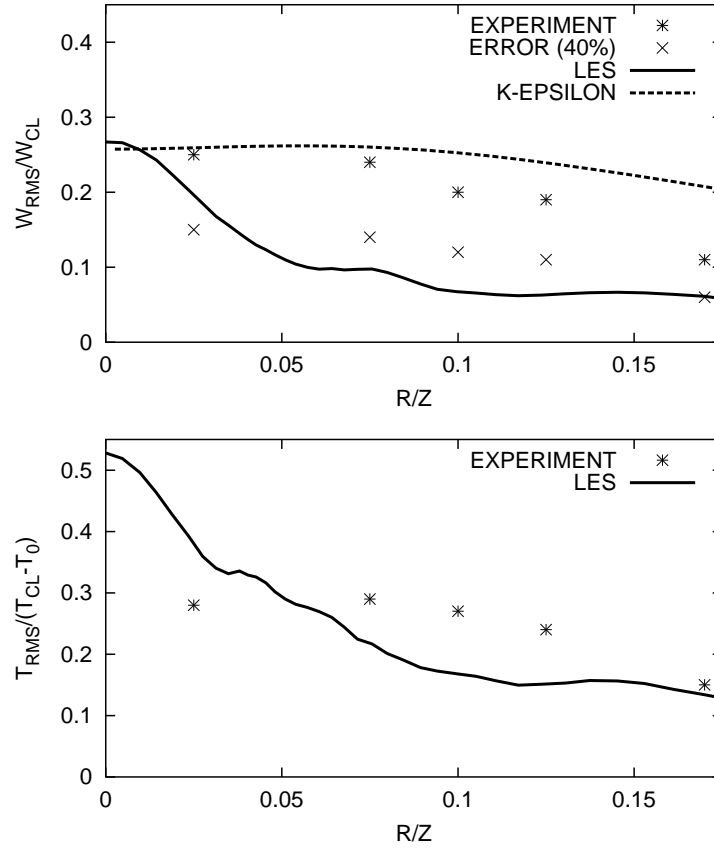


Figure 4.7: Radial distributions of intensity of vertical velocity fluctuations (top) and temperature fluctuations (bottom) at $z = 0.508 \text{ m}$. Values normalized by the centerline vertical velocity, and by the centerline temperature difference, respectively.

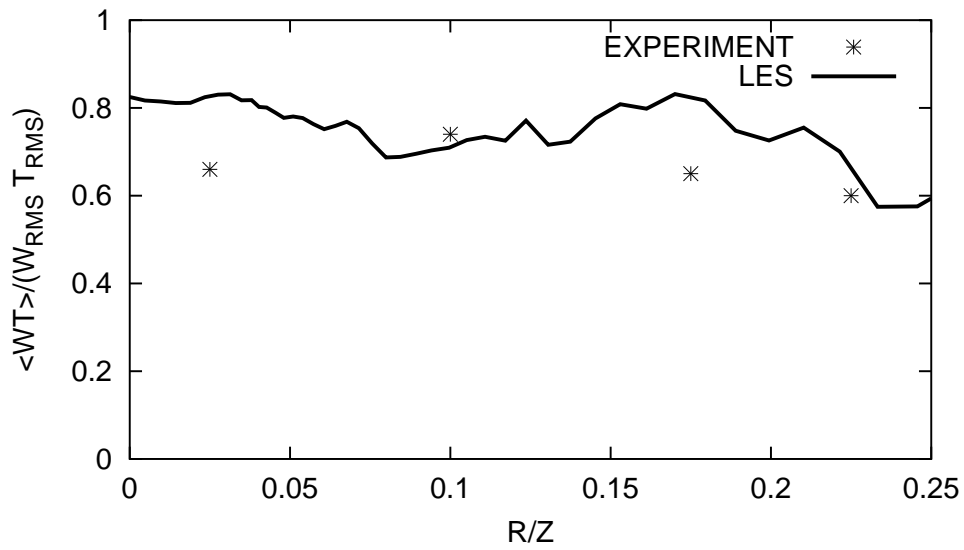


Figure 4.8: Radial distribution of velocity-temperature correlation coefficient at $z = 0.508 \text{ m}$.

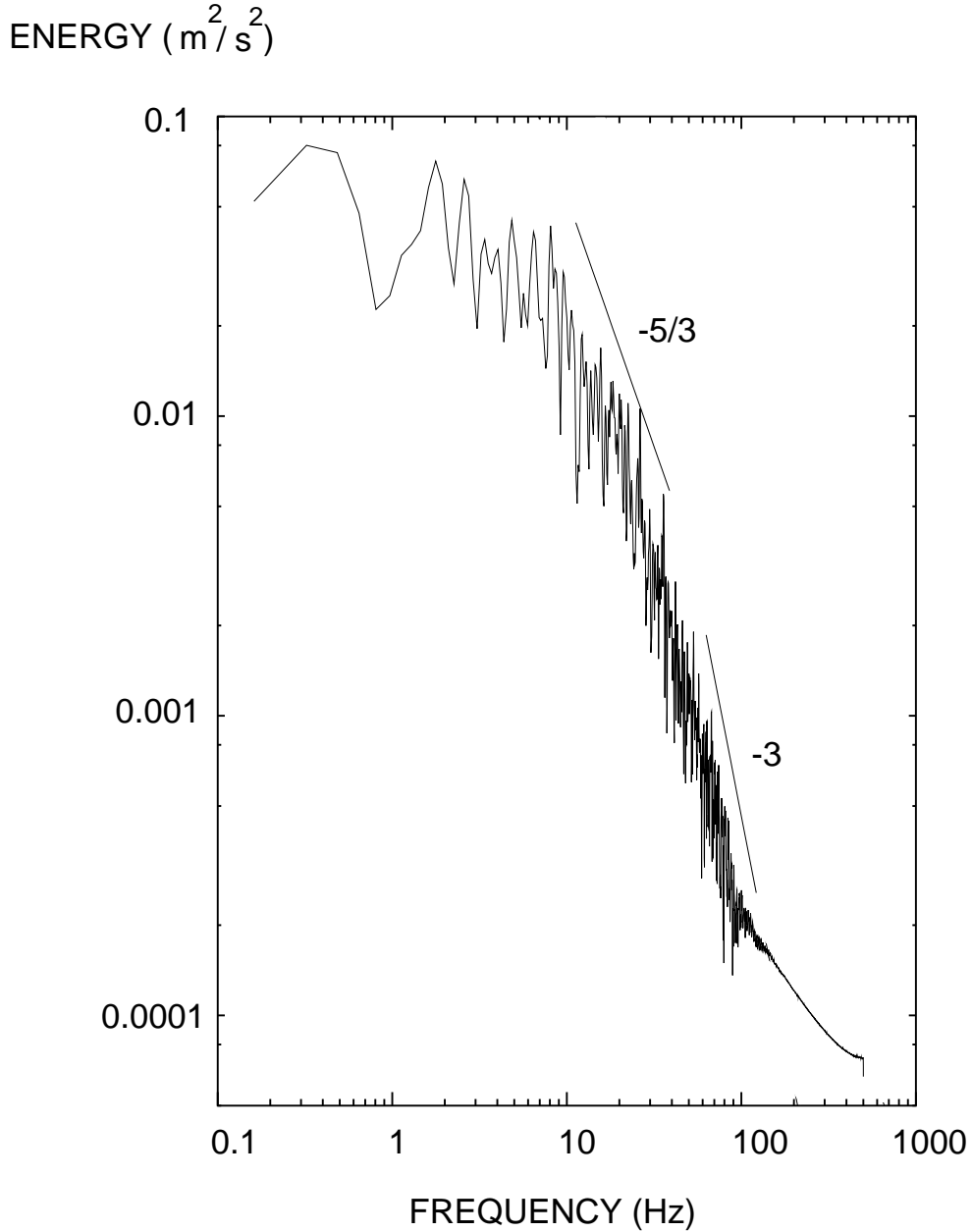


Figure 4.9: Power spectrum of axial velocity fluctuations in the centerline at $z = 0.508\text{ m}$ with the two subrange slopes.

The mean axial velocity and the mean buoyancy distributions are plotted in Fig. 4.6, together with the results of a $k - \epsilon$ model simulation. In general, the calculations show good agreement with the data but, in particular, it can be seen that the axial velocity is slightly overestimated by the LES model, and underestimated by the $k - \epsilon$ model. The latter also underpredicts the mean buoyancy at the centerline. Concerning the turbulent quantities, Fig 4.7 (up) shows the *rms* distribution of the turbulent intensities. Since, according to the paper of GEORGE ET AL., 1977, the velocity fluctuations might be overpredicted by 40%, we have plotted both the actual values given, and these values decreased by 40%. It can be seen (for LES) that only the values close to the centreline fit in the area defined by the two data sets. Away from the centreline, the values are slightly underestimated. This is consistent with the overestimation of the mean axial velocity, as previously discussed. In fact, the reduction of the velocity fluctuations leads to a mean-flw

kinetic energy which is too large, and thus to a higher mean velocity. In contrast, the $k - \epsilon$ model seems to overestimate the turbulent intensities over the whole domain. On the other hand, the *rms* distribution of the temperature intensities, which cannot be calculated by the $k - \epsilon$ model, Fig. 4.7 (down), reveals that the centerline value is overpredicted while, far from the centre of the plume, the calculation shows good agreement with the data, though the authors do not give an indication of the experimental errors. In Fig. 4.8, the correlation coefficient (Eq. 4.29) is compared with the computed distribution. It has to be pointed out again that there is no estimate of experimental errors, but the results are in reasonable agreement with the data, giving an average value of 0.75 (12% overprediction). Fig. 4.9 represents the power spectrum of the velocity fluctuations as a function of the frequency with indications of the $-5/3$ and the -3 slopes, which have been found correct for this type of flow (FISHER & BALL, 1999). In fact, in a buoyancy-driven flow where the temperature is not just a passive scalar, additional subranges, with different scaling relations, may develop. PAPANICOLAOU & LIST, 1987, have presented measurements for round turbulent buoyant jets showing the existence of a $-5/3$ inertial-convective subrange followed by an inertial-diffusive subrange where the spectrum decays with a power of -3 ; this latter is attributed to buoyancy-generated inertia forces. Finally, a snapshot of the temperature distribution (Fig 4.10), reveals that the flow looks laminar up to two diameters from the inlet, then the instability arises, and the rolling up of vortices begins. Further up, there is no evidence of laminar flow, but large and small turbulent structures evolve.

4.4 Conclusions

A test calculation has been run to validate the general-purpose code CFX-4.3, 1999, in which the Large Eddy Simulation subgrid turbulence model of Smagorinsky had been implemented. The model has been easily implemented through the Fortran user interface. The thermal plume experiment of GEORGE ET AL., 1977 has been simulated, and both mean and turbulent quantity profiles were reported. The aim of the calculation was to check code reliability in the case of a single-phase, highly buoyant flow before extending its application to more complicated cases, namely two-phase flow situations. The answer is essentially affirmative. The discrepancies observed (mainly in the underprediction of the velocity fluctuations, which leads to an overestimation of the mean kinetic energy), might be corrected with a more careful analysis of the problem (including for example, a parametric study of the mesh influence on the results, or a study of the influence of the subgrid model). Moreover, the initial conditions for the turbulence were not properly reported, and the experimental errors were not always estimated. In spite of these uncertainties, the simulation results agreed quite well with the experimental data, and a comparison with the standard $k - \epsilon$ model reveals that the LES results are, in general, qualitatively better, even though the LES approach needs an amount of *cpu* time considerably larger than any other RANS calculation. In any case, it has to be stressed that the amount of information provided by a three-dimensional, time-dependent simulation of a turbulent flow is incomparably larger than that given by any turbulence model based on the Reynolds closure.

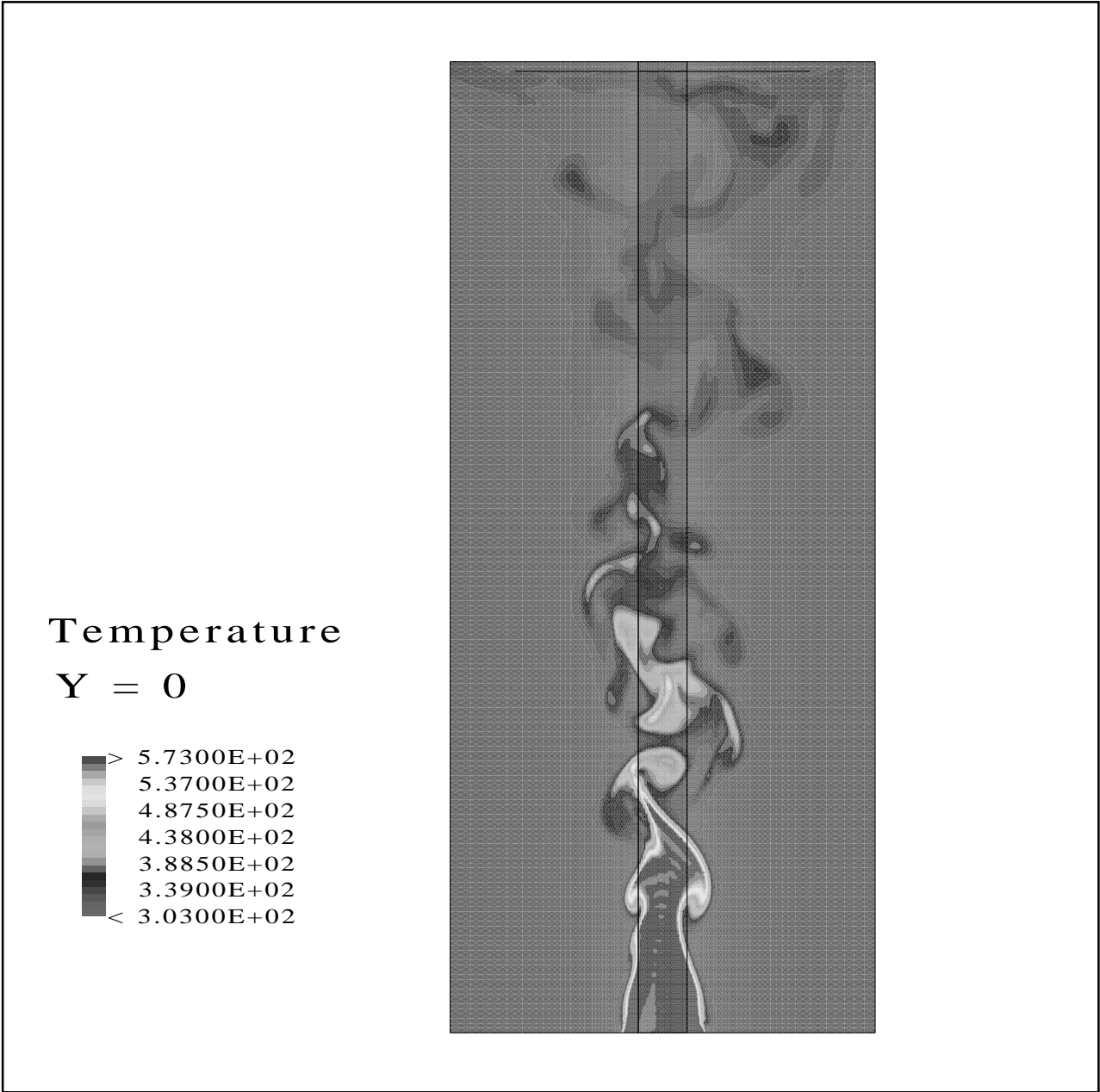


Figure 4.10: Snapshot of the temperature distribution.

5 Large Eddy Simulation: grid turbulence

5.1 Introduction

The study of the turbulence behind a grid has been a good starting point for the understanding of more complex turbulent phenomena in single-phase flows. Following an analogous path, we extend the study in this Chapter to include the influence of a second dispersed phase on the structure of the nearly isotropic flow field created behind a grid. There is some work on this subject (see LANCE & BATAILLE, 1991 and PANIDIS & PAPAILIOU, 2000), but much more is required to reach the level of comprehension already attained in single-phase turbulence.

It is interesting to show if there is an effect of the grid size on the results, how important it is and, in case, how it is coupled with the bubble diameter. For this reason, we have performed a parametric study with different mesh sizes and bubble diameters. In particular, in the first part of the Chapter, we examine the influence of the mesh size on the turbulence in a simple three-dimensional case with an isotropic turbulent field applied at the inlet of a box. In the second part, referring to the experiment of LANCE & BATAILLE, 1991, we test the capability of current models to predict turbulence decay behind a grid, for which measured data are available. In this case, only two-dimensional simulations are considered, since the calculations are much more time consuming.

5.2 3D calculations

The domain of the three-dimensional calculations is a simple box with dimensions $0.05 \times 0.05 \times 0.1 \text{ m}^3$ in the x, y and z directions, respectively. The mesh size is always kept uniform, and given by $\Delta_x = \Delta_y = \Delta_z = 1, 2, 3$ and 4 mm in successive runs. The bubble diameter is $d_b = 0.5$ and 2 mm . The case in which $\Delta = 1 \text{ mm}$ with $d_b = 2 \text{ mm}$ has not been considered, since the cut-off filter must not be smaller than the assumed characteristic length scale of the dispersed phase. The time interval is fixed at 0.001 s in order to fulfill the Courant number criterion, and the calculation using our extended version of CFX-4 was continued for about 5,000 time steps. As for the single-phase case, a second-order, central-differencing scheme was used for the spatial discretization, while a first-order, fully-implicit, backward-differencing scheme has been used for the time discretization. The SIMPLE-C algorithm has been employed for the pressure velocity coupling. The equations for the single-phase calculations are (4.9), (4.10), (4.12), while the following set of equations was used for the two-phase case:

$$\frac{D_l}{Dt} (\alpha_l \rho_l) + \alpha_l \rho_l \frac{\partial \tilde{u}_l^i}{\partial x^i} = 0 \quad (5.1)$$

$$\frac{D_g}{Dt} (\alpha_g \rho_g) + \alpha_g \rho_g \frac{\partial \tilde{u}_g^i}{\partial x^i} = 0 \quad (5.2)$$

$$\frac{D_l}{Dt} (\alpha_l \rho_l \tilde{u}_l^i) - \frac{\partial}{\partial x^j} [\alpha_l \sigma_l^{ij}] = -\alpha_l \frac{\partial \tilde{p}}{\partial x^i} + F_l^i \quad (5.3)$$

$$\frac{D_g}{Dt} (\alpha_g \rho_g \tilde{u}_g^i) - \frac{\partial}{\partial x^j} [\alpha_g \sigma_g^{ij}] = -\alpha_g \frac{\partial \tilde{p}}{\partial x^i} + F_g^i \quad (5.4)$$

in which

$$\frac{D_l}{Dt} = \frac{\partial}{\partial t} + \tilde{u}_l^j \frac{\partial}{\partial x^j} \quad \text{or} \quad \frac{D_g}{Dt} = \frac{\partial}{\partial t} + \tilde{u}_g^j \frac{\partial}{\partial x^j} \quad (5.5)$$

as appropriate, and

$$\sigma_g^{ij} = \mu_{lam}^g \left(\frac{\partial \tilde{u}_g^i}{\partial x^j} + \frac{\partial \tilde{u}_g^j}{\partial x^i} \right) \quad (5.6)$$

$$\sigma_l^{ij} = (\mu_{lam}^l + \mu_t) \left(\frac{\partial \tilde{u}_l^i}{\partial x^j} + \frac{\partial \tilde{u}_l^j}{\partial x^i} \right) \quad (5.7)$$

where

$$F_l^i = -F_g^i \quad (5.8)$$

and $\sigma_{l,g}^{ij}$ is the deviatoric part of the stress tensor $\tau_{l,g}^{ij}$

$$\sigma_{l,g}^{ij} = \tau_{l,g}^{ij} - \frac{\delta^{ij}}{3} \tau_{l,g}^{kk}.$$

The interfacial forces (5.8) are the following:

- Buoyancy Force

$$F_g^i = (\rho_g - \rho_l) g^i, \quad F_l^i = 0 \quad (5.9)$$

- Drag Force

$$F_l^i = -F_g^i = \frac{3}{4} \alpha_g \rho_l \frac{C_D}{d_b} |\tilde{u}_g^i - \tilde{u}_l^i| (\tilde{u}_g^i - \tilde{u}_l^i) \quad (5.10)$$

where $C_D = 0.48$, $Re_b \approx 800$ for $d_b = 2 \text{ mm}$, and $C_D = 1.5$, $Re_b \approx 40$ for $d_b = 0.5 \text{ mm}$.

- Virtual Mass Force

$$F_l^i = -F_g^i = \alpha_g \rho_l C_{VM} \left(\frac{D_g \tilde{u}_g^i}{Dt} - \frac{D_l \tilde{u}_l^i}{Dt} \right) \quad (5.11)$$

with $C_{VM} = 0.5$.

- Lift Force

$$F_l^i = -F_g^i = C_L \epsilon_{ijk} (\tilde{u}_g^j - \tilde{u}_l^j) \omega^k \quad (5.12)$$

where ω^k is the liquid vorticity, and ϵ_{ijk} is the Levi-Civita tensor defined as +1 for even permutations of the indices, -1 for odd permutations and 0 if two indices are repeated.

These equations have been derived from (1.7)-(1.10) in analogy with the procedure described in § 4.2, using the decomposition (4.4) and the filtering (4.5). The liquid velocity (in the axial direction) is 0.4 m/s and the gas velocity is 0.46 and 0.7 m/s, respectively, for the cases with $d_b = 0.5$ and 2 mm. The gas velocities were calculated using the empirical correlations of CLIFT ET AL., 1978 and WALLIS, 1969. The bubbles are initially uniformly distributed and the void fraction is 2%. The inlet liquid turbulence was arbitrarily imposed: 1.5% for the single-phase flow calculations, and 7.5% in the presence of the second phase. These values were taken from the experiments described in LANCE & BATAILLE, 1991 and have been measured at 1.5 m from the grid, where the flow is supposed to be fully developed and the bubbles have reached their terminal velocity. This energy, which includes the contribution due to the velocity perturbations around the bubbles, is linked to the added mass force and is given to the liquid during the acceleration of the bubbles. These perturbations have been used since this is an idealized test case, without direct comparison with experimental data. As boundary conditions, we employed constant pressure at the outlet, and periodic planes laterally. The *sgs* modelling for the bubble-induced dissipation (viscosity) in the liquid phase has been included. The model included here is the one of TRAN, 1997, which assumes that in two-phase flow the total rate of turbulent dissipation is given by the sum of the liquid turbulent dissipation plus the contribution given by the bubbles

$$\epsilon_t = \epsilon_l + \epsilon_g. \quad (5.13)$$

It is also assumed that the bubble-induced turbulent dissipation process is dominated by the drag force, so that

$$\epsilon_g \propto \alpha_g F^D u_r^{sgs} \quad (5.14)$$

where u_r^{sgs} is the sub-grid slip velocity, that is the non-resolved part of the relative velocity between the phases. As a consequence, in the case of dilute flow $\alpha_g \ll 1$,

$$\epsilon_t = \epsilon_l \left(1 + C_f \alpha_g 6\pi \frac{d_b \mu_{lam}^l}{\Delta \mu_{sgs}} \right) \quad (5.15)$$

or

$$\mu_t = \mu_{sgs}^l + \mu_{sgs}^g = \mu_{sgs} \left(1 + C_f \alpha_g 6\pi \frac{d_b \mu_{lam}^l}{\Delta \mu_{sgs}} \right)^{1/3} \quad (5.16)$$

where μ_{sgs} is the Smagorinsky term given in (4.14), with the constant C_s defined as 0.12, as suggested by TRAN, 1997, for the case of two-phase flow, and C_f is an empirical coefficient equal to 0.17 (TRAN, 1997). This parameterization has been derived for a statistically adequate number of bubbles in each cell, but realistically we cannot have a too coarse grid or we would lose too many length-scales. Consequently, we are interested in the turbulent quantities (no mean value is shown), and how these relate to the mesh size.

In Table 5.1, the ratios of vertical (w) to lateral (u) *rms* liquid velocities at $z = 0.05$ and $y = 0.025$ *m* along the x direction are displayed. All the values fluctuate around unity, which means that isotropy is preserved even in the presence of bubbles. This agrees with the findings of LANCE & BATAILLE, 1991, who measured $0.9 < w'/u' < 1.1$. The isotropy is evident also from Table 5.2, which shows the normalized Reynolds-stress component $\overline{u'w'}$. In fact, the values of this non-diagonal term in the stress tensor are small, as also found in the experiments of LANCE & BATAILLE, 1991, in which $-0.1 < \overline{u'w'}/u'w' < 0.1$. It is apparent, therefore, that the isotropy of the initial turbulent field is not modified by injection of bubbles.

Δ	no bubbles	$d_b=0.5$ mm	$d_b=2$ mm
1 mm	0.951	0.972	-
2 mm	0.992	0.86	0.989
3 mm	0.97	0.998	1.01
4 mm	1.05	1.02	1.03

Table 5.1: Ratio of vertical to lateral *rms* velocities for various mesh sizes and bubble diameters, averaged along the x direction at $y = 0.025$ *m* and $z = 0.05$ *m*, respectively.

Δ	no bubbles	$d_b=0.5$ mm	$d_b=2$ mm
1 mm	-0.048	-0.017	-
2 mm	0.016	0.028	0.027
3 mm	-0.013	0.003	0.003
4 mm	0.016	0.037	0.032

Table 5.2: Reynolds-stress tensor component $\overline{u'w'}$ normalized with respect to u_{rms} and w_{rms} , and averaged along the x direction at $y = 0.025$ *m* and $z = 0.05$ *m*.

In Fig. 5.1, are shown the *rms* fluctuations in single-phase flow and in two-phase flow for $d_b = 0.5$ mm and 2 mm. It can be noted that the variation with the mesh size is almost linear, which is

more evident in Fig. 5.2, where one also sees that there is no great variation in the *rms* values for different bubble sizes. Moreover, the *rms* values increase with the mesh because, for smaller filter widths, the resolved fluctuations are lower, as it can also be seen in Fig. 5.3, which shows the time history in the amplitude of w' for various grids.

Concerning the transfer of energy, looking at the power spectra in Figures 5.4 for single-phase flow, it can be seen that the classical $-5/3$ law does not hold properly: the decay is too fast. This is probably due to the subgrid model, which is valid in the case of shear flow (see Chapter 4 and Fig. 4.9), but might be inappropriate when the flow is uniform and homogeneous. In the case of two-phase flow (Fig. 5.5), the $-8/3$ law, which has been measured and explained by LANCE & BATAILLE, 1991 as a consequence of the energy dissipation taking place in the wakes of the bubbles, seems to be better predicted, even though the *sgs* model for the second phase can be considered as a first attempt to describe the bubble-induced viscosity effects.

5.3 2D calculations

The second part of the Chapter focuses on the experimental data of LANCE & BATAILLE, 1991, in which the decay of turbulence behind a grid in the presence of bubbles was measured. The bubble diameter in the experiment was $d_b = 5 \text{ mm}$, but we assume that the turbulence generated by bubbles with $d_b = 2 \text{ mm}$ is comparable. The reason for this is that a bubble with $d_b = 5 \text{ mm}$ cannot be realistically simulated with the code because we have to assume spherical bubbles, while big bubbles would be subject to deformation and break-up. The calculations are two-dimensional because we want to simulate the decay from the origin to the measurement location, which starts $\sim 80 \text{ cm}$ away from the grid, and a fully three-dimensional calculation would have taken too much computational time. For this reason, two planes of symmetry have been used in the y direction, while periodic boundaries have been retained in the x direction. The inlet level of turbulence (unknown) has been empirically tuned to obtain the correct levels at the measurement points. This has been done in single-phase flow with the help of a standard $k - \epsilon$ model, which is supposed to work quite well in this situation, since the model constants in eqs. (1.13), (1.14), (1.16) have been determined from grid turbulence data. The $k - \epsilon$ calculation gave predictions in very good agreement with the experimental data (with an inlet velocity of 0.6 m/s , and with an inlet turbulence level of 6%), as shown in Figure 5.6. Subsequently, LES calculations have been performed with this value. Figure 5.6 shows that the results with two different (uniform) meshes ($\Delta = 2 \text{ mm}$ and $\Delta = 4 \text{ mm}$) are quite different, for the same level of inlet turbulence. The calculation with $\Delta = 4 \text{ mm}$ overestimates the turbulence at the two measurement points $z = 0.856$ and 1.256 m , while with $\Delta = 2 \text{ mm}$, the prediction is closer to the measured value. This result is consistent with the results of the 3D calculations performed previously. Probably, a calculation with $\Delta = 1 \text{ mm}$ to 1.5 mm would match the data more accurately.

For the two-phase flow calculations, the inlet turbulence had to be estimated: for the 4 mm grid the values used were 17%, 30% and 50%. It can be seen in Fig. 5.7 that the latter calculation gives the best comparison against the experimental data. Calculations with smaller grids have not been carried out because of the time required and the difficulties in obtaining convergence, but, according to the previous results, a finer mesh would have produced a lower level of turbulence, for the same inlet turbulence. The fact that the inlet turbulence must be enhanced artificially to 50%, which is a high value even for two-phase flow, means that for this flow the turbulence production mechanism is not well reproduced. In other words, the pseudo-turbulence produced by the passage of the bubbles and transferred to the liquid through the added mass force (5.11), which is considered the main effect in this case, has not been described properly.

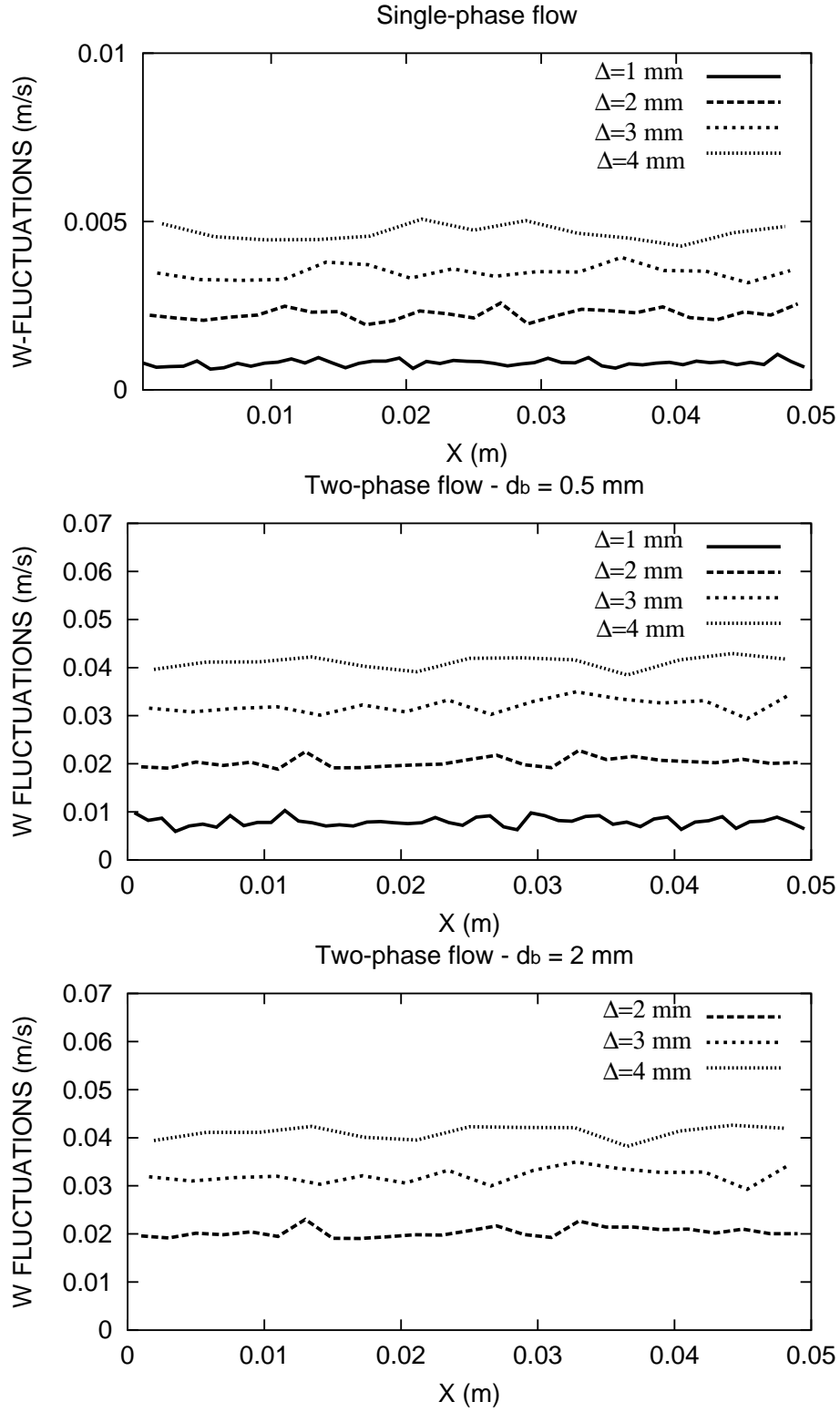


Figure 5.1: w_{rms} for different mesh sizes Δ with $d_b = 0, 0.5$ and 2 mm at $y = 0.025$ m and $z = 0.05$ m.

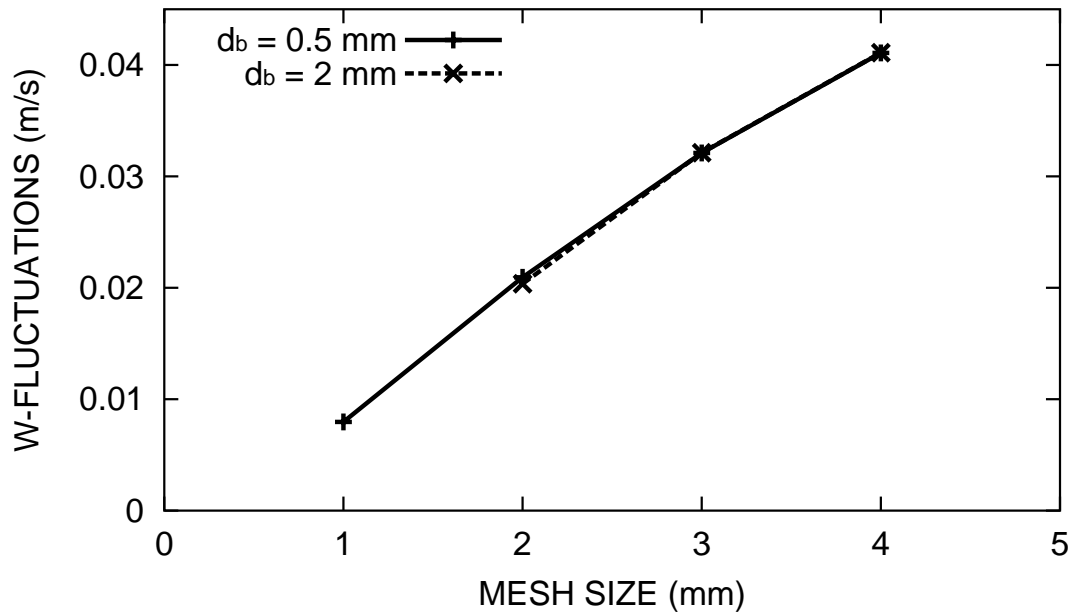


Figure 5.2: w_{rms} for $d_b = 0.5$ and 2 mm as function of the mesh size Δ .

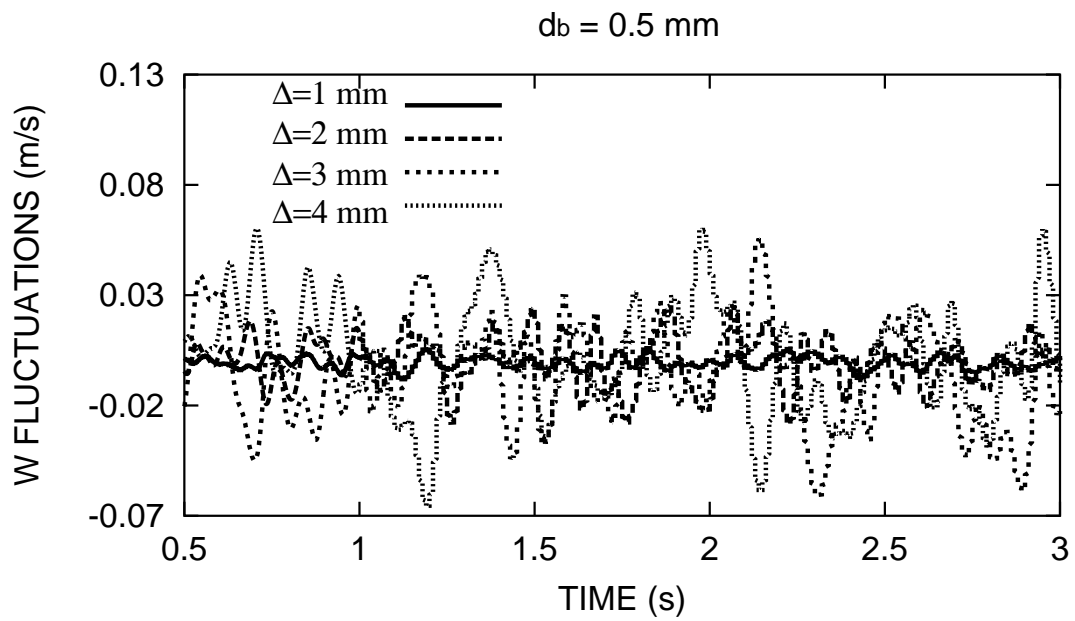


Figure 5.3: Time history of the velocity fluctuations w' for $d_b = 0.5$ mm and different mesh sizes in the point $x = y = 0.025$, $z = 0.1$.

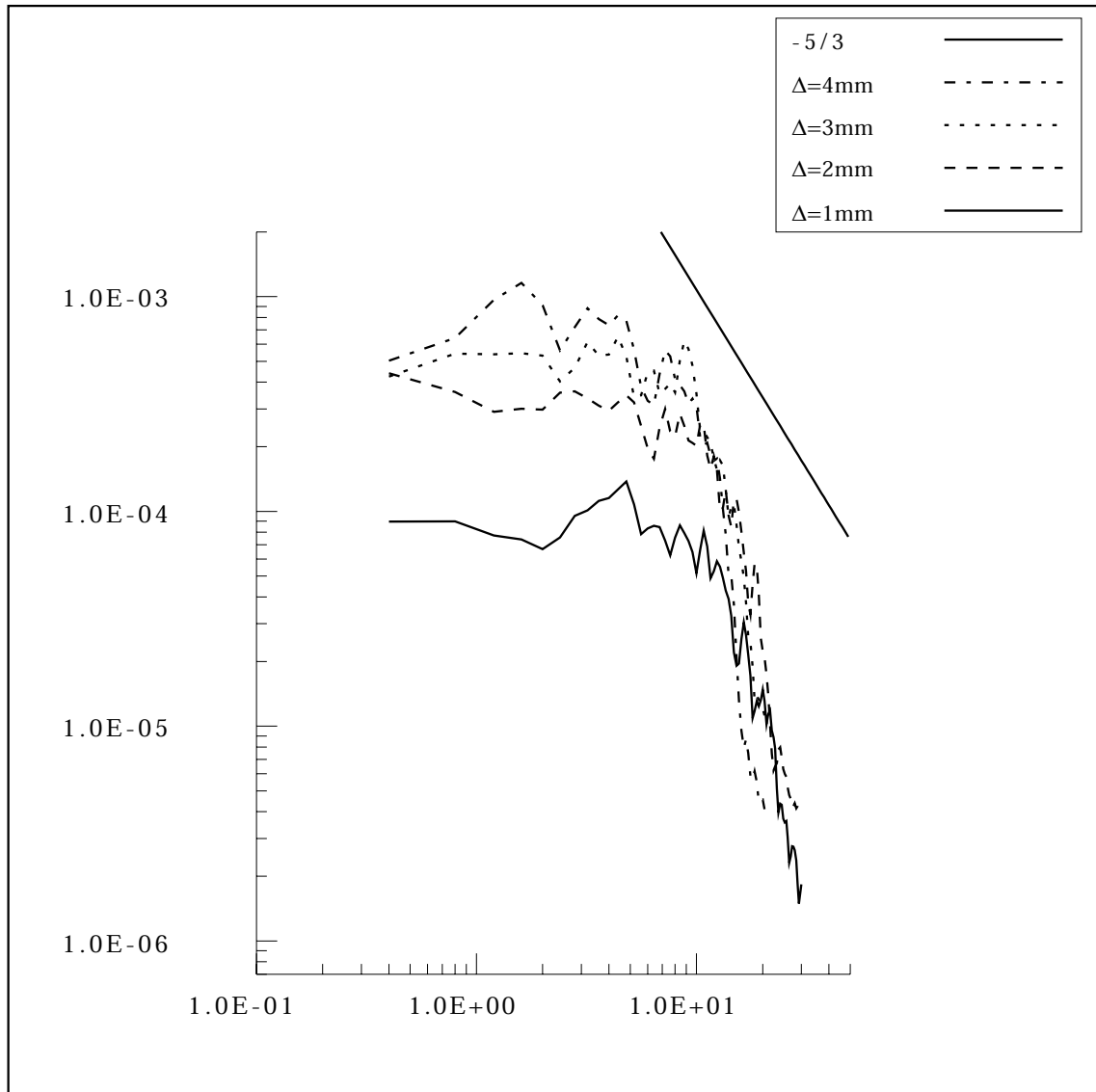


Figure 5.4: Power spectrum of axial velocity fluctuations in the center of the domain at $z = 0.05$ m for single-phase flow.

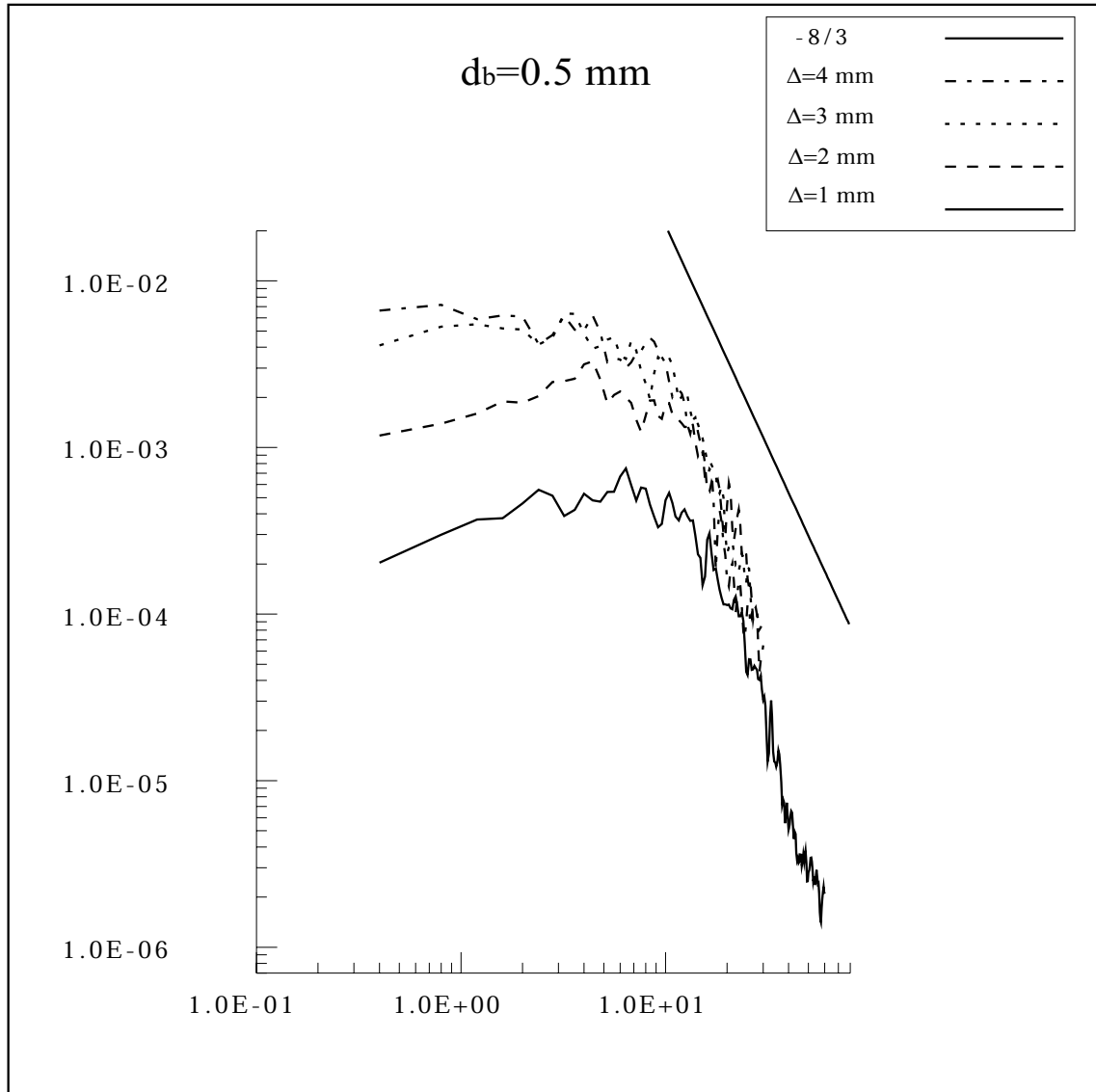


Figure 5.5: Power spectrum of axial velocity fluctuations in the center of the domain at $z = 0.05 \text{ m}$ for $d_b = 0.5 \text{ mm}$.

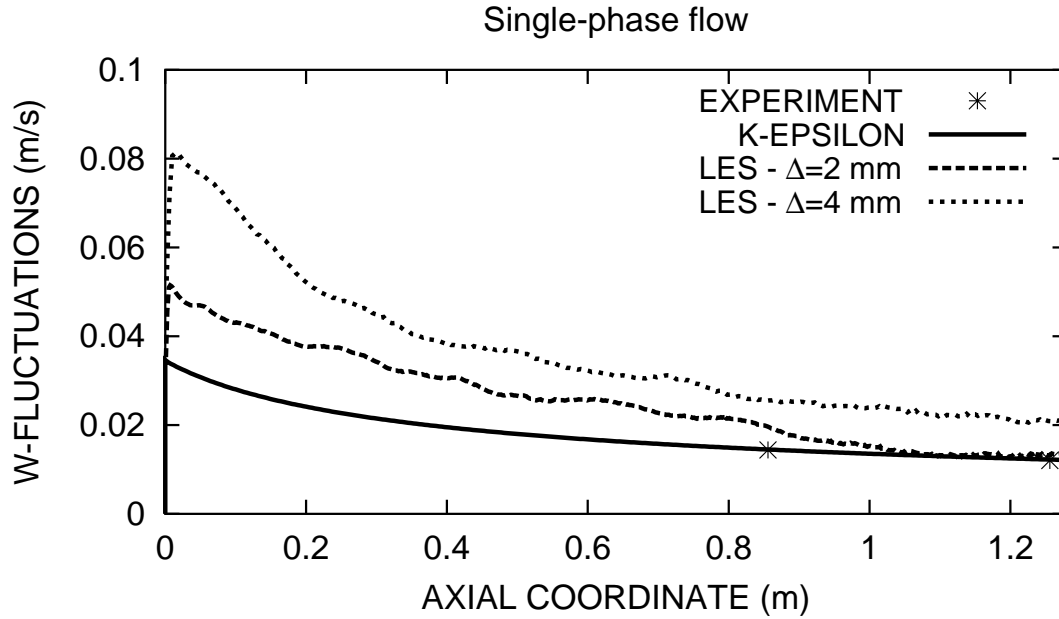


Figure 5.6: Decay of the vertical velocity fluctuations for different turbulence models and different grids, without bubbles. Inlet turbulence is 6%.

5.4 Conclusions

Two kinds of calculations have been run here: a fully three-dimensional case, which was used to study the effect of the mesh size on the turbulence intensity, and a two-dimensional one, the results from which were compared with the experimental data of LANCE & BATAILLE, 1991. The first important result is that the initial isotropy of the flow is preserved when the bubbles are injected, in agreement with the observations of LANCE & BATAILLE, 1991. Both cases have shown that the turbulent intensity depends primarily on the mesh size, and not on the bubble size. In particular, the turbulence level increases almost linearly with Δ , essentially because a larger filter width resolves larger scales of turbulence. The fact that the turbulence level does not depend on the bubble size reflects the lack of pseudo-turbulence production. In fact, this mechanism, which is created solely by the bubbles, is not represented. Only the bubble-induced dissipation effect is included via the TRAN, 1997 model (Eq. 5.4). This explains the necessity of increasing artificially the inlet turbulence in order to predict the decay of turbulence behind a grid, and the sharp decay of the energy spectrum in the three-dimensional calculations. Finally, for single-phase flow, the optimum mesh size is of the order of 1 mm, this being necessary to resolve the smaller scales, while for two-phase flow the mesh should in principle be larger than the bubble diameter, which creates problems if the bubbles are too big because then the mesh would be too coarse to resolve the smaller flow structures.

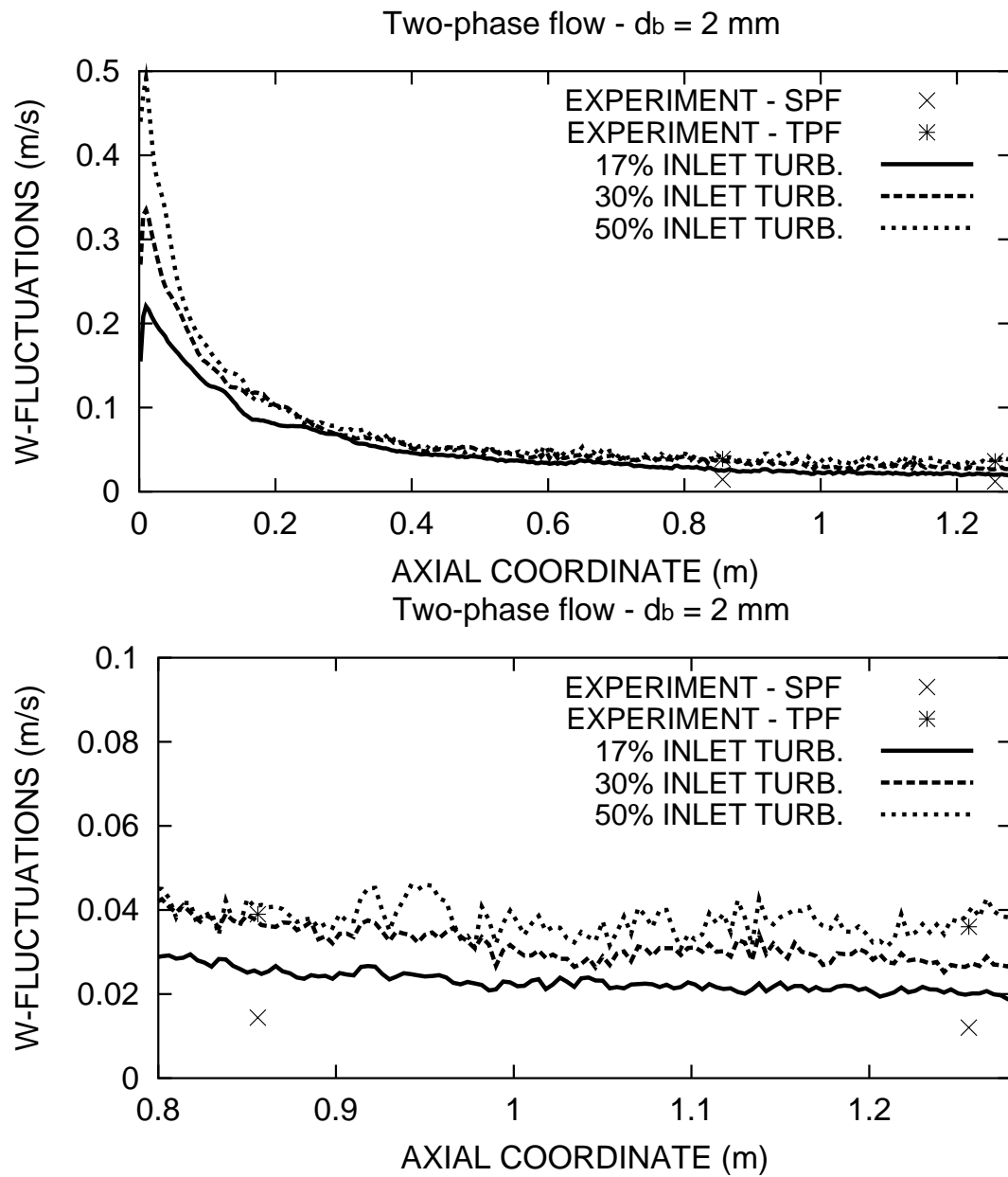


Figure 5.7: Top: decay of the vertical velocity fluctuations for $\Delta = 4$ mm and different inlet turbulence, with bubbles ($d_b = 2$ mm); bottom: detail.

6 Large Eddy Simulation: shear flow

6.1 Introduction

As an intermediate step on the way to a full bubble plume simulation using the LES model of turbulence, we have first investigated the case of a turbulent bubbly shear flow, making use of published data. The details of the experiment can be found in the thesis of ROIG, 1993. One advantage of this kind of flow is that it can be considered as statistically two-dimensional, which means that some important features can be captured, even with a 2D simulation. A positive aspect of 2D computations is the relatively low *cpu* time needed, which permits a parametric study of the problem to be undertaken. In particular, the influence of the mesh size, the lift coefficient and various subgrid models, have all been tested, both for the liquid and for the gas phases.

6.2 Experimental setup

The experimental situation, which is shown schematically in Fig. 6.1, is produced in an air/water loop supplying, from the bottom, a vertical square channel (2 m high and $0.4\text{ m} \times 0.4\text{ m}$ cross-section) in which the mixing layer develops. The inlet consists of a convergent channel divided into two parts by a vertical plate of 2 mm thickness, each part being supplied independently by a bubbly flow mixture of air and water at different flow rates. The bubbles are injected through porous tubes just before the convergent section in order to ensure uniform void fraction distributions in the two halves of the channel. Hot film anemometry was used in the experiments to measure the longitudinal instantaneous liquid velocity, while the local void fraction was measured with an optical fibre probe. The bubble velocities and sizes were measured with a double-fibre optical probe. Several experiments were performed, both with single-phase and two-phase flows, with different inlet velocities and void fractions. The configuration studied here is the one designated RUN 2.2 (ROIG, 1993), which features a constant void fraction distribution of 1.9% in both channels, and with bubbles of 2-3 mm diameter. This configuration has been chosen because these were the conditions which resulted in maximum turbulence intensities. The liquid velocity was 0.22 m/s and 0.54 m/s in the two channels respectively, and the measured inlet turbulence level was $\sim 27\%$ in the slower side (left) and $\sim 11\%$ in the faster side (right). Measurements were taken at several elevations: $x = -1\text{ cm}$ (at the end of the splitter plate), $x = 6\text{ cm}$, $x = 20\text{ cm}$, $x = 30\text{ cm}$, $x = 40\text{ cm}$ and $x = 50\text{ cm}$. The region above 50 cm was not considered because the lateral displacement of the mixing layer was already pronounced, and the influence of the walls was then no longer considered negligible.

6.3 Numerical setup

Since the flow is statistically two-dimensional, 2D calculations were run. As an example, the computational domain with a uniform mesh distribution of $3\text{ mm} \times 3\text{ mm}$ is shown in Fig. 6.2. Symmetry planes are assumed for the front, the back, and the sides of the computational domain. Modelling of the walls was not included in the simulations because the data measurements were taken in the central part of the domain only, where there was no wall influence. For this reason, the lateral dimension of the domain is taken as 30 cm instead of the actual 40 cm. The height is taken as 60 cm, because the maximum measurement elevation was 50 cm. At the top of the

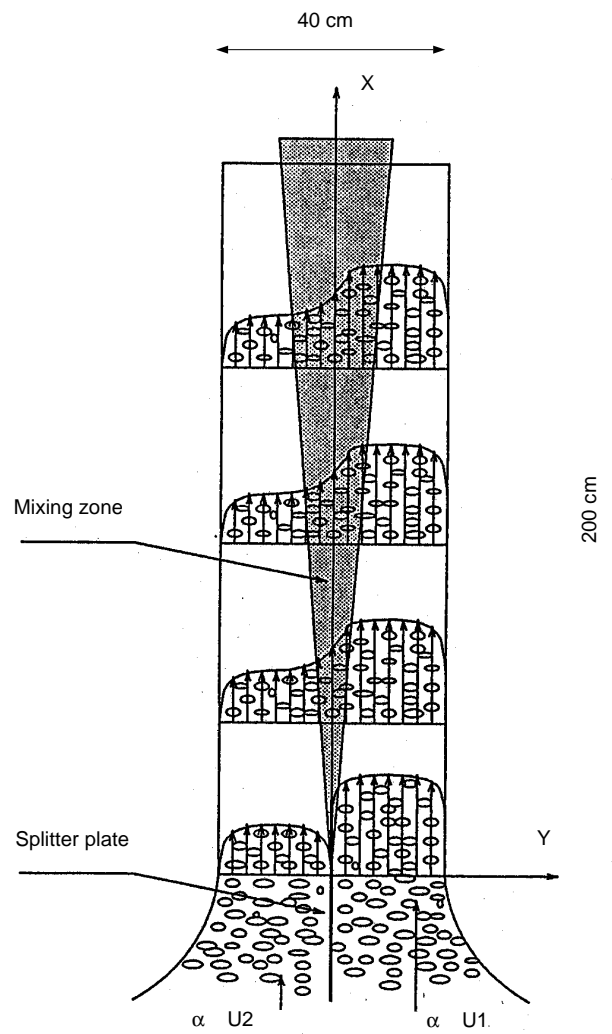


Figure 6.1: Experimental situation

domain, we have imposed a constant-pressure boundary condition and, at the bottom, the liquid and the gas are injected with the initial profiles measured at $x = -1$ cm: the end of the splitter plate, which was not modelled explicitly here. This level corresponds to $x = 0$ (inlet) for the simulations to be presented. The inlet void fraction, liquid and gas velocities, and liquid *rms* velocity profiles, are shown in Fig. 6.3. It can be seen that there is a peak in the void fraction distribution as a consequence of the development of the boundary layers on the two sides of the splitter plate. As far as the inlet turbulence is concerned, we assume here that the fluctuating velocity components are random deviates of a Gaussian probability distribution with zero mean and standard deviation given by the $u - rms$ profile of Fig. 6.3.

Considering the details of the numerical setup, the time interval was fixed to 0.001 s. Since the minimum mesh size used in our various computations was 3 mm, and the maximum velocity in the flow was 0.9 m/s, the Courant number criterion, which contributes to ensure numerical stability, is always fully satisfied. The calculations were continued for ≈ 5000 time steps in order to obtain sufficient statistical information. A second-order, central-differencing scheme was used for the spatial discretization, while a first-order, fully-implicit, backward-differencing scheme has been employed for the time discretization. The SIMPLE-C algorithm has been employed for the pressure-velocity coupling. All the calculations have been carried out using the commercial code CFX-4.3, 1999; the interfacial forces were introduced in the user-Fortran subroutine USRSRC, and the turbulent viscosity in USRVIS. The set of equations used is the same described in the previous Chapter (5.1)-(5.12).

As liquid subgrid-scale model, the SMAGORINSKY, 1963 (4.14) model has been applied, first with $C_s = 0.12$, and then with C_s given from the dynamic procedure of GERMANO ET AL., 1991, as described in § 4.2. As far as the effect of the bubbles on the subgrid-scale is concerned, the idea is to add a term to the usual Smagorinsky single-phase model to account for the extra dissipation imposed by the bubbles to the large-scale structures of the liquid. Two different approaches were investigated: the SATO ET AL., 1981, model (2.42), described in § 2.3.2, and the TRAN, 1997, model (5.16), described in § 5.2. Accordingly, μ_t is given by:

$$\mu_t = \mu_{sgs}^l + \mu_{sgs}^g = \mu_{sgs} (1 + C_f \alpha_g 6\pi \frac{d_b \mu_{lam}}{\Delta \mu_{sgs}})^{1/3} \quad (6.1)$$

or

$$\mu_t = \mu_{sgs}^l + \mu_{sgs}^g = \mu_{sgs} + \frac{1}{2} C_{\mu b} \rho_l \alpha_g d_b |\mathbf{u}_g - \mathbf{u}_l| \quad (6.2)$$

as appropriate, in which μ_{sgs} refers to the turbulent viscosity derived from the Smagorinsky model (4.14), μ_{lam} is the molecular viscosity, and C_f and $C_{\mu b}$ are model constants, estimated at 0.17 (TRAN, 1997) and 1.2 (SATO ET AL., 1981), respectively.

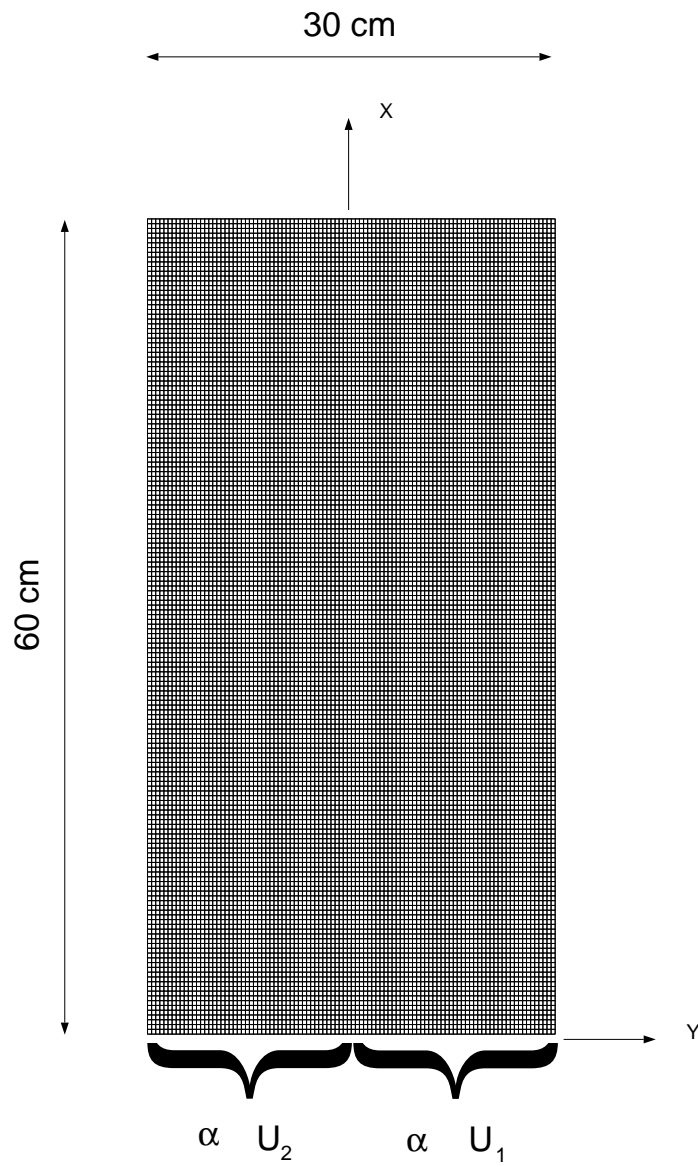


Figure 6.2: Uniform mesh distribution of $3\text{ mm} \times 3\text{ mm}$

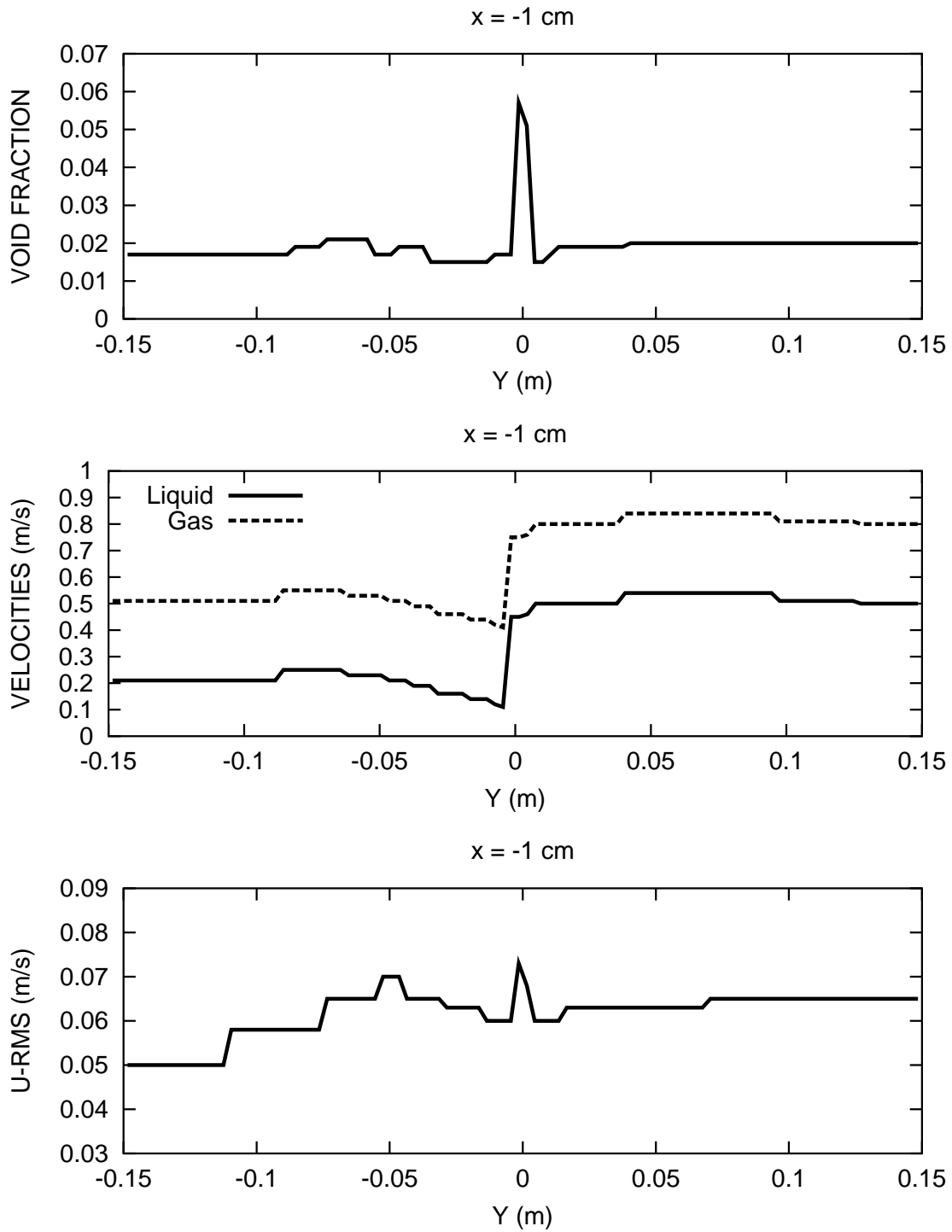


Figure 6.3: Inlet conditions for the void fraction, the liquid and gas velocities, and the liquid *rms* velocities.

6.4 Calculations

6.4.1 Effects of grid size and lift coefficient

Since we have seen in Chapter 2 and 3 that the lift coefficient is crucial for the spreading of the bubbles, we first checked the influence of the coefficient on the results obtained using two different grids: the first with a uniform mesh size of $10 \times 10 \text{ mm}^2$ (Figs. 6.4-6.7), and the second with a uniform mesh size of $3 \times 3 \text{ mm}^2$ (Figs. 6.8-6.11). In both cases, μ_t was evaluated from the Tran model (6.1) with $C_f = 0.17$. The results obtained with different lift coefficients ($C_L = 0.0, 0.125, 0.25, 0.5$) are compared with the experimental data of ROIG, 1993. In the experiment, the effects of the splitter plate wake disappeared at about 20 cm from the inlet, and since the plate has not been modelled here, the results at $x = 6 \text{ cm}$, where the flow is not fully developed, are not considered. Moreover, above $x = 30 \text{ cm}$, the measured gas and liquid velocities in the left side of the channel increased, causing an increase in the turbulent fluctuations, and a subsequent sudden spreading of the mixing layer. This increase (the reason for which has not yet been resolved), might be the result of three-dimensional effects, which cannot be represented with the two-dimensional simulation adopted here. Consequently, results at $x = 50 \text{ cm}$ are not included, but results are shown at $x = 40 \text{ cm}$ in order to emphasize the differences with the upstream development of the flow.

Comparing the results with the two grids, it is clear that the coarse grid is not adequate to resolve the details of the flow correctly. The void fraction profiles (Fig. 6.4) are flat, regardless of the lift coefficient, the liquid *rms* velocities are overestimated across the entire channel (Fig. 6.7), and the profile is not correct since there is no peak associated with the largest velocity gradient. The velocity distributions (Figs. 6.5-6.6) show a ragged profile, typical of a coarse-mesh resolution, and do not depend strongly on the lift force.

In contrast, the finer mesh simulations produce better results, both qualitatively and quantitatively, with the exclusion of the case with $C_L = 0.0$, which indicates that the lift force here plays an important role in the dispersion of the bubbles. The double-peak in the void fraction distribution is generally well predicted (Fig. 6.8), in particular for $C_L = 0.25$, and outside the mixing layer the void fraction follows the experimental profile, which is anyway rather flat. The large-scale velocities (Figs. 6.9-6.10) are rather insensitive to lateral forces, as already noted for the coarse mesh, but the liquid *rms* fluctuations (Fig. 6.11) are now somewhat more affected. In particular, the smaller the lift coefficient, the higher the *rms* values, and this is more evident in the mixing zone itself. The reason apparently is that, reducing the lateral dispersion, the liquid and the bubbles are more free to fluctuate in the vertical direction.

According to the previous results, it appears that a mesh much larger than the size of the bubbles is not able to capture the phenomena involved in the mixing layer. This trend goes against the idea of a bubble-induced, sub-grid turbulent viscosity as proposed by TRAN, 1997, because such a mechanism makes sense only if the size of the bubbles is smaller than some integral length scale, so that a statistically significant number of bubbles is contained within a single mesh. In fact that model was conceived for large reservoirs, where the bubbles are probably much smaller than the scale of turbulence. But, in practical terms, we are not dealing here with micro-bubbles, and such a mesh would be too coarse in our case, and the interactions at the scale of the bubble would then be filtered out. Moreover, we are using the Eulerian approach, which means that the bubbles are considered collectively as a continuum phase, with a drag coefficient they would have if they were really 3 mm diameter bubbles. Under these circumstances, it is difficult to justify such a theory. On this basis, we have tried to optimize the grid size, and the best mesh, with Δ slightly larger than the bubble diameter, combined with the optimum lift coefficient $C_L = 0.25$, gives the results shown in Figs. 6.12-6.14. There are some uncertainties regarding the quality of the measurements

at $x = 40$ cm, as explained above, but in general the agreement is seen to be rather good. The only discrepancy is with the liquid fluctuations (Fig. 6.14) outside of the mixing zone, where the fluctuations appear to be somewhat underestimated. This may mean that the *sgs* model for the bubbles needs to be revised when the most important source of turbulence is due to the motions of the bubbles themselves, and not induced by the liquid shear.

6.4.2 Effect of subgrid model

A comparison between the Smagorinsky model and the dynamic procedure of Germano explained in § 4.2 is given in Figs. 6.15-6.16. The mean quantities are not shown here since the differences were small. The vertical fluctuations are similar (Figs. 6.15), which is to be expected since C_s calculated from the dynamic model at the three different elevations (Fig. 6.16) oscillates around the value of the Smagorinsky constant, $C_s = 0.12$, with average values of 0.116, 0.121 and 0.119 for $x = 20$ cm, $x = 30$ cm and $x = 40$ cm, respectively. This result is important because it can be considered as a test case, since this is the first time the dynamic procedure has been implemented in the code CFX-4.3, 1999, and has been used for a two-phase simulation.

6.4.3 Effect of bubble-induced turbulence

It is also interesting to check the effective influence of the bubble-induced-turbulence subgrid-scale models, by comparing calculations with and without them. Consequently, we have performed simulations with the shear-induced term only (Eq. 4.14), then with the addition of the Tran model (6.1), and finally with the Sato model (6.2). The liquid fluctuations are shown in Fig. 6.17. The first two cases are practically overlapping, while smaller fluctuations are predicted with the Sato subgrid-scale model. Looking at Fig. 6.18, which shows the ratio of the total to laminar viscosity, the reason for this becomes clear. For the first two cases, the ratio (which is around 5) is basically the same, while for the Sato model, it is four times higher. The increase of viscosity is due to the magnitude of the second term on the *rhs* of (6.2); this produces an increase of diffusivity, which damps the turbulent fluctuations. On the other hand, the influence of the Tran model is small compared to the shear-induced effect, and the presence of the power $1/3$ in (6.1) also tends to limit the influence of the bubble-induced effect. It has to be pointed out that, with the dynamic procedure, it is possible to locally have negative values of $(C_s \Delta)^2$, and hence a negative turbulent viscosity, which is interpreted as a manifestation of the presence of backscatter (LILLY, 1992), that is, transfer of energy from smaller to larger scales. This is often regarded as a favorable aspect of this closure method, since it recognizes the ability of the subgrid scales to add randomness to the explicitly calculated scales. In practical terms however, the negative viscosity leads quickly to numerical instability, so that different ways of "clipping" $(C_s \Delta)^2$ have had to be introduced (see PIOMELLI, 1999, for instance). Here, we allow the turbulent viscosity to become negative as long as the total viscosity (laminar plus turbulent) remains positive: if $\mu_{tot} = \mu_{lam} + \mu_t < 0$, we set $\mu_{tot} = \mu_{lam}$. The superiority of the dynamic procedure over the Smagorinsky model is evident also at $x = 6$ cm. Since the splitter plate was not modelled here, the results at this elevation were not taken into consideration. But, as can be seen in Fig. 6.19 (top), the dynamic procedure follows the experimental data quite well, while the Smagorinsky model overpredicts the fluctuations. In Fig. 6.19 (bottom), the distribution of C_s shows that the calculated value is generally greater (with an average of 0.147) than the corresponding (constant) value 0.12 imposed by the Smagorinsky model. This increase in μ_t damps the fluctuations to a more reasonable level.

6.4.4 A new proposal for bubble-induced turbulence

A new subgrid-scale model for the gas phase has been introduced. This is actually just a modification of the Sato model (6.2) where a Prandtl mixing-length approach in which one half of the bubble diameter is used for the mixing length, and $C_{\mu b} \rho_l \alpha_g |\mathbf{u}_g - \mathbf{u}_l|$ is adopted for the mean eddy fluctuation. In the framework of the dynamic procedure, if we use $(C_s \Delta)$ instead of d_b as the mixing length, and $\rho_l \alpha_g |\mathbf{u}_g - \mathbf{u}_l|$ as the mean eddy fluctuation, we link directly the liquid and the bubble subgrid scales. The turbulent viscosity may then be written as:

$$\mu_t = \mu_{sgs}^l + \mu_{sgs}^g = (C_s \Delta)^2 \rho_l \sqrt{2 S_{ij} S_{ij}} + (C_s \Delta) \rho_l \alpha_g |\mathbf{u}_g - \mathbf{u}_l| \quad (6.3)$$

The liquid fluctuations are shown in Figs. 6.20-6.21, and it is evident that this model works as well as the Tran model, but has the advantage of having no additional empirical constants.

6.4.5 Effects of different bubble-induced turbulence terms

Finally, it was interesting to see the relative influence of the various subgrid-bubble-induced turbulence models in comparison with the basic Smagorinsky term (4.14). The results are shown in Fig. 6.22. The Tran model (6.1) has been modified slightly for practical purposes: since it has the form $(1+x)^{1/3}$, and x is small, it has been developed as $1 + \frac{x}{3} + O(x^2)$. Consequently, only the term

$$C_f \alpha_g 2\pi \frac{d_b \mu_{lam}}{\Delta} \quad (6.4)$$

has been plotted. The other terms come from the new model (second term on the *rhs* of Eq. 6.3), and the Sato model (second term on the *rhs* of Eq. 6.2). It is not surprising to see that the Tran, the Sato and the new models have the same profile, since they all depend on α_g , but their relative importance is significantly different. The Tran term has been multiplied by a factor 10^3 to reach the same order of magnitude of the Sato and the new models, which are, respectively, 3 to 4 times, and 2 times, larger than that of Smagorinsky. In general, every model induces small variations to the basic shear-induced term, and clearly the *rms* velocities cannot change dramatically.

6.5 Conclusions

In this chapter we have investigated a turbulent, bubbly, vertical shear flow, based on the experimental observations of ROIG, 1993. The test set-up permits a two-dimensional simplification, at least in a statistical sense. This allowed us to perform parameter studies (varying the mesh size, lift coefficient and subgrid-scale models), with the minimum computational overhead.

According to our simulations, the optimum configuration with a uniform mesh is given by $\Delta/d_b \approx 1.5$ and $C_L = 0.25$. The first indicates that a too coarse mesh is inappropriate to describe the turbulent phenomena observed in the experiment, because too many scales would be below the cut-off filter length, and would need to be represented by the subgrid model. This creates practical problems regarding the resolution of the flow field when the bubbles are not micro-bubbles, as in our case. The compromise is to use a mesh of the same order as the bubble diameter, or slightly

larger, so that 1) the bubble size determines the largest scale modelled, and 2) its interaction with the smallest calculated scale above the cut-off is captured. This choice also reflects the Scale Similarity Principle of BARDINA ET AL., 1980. As far as the lift force is concerned, it is crucial to include it, since it has been demonstrated that with $C_L = 0$ the double peak in the void fraction distribution is poorly predicted, or missed entirely (see Figures 6.4 and 6.8).

Another feature of the present work is the comparison of different subgrid-scale models for the liquid turbulence and the turbulence induced by the bubbles, and their relative importance. The simple Smagorinsky model with a constant $C_s = 0.12$ works quite well, and gives results similar to the improved model with the dynamic procedure of Germano and Lilly. Nevertheless, the advantage of the latter is more evident considering that no empirical constant is needed, and that the procedure allows the turbulent viscosity to become negative, which implies a backscatter energy transfer from smaller to larger scales. This effect, in principle, allows both an enhancement or attenuation of the turbulent intensity introduced by the bubbles. In fact, the presence of a dispersed phase often induces an agitation of the liquid, with a resulting increase of turbulence. But, on the other hand, there is an associated modification of the length scales leading to isotropy of the flow (LANCE & BATAILLE, 1991), with an accompanying reduction of the shear stress. In fact, the bubbles tend to break the big eddies into smaller ones of the size of the bubble diameter.

The modelling of the bubble-induced-turbulence subgrid-scales does not introduce any improvement. The Tran model seems to have negligible effects, while the Sato model overpredicts the turbulent diffusivity, and so over-damps the fluctuations. The reason could be that, for the case considered, the bubble-induced viscosity (and turbulence) is not crucial, the turbulence being mainly driven by the liquid shear, and a low void fraction ($\approx 2\%$) does not dramatically modify the situation. Probably, a case in which the bubbles actually drive the turbulence (via buoyancy and/or added mass forces) would be different. This idea is followed up in the next chapter in which the flow generated by a free bubble plume is investigated.

All this work has been performed in two dimensions, because the flow is two-dimensional, at least in a statistical sense, and because the relatively low *cpu* time needed permitted parametric studies; but some features of the flow remain undiscovered. For instance, an eventual backscatter effect of energy was not noticed here; moreover, above $x = 30\text{ cm}$ the measured gas and liquid velocities in the left side of the channel increased, causing an increase in the turbulent fluctuations, and a subsequent sudden spreading of the mixing layer. These effects might be the result of three-dimensional aspects, which cannot be represented with the two-dimensional simulation adopted here. A final conclusion in this respect could be made only in the light of three-dimensional simulations.

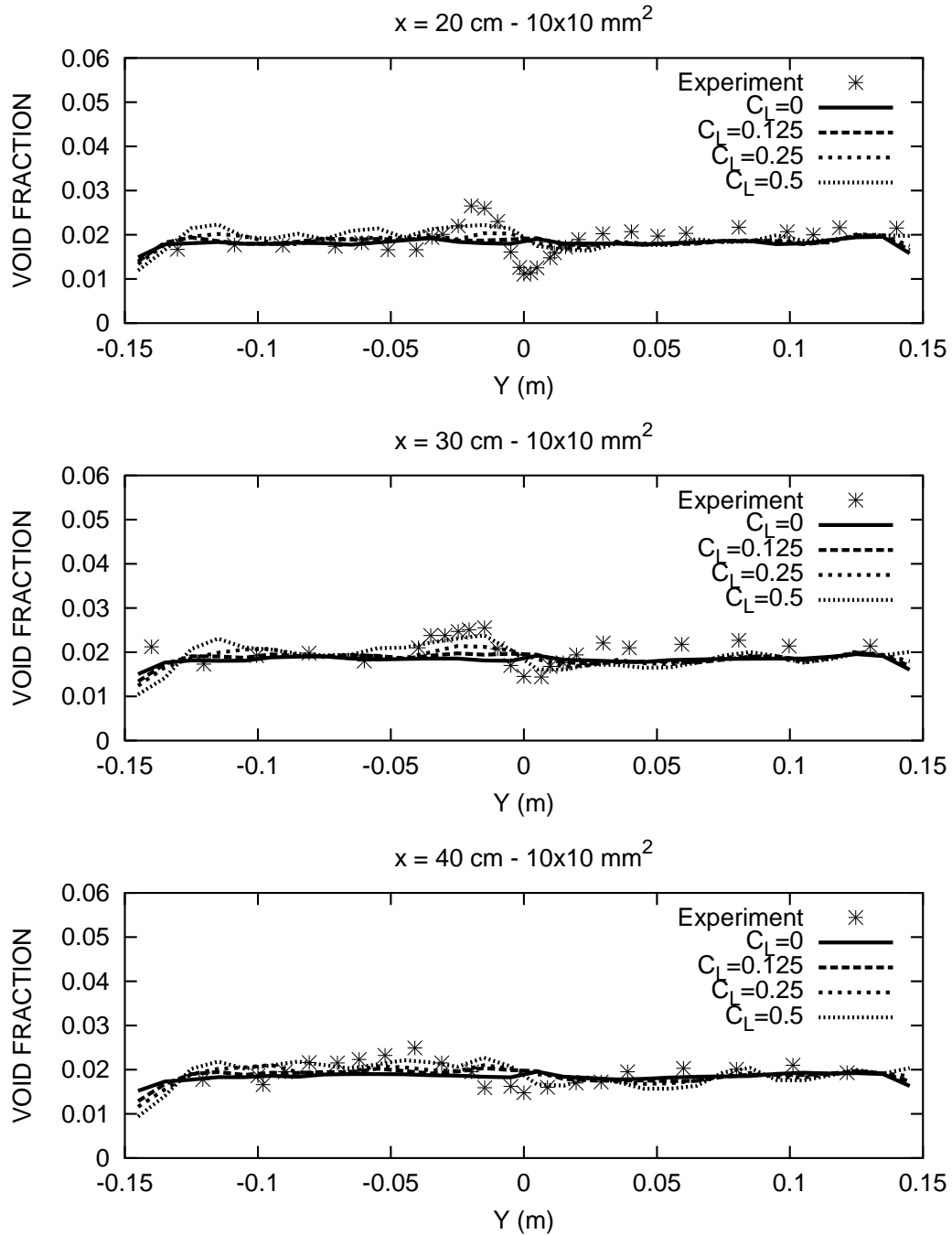


Figure 6.4: Void fraction distributions at different elevations for a uniform mesh size of $10 \text{ mm} \times 10 \text{ mm}$ (coarse mesh), with various lift coefficients, and with $C_s = 0.12$.

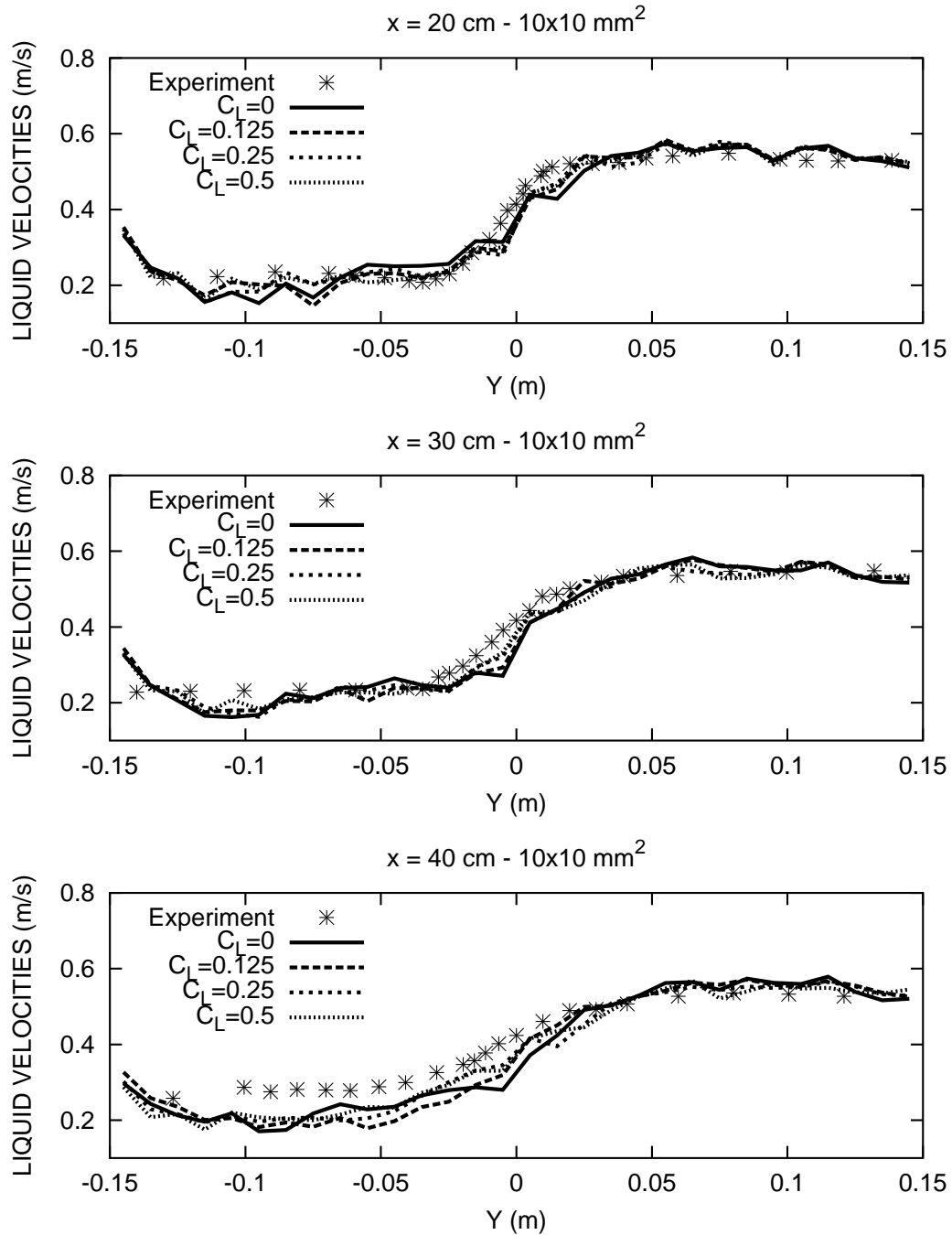


Figure 6.5: Liquid velocity distributions at different elevations for a uniform mesh size of $10 \text{ mm} \times 10 \text{ mm}$ (coarse mesh), with various lift coefficients, and with $C_s = 0.12$.

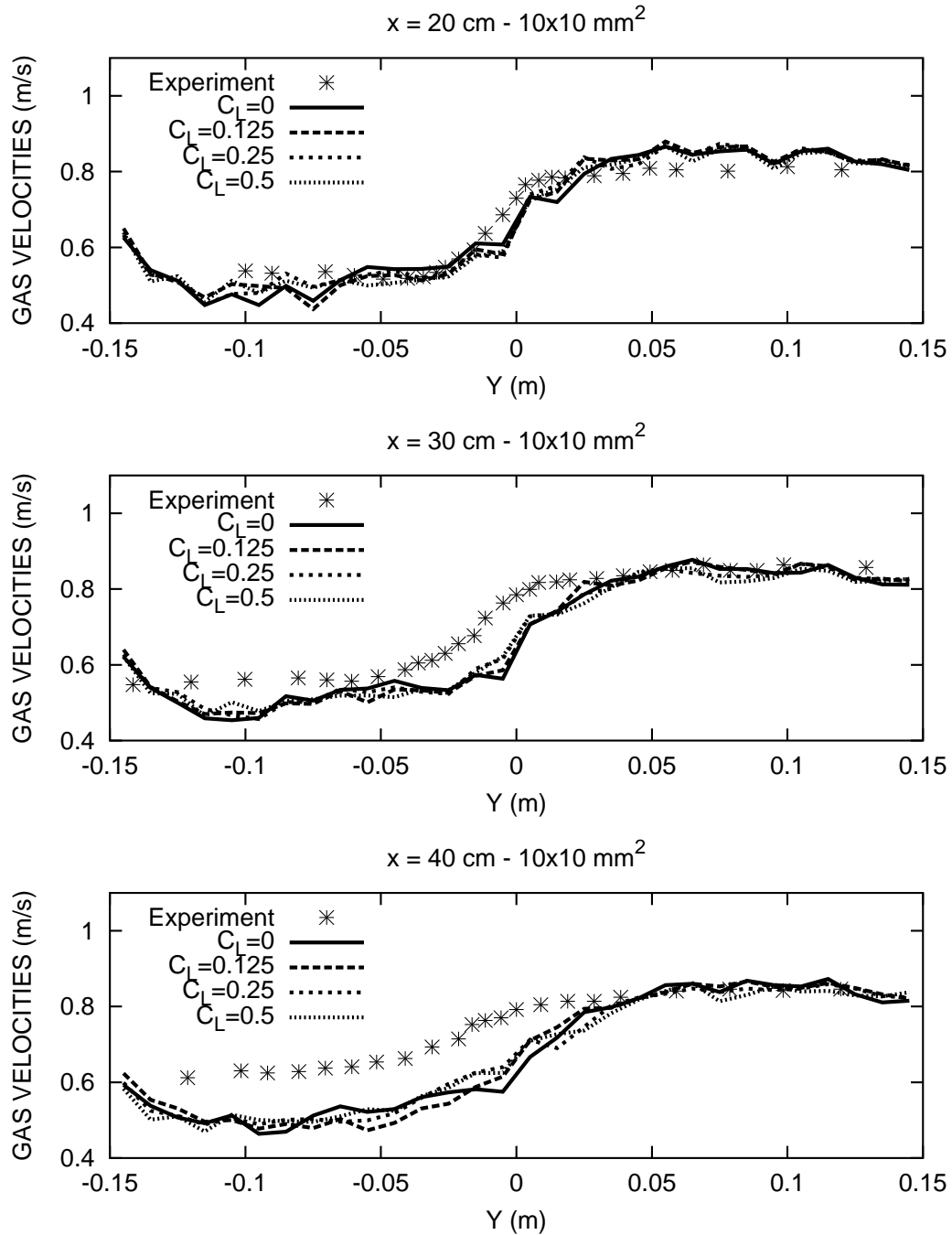


Figure 6.6: Gas velocity distributions at different elevations for a uniform mesh size of $10 \text{ mm} \times 10 \text{ mm}$ (coarse mesh), with various lift coefficients, and with $C_s = 0.12$.

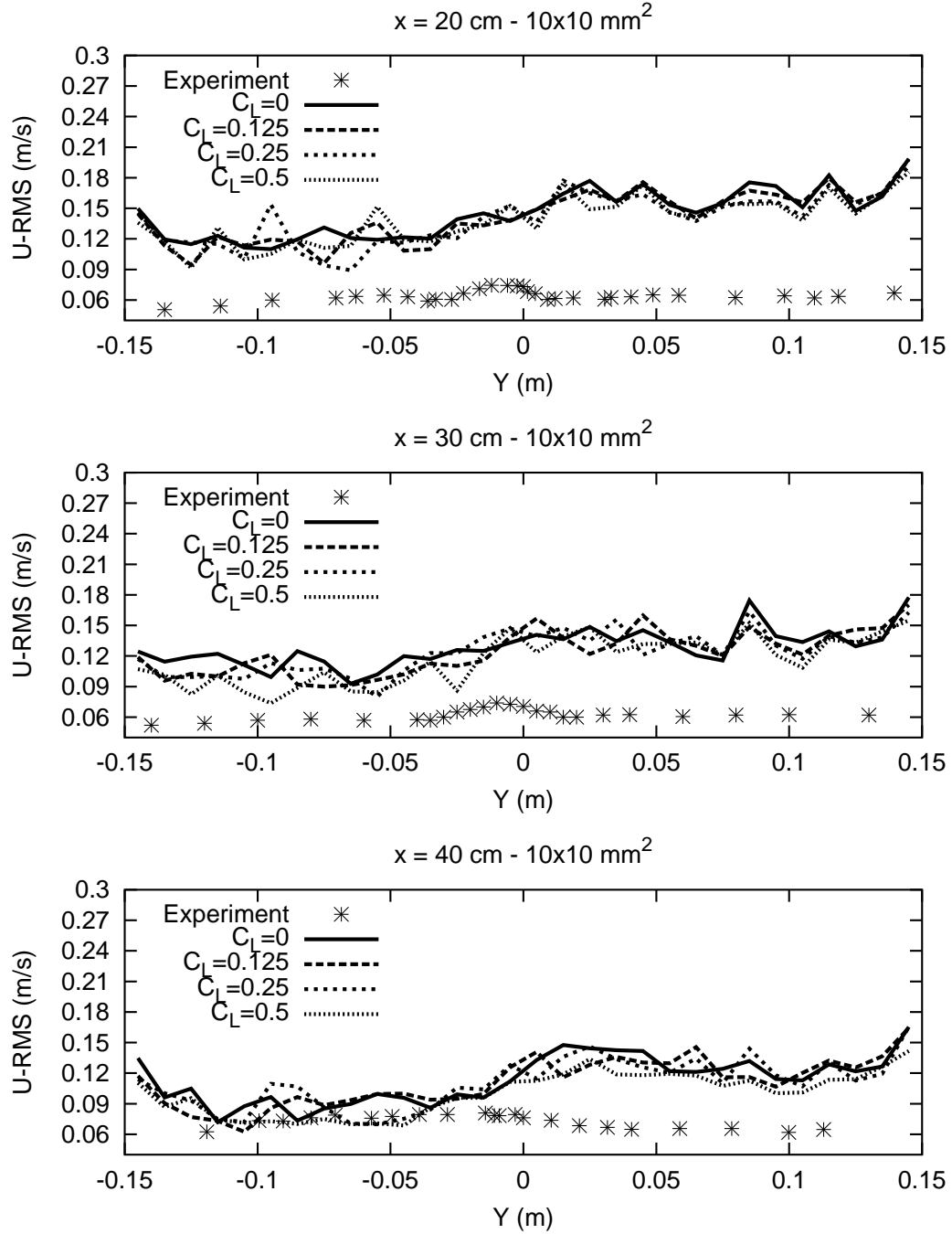


Figure 6.7: Liquid velocity fluctuations distributions at different elevations for a uniform mesh size of $10 \text{ mm} \times 10 \text{ mm}$ (coarse mesh), with various lift coefficients, and with $C_s = 0.12$.

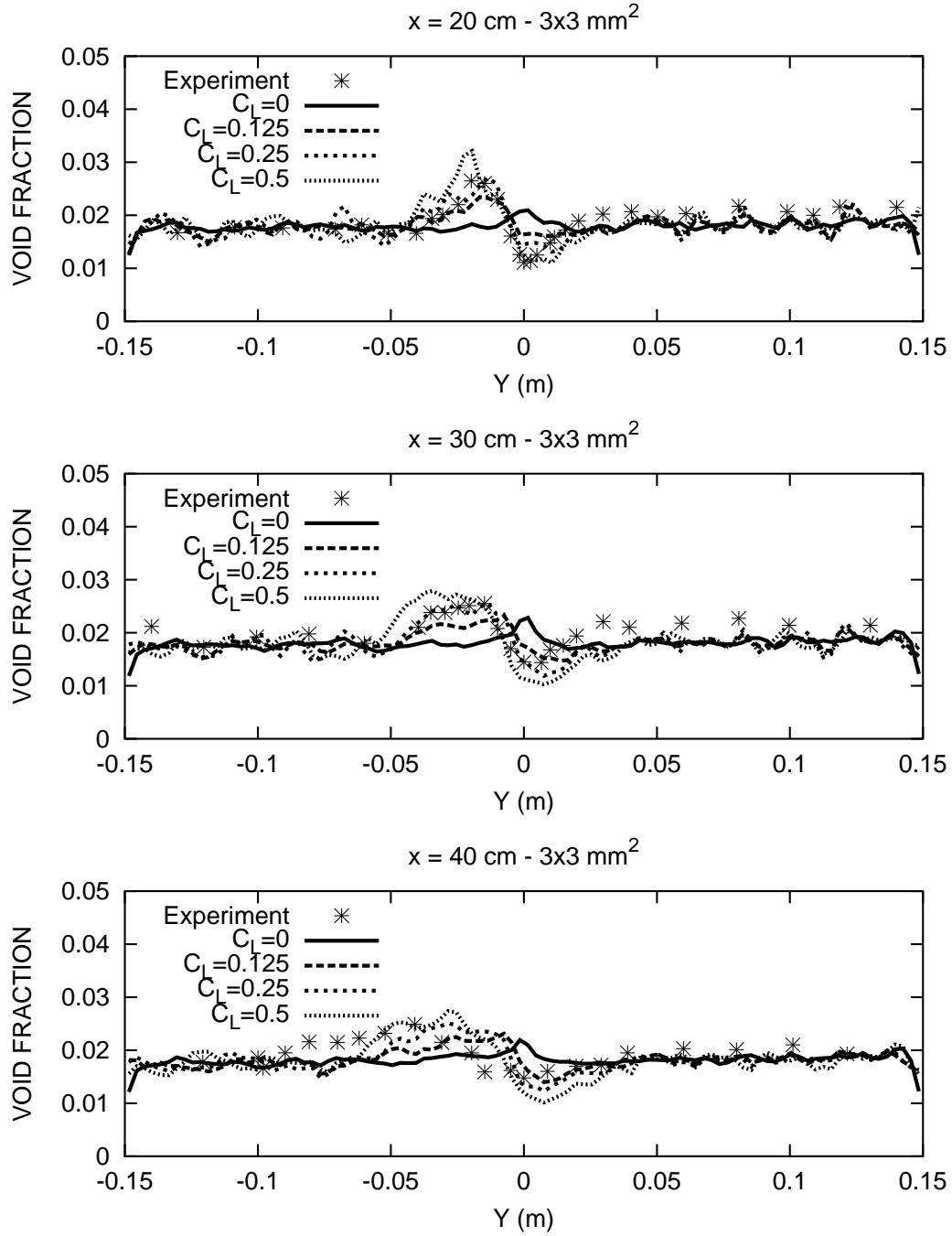


Figure 6.8: Void fraction distributions at different elevations for a uniform mesh size of $3 \text{ mm} \times 3 \text{ mm}$ (fine mesh), with various lift coefficients, and with $C_g = 0.12$.

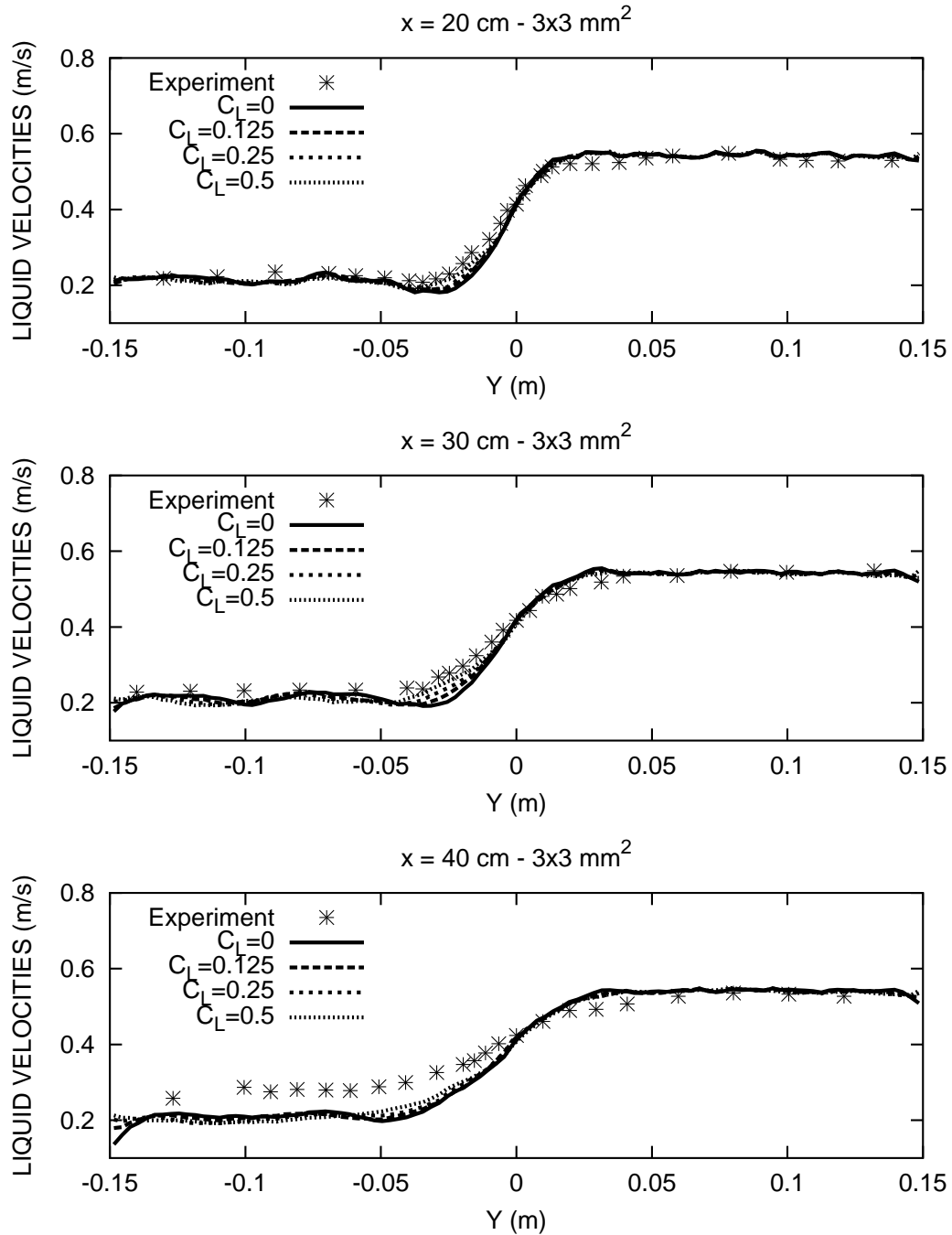


Figure 6.9: Liquid velocity distributions at different elevations for a uniform mesh size of $3 \text{ mm} \times 3 \text{ mm}$ (fine mesh), with various lift coefficients, and with $C_g = 0.12$.

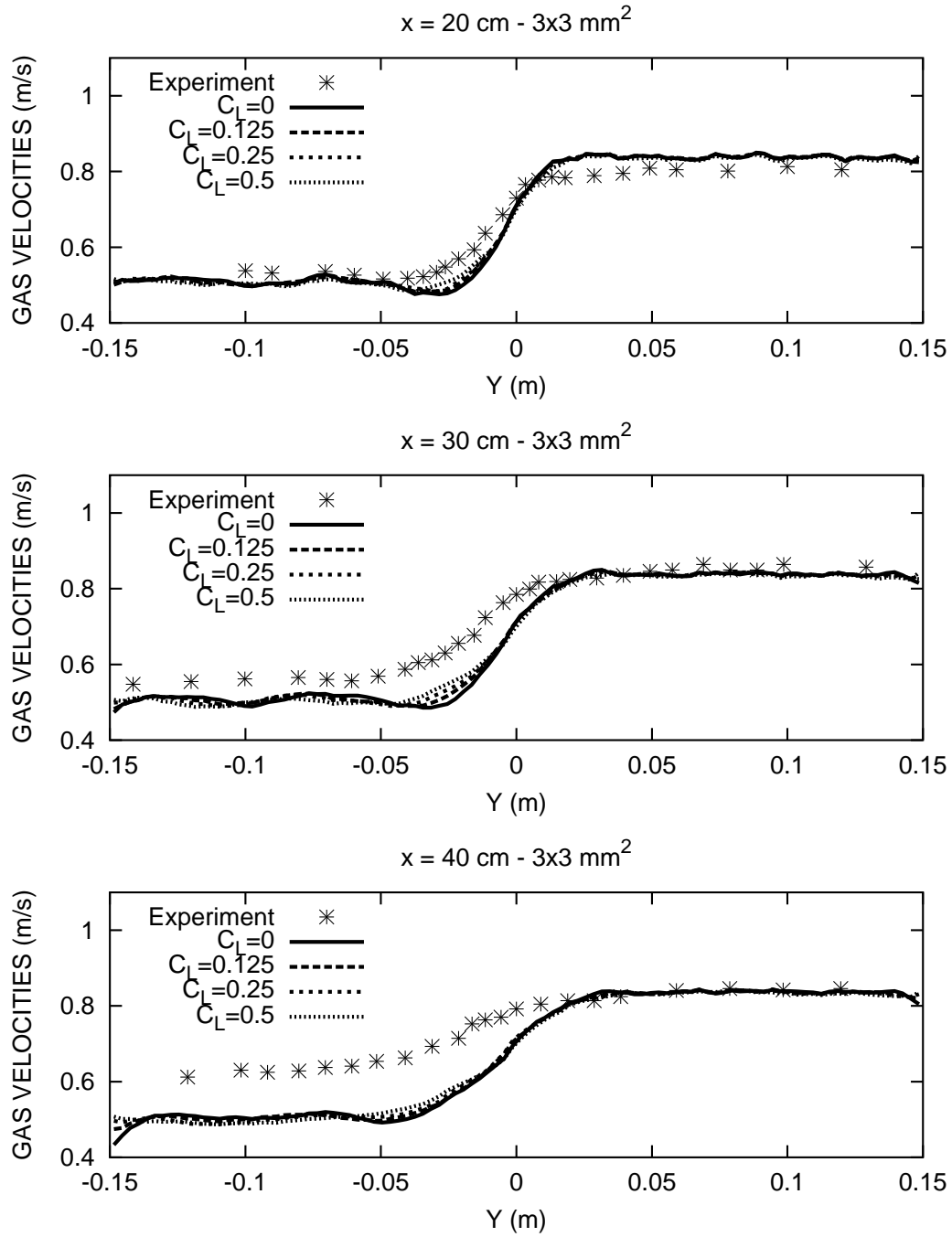


Figure 6.10: Gas velocity distributions at different elevations for a uniform mesh size of $3 \text{ mm} \times 3 \text{ mm}$ (fine mesh), with various lift coefficients, and with $C_g = 0.12$.

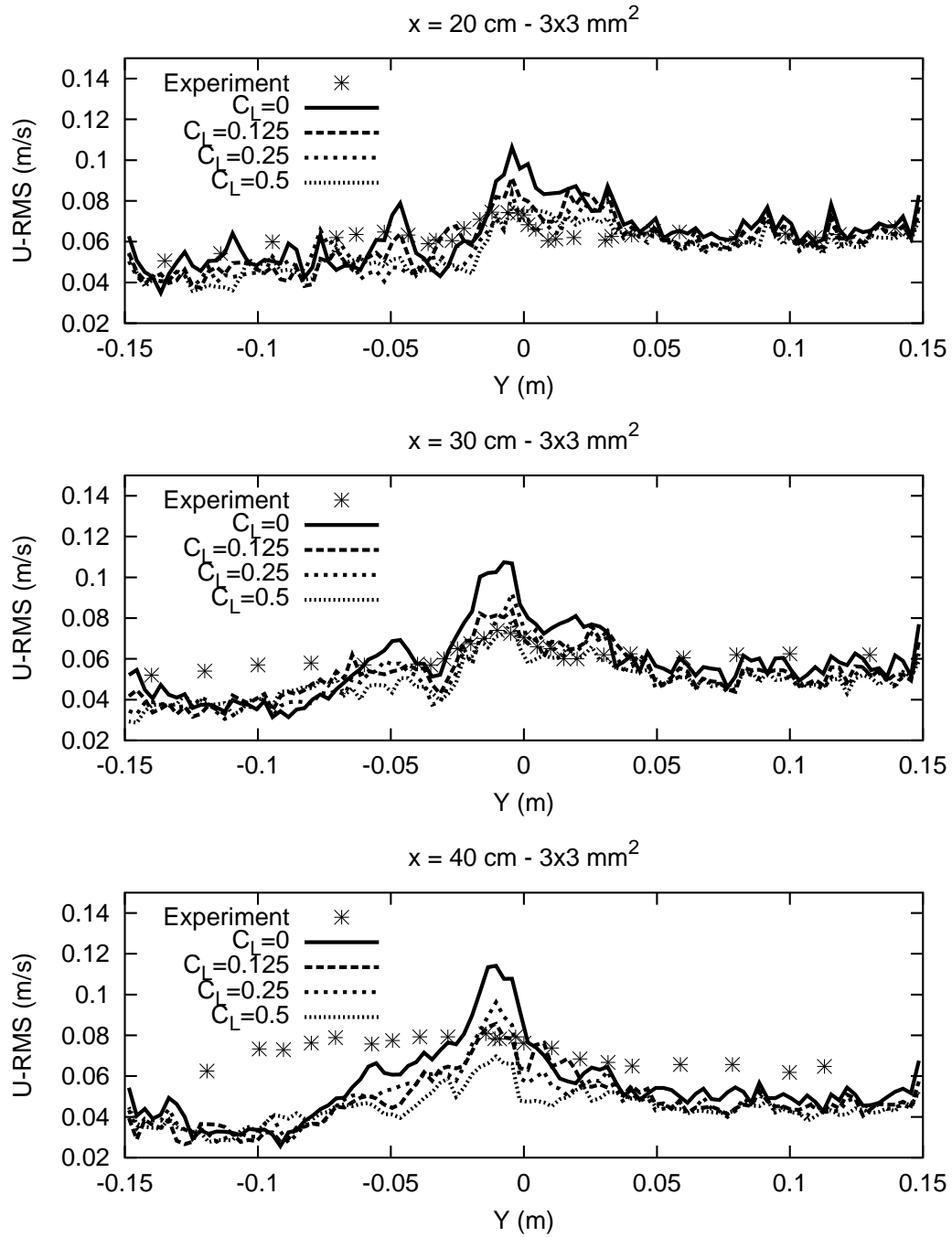


Figure 6.11: Liquid velocity fluctuations distributions at different elevations for a uniform mesh size of $3\text{ mm} \times 3\text{ mm}$ (fine mesh), with various lift coefficients, and with $C_s = 0.12$.

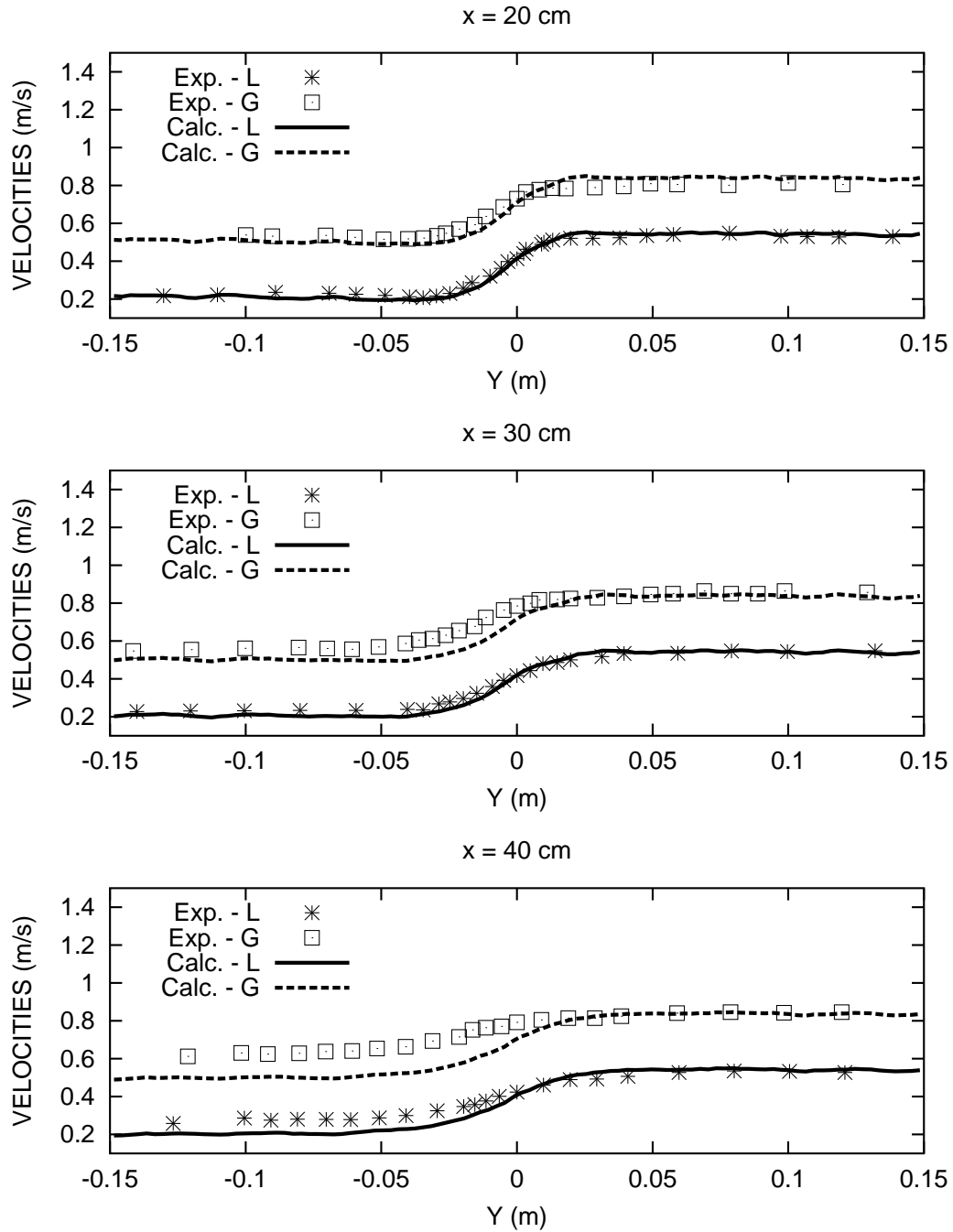


Figure 6.12: Velocity distributions at different elevations for an optimal combination of parameters: grid with $\Delta_x = 3.5$ mm, $\Delta_y = 3$ mm, $C_L = 0.25$. The subgrid-scale model for bubble-induced-turbulence is according to TRAN, 1997, liquid-turbulence by Smagorinsky model with $C_s = 0.12$.

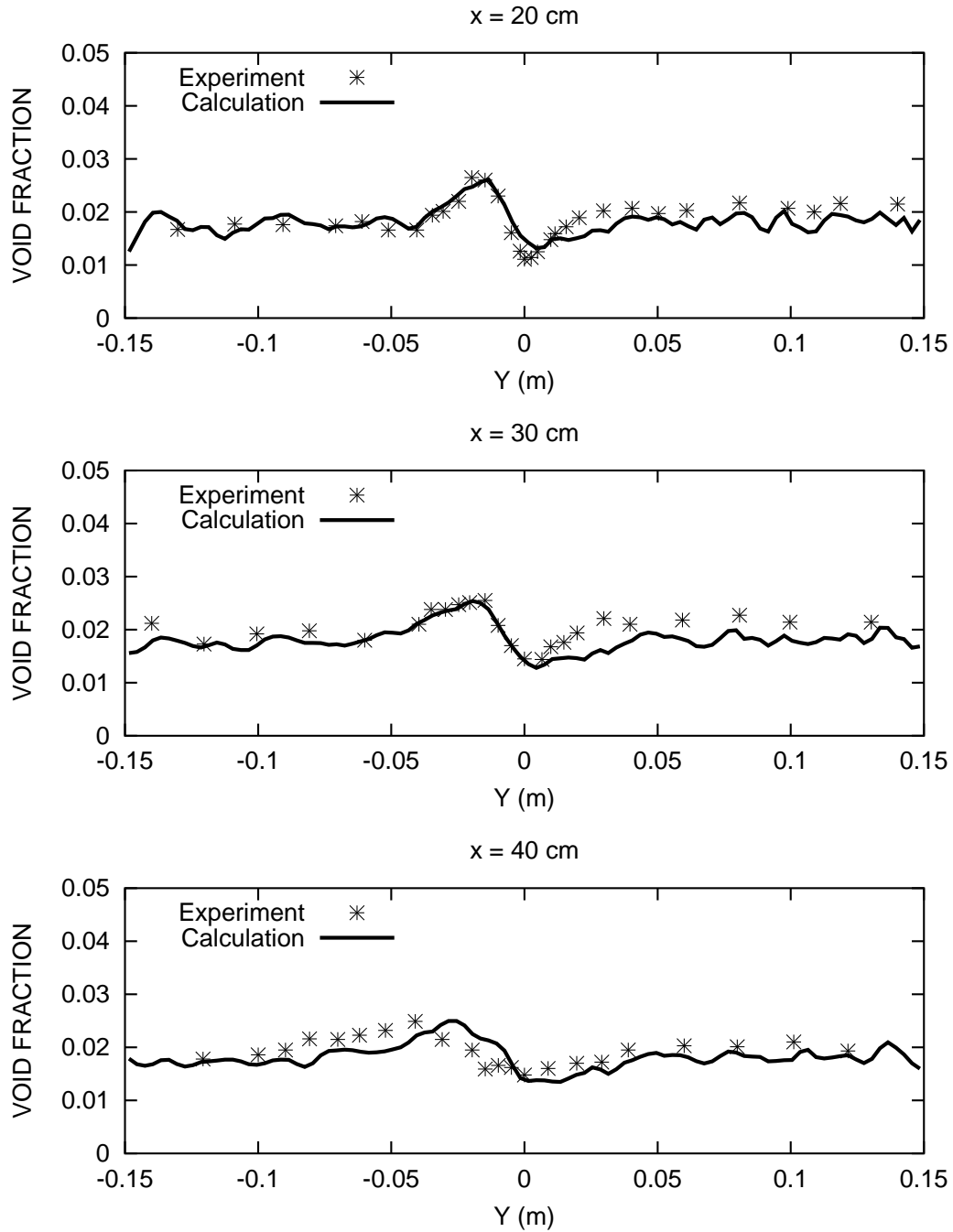


Figure 6.13: Void fraction distributions at different elevations for an optimal combination of parameters: grid with $\Delta_x = 3.5$ mm, $\Delta_y = 3$ mm, $C_L = 0.25$. The subgrid-scale model for bubble-induced-turbulence is according to TRAN, 1997, liquid-turbulence by Smagorinsky model with $C_s = 0.12$.

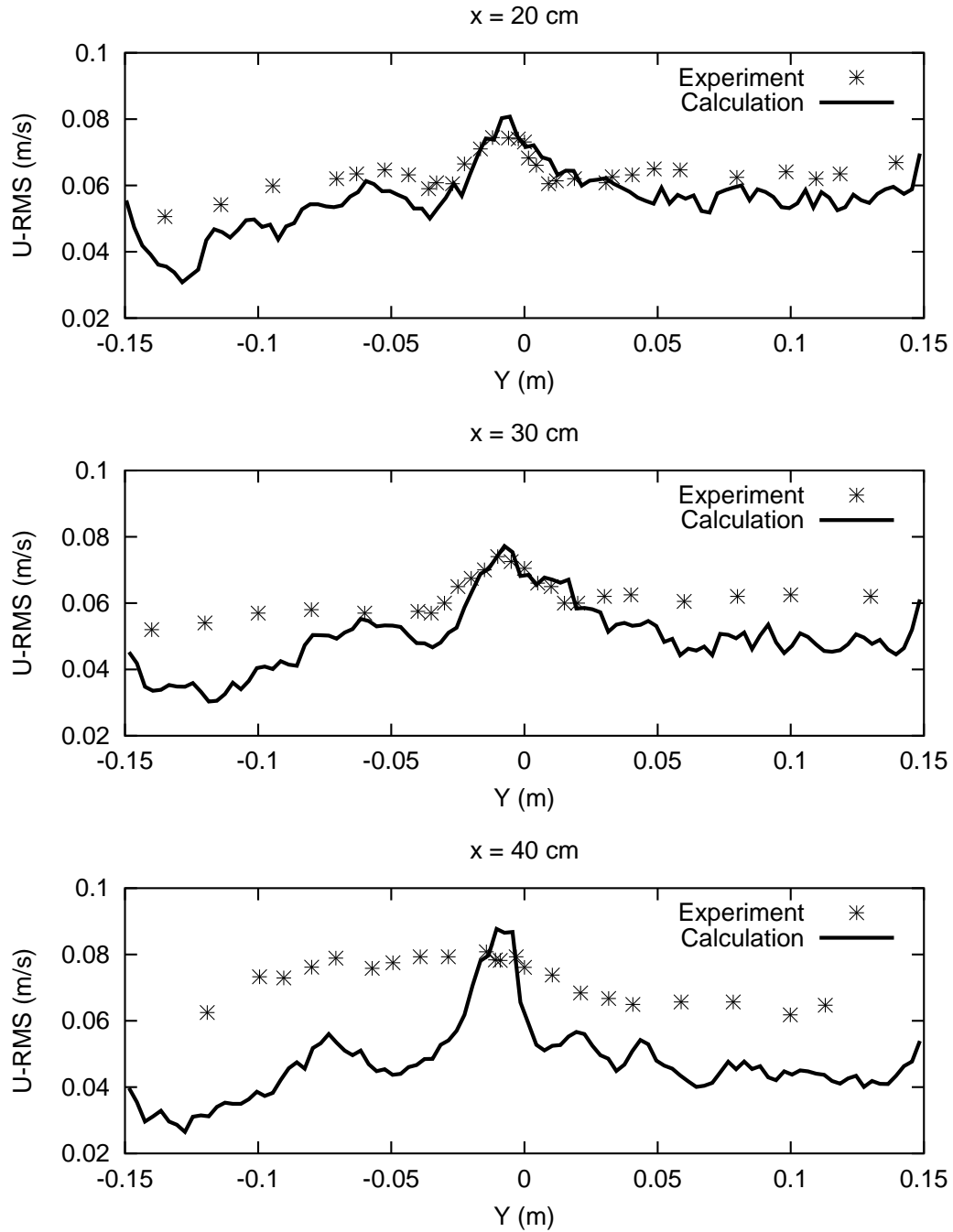


Figure 6.14: Liquid velocity fluctuations distributions at different elevations for an optimal combination of parameters: grid with $\Delta_x = 3.5$ mm, $\Delta_y = 3$ mm, $C_L = 0.25$. The subgrid-scale model for bubble-induced-turbulence is according to TRAN, 1997, liquid-turbulence by Smagorinsky model with $C_s = 0.12$.

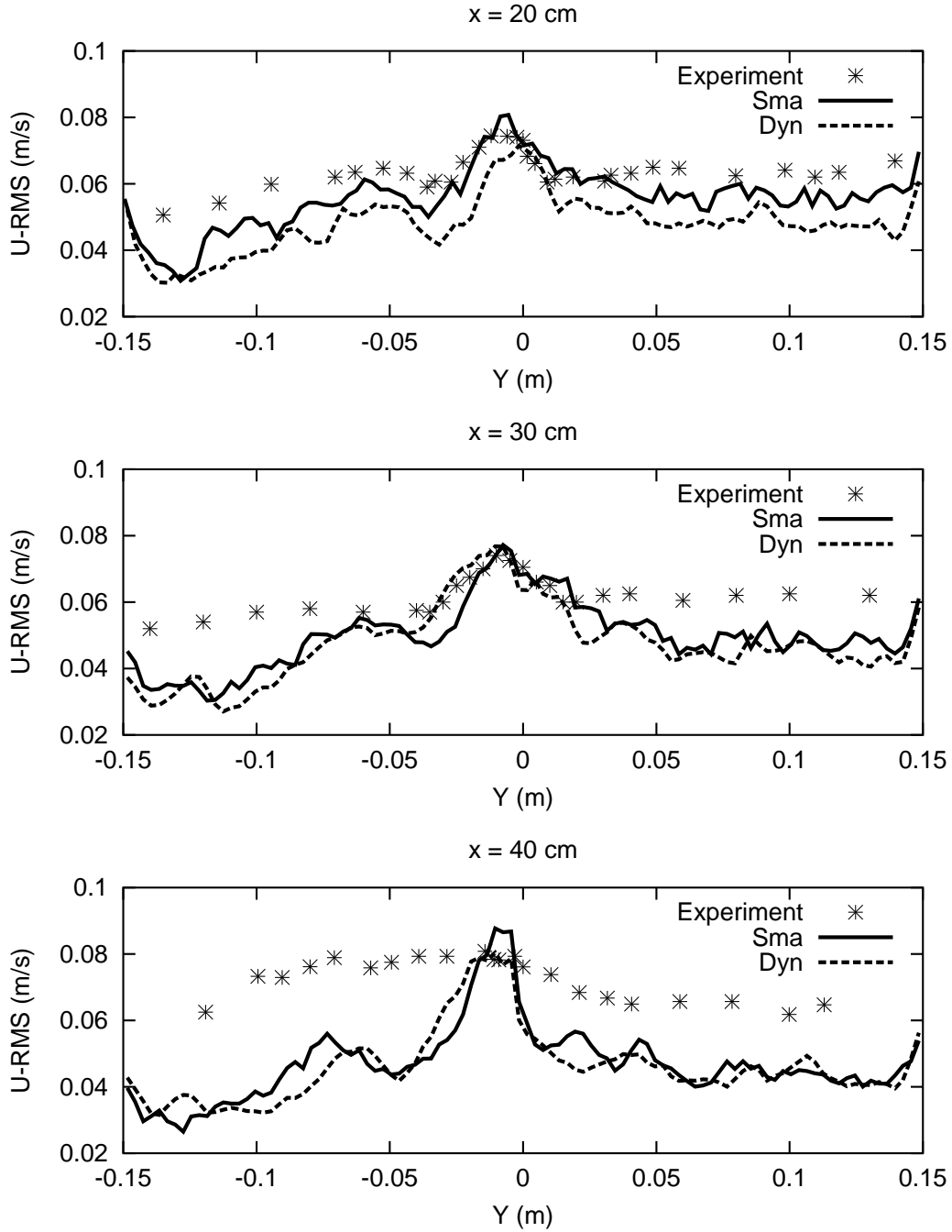


Figure 6.15: Liquid velocity fluctuation distributions at different elevations for the optimal grid with $\Delta_x = 3.5 \text{ mm}$, $\Delta_y = 3 \text{ mm}$ and $C_L = 0.25$. Comparison between the Smagorinsky subgrid-scale model with $C_s = 0.12$ (Sma) and with the dynamic procedure of Germano (Dyn). The subgrid-scale model accounting for the presence of the bubbles is according to TRAN, 1997.

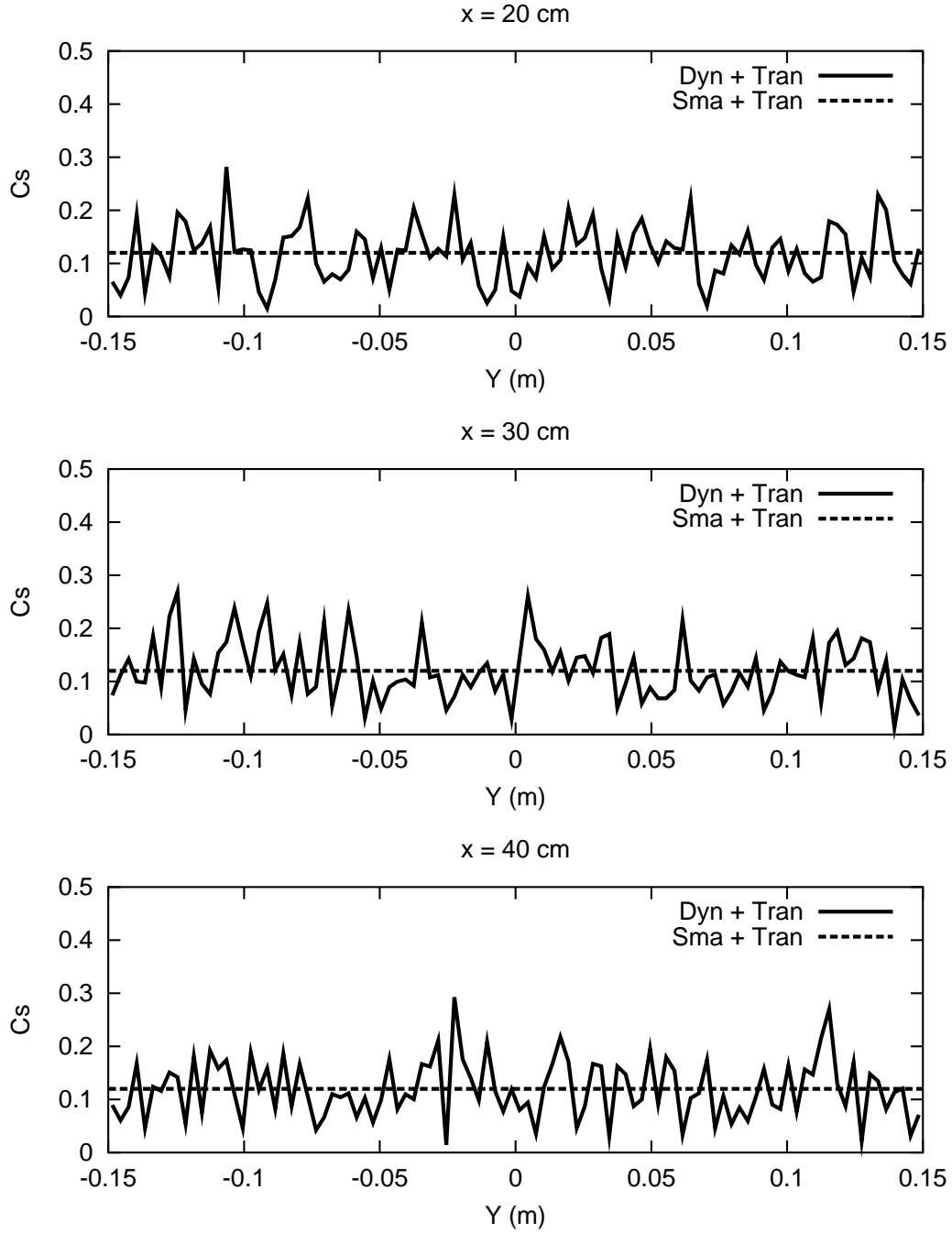


Figure 6.16: Distribution of C_s at different elevations for the optimal grid with $\Delta_x = 3.5$ mm, $\Delta_y = 3$ mm and $C_L = 0.25$. Comparison between the Dynamic procedure of Germano and the Smagorinsky model with $C_s = 0.12$. The TRAN, 1997 subgrid-scale model has been used for the effects of the gas phase.

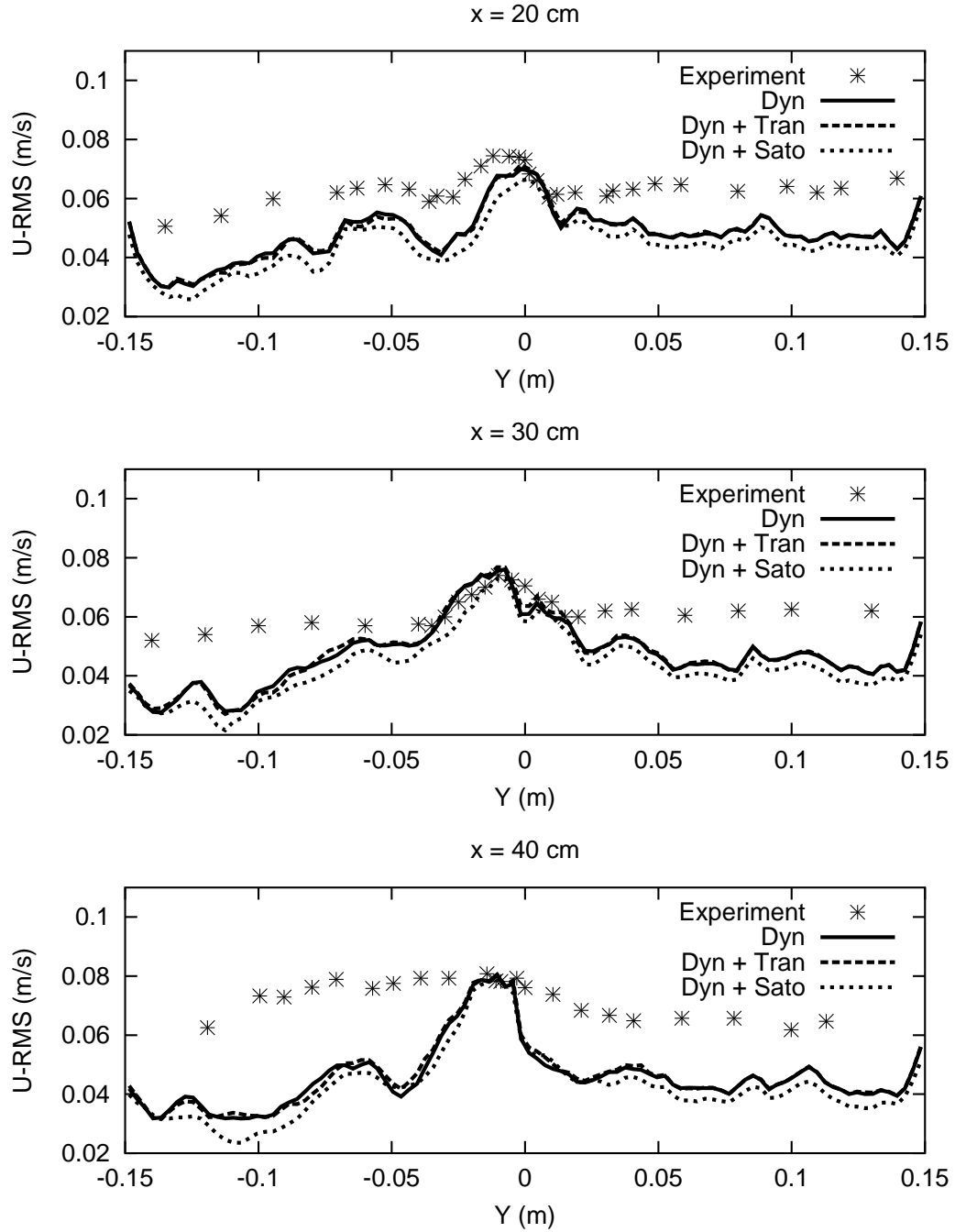


Figure 6.17: Liquid velocity fluctuation distributions at different elevations for the optimal grid with $\Delta_x = 3.5 \text{ mm}$ and $\Delta_y = 3 \text{ mm}$ and with $C_L = 0.25$. Comparison between different subgrid scale models for the influence of the gas phase: no model (Dyn), Tran subgrid-scale model (Dyn + Tran) and Sato model (Dyn + Sato). The liquid-turbulence subgrid-scale model is given by the dynamic procedure of Germano applied to the Smagorinsky model.

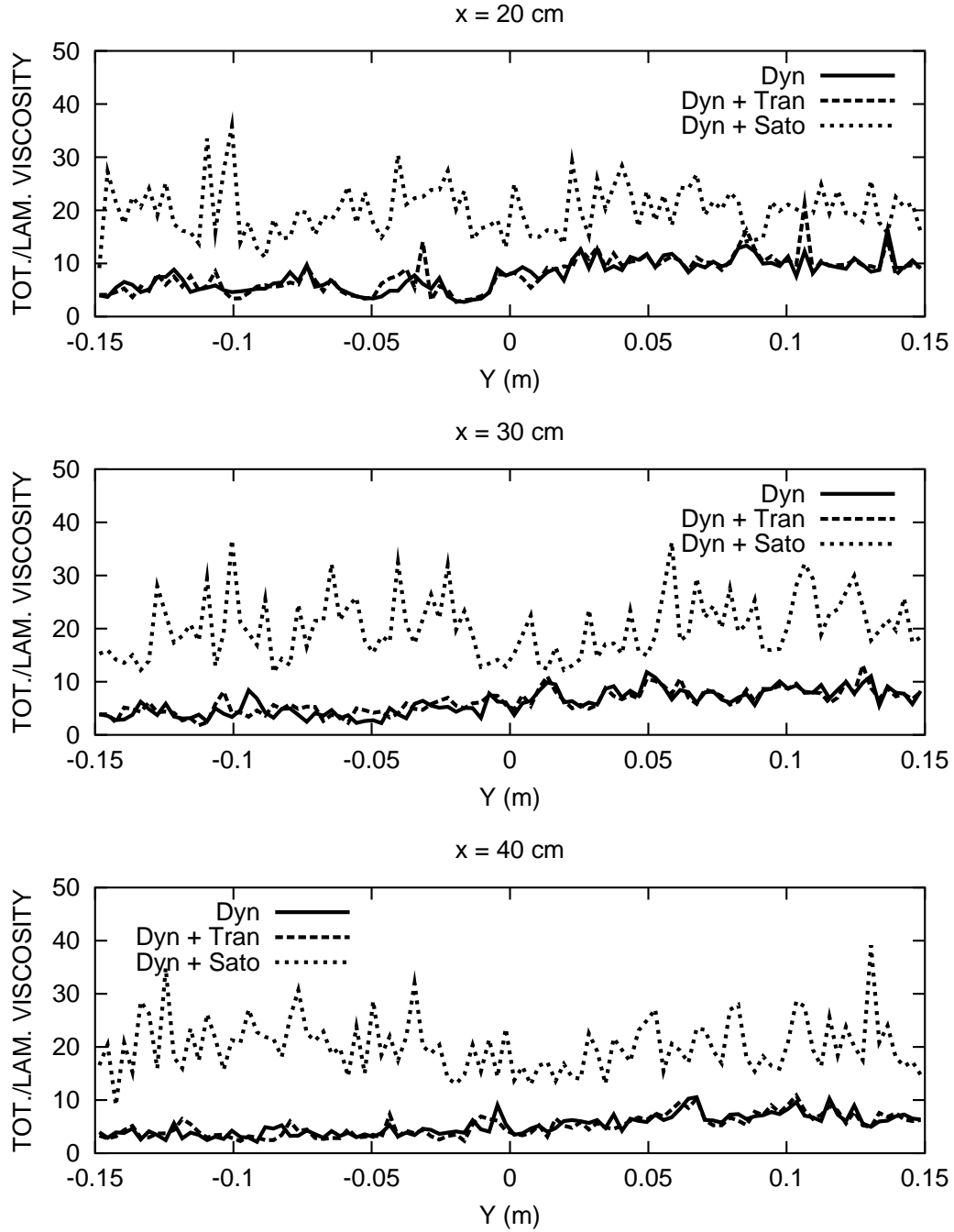


Figure 6.18: Distributions of total and laminar viscosity ratio at different elevations for the optimal grid with $\Delta_x = 3.5 \text{ mm}$, $\Delta_y = 3 \text{ mm}$ and $C_L = 0.25$. Comparison between different subgrid scale models for the gas-induced turbulence: no model (Dyn), Tran subgrid-scale model (Dyn + Tran) and Sato model (Dyn + Sato). The liquid-turbulence subgrid-scale model is given by the dynamic procedure of Germano applied to the Smagorinsky model.

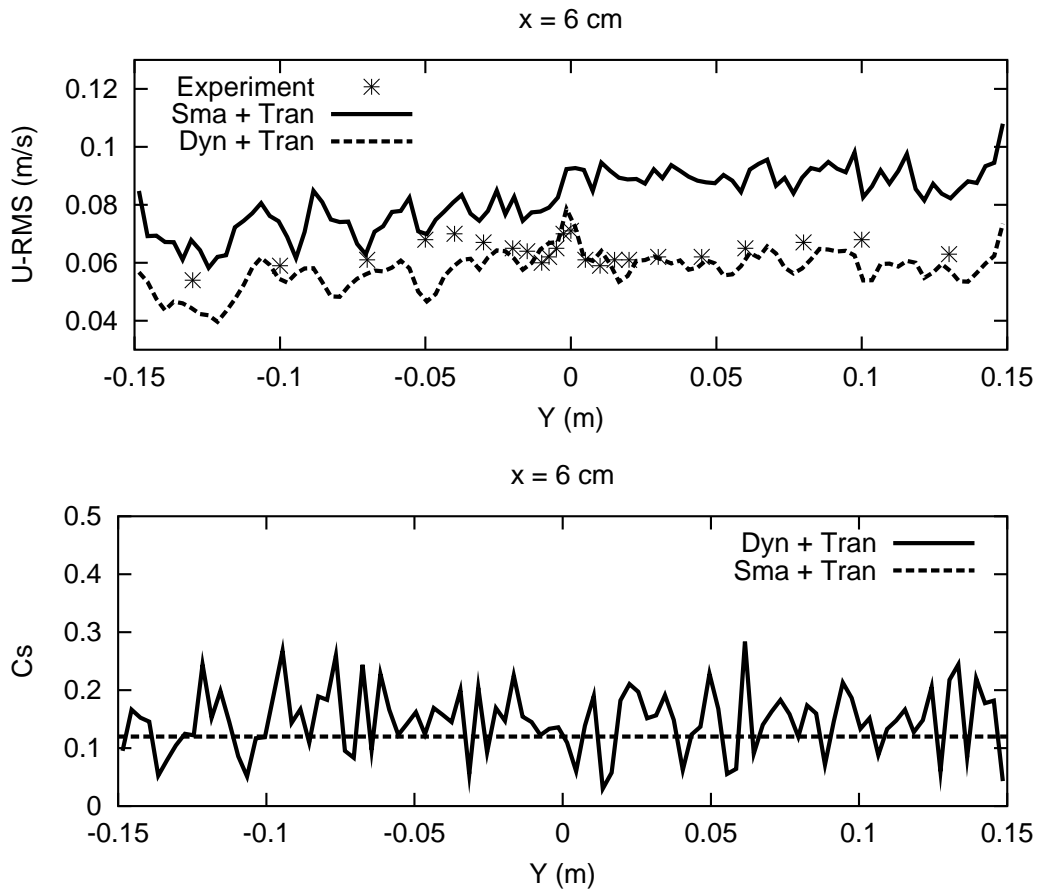


Figure 6.19: Liquid velocity fluctuations and C_s distributions at $x = 6 \text{ cm}$ for the optimal grid with $\Delta_x = 3.5 \text{ mm}$, $\Delta_y = 3 \text{ mm}$, $C_L = 0.25$. Comparison between the Smagorinsky model and the dynamic procedure of Germano.

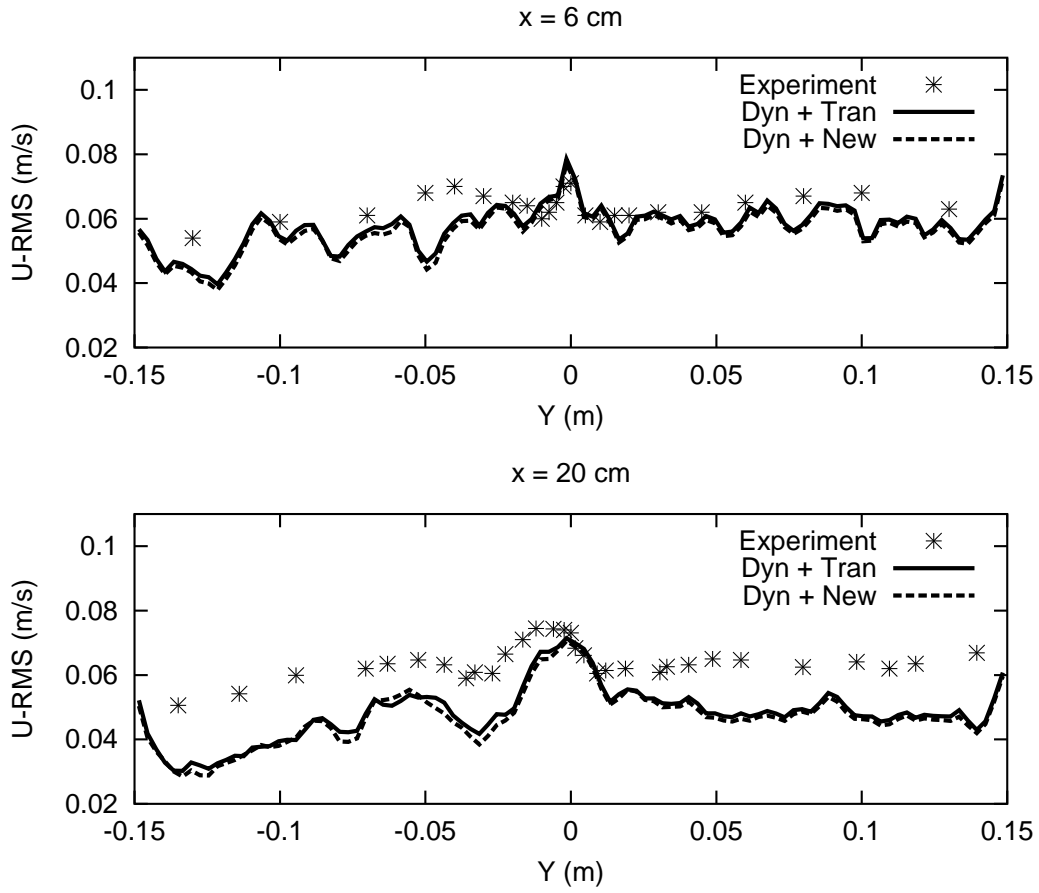


Figure 6.20: Liquid velocity fluctuations distributions at different elevations for the optimal grid with $\Delta_x = 3.5$ mm, $\Delta_y = 3$ mm and $C_L = 0.25$. Comparison between different subgrid scale models for the effect of bubbles: Tran subgrid-scale model (Dyn + Tran) and the new model (Dyn + New) described in the text. The liquid subgrid-scale model is given by the dynamic procedure of Germano applied to the Smagorinsky model.

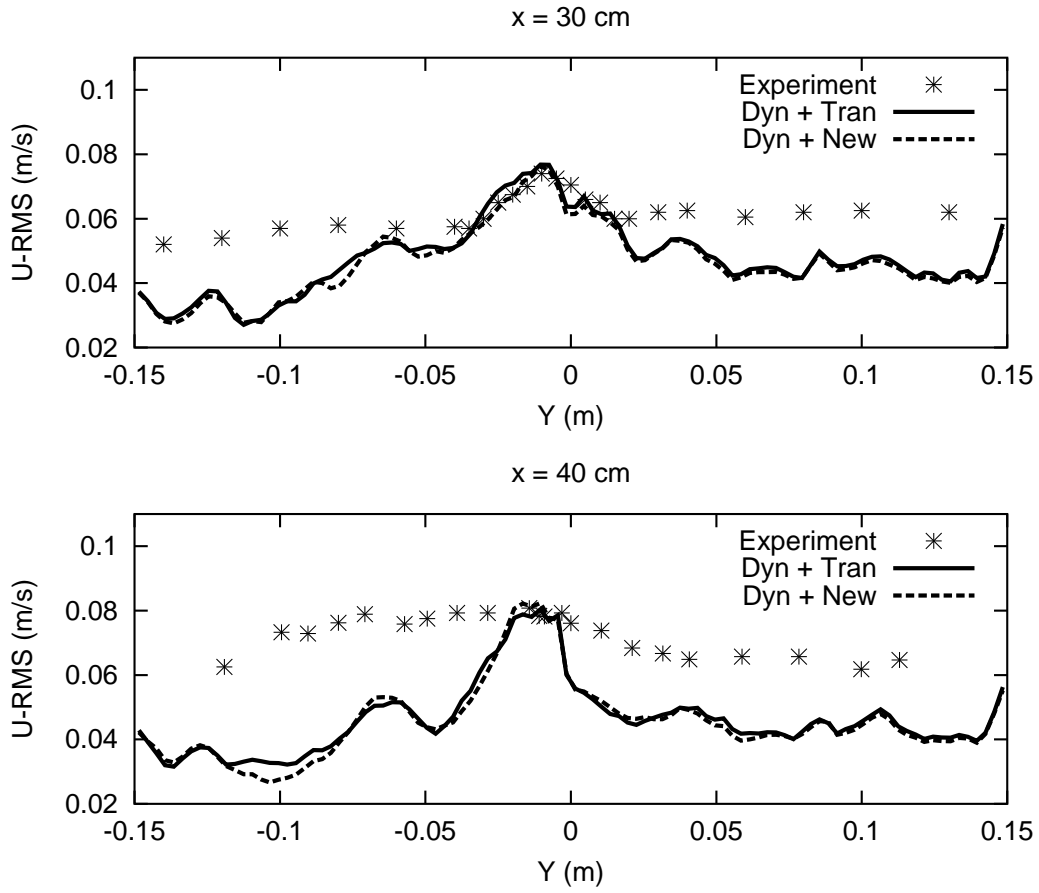


Figure 6.21: Liquid velocity fluctuations distributions at different elevations for the optimal grid with $\Delta_x = 3.5$ mm, $\Delta_y = 3$ mm and $C_L = 0.25$. Comparison between different subgrid scale models for the effect of bubbles: Tran subgrid-scale model (Dyn + Tran) and the new model (Dyn + New) described in the text. The liquid subgrid-scale model is given by the dynamic procedure of Germano applied to the Smagorinsky model.

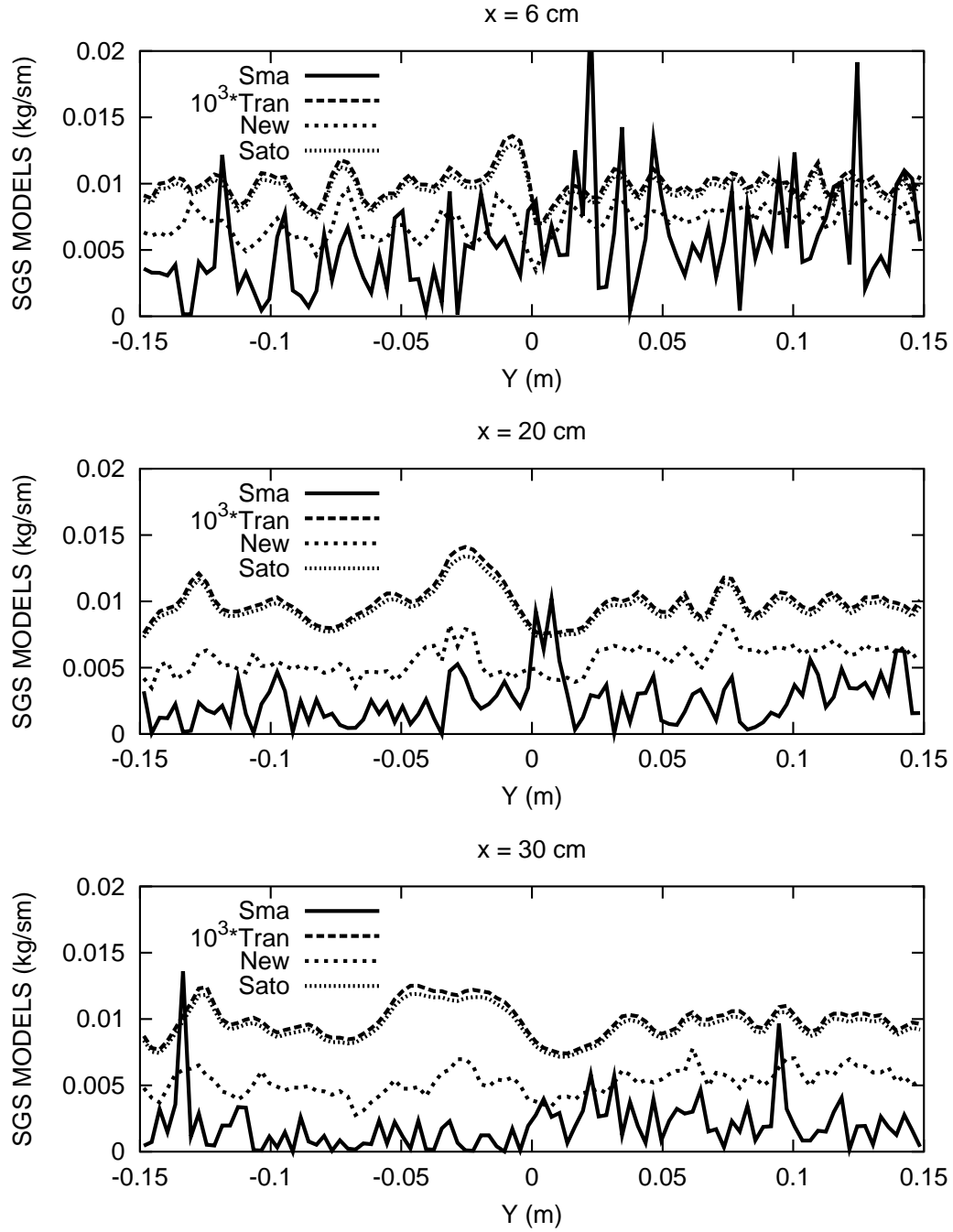


Figure 6.22: Comparison between different subgrid scale terms for bubble-induced-turbulence and the Smagorinsky term (Sma): Tran (approximated, see § 6.4.5, eq. (6.4)) term multiplied by 10^3 (Tran), the New term (New) and the Sato term (Sato).

7 Large Eddy Simulation: bubble plume

7.1 Introduction

Following the parameter studies reported in the last Chapter, in which an optimum mesh size and lift coefficient were found for a shear-driven, bubble-laden flow, the analysis is now extended to a bubble plume in which the flow is primarily buoyancy driven. Simulations are based on a series of experiments undertaken at the University of British Columbia, and reported by ANAGBO & BRIMACOMBE, 1990. These particular experiments were chosen because, at the lowest flow rates, uniform-sized air bubbles of 3 mm diameter were produced – the same as in the Roig experiment. Radial void fraction and velocity distributions were measured in the plume at several elevations, and circulation velocities in the water pool. The experimental set-up consists of a cylindrical perspex tank of 50 cm diameter filled with de-ionized water to a depth of 40 cm. The bubbles are produced by blowing air through a porous plug of 6 cm diameter, which is positioned centrally at the base of the tank. The bubble plume rises to the surface entraining liquid from the pool and generating a large-scale circulation. Measurements were taken at elevations 50, 100, 200, 300 and 380 mm above the plug. A double-contact, electro-resistivity probe, mounted on a movable carriage, was used to obtain gas fraction, bubble frequency, bubble (axial) chord lengths and bubble rise velocities in the plume. Laser-Doppler Velocimetry was used to determine the circulation velocities in the liquid pool. The simulations reported here refer to experiments carried out at the lowest gas flowrate, $\dot{Q} = 200 \text{ N cm}^3/\text{s}$ (flowrate normalized to *stp* conditions), in which a well-defined bubble swarm was observed; there was negligible coalescence or break-up, and a uniform bubble-size distribution with height was observed. Unfortunately, no turbulence data are available from these experiments.

7.2 Numerical setup

A typical mesh layout is displayed in side and plan views in Fig. 7.1. The calculations are fully three-dimensional, very *cpu* intensive, and consequently the scope of parameter studies is rather limited. Nonetheless, some variants were possible, and these are summarized in Table 7.1. Two mesh sizes have been used. Both are composed of 10 blocks, 5 below the water level and 5 above it. The central block, which contains the plume, has a uniform distribution of 4 mm meshes (37×37) in the x and y directions. Then the size of the meshes increases in the other blocks, where in the radial direction there are 15 meshes with a geometrical progression rate of 1/0.9. The grids differ only in the vertical direction: the fine grid had 133 meshes below the water surface ($\Delta_z = 3 \text{ mm}$) and 15 above it, with a geometrical progression ratio of 1.16. The coarse grid had 40 meshes below the water surface ($\Delta_z = 10 \text{ mm}$) and 13 above it, with a geometrical progression ratio of 1.07. Globally, there were $\approx 530,000$ meshes in the first grid and $\approx 200,000$ in the second, with $\Delta/d_b \approx 1.2$ and 1.8 respectively for an assumed bubble diameter of 3 mm and with $\Delta = (\Delta_x \Delta_y \Delta_z)^{1/3}$. The lift coefficient C_L varies in the range 0.15 to 0.25, conforming to the optimum choice from the shear-layer study.

As noted earlier, no turbulence data are available for these tests and the level of the inlet turbulence must be estimated from heuristic arguments. The liquid next to the inlet, which is initially at rest with $w_l(t_0 = 0) = 0.0 \text{ m/s}$, receives an impulse from the bubbles equal to their entry velocity, that is $w_l(t = t_0 + dt) = w_g = 0.1141 \text{ m/s}$. For this reason, the liquid velocity variation (fluctuation) $w_l(t) - w_l(t_0)$ is given by w_g . The used value for the liquid fluctuation is then 25% of w_g first,

which corresponds to the level measured for the faster stream in the Roig experiment (and used here for illustrative purposes only), and 100% of w_g after, which would be representative of the bubbles being produced from break-up of a blanket covering the porous plug (presumably the bubble-generation mechanism which actually took place in the tests). Most simulations employ the Smagorinski *sgs* model for the liquid phase, together with the Tran *sgs* model for the bubbles, again following the findings of the shear-layer study, but one cross-check is made with the dynamic modelling procedure together with the new *sgs* model described in §6.4.4 (Run 9 in Table 7.1).

Case name	Mesh size	Lift coefficient	Inlet turbulence	<i>sgs</i> models
Run 1	C	0.25	25%	S + T
Run 2	F	0.25	25%	S + T
Run 3	C	0.2	25%	S + T
Run 4	F	0.2	25%	S + T
Run 5	C	0.15	25%	S + T
Run 6	F	0.15	25%	S + T
Run 7	C	0.25	100%	S + T
Run 8	F	0.25	100%	S + T
Run 9	C	0.25	100%	D + N

C – Coarser grid, F – Finer grid, S – Smagorinsky, D – Dynamic, T – Tran, N – New

Table 7.1: List of calculations with various models.

A second-order, central-differencing scheme was used for the spatial discretization, while a first-order, fully-implicit, backward-differencing scheme has been employed for the time discretization. The SIMPLE-C algorithm has been employed for the pressure-velocity coupling. All the calculations have been carried out using the commercial code CFX-4.3, 1999; the interfacial forces were introduced in the user-Fortran subroutine USRSRC, and the turbulent viscosity in USRVIS. The set of equations used is the same described in Chapter 5 (5.1)-(5.12).

Only mean quantities were reported by ANAGBO & BRIMACOMBE, 1990, and these data are used here as the basis of the comparisons. All calculations were started from zero-fbw initial conditions and run until pseudo-steady fbw conditions had been established (~ 2 s) using eqs. (5.1)-(5.12); the time-step used was kept constant at $\Delta t = 0.001$ s. The calculations were then continued for a further 1 to 3 seconds in order to perform the data analysis. This consisted of separately averaging, at each time-step, the instantaneous void fraction and velocity information around the azimuth for each radial location over the horizontal planes $z = 100, 200, 300, 380$ mm, and then time-averaging these data. The radial distributions thus obtained can be compared directly with the time-averaged experimental data. (The data at $z = 50$ mm are excluded as being untrustworthy, since they will be influenced by the bubble generation mechanism.)

7.3 Results of the calculations

First, the effects of the lift coefficient combined with the two meshes were analyzed. In Fig. 7.2, the void fraction distribution appears to depend strongly on C_L , that took the values 0.25, 0.2 and 0.15, for Runs 1, 3 and 5, respectively. These computations refer to the coarse-mesh configuration

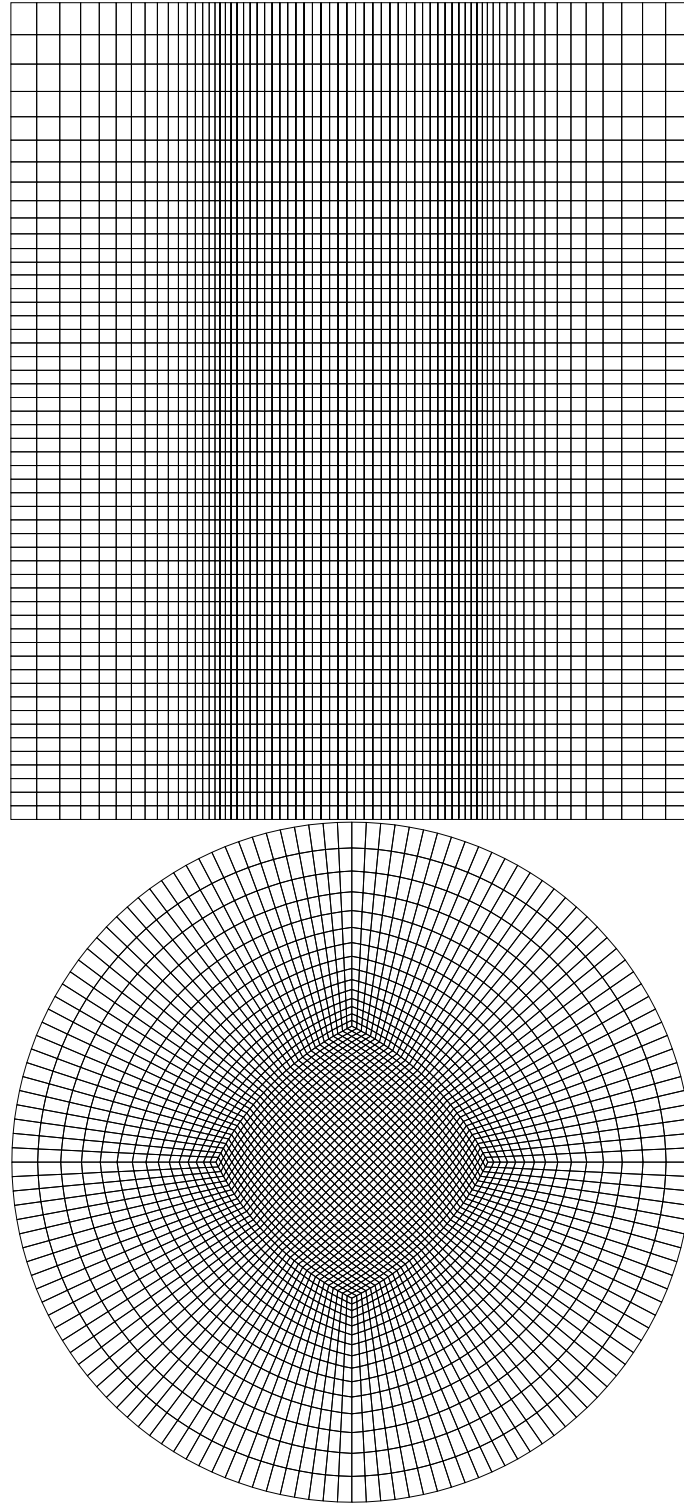


Figure 7.1: Side and plan view of a mesh layout

with $\Delta/d_b \approx 1.8$. The spreading is slightly more pronounced for higher values of C_L , but the most important effect is at the centreline, where at $z = 300 \text{ mm}$ a dip is present, at least for the larger values of C_L . Seemingly, the stronger lift force has led to an exaggerated migration of the bubbles away from the axis of the plume. In all cases the integrated volume flux is correct, and equal to that at inlet as expected.

The velocities, shown in Fig. 7.3, do not depend strongly on the lift force, as was also noted by SMITH, 1999 using a RANS approach. A common feature for all the calculations is that the entrainment of water into the plume is not well reproduced, resulting in an underprediction of the velocities at the edge of the plume for each elevation. In contrast, at the centreline, the velocity is overestimated, with the exception of the first measurement station ($z = 100 \text{ mm}$). Analogous computations performed with the fine mesh ($\Delta/d_b \approx 1.2$) follow the same general trends, but the centerline bubble velocities are higher (Fig. 7.5) and consequently the void fraction distribution (Fig. 7.4) has a more pronounced dip on the axis. Concerning the spreading of the plume, the variation with respect to the coarser mesh is only marginal (for corresponding values of C_L).

The increase of the inlet turbulence in Run 7 produces a reduction of the velocities (Fig. 7.7), and a consequent increase of the void fraction on the axis (Fig. 7.6) where the dip disappears. The spreading is better predicted, and the void fraction profile, in general, agrees better with the experimental data.

The influence at the sub-grid level studied next is not striking, though the Germano *sgs* model (Run 9) produces somewhat better comparisons than those obtained with the Smagorinski model (see Figures 7.8 and 7.9 for void fraction and velocity distributions, respectively).

The results deteriorate if a finer mesh is used (Run 8). Most noticeable is the reappearance of the dip on the axis, indicating overprediction of the bubble dispersion. The details of the spreading rate for the different runs are given in Table 7.2. It appears clearly that the best results, that are quite similar, are given by Runs 9 and 7. It can be noted that as the distance from the inlet increases, the spreading rate decreases: the same trend has been found for the Random Dispersion Model (see Table 3.1). The only exception is at $z = 380 \text{ mm}$ for Runs 2, 4 and 6, probably because of the stronger interaction of the gas surface with the pool.

The turbulent intensities for Runs 1, 2, 7 and 8 are shown in Figure 7.10. The following comments can be made:

- a comparison between calculations with the same mesh (Runs 1 vs. 7 and 2 vs. 8) shows that the intensities are higher for Runs with higher inlet turbulence;
- given the level of inlet turbulence, the intensities are higher for Runs with coarser grids (1 vs. 2 and 7 vs. 8), as was already stressed in Chapter 5 in the case of grid turbulence;
- at $z = 300 \text{ mm}$, the turbulence is stronger than at the other elevations, which can be explained by the stronger influence of the nearby liquid/air surface;
- the radial profile of the intensities follows the spreading of the bubble plume: in fact the border of the plume, according to the void fraction measurements, is at $x \approx 0.04, 0.06$ and 0.08 m for $z = 100, 200, 300 \text{ mm}$, respectively.

In Fig. 7.11, appears a direct comparison of the intensities at the three elevations for Runs 7 and 9. As was noticed before, the turbulence at 300 mm is higher than downstream, and this is valid for both the calculations. The bubble-induced turbulence effects, as represented by the Tran terms in the equation for μ_t (6.1) and by the new term (6.3), produce very similar results. In detail, for

Run 9, the centreline intensities are slightly lower than for Run 7. The intensities increase at 300 *mm* next to the wall because of the liquid recirculation induced by the presence of the surface and the wall itself. It is interesting to note in Fig. 7.12 that the distribution of the rate of strain tensor $\sqrt{2S_{ij}S_{ij}}$ (with summation over *i* and *j*), with $S_{ij} = 0.5(\partial_i u_j + \partial_j u_i)$, which appears in the Smagorinsky *sgs* model (6.3), is correctly peaked in the region of highest shear, which is the plume/pool interface. The distance between the nearly symmetric peaks increases with *z* because of the plume spreading, as shown by the vertical lines which indicate the end of the plume at different elevations taken from Fig. 7.8. At *z* = 380 *mm* the interaction with the surface of the pool makes the distribution more uniform. The dip in the middle of the plume where the void fraction is maximum indicates that the production of turbulence by shear is replaced by another mechanism, the so called 'pseudo-turbulence'.

Finally, in Fig. 7.13, the power spectra of the velocity fluctuations in the vertical direction for Runs 1, 2, 7 and 8 are shown. They are compared with the $-8/3$ slope measured by LANCE & BATAILLE, 1991 in the case of grid turbulence in the presence of bubbles. The hierarchical distribution at large scales (low frequencies) from the highest to the lowest turbulence levels (Runs 7, 8, 2, 1 respectively), reflects what has been shown in Fig. 7.10. It is difficult to assert if there is a real correspondence with the measured slope, since more data would have been necessary. Probably, the mechanism of transfer of energy is not well reproduced by the simulations because the *sgs* models are still too simplistic, in particular for the effect of the dispersed phase.

Case No.	Model Identifier	Elevation (mm)			
		100	200	300	380
0.	Expt.	100	100	100	100
1	Run 1	96	89	86	89
2	Run 2	91	83	81	100
3	Run 3	92	84	81	85
4	Run 4	90	80	75	100
5	Run 5	90	82	80	82
6	Run 6	87	73	71	100
7	Run 7	105	97	90	91
8	Run 8	92	85	80	97
9	Run 9	108	97	94	94

Table 7.2: A comparison of plume spreading statistics for various model assumptions

7.4 Conclusions

Three-dimensional bubble plume simulations have been performed with the LES model of turbulence, using different combination of mesh, lift coefficient and *sgs* models. Parameter studies carried out in the context of the mixing layer simulation (and reported in the previous chapter) showed that the optimum grid size has to be such that the ratio of the cut-off filter to the dispersed-phase length scale falls within the range of $1.2 < \Delta/d_b < 1.8$, with slightly better results for the higher ratio. Forcing the cut-off length scale to coincide with that of the dispersed phase permits the interaction with the smallest-resolved scale to be captured without additional approximation, in line with the Scale Similarity Principle of BARDINA ET AL., 1980, but in contradiction to Tran's

(TRAN, 1997) arguments of the necessity to use a computational grid much coarser than the diameter of the bubbles; that argument should apply to the case of micro-bubbles. The simulations also revealed the importance of considering the lift force on the bubbles: good comparisons with experimental data were obtained with $C_L = 0.25$.

The investigation has also brought new insights into subgrid-scale modelling for bubbly flows. The conventional Smagorinsky (1963) model with $C_s = 0.12$ performs quite well, and gives results almost similar to those returned by the dynamic procedure of GERMANO ET AL., 1991. In fact, it has been found that the averaged C_s values obtained with the latter converge towards $C_s = 0.12$, and no backscatter effect of energy was noticed. The modifications to the subgrid-scale model to account for bubble-induced turbulence effects in the ways proposed by SATO ET AL., 1981 or MILELLI ET AL., 2001 were not implemented because the turbulent quantities were not measured and the mean variables are not affected.

Application of the model to a bubble plume, in which the flow is buoyancy-driven rather than shear-induced, has generally confirmed the optimum value for the lift coefficient, and the importance of the level of the inlet turbulence on bubble dispersion. Evidence of a universal scale for the filter-width (i.e. mesh-size) to bubble-diameter ratio is less conclusive, and better comparisons were obtained with a coarse mesh in the vertical direction. Nonetheless, though there remain some outstanding discrepancies between prediction and measurement regarding the detailed void fraction and velocity profiles, the overall plume spreading is reproduced quite well with respect also to the RANS calculations performed in Chapters 2 and 3, with the advantage that using LES it is no longer necessary to introduce an empirical turbulent dispersion force into the momentum equations, as advocated by DAVIDSON, 1990 and LOPEZ DE BERTODANO, 1992. Moreover, the number of empirical constants are reduced to the minimum: the lift coefficient and the Smagorinsky constant (though not for the dynamic procedure).

It is difficult to judge the correctness of the turbulent quantities, since they are not described in the paper of ANAGBO & BRIMACOMBE, 1990. Qualitatively, they are in agreement with the expectations and with the results of the previous investigations (Chapters 5 and 6), but the details have to be checked. In particular, the transfer of energy from the large to the smaller scales is not described satisfactorily and this is due to the roughness of the *sgs* models: the Smagorinsky-type model for the liquid is too simplistic for this kind of situation, and the *sgs* models for the effect of the dispersed phase are still in their infancy. Nevertheless, the perspectives are encouraging.

Finally, concerning the numerical aspect, the *cpu* time needed for the simulations performed here is quite larger than for an equivalent three-dimensional RANS simulation, but on the other hand the amount of information that can be retrieved is also larger than in any standard RANS calculation. The simulations have been run with a single-processor machine, because the code CFX-4.3, 1999 was not yet ready to be parallelized, even though works in this direction are in progress. Is it plausible to assume that in the new implementation of the code the parallel version will be available and this will reduce considerably the computational time and increase the feasibility of the approach.

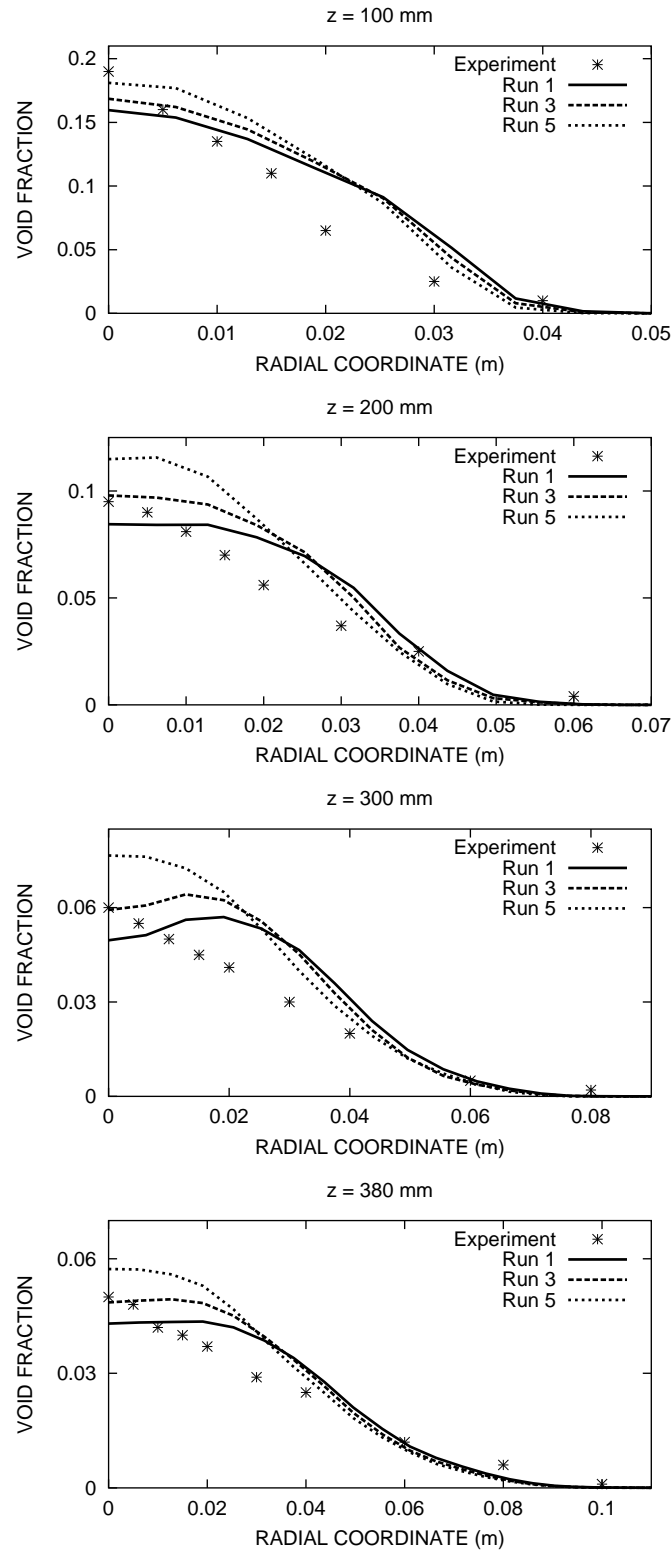


Figure 7.2: Computations with coarse mesh ($\Delta/d_b \approx 1.8$): void fraction distributions at different elevations for Runs 1, 3, 5 with $C_L = 0.25, 0.2, 0.15$, respectively. Inlet turbulence at 25%, $C_s = 0.12$.

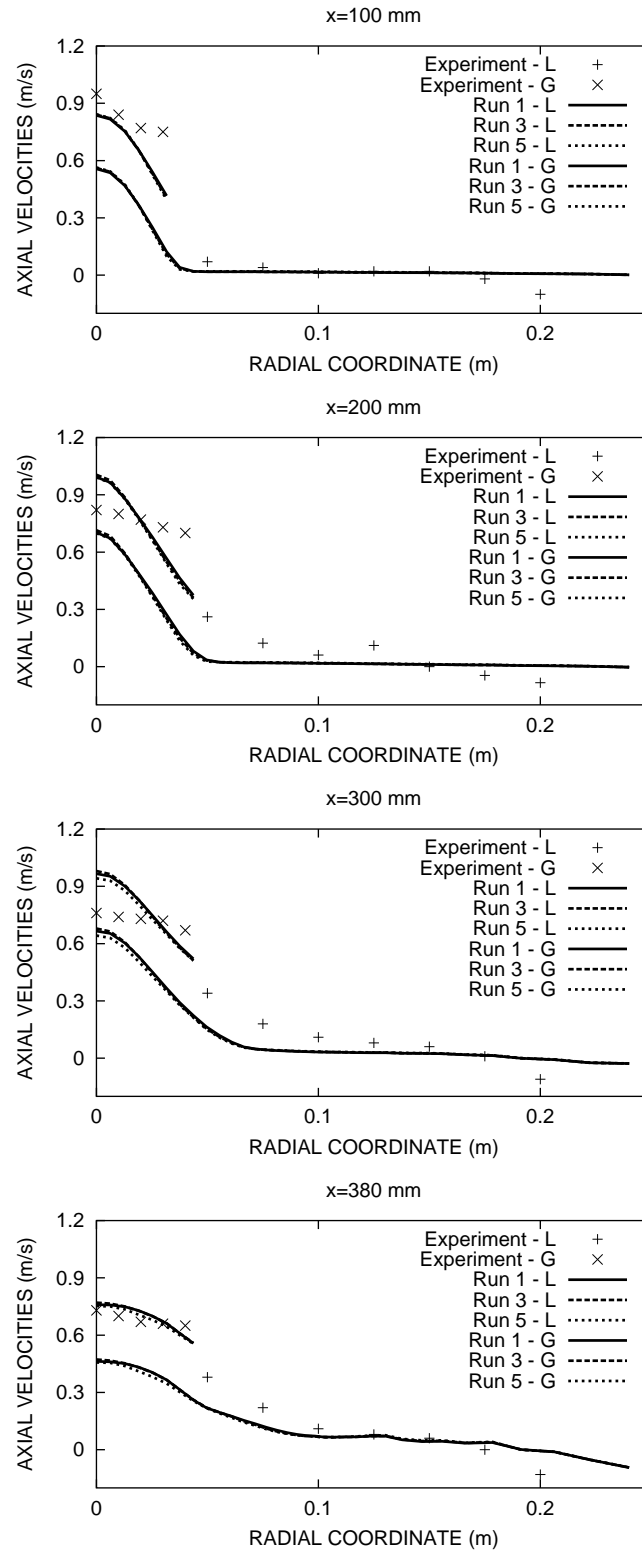


Figure 7.3: Computations with coarse mesh ($\Delta/d_b \approx 1.8$): gas and liquid velocity distributions at different elevations for Runs 1, 3, 5 with $C_L = 0.25, 0.2, 0.15$, respectively. Inlet turbulence at 25%, $C_s = 0.12$.

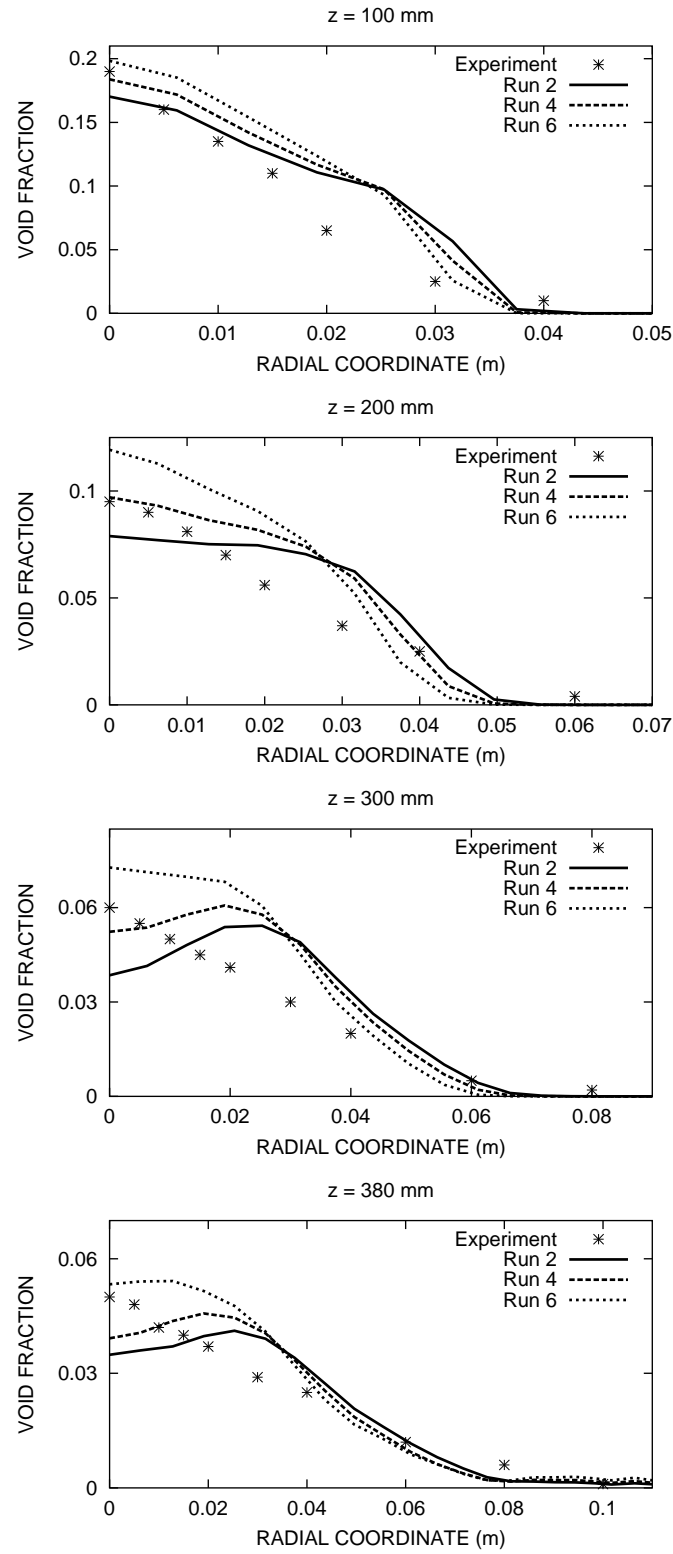


Figure 7.4: Computations with fine mesh ($\Delta/d_b \approx 1.2$): void fraction distributions at different elevations for Runs 2, 4, 6 with $C_L = 0.25, 0.2, 0.15$, respectively. Inlet turbulence at 25%, $C_s = 0.12$.

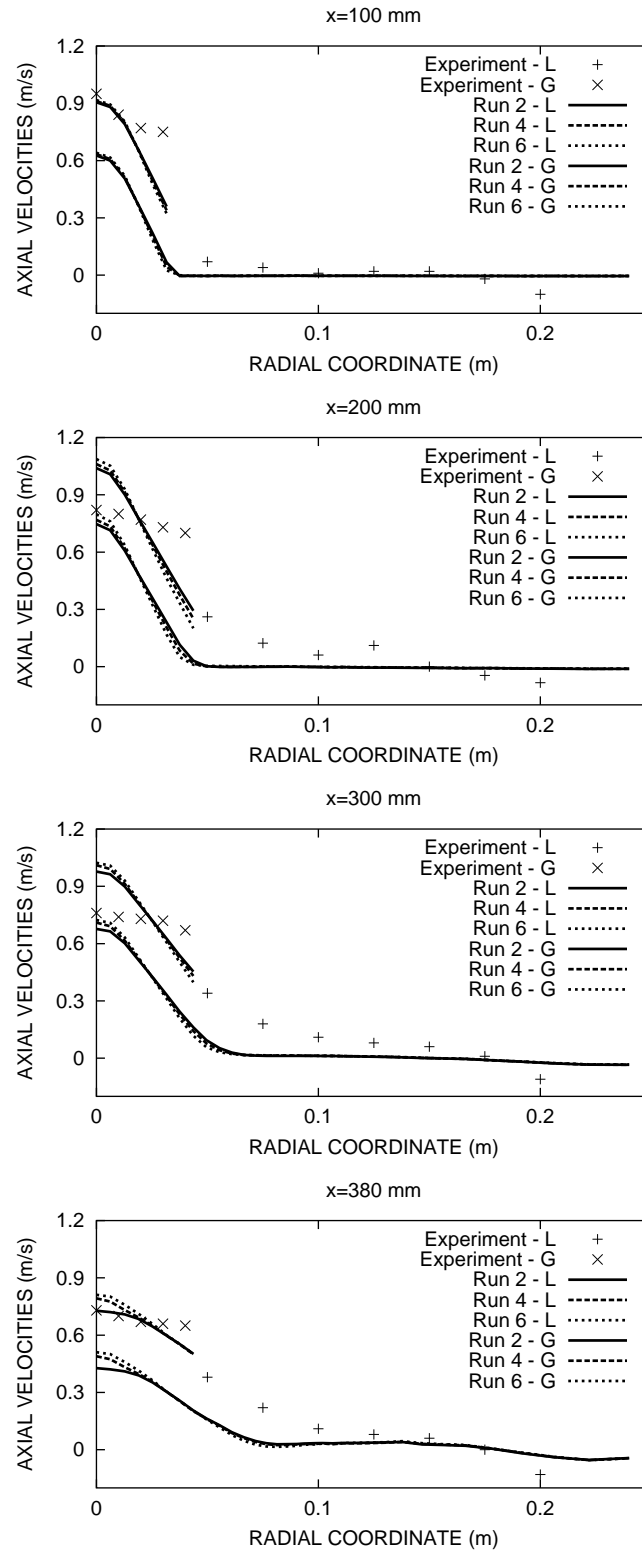


Figure 7.5: Computations with fine mesh ($\Delta/d_b \approx 1.2$): gas and liquid velocity distributions at different elevations for Runs 2, 4, 6 with $C_L = 0.25, 0.2, 0.15$, respectively. Inlet turbulence at 25%, $C_s = 0.12$.

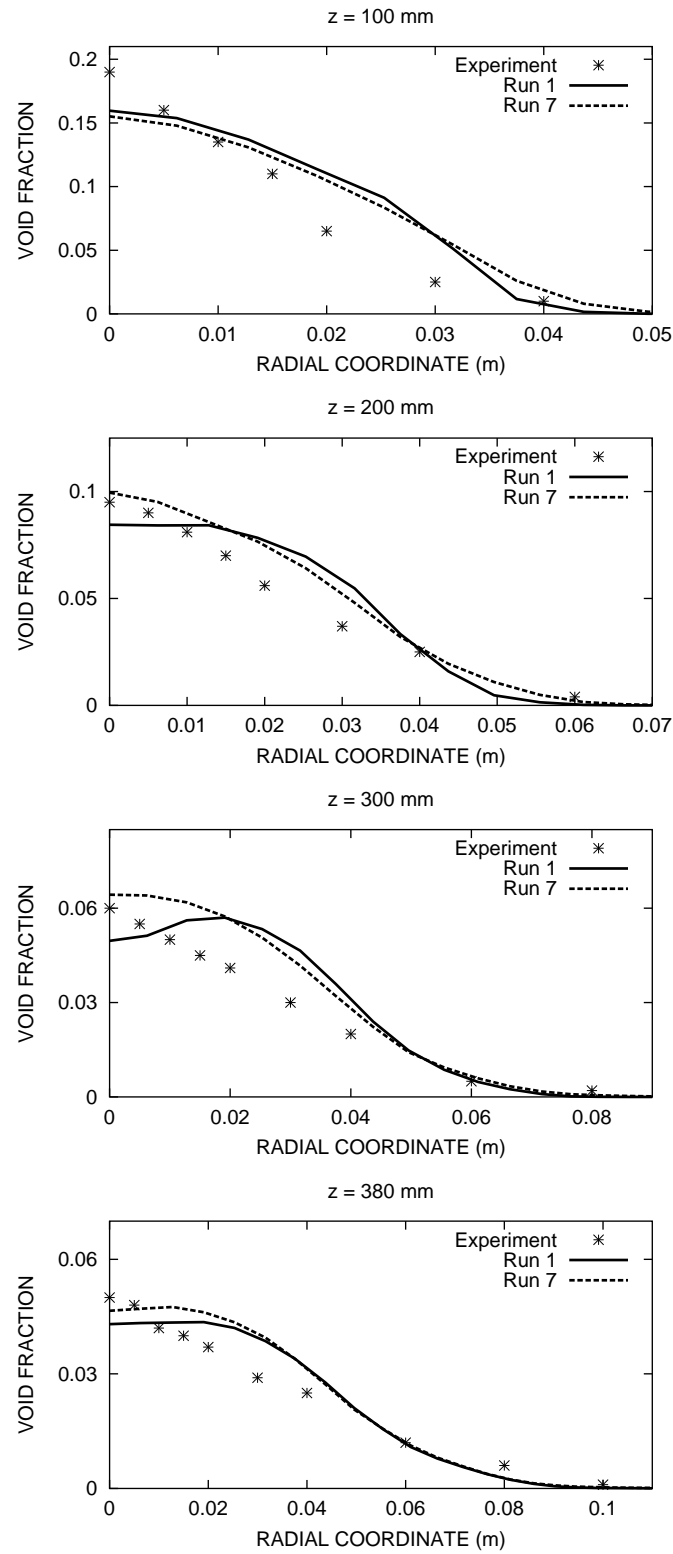


Figure 7.6: Effect of high inlet turbulence: void fraction distributions at different elevations for Runs 1, 7 with $C_L = 0.25$. Inlet turbulence at 25% and 100%, respectively and $\Delta/d_b \approx 1.8$. $C_s = 0.12$.

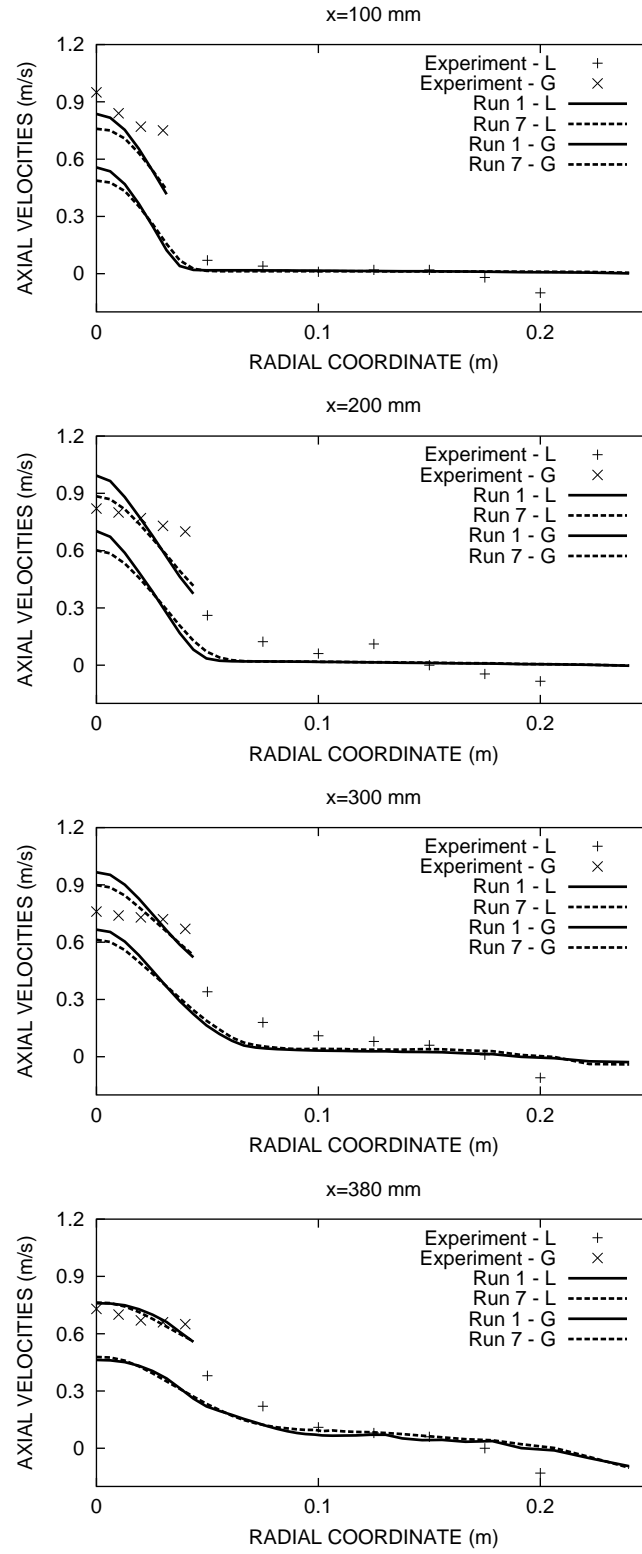


Figure 7.7: Effect of high inlet turbulence: gas and liquid velocity distributions at different elevations for Runs 1, 7 with $C_L = 0.25$. Inlet turbulence at 25% and 100%, respectively and $\Delta/d_b \approx 1.8$. $C_s = 0.12$.

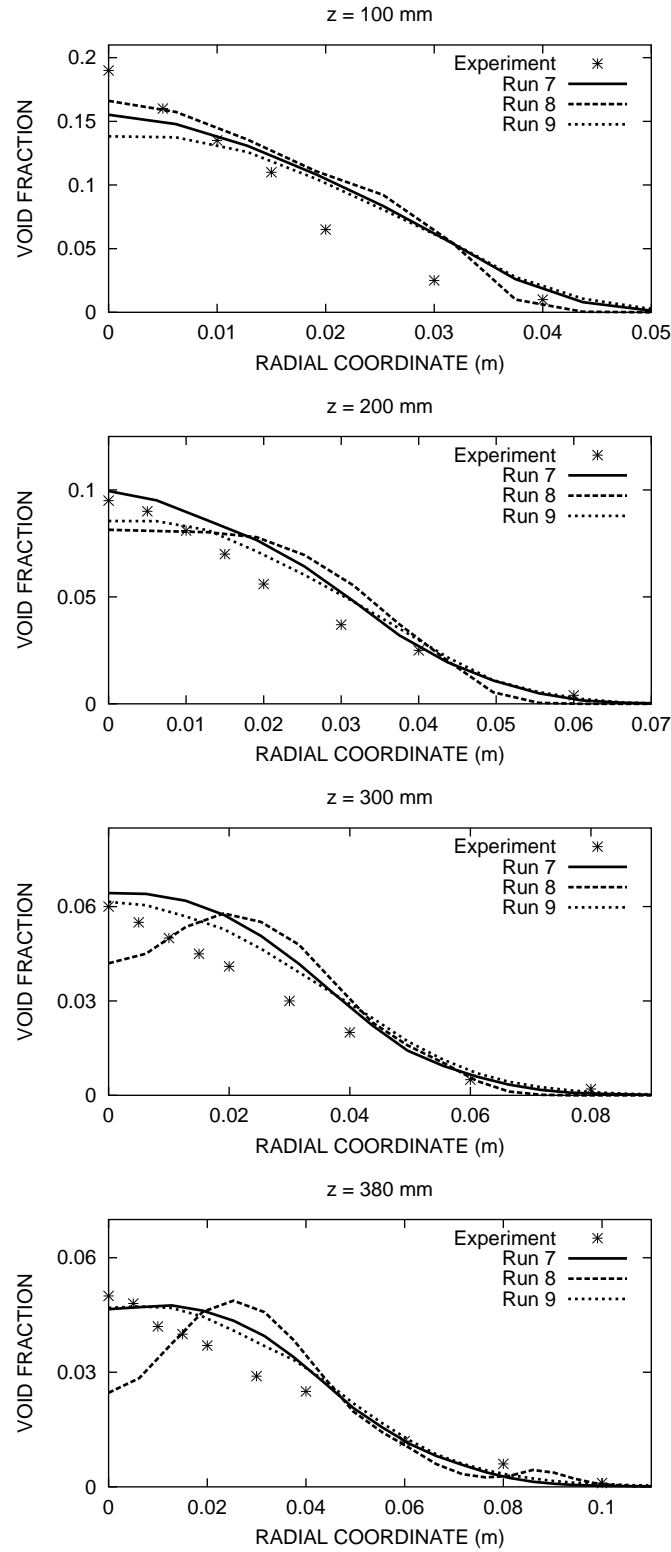


Figure 7.8: Influence of subgrid-model and grid size: void fraction distributions at different elevations for Runs 7, 8, 9 with $C_L = 0.25$ and inlet turbulence at 100%. $\Delta/d_b \approx 1.8$ and for Runs 7 and 9, $\Delta/d_b \approx 1.2$ for Run 8. $C_s = 0.12$ for Runs 7 and 8, dynamic procedure for Run 9.

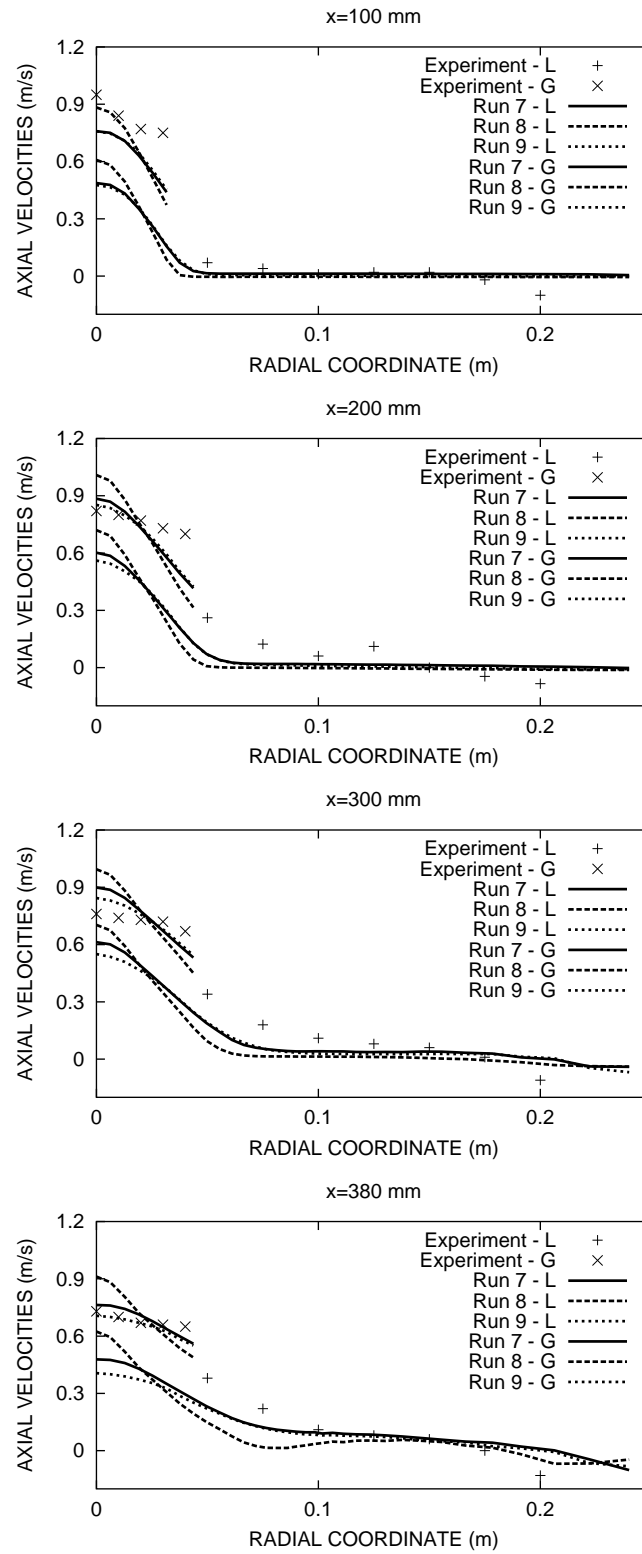


Figure 7.9: Influence of subgrid-model and grid size: gas and liquid velocity distributions at different elevations for Runs 7, 8, 9 with $C_L = 0.25$ and inlet turbulence at 100%. $\Delta/d_b \approx 1.8$ and for Runs 7 and 9, $\Delta/d_b \approx 1.2$ for Run 8. $C_s = 0.12$ for Runs 7 and 8, dynamic procedure for Run 9.

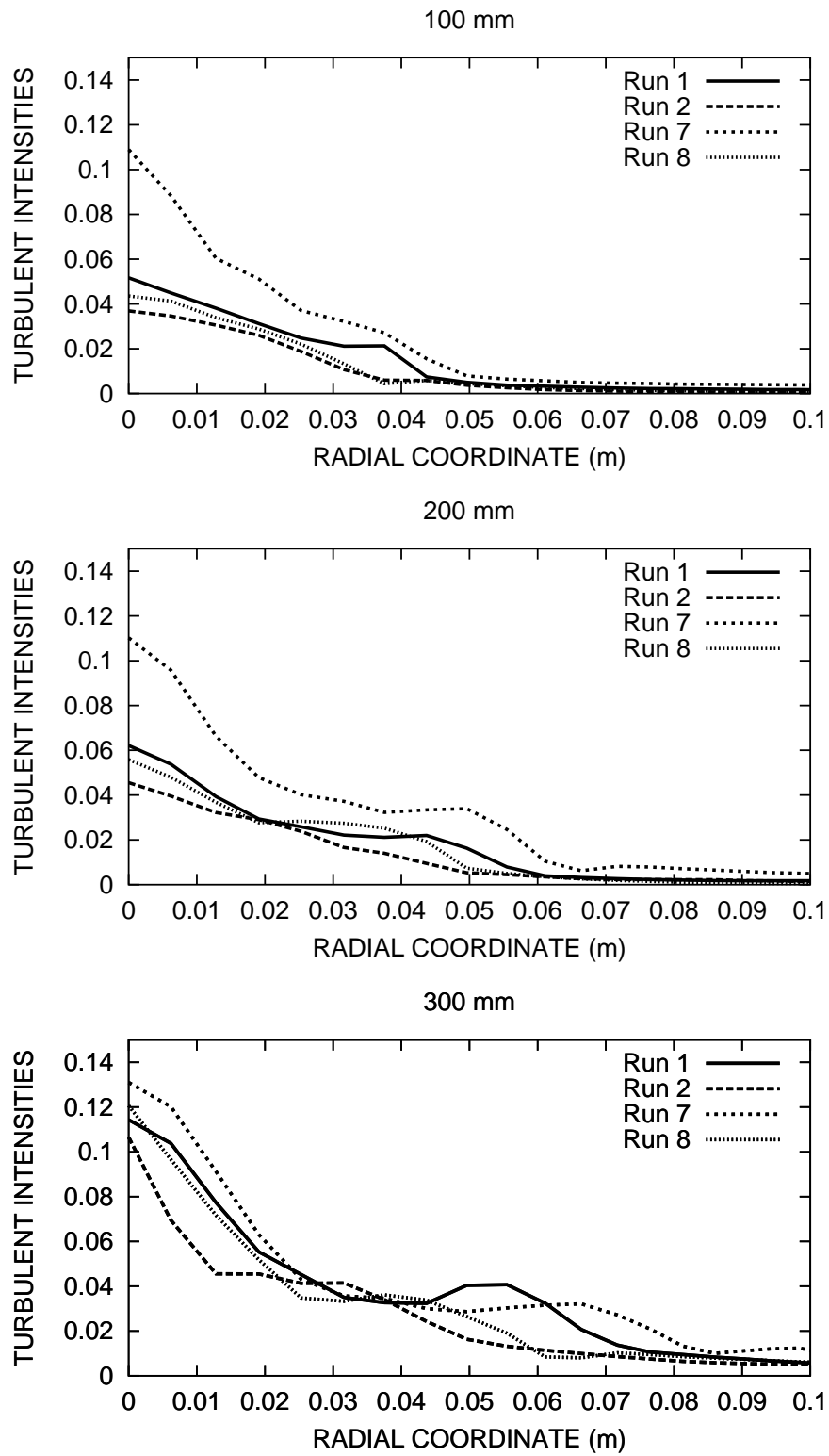


Figure 7.10: Vertical turbulent intensities at different elevations for Runs 1, 2, 7 and 8 with inlet turbulence at 100% for Runs 7, 8 and 25% for Runs 1, 2. $\Delta/d_b = 1.8$ and for Runs 1 and 7, $\Delta/d_b = 1.2$ for Run 2 and 8. $C_L = 0.25$ and $C_s = 0.12$.

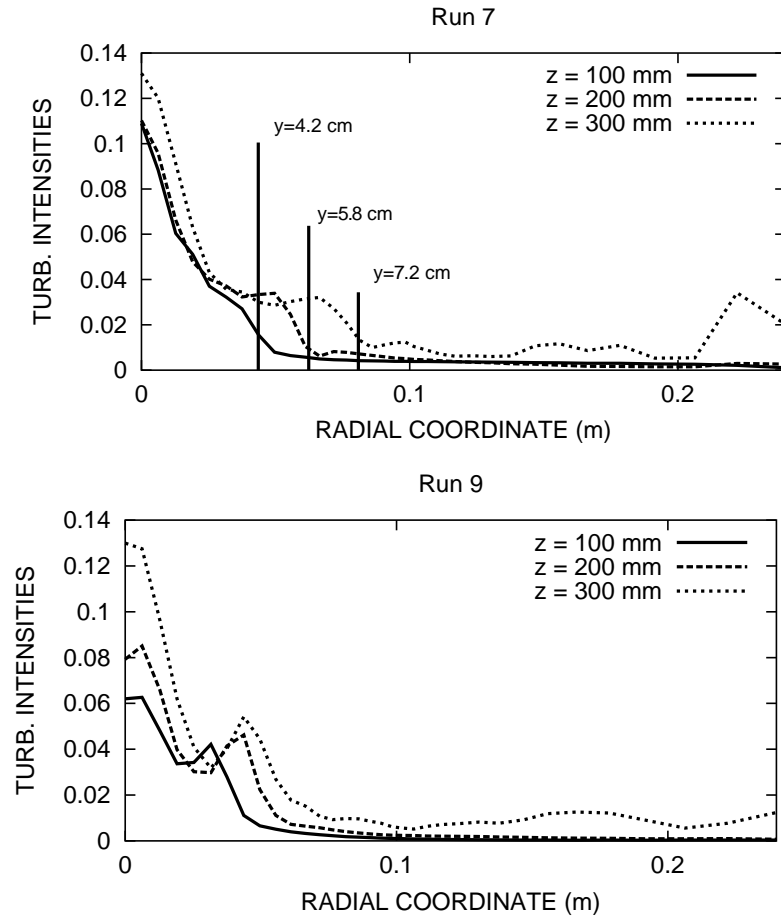


Figure 7.11: Vertical turbulent intensities at different elevations for Runs 7 and 9 with inlet turbulence at 100%, $\Delta/d_b = 1.8$ and $C_L = 0.25$. $C_s = 0.12$ for Run 7 and dynamic procedure for Run 9. The end of the plume at $z = 100, 200, 300$ mm respectively, is indicated by the vertical lines.

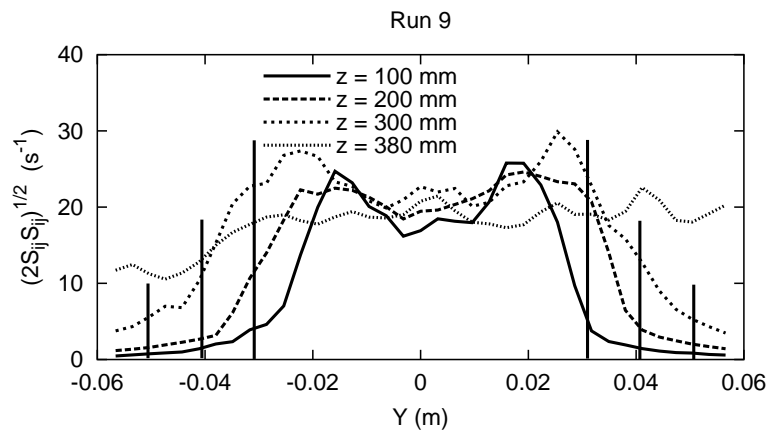


Figure 7.12: Distribution of the rate of strain tensor for Run 9 at different elevations. The vertical lines indicate the end of the plume at $z = 100, 200, 300$ mm from the centre to the right (and left) respectively.

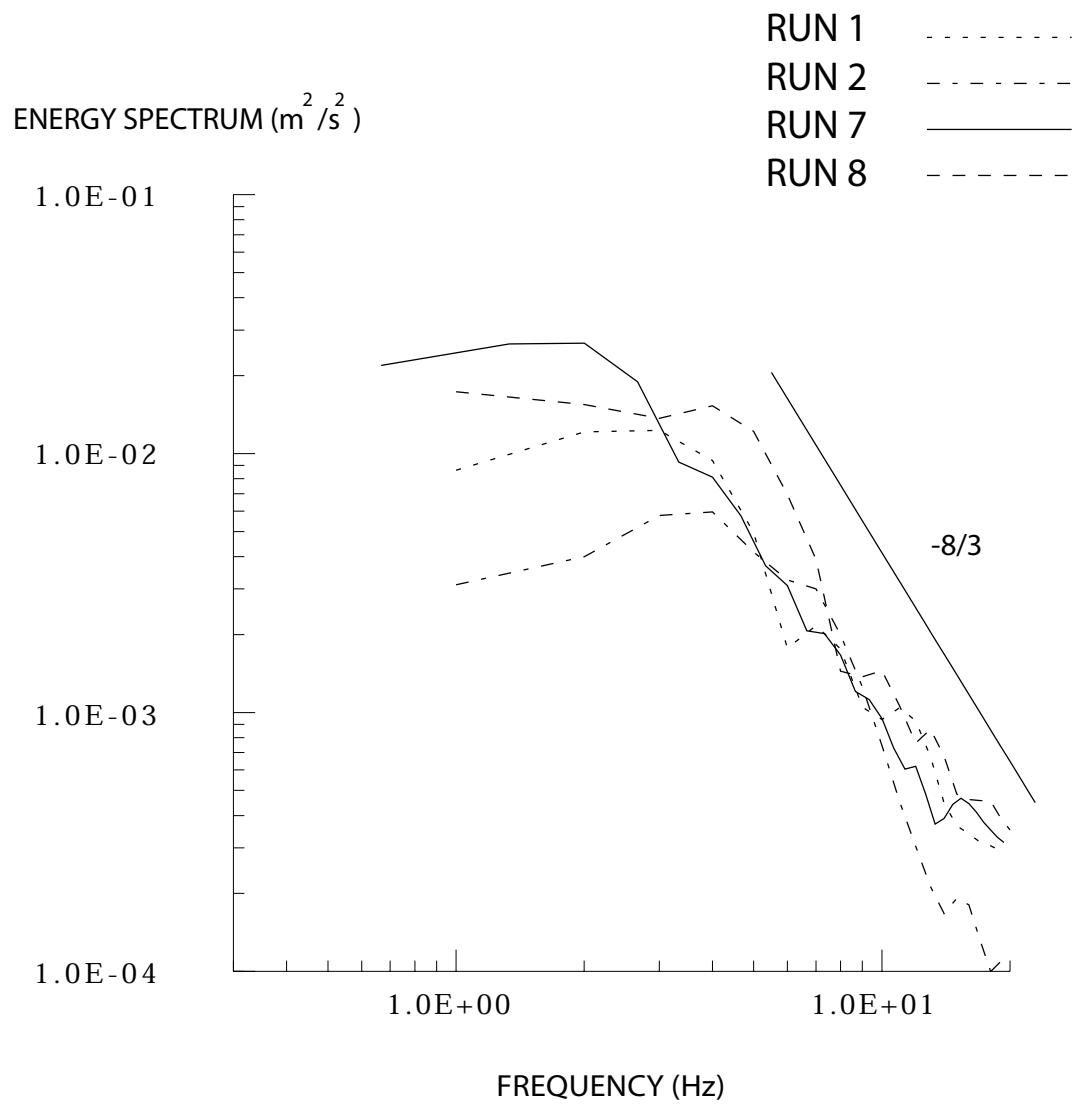


Figure 7.13: Power spectrum of axial velocity fluctuations at the centreline ($z = 200 \text{ mm}$) for Runs 1, 2, 7 and 8, compared with the $-8/3$ slope described by LANCE & BATAILLE, 1991.

8 Conclusions and future perspectives

*"The Road goes ever on and on
 Out from the door where it began.
 Now far ahead the Road has gone,
 Let others follow it who can !
 Let them a journey new begin,
 But I at last with weary feet
 Will turn towards the lighted inn,
 My evening-rest and sleep to meet."*
 J.R.R. Tolkien (Lord of the Rings)

The analysis of a turbulent bubble plume, both in confined and unconfined environments, has been the subject of many investigations in the past. Many papers have been published, but recently, for some reason, the number of works on the subject is noticeably decreasing. This is surprising, since a lot of information is still missing, in particular on the role played by turbulence, and further studies seem to be necessary. A deeper understanding would be useful not only to the nuclear industry (which gave the impetus for this work), but also to the metallurgical and environmental fields. The available literature (on confined bubble plumes only) has been collected and critically analyzed in order to define a fruitful research path (Chapter 1).

8.1 Summary and conclusions

The standard approach to the problem starts with the use of the Reynolds-Averaged Navier-Stokes (RANS) equations in order to reduce the *cpu* overhead, but this introduces the so-called closure problem. The Reynolds stress tensor in fact has to be modelled, and this represents the major difficulty, at least for two-phase flows. The most often used turbulence model in the framework of the eddy viscosity approach is the $k - \epsilon$ model with all its variants, which requires two extra equations to be solved: one for the turbulent kinetic energy (k_t) and another for the turbulent dissipation (ϵ_t). While for single-phase flows this model has been widely tested and successfully accepted, it is considered as inadequate in the case of multi-phase flow. In particular, for our case, the second (dispersed) phase generates extra turbulence and dissipation, the effects of which have to be included, often by the use of *ad hoc* adjustments and the inclusion of empirical parameters. The results given by different models used in the literature are compared with the experimental data published by ANAGBO & BRIMACOMBE, 1990 (Chapter 2).

Another difficulty with the RANS approach is the necessity of introducing the interfacial forces in the momentum equations. Standard correlations exist for the drag coefficient, but the added mass and the lift coefficients need more careful investigation. Moreover, the lift force alone is not able to explain the dispersion of the bubbles, which is partially due to the effect of the turbulent eddies in the liquid. This force is usually included in a rather empirical way, and different versions exist. An attempt to bypass the inclusion of a Turbulent Dispersion Force (TDF) has been carried out by the introduction of the concept of a Random Dispersion Model, and the results are given in Chapter 3. The effect was included in the equations via a purely statistical mechanism, introducing in the lift and drag force fluctuations with zero mean and variance proportional to the local turbulent kinetic energy. This approach does not require any empirical coefficient, and assumes isotropy of the

fluctuations which is already implicit in the $k - \epsilon$ formulation. The results show that this method can replace the empirical Turbulent Dispersion Force, but some fundamental limitations remain, as a result of the basic approach to the problem. All the $k - \epsilon$ -like models are originally single-phase models, and the corrections we can make are only patch-ups. Besides, the hypothesis of turbulence isotropy has still to be proved, since there are only a few measurements available in the literature, and even these are in contradiction to each other. More advanced turbulent models are required, but the Reynolds Stress Model (RSM) for instance is quite delicate and it is often difficult to obtain a solution even for single-phase applications. To the author's knowledge there is no example of RSM in turbulent two-phase flow for a transient calculation with a commercial CFD code.

Therefore, we explored the use of Large Eddy Simulation of turbulence (LES) for two-phase flow. In this approach, the large scales of turbulence are directly resolved, whereas the smallest ones are modelled. The idea behind this implementation is to allow the bubbles to directly interact with eddies which have at least the same size, but not with the smaller ones because these are not responsible for bubble dispersion. In this way, the large-scale fluctuations are directly calculated and it is not necessary to impose their isotropy. The model has been implemented into the CFD code CFX-4 and a single-phase test case has been run to validate it firstly. It was the first time that this approach was used in the code for a highly buoyant flow (thermal plume), and the simulations gave good results for both mean and turbulent quantities (Chapter 4) compared with the experimental data of GEORGE ET AL., 1977.

In the case of two-phase flow, a new fundamental problem arises: the definition of the mesh size (filter width) compared with the bubble diameter and the turbulent length scales. In fact, since the equations are already volume-averaged, the cut-off filter must not be smaller than the length-scale characteristic of the dispersed phase, i.e. the bubble diameter. At the other extreme, the mesh should be much larger than the bubble diameter to ensure that there are enough bubbles in each computational cell to produce good statistics. This poses practical limitations to the simulations in the case of large bubbles ($d_b \geq 1\text{ mm}$) because the mesh might become too coarse in comparison with other length-scales of importance. Before starting with the bubble plume simulation, intermediate steps were considered. The grid turbulence problem was first analyzed (Chapter 5) in two dimensions. The relative simplicity of the setup permitted a parametric study of the behaviour of turbulence with respect to mesh size. The results were compared with the experiment data of LANCE & BATAILLE, 1991, and it was found that the turbulence intensities increase with mesh size, and this suggests an optimum mesh not larger than two bubble diameters. The explanation is that while a coarse mesh cannot capture all the important scales involved in the flow, requiring most of them to be modelled and not directly calculated, a mesh almost coinciding with the length-scale of the dispersed phase (bubble diameter) permits the interaction of the bubbles (first unresolved scale) with the smallest resolved scales. The idea recalls the Scale-Similarity Principle of BARDINA ET AL., 1980. This conclusion needs to be confirmed and generalized for different bubble sizes.

In order to obtain a more comprehensive overview of the problem with different types of flow a turbulent shear flow with a low percentage of bubbles has been simulated, and the results compared against the experimental data of ROIG, 1993 (Chapter 6). The advantage of this kind of flow is that it can be considered as statistically two-dimensional, which means that some important features can be captured, even with 2D simulations. The results showed good agreement with the experiment, especially in the centre of the domain where the contribution to turbulence from shear is strongest, and less outside the shear layer, where probably the turbulence is more bubble-induced than shear-induced. This implies the necessity of a more detailed study about bubble-induced turbulence (or pseudo-turbulence), and its introduction in the equations. A first step in this direction was the introduction of a new subgrid model for the bubble-induced turbulence which has been successfully tested here with the advantage of having no empirical parameters. Also made evident was the

importance of the lift force, which has to be included and whose coefficient has to be tuned. For this case, the dynamic procedure of GERMANO ET AL., 1991, was introduced and tested for the first time in two-phase flow. Results were in good agreement with those obtained with the classic SMAGORINSKY, 1963 model.

The final step was the simulation of a free bubble plume with various model configurations (Chapter 7). For the investigated cases, at high void fraction, the effect of bubble-induced turbulence should be dominant. In fact, here the turbulence is driven by the bubbles, while in the shear-flow situation, the bubbles are immersed in the liquid flow and contribute only partially to turbulence generation. Unfortunately, the turbulent quantities were not measured in the experiment of ANAGBO & BRIMACOMBE, 1990, and the mean quantities are not strongly affected by the different subgrid models. Therefore, definitive conclusions could not be drawn. Globally, the LES approach has interesting properties because it reduces empiricism to a minimum. However, the lift coefficient has to be tuned. Although for both the shear-flow and the bubble-plume calculations performed the optimum was found to be the same ($C_L = 0.25$, confirming the results of LANCE & LOPEZ DE BERTODANO, 1995 for deformable bubbles), and the optimum mesh size was found to be between 1.5 and 2 times the bubble diameter, these values may well not be adequate for other bubble sizes. No other empirical constant is present in the equations since even the Smagorinsky constant could be calculated using the dynamic procedure of GERMANO ET AL., 1991.

8.2 Suggestions for future work

A clean bubble plume experiment in which turbulence quantities are directly measured does not exist yet, and this is a big disadvantage. In the meantime, a study of the influence of the mesh size on the turbulence level in the presence of bubbles of different diameters should be undertaken because in the present work the diameter was constant and equal to 3 mm.

Concerning the CFD code CFX-4.3, 1999 (and its previous versions), there are some limitations due to the fact that it is a general-purpose code and it was not created for such a specific problem. For example, in spite of the fact that most of the time an accurate second-order scheme has been used, it is only possible to solve the equations in physical space, while classically the LES model has been developed for the phase space, and there it would be easier to define the cut-off filter independently from the mesh size.

The added mass force that we used had a constant coefficient, but dependence on the void fraction has been demonstrated in previous studies. The possibility of having a correct description of the added mass force will lead to a better estimation of the effects of pseudo-turbulence, which is fundamental for this kind of flow, as has been widely demonstrated experimentally (LANCE & BATAILLE, 1991, for instance). It would also be better to introduce a model for bubble breakup and coalescence; here we had to assume perfectly spherical bubbles, which is an ideal assumption. Moreover, it would be interesting to study the interaction of the free plume with the surface of the pool, because it might be as important as the definition of all the forces in the momentum equation. To the author's knowledge, no analytical study has been undertaken on this subject.

Concluding, this work can be considered just as a starting point in the direction of Large Eddy Simulation of turbulence for two-phase flows. Further developments have still to be made, but the perspectives look promising.

References

- Anagbo, P. E. & Brimacombe, J. K. (1990) *Plume Characteristics and Liquid Circulation in Gas Injection Through a Porous Plug*. Metallurgical Transactions 21B, 637-647, 1990.
- Anglart, H., Andersson, S., Podowski, M. Z. & Kurul, N. (1993) *An Analysis of Multidimensional Void Distribution in Two-Phase Flows*. Proc. Sixth International Topical Meeting on Nuclear Reactor Thermal Hydraulics (NURETH 6), 1, Grenoble, France, Oct. 5-8, 1993.
- Auton, T. R. (1987) *The Lift Force on a Spherical Body in a Rotational Flow*. J. Fluid Mech. 199-218, 1987.
- Bardina, J., Ferziger, J. H. & Reynolds, W. C. (1980) *Improved Subgrid Models for Large Eddy Simulation*. AIAA paper, 1980.
- Bel F'Dhila, R. & Simonin, O. (1992) *Eulerian Prediction of a Turbulent Bubbly Flow Downstream of a Sudden Pipe Expansion*. Proc. 6th Workshop on Two-Phase Flow Predictions, Erlangen, 30 March-2 April, 1992.
- Bocksell, T. L. & Loth, E. (1999) *A Random Walk Model for Bubbles and Particles*. Proc. 3rd ASME/JSME Joint Fluid Engineering Conference, San Francisco, California, July 18-23, 1999.
- Brevik, I., & Kluge, R. (1999) *On the Role of Turbulence in the Phenomenological Theory of Plane and Axisymmetric Air-Bubble Plumes*. International Journal of Multiphase Flow, 25, 87-108, 1999.
- Burns, A. D., Jones, I. P., Kightley, J. R. & Wilkes, N. S. (1989) *Harwell-Flow3D, Release 2 User Manual*. Harwell Report AERE-R (Draft), 1989.
- Castello-Branco, M. A. S. C. & Schwerdtfeger, K. (1994) *Large-Scale Measurements of the Physical Characteristics of Round Vertical Bubble Plumes in Liquids*. Metallurgical and Materials Transactions B, 25B, 359-371, 1994.
- Castillejos, A. H. & Brimacombe, J. K. (1987) *Measurement of Physical Characteristics of Bubbles in Gas-Liquid Plumes: Part II. Local Properties of Turbulent Air-Water Plumes in Vertically Injected Jets*. Metallurgical Transactions B, 18B, 659-671, 1987.
- Castillejos, E. A. H. & Brimacombe J. K. (1989) *Physical Characteristics of Gas Jets Injected Vertically Upward into Liquid Metal*. Metallurgical Transactions B, 20B, 595-601, 1989.
- CFX-F3D Version 4.1 User Manual (1995) AEA Technology, Harwell, UK, 1995.
- CFX-F3D Version 4.2 User Manual (1997) AEA Technology, Harwell, UK, 1997.
- CFX-F3D Version 4.3 User Manual (1999) AEA Technology, Harwell, UK, 1999.
- Crowe, C. T., Sharma, M. P. & Stock, D. E. (1977) *The Particle-Source-in-Cell (PSI-CELL) Model for Gas-Droplet Flows*. Journal of Fluids Engineering, 104, 297-303, 1977.
- Crowe, C. T., Troutt, T. R. & Chung, J. N. (1996) *Numerical Models for Two-Phase Flows*. Annu. Rev. Fluid Mech., 28, 11-43, 1996.
- Dang, P. & Schwarz, M. P. (1991) *Simulation of Mixing Experiments in Cylindrical Gas-Stirred Tanks*. Proc. Fourth International Symposium on Transport Phenomena in Heat and Mass Transfer, Sydney, Australia, July 14-19, 1991.
- Davidson, M. R. (1990) *Numerical Calculations of Two-Phase Flow in a Liquid Bath with Bottom Gas Injection: The Central Plume*. Appl. Math. Modelling, 14, 67-76, 1990.
- De Cachard, F. et al. (1997) *The First LINX-2 Tests*. Proc. 5th International Conference on Nuclear Engineering (ICONE 5-2448), Nice, France, May 26-30 1997.
- Deb Roy, T., Majumdar, A. K. & Spalding, D. B. (1978) *Numerical Prediction of Recirculation Flows with Free Convection Encountered in Gas-Agitated Reactors*. Appl. Math. Modelling, 2, 146-150, 1978.

- Delnoij, E., Lammers, F. A., Kuipers, J. A. M. & Van Swaaij, W. P. M. (1997) *Dynamic Simulation of Dispersed Gas-Liquid Two-Phase Flow Using a Discrete Bubble Model*. Ch. Eng. Sc., 52 (9), 1429-1458, 1997.
- Domgin, J. F., Gardin, P. & Brunet, M. (1999) *Experimental and Numerical Investigation of Confined Bubble Plumes*. Proc. Third ASME/JSME Joint Fluids Engineering Conference, San Francisco, California, USA, July 18-23, 1999.
- Drew D. A. & Lahey R. T. Jr. (1981) *Phase Distribution Mechanisms in Turbulent Two-Phase Flow in Channels of Arbitrary Cross Section*. ASME Journal of Fluids Engineering, 103, 583-589, 1981
- Drew, D. A. & Lahey, R. T. Jr. (1987) *The Virtual Mass and Lift Force on a Sphere in Rotating and Straining Inviscid Flow*. Int. J. Multiphase Flow, 13 (1), 113-121, 1987.
- Drew, D. A. (1983) *Mathematical Modelling of Two-Phase Flow*. Ann. Rev. Fluid Mech., 15, 261-291, 1983.
- Fogt, H. & Hafner, W. (1996) *Application of Two-Phase Modelling to the Time Dependent Flow in a Gas-Stirred Vessel*. ASME-FED, 236, 143-151, 1996.
- Friedl, M. J. (1998) *Bubble Plumes and Their Interactions with the Water Surface*. Diss. ETH No. 12667, 1998.
- Germano, M., Piomelli, U., Moin, P. & Cabot, W. H. (1991) *A Dynamical Subgrid-Scale Eddy Viscosity Model*. Phys. Fluids A, 3 (7), 1760-1765, 1991.
- Gouesbet, G., Berlemont, A. & Picart, A. (1984) *Dispersion of Discrete Particles by Continuous Turbulent Motions: Extensive Discussion of the Tchen's Theory, Using a Two-Parameter Family of Lagrangian Correlation Functions*. Physics of Fluids, 27 (4), 827-837, 1984.
- Goyal, P., Themelis, N. J. & Zanchuk, W. A. (1982) *Gaseous Refining of Anode Copper*. J. Met., 34, 22-28, 1982.
- Grevet, J. H., Szekely, J. & El-Kaddahn, N. (1982) *An Experimental and Theoretical Study of Gas Bubble Driven Circulation Systems*. Int. J. Heat Mass Transfer, 25 (4), 487-497, 1982.
- Gross, R. W. & Kuhlman, J. M. (1992) *Three-Component Velocity Measurements in a Turbulent Recirculating Bubble-Driven Liquid Flow*. Int. J. Multiphase Flow, 18 (3), 413-421, 1992.
- Iguchi, M., Demoto, Y., Sugawara, N. & Morita, Z. (1992) *Bubble Behavior in Hg-Air Vertical Bubbling Jets in a Cylindrical Vessel*. ISIJ International, 32 (9), 998-1005, 1992.
- Iguchi, M., Kawabata, H., Ito, Y., Nakajima, K. & Morita, Z. (1994) *Continuous Measurements of Bubble Characteristics in a Molten Iron Bath with Ar Gas Injection*. ISIJ International, 34 (12), 980-985, 1994.
- Iguchi, M., Kawabata, H., Nakajima, K. & Morita, Z. (1995) *Measurement of Bubble Characteristics in a Molten Iron Bath at 1600 °C Using Electroresistivity Probe*. Metallurgical and Material Transactions B, 26B, 67-74, 1995.
- Iguchi, M., Kondoh, T., Morita, Z., Nakajima, K., Hanazaki, K., Uemura, T. & Yamamoto, F. (1995) *Velocity and Turbulence Measurements in a Cylindrical Bath Subject to Central Bottom Gas Injection*. Metallurgical and Material Transactions B, 26B, 241-247, 1995.
- Iguchi, M., Shinkawa, M., Nakamura, H. & Morita, Z. (1995) *Mean Velocity and Turbulence of Water Flow in a Cylindrical Vessel Agitated by Bottom Air Injection*. ISIJ International, 35 (12), 1431-1437, 1995.
- Iguchi, M., Takeuchi, H. & Morita, Z. (1991) *The Flow Field in Air-Water Vertical Bubbling Jets in a Cylindrical Vessel*. ISIJ International, 31 (3), 246-253, 1991.
- Iguchi, M., Ueda, H. & Uemura, T. (1995) *Bubble and Liquid Flow Characteristics in a Vertical Bubbling Jet*. Int. J. Multiphase Flow, 21 (5), 861-873, 1995.
- Ilegbusi, O. J. & Szekely, J. (1992) *The Mathematical Modelling of Two-Phase Flow Phenomena in Secondary Steel Processing*. Proc. Tenth Process Technology Conference, Toronto, Canada, April 5-8, 1992.

- Ilegbusi, O. J. & Szekely, J. (1990) *The Modeling of Gas-bubble Driven Circulations Systems*. ISIJ International, 30 (9), 731-739, 1990.
- Ishii, M. & Mishima, K. (1984) *Two-Fluid Model and Hydrodynamic Constitutive Relations*. Nuclear Engineering and Design, 82, 107-126, 1984.
- Issa, R. I. & Oliveira, P. J. (1996) *Validation of Two-Fluid Model in Shear-Free Mixing Layers*. Fluids Engineering Division Conference, 236, 1996.
- Johansen, S. T., Boysan, F. & Ayers, W. H. (1987) *Mathematical Modelling of Bubble Driven Flows in Metallurgical Processes*. Applied Scientific Research, 44, 197-207, 1987.
- Johansen, S. T., Robertson, D. G. C., Woje, K. & Engh, T. A. (1988) *Fluid-Dynamics in Bubble Stirred Ladles: Part I. Experiments*. Metallurgical Transactions B, 19B, 745-754, 1988.
- Johansen, S. T. & Boysan, F. (1988) *Fluid-Dynamics in Bubble-Stirred Ladles: Part II. Mathematical Modelling*. Metallurgical Transactions B, 19B, 755-764, 1988.
- Joo, S. & Guthrie, R. I. L. (1992) *Modelling Flows and Mixing in Steelmaking Ladles Designed for Single- and Dual-Plug Bubbling Operations*. Metallurgical Transactions B, 23B, 765-778, 1992.
- Josson, P. & Jonsson, L. (1995) *A Model of Gas-Stirred Ladle*. Scandinavian Journal of Metallurgy, 24, 194-206, 1995.
- Kawakami, M., Kitazawa, Y., Nakamura, T., Miyake, T. & Ito, K. (1985) Trans. Iron Steel Inst. Jpn., 25, 394, 1985.
- Kitscha, J. & Kocamustafaogullari, G. (1989) Int. J. Multiphase Flow, 15 (4), 573-588, 1989.
- Kodama, S., Toi, T., Kataoka, I., Gofuku, A. & Serizawa, A. (1995) *Numerical Simulation of Two-Phase Natural Circulation Induced by a Bubble Plume*. Two-Phase Flow Modelling and Experimentation, 1, 117-124, 1995.
- Koh, P. T. L. (1987) *Measurement of Liquid Splashes Generated by Submerged Gas Injection*. CHEMECA 87, Melbourne, 1,36.1-36.8., 1997
- Koria, S. C. & Singh, S. (1989) *Measurements on the Local Properties of the Vertical Heterogeneous Buoyant Plume*. Steel Research, 60 (7), 301-307, 1989.
- Krishna Murthy, G. G., Ghosh, A. & Mehrotra, S. P. (1988) *Characterization of Two-Phase Axisymmetric Plume in a Gas-Stirred Liquid Bath - A Water Model Study*. Metallurgical Transactions B, 19B, 885-892, 1988.
- Kuo, J. T. & Wallis G. B. (1988) *Flow of Bubbles Through Nozzles*. Int. J. Multiphase Flow, 14(5), 1988.
- Kuo, T. C., Pan, C. & Chieng, C. C. (1997) *Eulerian-Lagrangian Computations on Phase Distributions of Two-Phase Bubbly Flows*. International Journal for Numerical Methods in Fluids, 24, 579-593, 1997.
- Kuwagi, K. & Ozoe, H. (1999) *Three-Dimensional Oscillation of Bubbly Flow in a Vertical Cylinder*. International Journal of Multiphase Flow, 25, 175-182, 1999.
- Lamb, H. (1932) *Hydrodynamics*. Cambridge University Press, 1932.
- Lance, M. & Bataille, J. (1991) *Turbulence in the Liquid Phase of a Uniform Bubbly Air-Water Flow*. J. Fluid Mech., 222, 95-118, 1991.
- Lance, M. & Lopez De Bertodano, M. (1994) *Two-Phase Flow Fundamentals*. Multiphase Science and Technology, 8, 69-124, 1994.
- Lathouwers, D. & Van Den Akker, H. E. A., *An Evaluation of Two-Fluid Models for Two-Phase Turbulent Bubbly Flows*. to be published in Merseburg Proceedings.
- Lee, S. L., Lahey, R. T. Jr. & Jones, O. C. Jr. (1989) *The Prediction Of Two-Phase Turbulence and Phase Distribution Phenomena Using a $k - \epsilon$ Model*. Japanese J. Multiphase Flow, 3 (4), 1989.
- Lee, S. L. (1987) *A Unified Theory of Particle Transport in a Turbulent Dilute Two-Phase Suspension Flow - II*. Int. J. Multiphase Flow, 13, 137-144, 1987.

- Leonard, A. (1974) *Energy Cascade in Large Eddy Simulations of Turbulent Fluid Flows*. Adv. in Geophys., A18, 237-248, 1974.
- Lilly, D. K. (1992) *A Proposed Modification of the Germano Subgrid-Scale Closure Method*. Phys. Fluids A, 4 (3), 633-635, 1992.
- Lopez De Bertodano, M. (1992) *Turbulent Bubbly Two-Phase Flow in a Triangular Duct*. Ph.D. Thesis, Rensselaer Polytechnic Institute, Troy, NY, 1992.
- MacInnes, J. M. & Bracco, F. V. (1992) *Stochastic Particle Dispersion Modeling and Tracer-Particle Limit*. Phys. Fluids A, 4 (12), 2809-2824, 1992.
- Malin, M. R. & Spalding, D. B. (1984) *A Two-Fluid Model of Turbulence and its Application to Heated Plane Jets and Wakes*. PCH Physico Chemical Hydrodynamics, 5 (5/6), 339-362, 1984.
- Matsumoto, Y. & Murai, Y. (1992) *Flow Structure in Bubbly Flow - Bubble Driven Plume in Aeration Tank*. Proc. Japan-U.S. Seminar on Two-Phase Flow Dynamics, Berkeley, California, USA, July 5-11, 1992.
- Mazumdar, D. & Guthrie, I. L. (1995) *The Physical and Mathematical Modelling of Gas-Stirred Ladle Systems*. ISIJ International, 35 (1), 1-20, 1995.
- Mazumdar, D. & Guthrie, R. I. L. (1986) *Numerical Computation of Flow and Mixing in Ladle Metallurgy Steelmaking Operations (C. A. S. Method)*. Appl. Math. Modelling, 10, 25-32, 1986.
- Mazumdar, D. (1992) *Mathematical Modelling of Ferroalloy Dissolution in Argon-Stirred Ladles*. Proc. Tenth Process Technology Conference, Toronto, Canada, April 5-8, 1992.
- Mietz, J. & Oeters, F. (1989) *Flow Field and Mixing with Eccentric Gas Stirring*. Steel Research, 60 (9), 1989.
- Milelli, M. (1998) *A State of the Art on Bubble Plumes Modelling and Experiments - Confined Bubble Plumes*. PSI internal report TM-42-98-30, ALPHA-829, 1-32, 1998.
- Milelli, M., Smith B. L., & Lakehal, D. (2001) *Subgrid-Scale Dynamic Modelling in LES of Turbulent Bubbly Flows*. Proc. TSFP2, Stockholm, Sweden, June 27-29, 2001.
- Mostafa, A.A. & Mongia, H. C. (1988) *On the Interaction of Particles and Turbulent Fluid Flow*. Int. J. Heat Mass Transfer, 31 (10), 2063-2075, 1988.
- Mudde, R. F. & Simonin, O. (1999) *Two- and Three-Dimensional Simulations of a Bubble Plume Using a Two-Fluid Model*. Chemical Engineering Science, 54, 5061-5069, 1999.
- Murai, Y., Yamamoto, F. & Matsumoto, Y. (1996) *Measurements of Bubble Motions in Bubble Plumes Using Image Processing*. Proc. Fourth Asian Symposium on Visualization, Beijing, China, May, 1996.
- Murai, Y. & Matsumoto, Y. (1996) *Numerical Simulation of Turbulent Bubble Plumes Using Eulerian-Lagrangian Bubbly Flow Model Equations*. ASME-FED, 236, 67-74, 1996.
- Murai, Y. & Matsumoto, Y. (1995) *Three-Dimensional Structure of a Bubble Plume - Measurement of the Three Dimensional Velocity*. ASME-FED, 209, 187-194, 1995.
- Pan, S. M., Ho, Y. H. & Hwang, W. S. (1997) *Three-Dimensional Fluid Flow Model for Gas-Stirred Ladles*. Journal of Materials Engineering and Performance, 6 (3), 311-318, 1997.
- Panidis, T. & Papailiou, D. D. (2000) *The Structure of Two-Phase Grid Turbulence in a Rectangular Channel: an Experimental Study*. International Journal of Multiphase Flow, 26, 1369-1400, 2000.
- Papanicolaou, P. N. & List, E. J. (1987) *Statistical and Spectral Properties of Tracer Concentration in Round Buoyant Jets*. Int. J. of Heat and Mass Transfer, 30, 2059-2071, 1987.
- Park, H-J. & Yang, W-J. (1996) *Numerical Study of Flow in Gas-Stirred Ladle Systems with and without Throughflow*. ASME-HTD, 334, 361-369, 1996.
- Park, H-J. & Yang, W-J. (1999) *Turbulent Two-Phase Mixing in Gas-Stirred Ladle Systems for Continuous Casting Applications*. Numerical Heat Transfer, Part A, 31, 493-515, 1997.

- Piomelli, U. (1999) *Large-Eddy Simulation: Achievements and Challenges*. Progress in Aerospace Sciences, 35, 335-362, 1999.
- Press, W. H. et al. (1989) *Numerical Recipes, The Art of Scientific Computing*. CUP, 1989.
- Ranade, V. V. (1997) *Modelling of Turbulent Flow in a Bubble Column Reactor*. Trans. IChemE, 75, part A, 1997.
- Rodi, W. (1984) *Turbulence Models and their Application in Hydraulics*. Institut für Hydromechanik, University of Karlsruhe, Germany, 1984.
- Roig, V., Suzanne, C. & Masbernat L. (1993) *Measurements in a Two-Phase Mixing Layer*. Experimental Heat Transfer, Fluid Mechanics and Thermodynamics, Elsevier Science, 1993.
- Roig, V. (1993) *Zones de Mélange d'Écoulements Diphasiques à Bulles*. PhD Thesis, Institut de Mécanique des Fluides de Toulouse, 1993.
- Sahajwalla, V., Castillejos, A. H. & Brimacombe, J. K. (1990) *The Spout of Air Jets Upwardly Injected into a Water Bath*. Metallurgical Transactions B, 21B, 71-80, 1990.
- Sato, Y. & Sekoguchi, K. (1975) *Liquid Velocity Distribution in Two-Phase Bubbly Flow*. Int. J. Multiphase Flow, 2, 79-95, 1975.
- Sato, Y., Sadatomi, M. & Sekoguchi K. (1981) *Momentum and Heat Transfer in Two-Phase Bubbly Flow - I Theory*. Int. J. Multiphase Flow, 7, 167-177, 1981.
- Schwarz, M. P., Musgrove, A. R., Hooper, J. D. & Dang, P. (1992) *Validation of Numerical Simulation of Gas Driven Bath Circulation by LDV Measurements*. Proc. Tenth Process Technology Conference, Toronto, Canada, April 5-8, 1992.
- Schwarz, M. P. & Turner, W. J. (1988) *Applicability of the Standard $k - \epsilon$ Model to Gas-Stirred Baths*. Appl. Math. Modelling, 12, 273-279, 1988.
- Schwarz, M. P. (1996) *Simulation of Gas Injection into Liquid Melts*. Appl. Math. Modelling, 20, 41-51, 1996.
- Serizawa, A. (1974) *Fluid Dynamics Characteristics of Two-Phase Flow*. Ph.D. Thesis, Kyoto University, Japan, 1974
- Sheng, Y. Y. & Irons, G. A. (1993) *Measurement and Modeling of Turbulence in the Gas/Liquid Two-Phase Zone During Gas Injection*. Metallurgical Trans. B, 24B, 695-705, 1993.
- Sheng, Y. Y. & Irons, G. A. (1995) *The Impact of Bubble Dynamics on the Flow in Plumes of Ladle Water Models*. Metallurgical Trans. B, 26B, 625-635, 1995.
- Simonin, O. & Viollet, P. L. (1988) *On the Computation of Turbulent Two-Phase Flows in the Eulerian Formulation*. EUROMECH 234, Toulouse, France, 1988.
- Sinha, U. P. & McNallan M. J. (1985) *Mixing in Ladles by Vertical Injection of Gas and Gas-Particle Jets - A Water Model Study*. Metallurgical Transactions B, 16B, 850-853, 1985.
- Smagorinsky, J. (1963) *General Circulation Experiments with the Primitive Equations*. Mon. Weather Rev., 91 (3), 99-165, 1963.
- Smith, B. L. & Milelli, M. (1998) *An Investigation of Confined Bubble Plumes*. Proc. 3rd International Conference on Multiphase Flow 98 - ICMF' 98, Lyon, France, 8-12 June 1998.
- Smith, B. L. (1999) *On the Modelling of a Bubble Plume in a Liquid Pool*. Appl. Math. Modelling, 22, 773-797, 1999.
- Sokolichin, A. & Eigenberger G. (1994) *Gas-Liquid Flow in Bubble Columns and Loop Reactors: Part I. Detailed Modelling and Numerical Simulation*. Ch. Eng. Sc., 49 (24B), 5735-5746, 1994.
- Stoop, P. M. et al. (1997) *TEPSS – Technology Enhancement of Passive Safety Systems*. Proc. 5th International Conference on Nuclear Engineering (ICONE 5-2172), Nice France, May 26-30 1997.
- Stuhmiller, J. H. (1977) *The Influence of Interfacial Pressure Forces on the Character of Two-Phase Flow Model Equations*. Int. J. Multiphase Flow, 3, 551-560, 1977.
- Szekely, J., Lehner, T. & Chang, C. W. (1979) *Flow Phenomena, Mixing and Mass Transfer in Argon-Stirred Ladles*. Ironmaking and Steelmaking, 6, 285-293, 1979.

- Tacke, K. H., Schubert, H. G., Weber, D. J. & Schwerdtfeger, K. (1985) *Characteristics of Round Vertical Gas Bubble Jets*, Metallurgical Transactions B, 16B, 263-275, 1985.
- Taylor, J. J. & Stahlkopf, K. E. (1988) *The U.S. Advanced Light Water Reactor Program – A Case for Simple, Passive Safety Systems*,. Proc. Int. Topl. Mtg. Safety of Next Generation Power Reactors, Seattle, Washington, May 1-5, 1988, p. 22, American Nuclear Society (1988).
- Theofanous, T. G. & Sullivan, J. (1982) *Turbulence in Two-Phase Dispersed Flows*. J. Fluid Mech., 116, 343-362, 1982.
- Tran, M. L. (1997) *Modélisation Instationnaire de la Distribution Spatiale des Phases dans les Écoulements Diphasiques en Régime à Bulles*. PhD thesis Université Lyon 1, 1997.
- Tsuji, Y., Morikawa, Y. & Terashima, K. (1982) *Fluid-Dynamic Interaction Between Two Spheres*. Int. J. Multiphase Flow, 8 (1), 71-82, 1982.
- van Wijngaarden, L. (1976) *Hydrodynamic Interaction Between Gas Bubbles in Liquid*. J. Fluid Mech., 77 (1), 27-44, 1976.
- Viollet, P. L., Simonin, O., Olive, J. & Minier J. P. (1992) *Modelling Turbulent Two-Phase Flows in Industrial Equipments*. Computational Methods in Applied Sciences, Elsevier, 1992.
- Viollet, P. L. & Simonin O. (1994) *Modelling Dispersed Two-Phase Flows: Closure, Validation and Software Development*. Appl. Mech. Rev., 47 (6), part 2, 1994.
- Wallis, G. B. (1969) *One-Dimensional Two-Phase Flow*. McGraw-Hill, 1969.
- Wang, D. M., Issa, R. I. & Gosman, A. D. (1994) *Numerical Prediction of Dispersed Bubbly Flow in a Sudden Enlargement*. Numerical Methods in Multiphase Flow, 185, 1994.
- Wang, S. K., Lee, S. J., Lahey, R. T. Jr. & Jones, O. C. (1987) *3-D Turbulence Structure and Phase Distribution Measurements in Bubbly Two-Phase Flows*. Int. J. Multiphase Flow, 13 (3), 327-343, 1987.
- Watanabe, S., Murai, Y. & Yamamoto, F. (1997) *Three-Dimensional Restoration of Bubble Distribution Using Stereo Image Processing*. Proc. Third International Conference on Fluid Dynamic Measurement and Its Applications, Beijing, China, October, 1997. (in press).
- Xie, Y., Orsten, S. & Oeters, F. (1992) *Behaviour of Bubbles at Gas Blowing into Liquid Wood's Metal*. ISIJ International, 32 (1), 66-75, 1992.
- Xie, Y. & Oeters, F. (1992) *Experimental Studies on the Flow Velocity of Molten Metals in a Ladle Model at Central Gas Blowing*. Steel Research, 63 (3), 93-104, 1992.
- Xie, Y. & Oeters, F. (1992) *Experimental Studies on the Bath Oscillation During Gas Blowing into Liquids, Part 1: Measurements Using a Single Nozzle*. Steel Research, 6, 227-233, 1992.
- Xie, Y. & Oeters, F. (1994) *Measurement of Bubble Plume Behaviour and Flow Velocity in Gas-Stirred Liquid Wood's Metal with an Eccentric Nozzle Position*. Steel Research, 65 (8), 315-319, 1994.
- Yamamoto, F., Murai, Y., Song, X-Q. & Iguchi, M. (1997) *Advances in PIV Measurement of Multiphase Flow*. Proc. International Symposium on Multiphase Fluid, Beijing, China, October, 1997 (in press).
- Zhou, X., Luo, K. H. & Williams, J. J. R. (1999) *Large Eddy Simulation of Spatially Developing Isothermal and Buoyant Jets*. Proc. Third ERCOFTAC Workshop on Direct and Large Eddy Simulation, Cambridge, UK, May 12-14, 1999.
- Zhu, M., Sawada, I., Yamasaki, N. & Hsiao T. (1996) *Numerical Simulation of Three-Dimensional Fluid Flow and Mixing Process in Gas-Stirred Ladles*. ISIJ International, 36 (5), 503-511, 1996.
- Zuber, N. (1964) *On the Dispersed Two-Phase Flow in the Laminar Flow Regime*. Chemical Engineering Science, 19, 897, 1964.

Curriculum Vitae

Name: Massimo Milelli

Nationality: Italian

Birth: September 4, 1970, in Torino, Italy

Education:

Oct. 1976 – Jun. 1984	Primary and Secondary School in Torino, Italy
Oct. 1984 – Jun. 1989	High school in Cirie' (TO), scientific division.
Oct. 1989 – Mar. 1995	Study of Physics at the University of Torino, Italy.
Apr. 1995 – Apr. 1996	Mandatory civil service.
Feb. 1997 – Mar. 2001	Doctoral work at PSI and ETH.